Functional Microcircuitry of the Granular Retrosplenial Cortex

by

Ellen K.W. Brennan

A dissertation submitted in partial fulfillment
of the requirements for the degree of
Doctor of Philosophy
(Neuroscience)
in the University of Michigan
2021

Doctoral Committee:

Assistant Professor Omar J. Ahmed, Chair
Professor Victoria Booth
Professor Lori Isom
Assistant Professor Michael Roberts
Associate Research Scientist Kelli A. Sullivan

Ellen K.W. Brennan

ewixted@umich.edu

ORCID iD: 0000-0001-8535-7188

© Ellen KW Brennan 2021

DEDICATION

To Apollo, for getting me to the beginning;

to Kitty, for making sure I wasn't alone;

to Guinness, for his constant vigilance;

and to Gunner, for seeing me through every step of the way.

ACKNOWLEDGEMENTS

This dissertation would not have been possible without the people and dogs who were by my side. There are truly so many of you who have had such a positive and lasting impact on my life, and I hope you know how valuable you are.

First, I must thank my advisor and mentor, Dr. Omar Ahmed. I first met Omar when I was a senior in undergrad over a video call, long before zoom calls were cool. Over this video call, I was inspired by Omar's knowledge, approachability, and genuine excitement for science. What stood out the most during this meeting was his immediate support and faith in me. Upon this very first conversation, he offered to help me apply to and then completely pay for a prestigious month-long training program in electrophysiology, and this was *before* I joined his lab. His commitment to my progress never changed, even though I am *sure* I did not always make it easy for him. Whether I came into Omar's office with new ideas for projects or with thoughts of leaving the program, his support never wavered. He encouraged my decision to pursue a career in science communication rather than research, writing countless letters for me to attend conferences and events unrelated to my work in the lab. He set rigorously high expectations, and he always helped me reach them. His vision of the lab and the projects we could accomplish combined with his personalized approach to mentoring pushed me to achieve far more than I thought I could. With his guidance, I became a (mostly) confident independent researcher and a far better communicator. It is no

exaggeration when I say that I would not have finished this Ph.D. had I worked with another mentor. So I think, in the fewest words possible, I have to say thank you for always encouraging my goals regardless of their purpose, never turning me away from a new idea or challenge, and never allowing me to lose faith in myself.

Second, I must thank the team Omar has cultivated. I have never known more capable, curious, and delightful scientists, and I have no doubt that this is a lab and a people who will achieve greatness. To everyone who ever passed through the Omar Lab, thank you for being such a profoundly talented and welcoming group of people. To Shyam, thank you for your endless patience as I battled MATLAB (unsuccessfully). And to Danny, thank you so much for taking up the role of MATLAB savior when Shyam moved on to his new position. You may have thought our brief zoom chats were minor, but they truly saved me days of confusion. You are an artist. To Sameer, thank you for always being fun to work with. Even when deadlines got tight, meetings with you were always relaxed and productive. You swooped in and rocked our computational modeling in the most impressive ways. To Alcides, Megha, Tibin, Sharena, and everyone else thank you so much for your fun conversation and companionship. You all made an environment that could have so easily been stressful a comfortable place. To Vaughn, thank you for knowing far more than one would think capable of a single person. You truly are inhuman, but you were never intimidating or unwilling to help. After five years of working alongside you and seeing unrelenting noise issues disappear in your presence, my only conclusion is that you are a practitioner of dark magic. Some of the most frustrating troubleshooting moments became fun because who doesn't love seeing a literal wizard stumped. Thank you for always helping without hesitation, even when we

had no idea what we were doing. And to Izabela, thank you for remaining ever hopeless with me in the rig room. You completely brightened my graduate experience, and you are without a doubt the most capable researcher I have ever, and likely will ever, meet. You have had a hand in so much of what this lab has accomplished, and you've become someone we all rely on. If you ever question yourself, just remember how much you taught yourself and how much you've already achieved. This work is yours, too. I will never be able to express how much I cherish our friendship, even though you don't like food. I almost, ever so slightly, just a teensy tiny bit, *might* miss running experiments in the rig room with you. Almost. To all of you and everyone else, thank you for being exactly who you are. I stayed because of all of you, so it is because of you that I made it here.

Next, I need to thank my committee members for their constant support and encouragement. Drs. Lori Isom, Kelli Sullivan, Michael Roberts, and Victoria Booth were perhaps the ultimate dream committee. Their diverse skillsets meant that they always had helpful comments and suggestions on my work, and they complemented one another perfectly. I looked forward to committee meetings rather than being nervous because they had become a space where we celebrated the work accomplished and talked casually and enthusiastically about the next options. There was no pressure to perform, only excitement to share. I have always deeply appreciated their support for my individuality; they never asked me to be more "academic" or impersonal with my delivery, instead supporting and outright encouraging my presentation styles and love of bright colors, fun graphics, and jokes. Outside of these meetings, they were always available for instant support, whether I needed to borrow some water from Dr. Roberts

to troubleshoot unhappy slices or wanted a hot cocoa break with Dr. Sullivan while considering my future path outside of research. Thank you so much for helping me learn what I am capable of and who I am as a scientist.

I became a lot more than just a researcher in my time as a graduate student. I became a presenter, communicator, performer, and advocate all because some amazing people within the scicomm world accepted me as soon as I reached out. In my second year, I decided to apply for the Michigan ComSciCon conference, and that was the weekend my life fell into place. This conference was the first time in my graduate experience when I felt like the people with whom I was engaging had the same values as me. It was a community in which I truly belonged. At this conference, I met amazing people like Drs. Sarah Kearns, Stephanie Deppe, and Jess Chen who would transform my entire life trajectory. Whether it was Jess getting me my first internship on a communications team, Stephanie helping me negotiate job offers, or Sarah teaching me how to run a scicomm blog, they all helped me navigate the world I had chosen to enter for my career. Their encouragement helped me co-chair future conferences, where I got to meet even more amazing people like Sara Hugentobler and create my own workshops on inclusive communication. Jess and I cheered each other on while we each gave award-winning presentations at the 2020 AAAS Annual Meeting, and at this same meeting, I finally got to meet the inspiring Dr. Susanna Harris in person who, alongside the wonderful Tayler Catherine Kent, had helped me find a voice and community through PhD Balance just one year prior. Meeting each of these individuals shaped my goals and my path, and I am so thankful for their guidance and friendship.

When I think of individuals who have had the biggest impact on my graduate experience, Dr. Keith Duncan is right up at the top of the list. His commitment to bettering the scientific community and the researcher experience is inspiring, and the many programs he has dreamed up, funded, and implemented have without a doubt helped countless professionals at our university. Keith is the one who got me into improv classes, and it is that unconventional program that served as the catalyst for my greatest growth in graduate school. I became more confident, clear, and capable in the Pointless classrooms than I ever had in the lab. From my troupe mates in Kitty's Book Corner to my graduating classmates to all the instructors I had, the Pointless community is the part of Michigan I will miss most when I leave. I have never laughed harder, been more nervous, or felt prouder than the times we shared in the theater and zoom rooms. From these experiences, Keith encouraged me to leverage improv fundamentals to create communication tools for researchers. This endeavor helped me realize what my passions surrounding science communication were and directly influenced my career trajectory. Whether things in lab or on the Pointless stage went right or wrong, Keith was usually the first person I would email. If every STEM program had a few more Keiths, the academic landscape would be a much better place.

Beyond the lessons I learned from my many mentors, I am eternally grateful for the many insights shared by my friends. My Burlington friends, especially Katie, inspired me to apply for graduate school and pursue my dreams of academia. Although those dreams changed almost instantly, the Box from East Ave stood by me every step of the way. While we were scattered across the country, we always connected and laughed as we each stumbled our way into our various disciplines. To Katie, Sarah, Dennis, Rosa,

Irene, and all the rest of you, thank you so much for being true friends in these wild times. I was also extremely lucky to make some of the finest friends a person could have in my first few weeks here in Michigan. Veronica, I am beyond thankful that you followed me home to invade our study group that day in our first semester. I could not have asked for a better friend, drinking partner, co-house hunter, and quest narrator. While we got cheated out of our trip to Spain, I still plan on galivanting around Europe with you one day. Vinodh, we have said many things, and I want you to know that I meant every single one of them. Thank you for consistently providing some rational thinking as Veronica and I panicked about minor things, but perhaps most importantly, thank you for ordering cookies nearly every time you came over. Michael, your sunny disposition was a welcome ray of positivity, and your couch is one of my favorite places in Ann Arbor. Kachi, I could not have asked for a better estate sale questing partner. If I am ever in need of a bard, you will be the first person I call. I could not have done this Alone, and the times I spent with all of you were truly the best part of graduate school. I suggest you let that one marinate.

And of course, I also need to thank my family, particularly my parents. Both of my parents left their Ph.D. programs early after realizing that academic research careers were not what they wanted in life. From the moment I said I wanted to apply to graduate school, my parents provided the perfect balance of support and honesty. They knew how difficult a path it would be, especially if research was not what I truly enjoyed. Whether I called them excited about something I had discovered or in tears questioning why I made this choice, they supported every step I took and every step I considered taking without judgement or hesitation. When we were kids, my parents never told my

sisters or I what we had to do; they let us discover our own paths for ourselves. They taught us that grades and numbers do not define success; our choices do. If we pursued something that makes us happy and we never gave up, we had succeeded regardless of the outcome. To be raised with that mentality is a really powerful thing. So much of my determination comes directly from who they taught me to be, and I am so grateful for that. I was also often inspired by my older sisters, as they each found their passions and pursued them regardless of the many challenges they faced along the way. My family is made up of resilient women, and their support throughout my life made me strong enough to reach where I am today.

Lastly, I need to thank my husband, Gunner, and our little pack. Shooter has always been the fun and adventurous one, and he made sure I still enjoyed life during the most stressful times of graduate school. He was endlessly patient and supportive, always picking me up from lab if I missed the bus, making dinner, cleaning the kitchen, or doing anything else I asked with just the right amount of grumbling. Whether things went right or terribly wrong, Archer often had flowers or dessert waiting for me. He prioritized my goals and dreams above his own, moving halfway across the country from where he would rather be just so I could learn what I wanted out of my career. And above it all, he has always reminded me what was truly important and that I was still capable having some fun and enjoying life. I could not have made it through a single moment without Pistol, Apollo, Kitty, and Guinness by my side. Truly, Bomber, I have spent weeks trying to write this section to thank you and have yet to come up with words that will do it justice. Just know that I love you, and I am beyond excited to finally start living the life we've been dreaming of together. Now pitter patter, let's get going.

TABLE OF CONTENTS

LIST OF TABLES

LIST OF FIGURES

ABSTRACT

The granular retrosplenial cortex (RSG) is essential for successful spatial navigation and memory, but the cell types and cellular computations underlying these functions remain poorly understood. Using a multifaceted approach combining whole-cell patch clamp recordings, imaging, pharmacological interventions, and computational models, this dissertation provides a comprehensive investigation of the cells, circuits, and computations employed by the RSG to support navigational functions. In Chapter 2, we identify a unique, hyperexcitable pyramidal cell type localized to the superficial layers of RSG, which we name the low-rheobase (LR) neuron. We show that the intrinsic properties of LR cells make them ideally suited to encode persistent spatial information over long durations. In Chapter 3, we then show that these LR neurons are strongly and preferentially targeted by directional and spatial inputs from the anterior thalamus and dorsal subiculum due to the precise anatomical overlap of LR dendrites and thalamic/subicular afferents. In contrast, neighboring regular-spiking (RS) cells are targeted by mostly non-spatial claustral and anterior cingulate inputs, establishing parallel RSG circuits that encode spatial versus non-spatial signals. Using computational modeling, we show that LR cells can conjunctively encode head direction and speed as a result of the uniquely depressing nature of their anterior thalamic synaptic inputs, providing a robust mechanism for the conjunctive encoding of spatial orientation information in the RSG. Lastly, in Chapter 4, we show that LR neuron activity

is not directly modulated by acetylcholine, suggesting that LR spatial coding is consistent across behavioral states and independent of cholinergic tone. Taken together, the results presented in this dissertation strongly suggest that LR neurons are critical for the encoding of spatial orientation information in the RSG and provide a specific circuit and synaptic mechanisms underlying retrosplenial contributions to successful navigational control.

CHAPTER 1: Introduction

1.1 Abstract

Since the case study of patient H.M. was published in 1957, the hippocampus has dominated the spotlight in memory and navigation research more than any other region in the brain. However, an exponential increase of work over the past two decades has established the retrosplenial cortex as an equally important contributor to learning, memory, and spatial navigation. Here, we review the inputs, outputs, and spatial codes employed by the retrosplenial cortex to support successful navigation. We explore the various ways in which retrosplenial neurons and ensembles encode space to demonstrate that this region is capable of the integration of egocentric and allocentric information to generate novel representations of space that directly support the larger navigational circuits of the brain. Lastly, we highlight the importance of multifaceted examinations of the neuronal subtypes and synaptic dynamics that facilitate the differential spatial functions of the distinct subregions of the retrosplenial cortex.

1.2 Introduction

1.2.1 Introduction to the retrosplenial cortex as a navigationally important region

In 1987, one of the first case studies of a patient with damage localized to a region called the retrosplenial cortex (RSC) was published (Valenstein et al., 1987). This case study reported significant impairments in the patient's ability to recall memories, form new memories, and navigate familiar environments (Valenstein et al., 1987). These same memory and spatial impairments were reported in a prior case study of a patient with more widespread bilateral lesions that damaged the fornix, retrosplenial cortex, and posterior cingulate cortex (Heilman and Sypert, 1977). While these findings provided clear evidence for the necessary role of the RSC in both memory and navigation, the RSC remains relatively understudied. Since the publishing of the retrosplenial case study in 1987, only 9,805 studies on the RSC have been uploaded to PubMed when searching the term "retrosplenial cortex", with 457 new publications in 2020. In contrast, a search for "hippocampus" returns 167,349 studies since the famous case study of patient H.M. was published 30 years prior in 1957, with 8,279 published in 2020 alone (Figure 1-1).

Examinations of patients with retrosplenial damage have established a distinct profile of disorientation that manifests as an inability to navigate routes through even familiar environments (Bottini et al., 1990; Heilman and Sypert, 1977; Ino et al., 2007; Osawa et al., 2007; Valenstein et al., 1987). This disorientation is not a result of the patient forgetting the spatial landmarks that identify these locations, but rather the

inability to use those landmarks to orient themselves (Ino et al., 2007; Osawa et al., 2007). Without this clear sense of orientation, or direction, patients are unable to identify how physical spaces are linked to one another and successfully navigate between them. This specific disorientation profile parallels that seen in degenerative diseases like Alzheimer's disease (Grossi et al., 2007; Guariglia and Nitrini, 2009; Henderson et al., 1989; Monacelli et al., 2003) and Parkinson's disease (Hovestadt et al., 1987), which both also exhibit retrosplenial impairment (Chen et al., 2017; Hou et al., 2020; Minoshima et al., 1997; Nagano-Saito et al., 2004; Nestor et al., 2003; Pengas et al., 2010; Potvin-Desrochers et al., 2019; Scheff et al., 2015). In animals, retrosplenial lesions significantly impair performance on spatial (Harker and Whishaw, 2004; Pothuizen et al., 2010; van Groen et al., 2004; Vann et al., 2003; Vann and Aggleton, 2005, 2002) and contextual fear learning tasks that rely on spatial features (Katche et al., 2013; Keene and Bucci, 2008b; Lukoyanov and Lukoyanova, 2006). While the RSC's role in navigation is now well-established, the exact mechanisms by which it supports this function, and thus how these mechanisms may become impaired in disease, are still largely unknown.

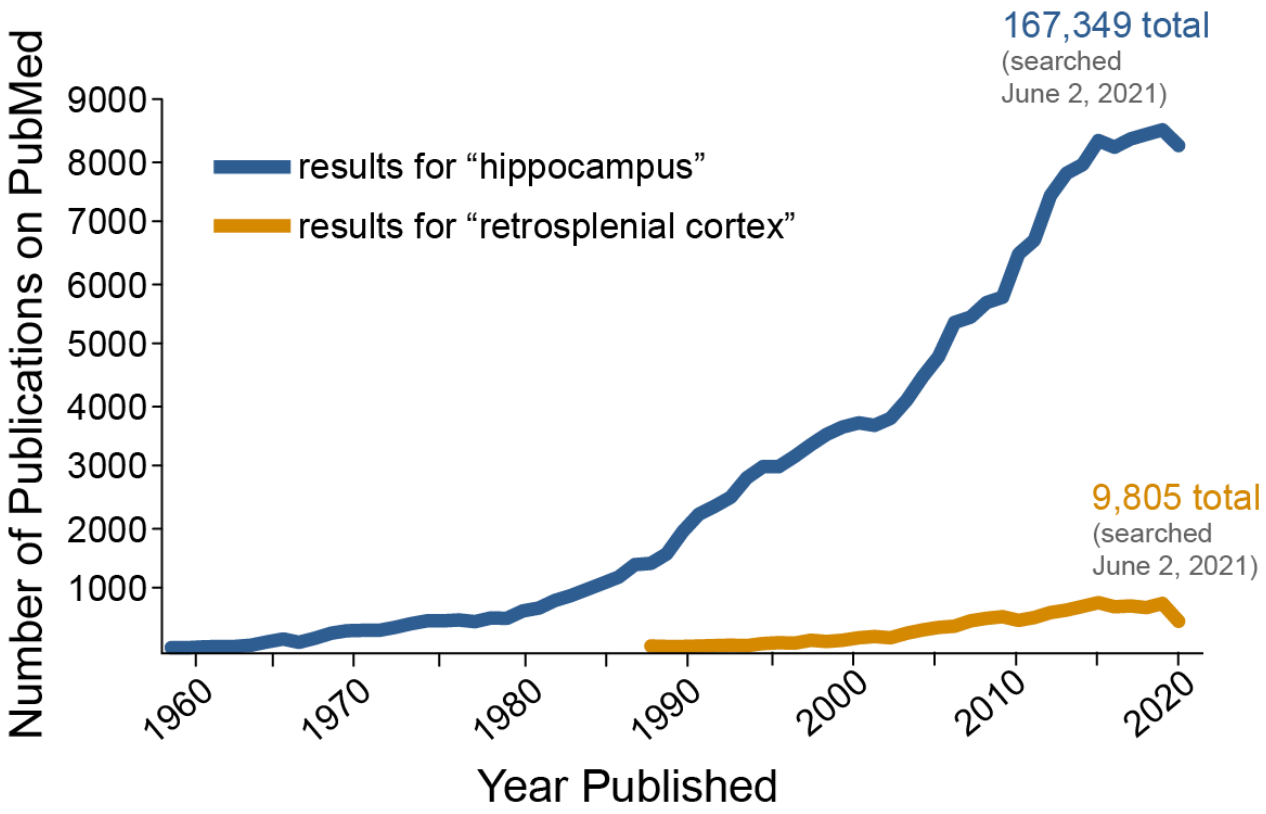

Figure 1-1. Hippocampal and retrosplenial publication records on the PubMed.gov search engine. The terms “hippocampus” and “retrosplenial cortex” were each searched on PubMed.gov on June 2, 2021. The resulting publication counts for hippocampal and retrosplenial studies since the publication of their first significant case reports in 1957 and 1987, respectively, are plotted by year to highlight the extent to which the RSC remains understudied.

1.2.2 Spatially relevant inputs to the retrosplenial cortex

The importance of the RSC in navigation is highlighted by the wide array of precisely organized spatially relevant inputs it receives, serving as a primary site of convergence for spatial, sensory, and motor signals in the brain (Figures 1-2 to 1-5; Greicius et al., 2009; Kaboodvand et al., 2018; Liu et al., 2019; van Groen and Wyss, 2003, 1992, 1990; Whitesell et al., 2021). The RSC is divided into two anatomically distinct subregions, the dysgranular (RSD) and granular (RSG) areas, that each exhibit unique neuronal populations, laminar organization, inputs, and outputs (Figures 1-2 to 1-5; Ichinohe et al., 2008; Pothuizen et al., 2009; Sripanidkulchai and Wyss, 1987; van Groen and Wyss, 2003, 1992, 1990). The granular region is further divided into areas a and b, with some studies also including an area c, which also display unique connectivity patterns (van Groen and Wyss, 2003, 1992, 1990). Distinct inputs to each retrosplenial subregion provide an anatomical basis for the differential contributions of RSD and RSG to the encoding of space (Pothuizen et al., 2010, 2009; van Groen et al., 2004; Vann and Aggleton, 2005). For example, the RSD, specifically, receives dense visual inputs and subsequently has been implicated in visuospatial processes (Hindley et al., 2014; Hindley et al., 2014; van Groen and Wyss, 1992; Vann and Aggleton, 2005), while area b of RSG, but not area a, serves as a major site of direction and location integration and is more implicated in spatial learning rather than processing relevant sensory cues (Pothuizen et al., 2009; van Groen et al., 2004; van Groen and Wyss, 2003). It is important, then, to establish a detailed retrosplenial connectome in order to facilitate a comprehensive view of the microcircuits underlying its navigational

functions, with extra care being taken to acknowledge differential targeting of distinct retrosplenial subregions and cells.

Anterior Thalamus

One of the main sources of spatial input to the RSC is the anterior thalamus, specifically the anterodorsal and anteroventral nuclei (ADAV; Robertson and Kaitz, 1981; Shibata, 1993; van Groen and Wyss, 2003, 1992, 1990). The ADAV contains the highest proportion of specialized neurons that encode head direction (HD) in the brain, with the majority of these cells located in AD (Blair et al., 1997; Taube, 1995). Individual HD cells each exhibit a preferred orientation at which they will fire continuously so long as the animal's head is facing that preferred direction with respect to the environmental surroundings (Taube, 1998, 1995). These preferred orientations can be controlled by external cues, such as visual landmarks (Goodridge et al., 1998; Taube, 1995), as well as idiothetic cues, such as vestibular inputs or internal representations of space (Goodridge et al., 1998; Stackman and Taube, 1997), and the specificity with which an HD cell is tuned to its preferred orientation can vary based on whether the animal is turning clockwise or counterclockwise (Blair et al., 1997). HD cells in AD are thought to compute head direction via the integration of the angular head velocity with current head direction (McNaughton et al., 1991) in order to predict which direction the head will be facing in the near future. Indeed, AD HD cells exhibit an anticipatory time interval (ATI) at which they will increase their firing rate before the animal's head is facing their preferred direction, providing an updated sense of direction over time that can then inform path integration processes (Blair et al., 1997; Blair and Sharp, 1995; McNaughton et al., 1991; Redish et al., 1996).

The anterior thalamic nuclei are among the matrix thalamic nuclei group (Jones, 2001, 1998; Morison and Dempsey, 1941; Rubio-Garrido et al., 2009), and matrix thalamocortical projections predominantly target layer 1 (Herkenham, 1986, 1980; Rubio-Garrido et al., 2009) to innervate multiple neuronal subtypes at their apical dendrites (Anastasiades et al., 2021; Collins et al., 2018; Cruikshank et al., 2012; Delevich et al., 2015; Guo et al., 2018; Rodriguez-Moreno et al., 2020; Rubio-Garrido et al., 2009; Van Der Werf et al., 2002; Yamawaki et al., 2019b). Consistently, projections from ADAV exhibit a precise targeting of retrosplenial layer 1 (Figure 1-2; van Groen et al., 1993; Yamawaki et al., 2019b). Both AD and AV project to the entire longitudinal extent of the RSG in a topographic manner, such that neurons in the caudal ADAV project to rostral RSG and vice versa (Robertson and Kaitz, 1981; Shibata, 1993; Sripanidkulchai and Wyss, 1987; van Groen et al., 1993). AV projects to layer 1a and the border of layers 3/5 of RSG, while AD projects more broadly to upper layer 1, layer 3, and the border of layers 3/5 (van Groen and Wyss, 2003, 1990). These AV projections also extend to RSD layer 1, though to a much weaker degree (van Groen and Wyss, 1992), while AD projections are more precisely localized to RSG (van Groen and Wyss, 2003, 1992, 1990). Functional studies have shown that layer 5 pyramidal cells in RSG, specifically, are directly innervated by AV inputs most strongly at their apical dendrites (Yamawaki et al., 2019b), though little research has examined how superficial RSG neurons whose cell bodies and dendrites exist in the layers targeted by these inputs (van Groen et al., 1993) interact with ADAV afferents.

How might these ADAV inputs contribute to the navigational functions of the RSC? Other spatial regions like the hippocampus and dorsal subiculum (DS) partly rely

on the anterior thalamic directional code (Goodridge and Taube, 1997; Hargreaves et al., 2007; Viejo and Peyrache, 2020), such that hippocampal replay of sequences during NREM sleep are coupled with precise, homogenous ADAV HD cell activity to support more precise spatial representations (Viejo and Peyrache, 2020), and DS neuronal populations lose their ability to code for direction in the absence of ADAV HD input (Goodridge and Taube, 1997). Similarly, lesions of ADAV significantly reduce retrosplenial activity (Dupire et al., 2013; Mendez-Lopez et al., 2013; Poirier and Aggleton, 2009) and synaptic plasticity (Garden et al., 2009), mostly in the granular region, while lesions to neighboring thalamic nuclei such as the laterodorsal nucleus have no effect on the RSC (Poirier and Aggleton, 2009). Thus, it is likely that these directional projections from ADAV, specifically, provide necessary inputs for maintaining healthy retrosplenial signaling and spatial coding.

Hippocampus

The hippocampus is perhaps the most well-known of the spatially relevant regions, particularly for the discovery of place cells within CA1 (O'Keefe and Dostrovsky, 1971). Individual place cells selectively fire when the animal is in a specific location in the environment, creating "place fields" which adapt, or remap, with changes in the environment (Alvernhe et al., 2011; Burke et al., 2011; Knierim, 2003; Roth et al., 2012). The sequences with which a group of place cells fire then provide a map of the animal's trajectory through that environment (Dragoi and Buzsáki, 2006; O'Keefe and Recce, 1993), and the replay of these sequences in sharp wave ripples during sleep facilitates spatial memory consolidation (Buzsáki, 2015; Taxidis et al., 2015; Wilson and McNaughton, 1994). In addition to place cells, hippocampal neurons employ rate codes

to encode a wide variety of spatial features, such as direction (Acharya et al., 2016; McNaughton et al., 1983), turning behavior (Ainge et al., 2007; Frank et al., 2000; Wood et al., 2000), speed (McNaughton et al., 1983), and context (GoodSmith et al., 2017; Hunsaker et al., 2008; Jinde et al., 2012; Scharfman, 2019, 1992). This spatial information is then transmitted to other regions, including the RSC, predominantly via the subiculum and entorhinal cortex (Andersen et al., 1973; O'Mara, 2006; Wyss and van Groen, 1992; Yamawaki et al., 2019a), though direct projections from CA1 to the RSC have also been identified (Figure1-3; Wyss and van Groen, 1992; Yamawaki et al., 2019b). Long-range inhibitory projections from dorsal CA1 precisely target layer 1a of RSG areas a and b, directly innervating and inhibiting layer 5 pyramidal neurons at their apical tufts (Yamawaki et al., 2019b).

In humans, both hippocampal and retrosplenial volume are positively correlated with performance on location tracking and path integration tasks (Chrastil et al., 2017), which require recruitment of both regions (Chrastil et al., 2017, 2015; Sherrill et al., 2013). Retrosplenial coding of spatial sequences partly relies on hippocampal input, as bilateral lesions of the hippocampus result in a decreased proportion of place cells and significant disorganization of place sequence firing in RSD (Mao et al., 2018), while significant decreases of cellular activity are observed in all layers and subregions of the RSC (Albasser et al., 2007). Thus, the hippocampus works in tandem with the RSC performing analogous spatial functions, and the interaction between these two regions likely plays a key role in supporting retrosplenial spatial codes.

Entorhinal Cortex

The entorhinal cortex is part of the larger hippocampal formation and contains several distinct spatially responsive cell types (Gu et al., 2018; Hafting et al., 2005; Iwase et al., 2020; Savelli et al., 2008). Grid cells, which are located in the medial entorhinal cortex (MEC), fire at regular intervals as the animal traverses an environment to form a grid-based map of the environment that is anchored to external landmarks (Gu et al., 2018; Hafting et al., 2005; Savelli et al., 2008). Similar to hippocampal place cells, grid cells exhibit remapping via both the changing of their firing rates and realignment of their grid fields when exposed to significant changes in environment location, size, or shape (Fyhn et al., 2007; Savelli et al., 2008), but they provide a stable representation of space when exposed to contextual changes that are sufficient to induce rate remapping in hippocampal place cells, such as color or light adjustments (Fyhn et al., 2007). The MEC also contains speed cells whose firing rates exhibit a linear relationship with the animal's running speed (Iwase et al., 2020; Kropff et al., 2015), relying on both self-motion and visual cues (Campbell et al., 2018; Pérez-Escobar et al., 2016). It has been proposed that the integration of these grid and speed cell signals in the MEC facilitate its role in path integration (Gil et al., 2018; McNaughton et al., 2006; Sargolini et al., 2006), as the combination of location and locomotion information from grid and speed cells, respectively, is necessary to maintain an updated representation of the animal's location at any given moment (Fuhs and Touretzky, 2006; McNaughton et al., 2006; Redish et al., 1996).

The entorhinal cortex sends projections to the RSC both directly and through extensive connections with the subiculum (Figure 1-3; Aggleton et al., 2012; Witter, 2006; Wyss and van Groen, 1992). Layers 5/6 of the caudal entorhinal cortex project

predominantly to layer 1 of the RSD, though these projections are relatively sparse (Aggleton et al., 2012; Insausti et al., 1998; Wyss and van Groen, 1992). In contrast, the entorhinal cortex is extensively interconnected with the dorsal subiculum (Witter, 2006), which then sends precisely targeted projections to layer 3 of RSG (Wyss and van Groen, 1992; Yamawaki et al., 2019a). Thus, it is possible that the complex spatial representations facilitated by grid and speed coding in the MEC are relayed to the RSC through both mono- and disynaptic streams.

Dorsal Subiculum

Another key source of spatial input to the RSC is the dorsal subiculum (DS; (Nitzan et al., 2020; Wyss and van Groen, 1992; Yamawaki et al., 2019a), which serves as the main output structure of the hippocampus (Amaral et al., 1991; Witter, 2006), relaying hippocampal and entorhinal signals, in addition to its own spatial signals, to widespread areas across the brain (Aggleton and Christiansen, 2015; Honda and Ishizuka, 2015; Kinnavane et al., 2018; Kloosterman et al., 2003; Swanson and Cowan, 1977). In contrast to the uniform presence of HD cells in ADAV, the vast majority of DS neurons represent a heterogenous mix of spatially responsive cells (Sharp, 1999; Sharp and Green, 1994; Simonnet and Brecht, 2019). Approximately 15-25% of neurons in the DS are HD cells that encode present or past head direction rather than future HD (Blair and Sharp, 1995; Kitanishi et al., 2021), while 10% exhibit bidirectional tuning to encode the axis of travel rather than a single head direction (Olson et al., 2017). 29-60% of DS cells show spatially specific firing similar to that seen in CA1 place cells (Brotons-Mas et al., 2017; Kim et al., 2012; Kitanishi et al., 2021; Olson et al., 2017; Sharp and Green, 1994), though these neurons have broader place fields compared to CA1 place cells

and often conjunctively encode direction signals (Sharp, 2006), leading to diverse definitions of what is considered a “place cell” in DS and thus the wide range of percentages reported. In addition to place and direction signals, the DS also encodes various features of the environment (Brotons-Mas et al., 2017; Kim et al., 2012; Lever et al., 2009; Poulter et al., 2021; Shine et al., 2019; Simonnet and Brecht, 2019), including the location of boundaries and cues relative to the animal’s position (Brotons-Mas et al., 2017; Evans et al., 2016; Lever et al., 2009; Poulter et al., 2021; Shine et al., 2019; Simonnet and Brecht, 2019). Specifically, boundary vector cells encode the location of directly perceived boundaries, such as walls or ledges (Brotons-Mas et al., 2017; Evans et al., 2016; Lever et al., 2009; Shine et al., 2019; Simonnet and Brecht, 2019), while vector trace cells provide “trace memories” of boundaries and cues previously encountered in the environment that do not rely on direct perception of those cues (Poulter et al., 2021).

DS projections precisely target layer 3 of RSG (Figure 1-3; Nitzan et al., 2020; Wyss and van Groen, 1992; Yamawaki et al., 2019a), with weak projections also terminating in RSD, and evoke larger excitatory postsynaptic responses in superficial RSG cells compared to deep layer cells (Yamawaki et al., 2019a). Silicon probe recordings in awake mice revealed ripple-like analogs in RSG, specifically, that are coupled to hippocampal sharp wave ripples (Nitzan et al., 2020). Superficial pyramidal cells in RSG showed the strongest coupling to hippocampal ripples due to the ripple-related outputs from the hippocampus being relayed to RSG via subicular projections (Nitzan et al., 2020). However, recordings of hippocampal and retrosplenial activity during slow-wave sleep showed that RSG ripple-like events were followed by a

substantial silencing of putative pyramidal cells via direct activation of local inhibitory interneurons by DS projections (Opalka et al., 2020). This suggests that the temporal coordination of hippocampal and retrosplenial activity is modulated in a brain state-dependent manner (Nitzan et al., 2020; Opalka et al., 2020).

Secondary Motor Cortex

The motor cortex supports the planning and execution of voluntary motion, and it is heavily interconnected with the RSC and other key spatial regions (Figure 1-4; Barthas and Kwan, 2017; Yamawaki et al., 2016). Classically, the secondary motor cortex (M2) has been associated with motor planning (Barthas and Kwan, 2017; Erlich et al., 2011; Hanks et al., 2015; Li et al., 2016; Murakami et al., 2014; Sul et al., 2012), exhibiting preparatory activity between sensation and resulting motor action (Guo et al., 2014; Inagaki et al., 2018). More recent work has also identified widespread spatial representations of context within M2, with population activity reliably encoding turning behavior regardless of spatial context (Olson et al., 2020). Thus, it has been hypothesized that M2 directly contributes to action planning during navigation. Bidirectional projections between M2 and RSD, predominantly, establish a circuit by which M2 receives mnemonic spatial information to inform navigational motor planning (Yamawaki et al., 2016). These motor plans may then be relayed back to RSD, most prominently to layers 2/3, to refine spatial encoding (Yamawaki et al., 2016) and establish a corticocortical loop that regulates navigational action.

Visual Cortex

The visual cortex is also densely connected with the RSC, predominantly targeting layers 1 and 5 of RSD with weaker projections to layer 5 of RSG (Figure 1-4;

van Groen and Wyss, 1992; Vogt and Miller, 1983). These projections provide RSD with information on relevant visual cues during navigation (Hindley et al., 2014; Mao et al., 2020; Powell et al., 2020), and RSD activity during spatial memory tasks is partly dependent on these visual inputs (Pothuizen et al., 2009). Such precise targeting of RSD by visual input has led to the hypothesis that RSD is more heavily involved in the visuospatial aspects of navigation (Hindley et al., 2014; Hindley et al., 2014; Mao et al., 2020; Pothuizen et al., 2009; Powell et al., 2020), corroborated by rats exhibiting significantly poorer performance on the radial arm maze after RSD lesions due to an inability to utilize visually based spatial codes (Vann and Aggleton, 2005). 2-photon imaging also identified visually responsive neuronal activity localized to the caudal regions of RSD that receive direct innervation from visual cortex (Powell et al., 2020), indicating that these visual inputs may support a representation of visuospatial information within RSD, specifically.

Intraretrosplenial Connections

In addition to extrinsic inputs to the RSC, there is also substantial local connectivity both within and between the retrosplenial subregions and hemispheres (Figure 1-4; van Groen and Wyss, 2003, 1992, 1990). While selective lesion studies have found that the RSD is more involved in visuospatial processing and RSG in location-based spatial processing (Hindley et al., 2014; Pothuizen et al., 2010; van Groen et al., 2004; Vann and Aggleton, 2002), the communication between these two regions, mediated by reciprocal projections from both superficial and deep layers of both the granular and dysgranular regions (Figure 1-4; van Groen and Wyss, 2003, 1992, 1990), is thought to facilitate the formation of stable and complex spatial

representations within the RSC as a whole. Dense contralateral projections exist between the two hemispheres of RSC, with predominantly superficial neurons crossing the midline via the corpus callosum and synapsing on both superficial and deep layer neurons in the homotypic region (Sempere-Ferràndez et al., 2018; Sripanidkulchai and Wyss, 1987). These contralateral projections also evoke strong feed-forward inhibition via the recruitment of layer 5 parvalbumin (PV)-positive fast-spiking (FS) interneurons (Sempere-ferràndez et al., 2019; Sempere-Ferràndez et al., 2018).

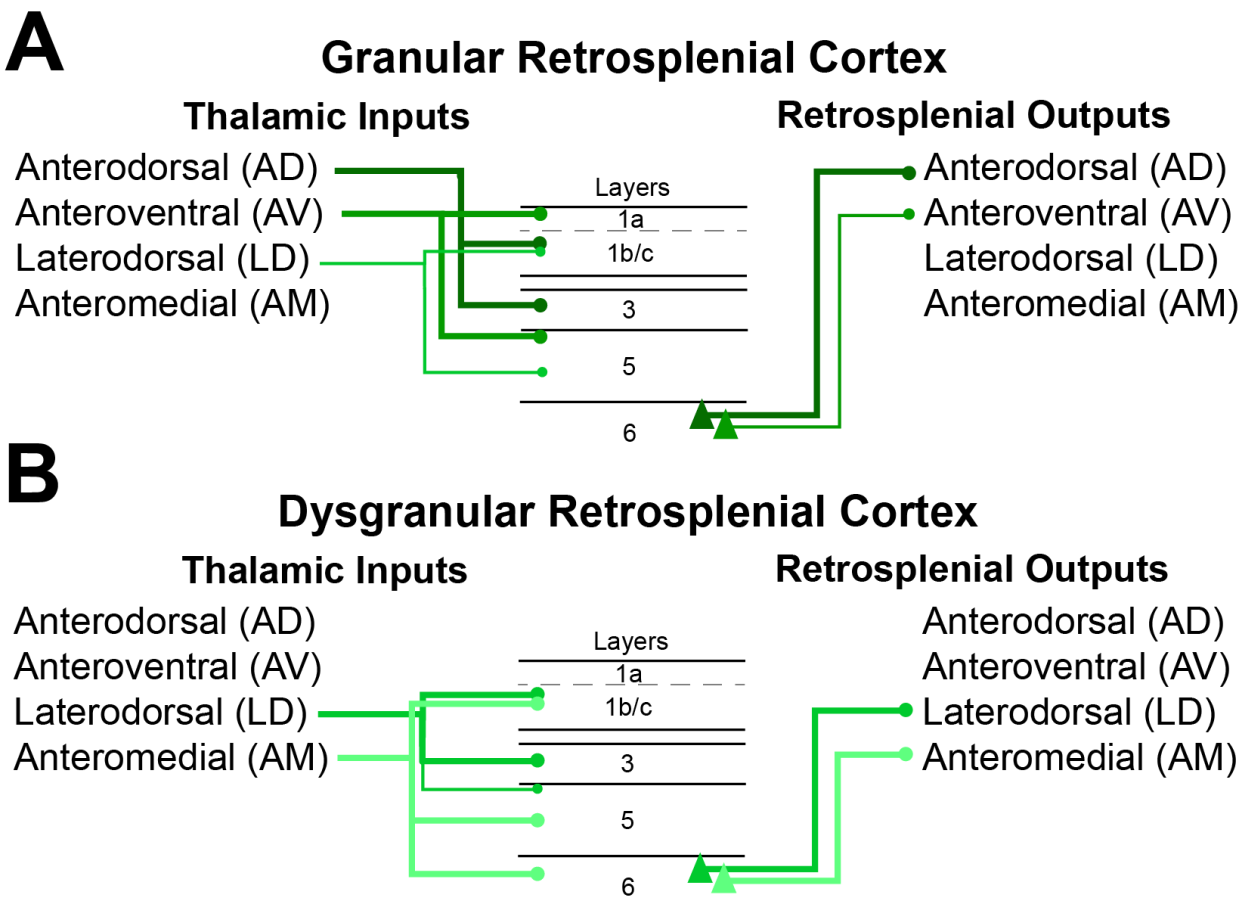

Figure 1-2. Key connections between the thalamus and retrosplenial cortex.

A. Schematic of input-output connectivity between key thalamic nuclei and the granular retrosplenial cortex separated by layer. The AD and AV nuclei compose the strongest thalamic projections to RSG, predominantly targeting upper layer 1 and layer4, while layer 6 RSG neurons project back to AD and, to a lesser degree, AV. Thickness of lines indicate relative strength of projections.

B. Same as ***A*** for the dysgranular region. The LD and AM nuclei compose the strongest thalamic projections to RSD, targeting across the layers, while layer 6 RSD cells project back to LD and AM.

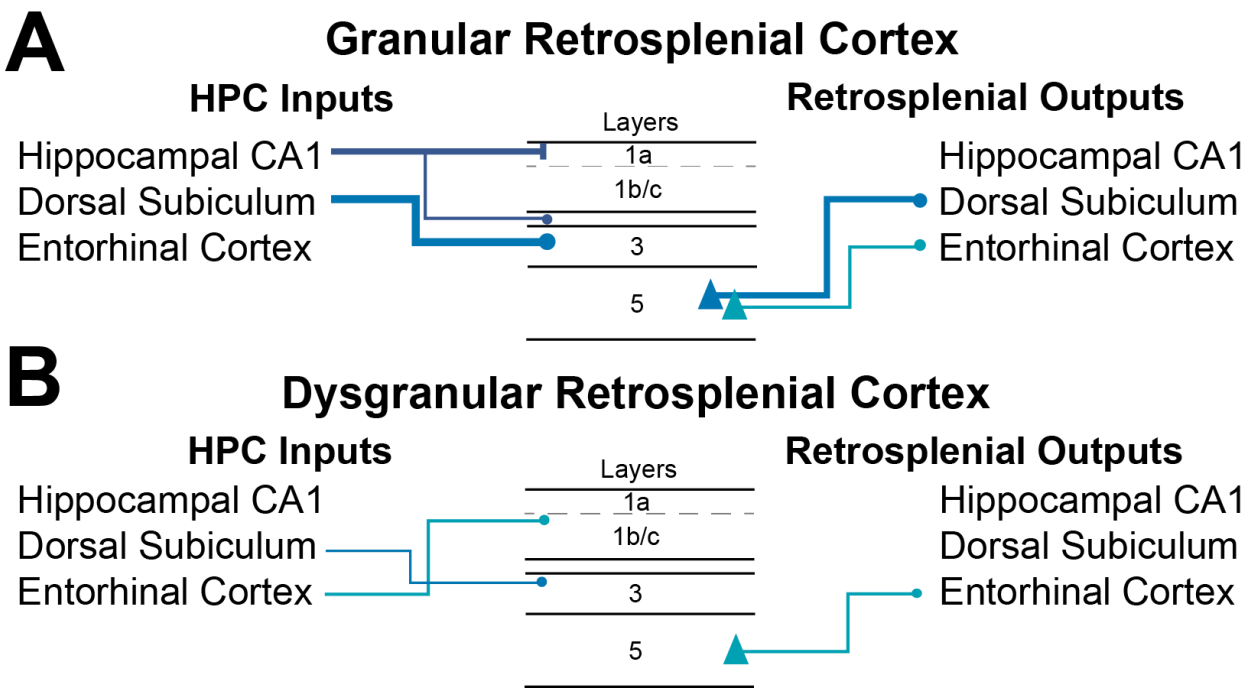

Figure 1-3. Key connections between the hippocampal formation and retrosplenial cortex.

A. Schematic of input-output connectivity between key structures in the hippocampal formation and the granular retrosplenial cortex separated by layer. CA1 and the dorsal subiculum both send projections to layer 1 and layer 3 of RSG, respectively, while layer 5 RSG neurons project to the dorsal subiculum and medial entorhinal cortex. Thickness of lines indicate relative strength of projections.

B. Same as ***A*** for the dysgranular region. RSD receives weak projections from the dorsal subiculum and entorhinal cortex, and layer 5 RSD neurons send reciprocal projections back to the lateral entorhinal cortex.

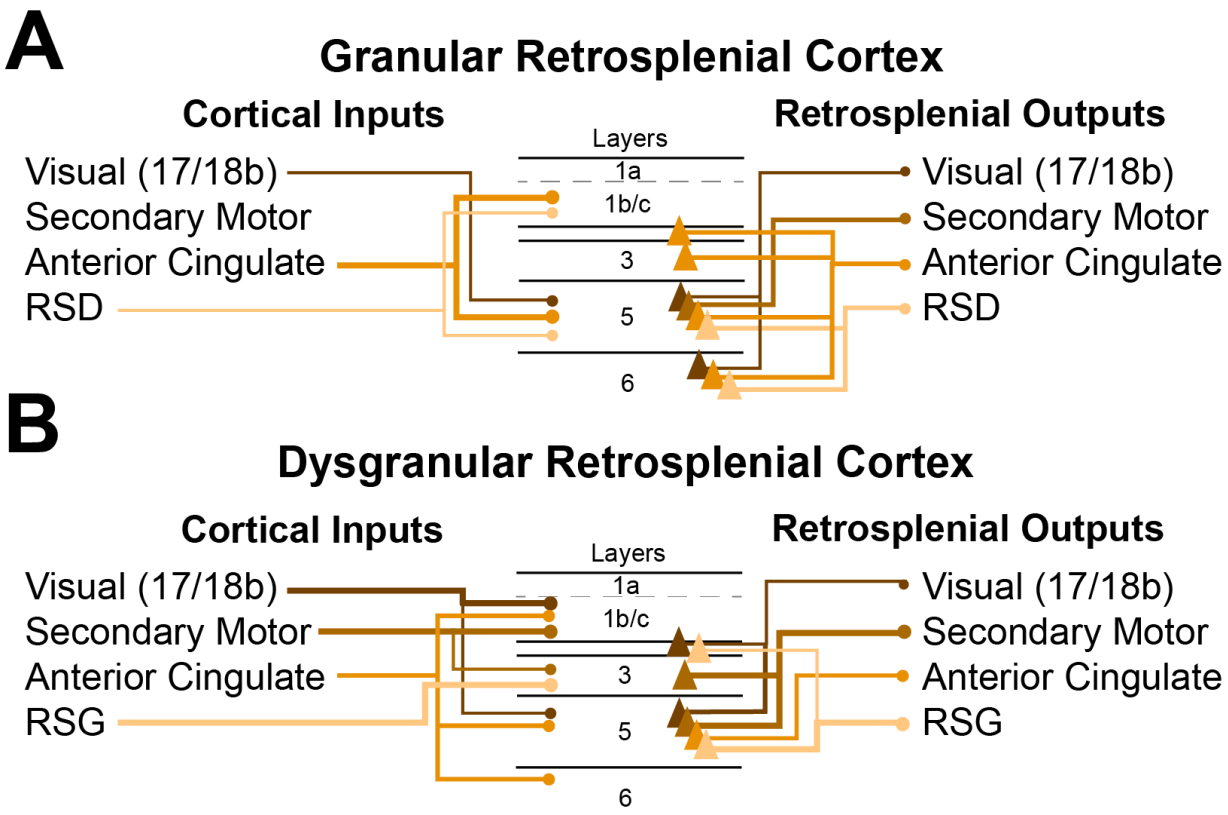

Figure 1-4. Connections between key cortical regions and the retrosplenial cortex.

A. Schematic of input-output connectivity between key cortical structures and the granular retrosplenial cortex. Note the strong reciprocal projections between the anterior cingulate and granular RSC, as well as RSG outputs to RSD and secondary motor cortex. Thickness of lines indicate relative strength of projections.

B. Same as ***A*** for the dysgranular region. Note the strong projections from visual and motor cortices to RSD, as well as strong RSD outputs to RSG and secondary motor cortex.

1.2.3 Functional coding of space in the retrosplenial cortex

As a result of the convergence of spatial, motor, and sensory inputs into both RSD and RSG, many retrosplenial neurons can either individually code for space or collectively facilitate population spatial codes (Alexander et al., 2020; Cho and Sharp, 2001; Miller et al., 2020; Olson et al., 2017). These codes support both “allocentric,” or referenced to external cues, and “egocentric,” or referenced to the self, frames that are then integrated to form complex spatial representations (Alexander and Nitz, 2015; Bicanski and Burgess, 2018; Byrne et al., 2007; Miller et al., 2019; van Wijngaarden et al., 2020). These diverse synapses and cells are also promising targets for future research to identify where and when dysfunction in retrosplenial spatial coding appears in the progression of diseases that are accompanied by profound disorientation.

Directional Coding

Approximately 10% of neurons in the RSC are HD cells, with equal proportions expressed in RSD and RSG (Chen et al., 1994; Cho and Sharp, 2001; Jacob et al., 2017), while axis cells are localized to RSD and account for 11% of dysgranular neurons (Jacob et al., 2017). Retrosplenial HD cells are highlight anticipatory, exhibiting large ATIs similar to those in AD of the thalamus and thus begin firing early before the animal is facing an HD cell’s preferred direction, as well as exhibit narrow tuning widths (Table 1-1; Blair et al., 1997; Cho and Sharp, 2001). The activity of RSD populations of HD cells that have opposite preferred directions (e.g., 0º and 180º) is correlated with neighboring axis cells that represent that same bidirectional tuning (in this example, 0º and 180º; Jacob et al., 2017). These axis cells are also landmark driven, such that their

tuning curves are sensitive to the position of visual landmarks, changing their tuning widths or reversing their preferred orientation when landmarks are reversed, while neighboring HD cells are not influenced by landmark location (Jacob et al., 2017). Thus, these axis cells are sensitive to landmark cues. The coactivity between retrosplenial axis and HD cells is thought to provide a stable representation of both direction, from HD signals, and landmark stability, measured by the additional drive from axis inputs, via two-way integration of direction and landmark integration (Auger et al., 2012; Jacob et al., 2017; Marchette et al., 2014; Page and Jeffery, 2018). Indeed, maintenance of visually acquired landmark representations under varying contextual conditions is a key navigational function attributed to the RSD (Cooper et al., 2001; Pothuizen et al., 2009; Robertson et al., 2016).

Computational models also suggest that RSC HD and axis cells utilize the conjunctive encoding of head direction and location relative to visual landmarks to code for direction in a global reference frame (Bicanski and Burgess, 2016; Page and Jeffery, 2018; Shine et al., 2016). Spatially relevant visual inputs may be integrated with direction and angular motion signals to form a representation of the distance and direction to the visual cues in the environment (Evans et al., 2016). Essentially, the allocentric cues of objects in the environment are combined with egocentric self-motion cues to provide an internal map of the environment. The rapid learning of this representation (Bicanski and Burgess, 2016; Goodridge et al., 1998) then enables stable navigation through the environment even in the absence of the visual cues (Cooper et al., 2001; Jacob et al., 2017). Thus, the directional codes employed by the RSC and their interactions with relevant sensory cues facilitate the encoding and

learning of spatial landmarks to support a stable sense of orientation, a sense that is significantly impaired after loss of retrosplenial activity (Ino et al., 2007; Osawa et al., 2007; Valenstein et al., 1987).

Reference	Region	% Cells	Peak firing rate (Hz)		Baseline or Mean		Tuning curve width		ATI (ms)	
			Mean	SEM	Mean	SEM	Mean	SEM	Mean	SEM
Taube 1995, Journal of Neuroscience	ATN	56.10%	41.08	4.4	1.99	0.35	96.24[1]	3.25	48.56	5.25
Lozano et al. 2017, Brain & Neuroscience Advances	RSC	not reported	22.4	2.58	5.07	0.52	49.29	1.28	47.91	4.28
Blair et al. 1998, Neuron	LMN	56%	37.2	5.5	1.5	0.7	79.9	3.5	38.5	3.2
Blair & Sharp 1995, Journal of Neuroscience	AD	not reported	66.6	14.5 (SD)	12.3	1 (SD)	69.4	3.9 (SD)	36.875	N/A
Cho & Sharp 2001, Behavioral Neuroscience	RSC	10%	32.3	10.7			44.6	2.7	25.05	3.3
Taube & Muller 1998, Hippocampus	PoS	not reported	34.16	6.39					23.2	
Blair et al. 1998, Neuron	ATN	not reported	50.3	6	0.6	0.1	57.4	2.4	23.2	3.4
Lozano et al. 2017, Brain & Neuroscience Advances	PoS	not reported	8.14	0.63	1.83	0.19	43.65	1.13	14.37	8.19
Blair & Sharp 1995, Journal of Neuroscience	PoS	not reported	24.3	3.7 (SD)	5.7	1.3 (SD)	63.9	6.3 (SD)	2.01	N/A
Taube & Muller 1998, Hippocampus	ATN	not reported	47.77	4.95					-6.2	N/A
Taube 1990, Journal of Neuroscience	PostSub	25.50%	34.51	5.44	1.12	0.307	89.93[1]	3.62		
Chen et al. 1994, Experimental Brain Research	RSD RSG	8.40% 8.50%	17.3 23.5	3.2 5.3						
Jacob et al. 2017, Nature Neuro	RSC	9%	7.59	0.88						

Table 1-1. Properties of HD cells compared across regions.
Table 1-1 reports various published properties of HD cells recorded in the anterior thalamic nuclei (ATN), anterodorsal nucleus of the thalamus (AD), lateral mammillary nucleus (LMN), retrosplenial cortex (RSC), granular RSC (RSG), dysgranular RSC (RSD), and postsubiculum (PoS). The table is sorted by highest to lowest ATI.
[1]These tuning curve width values were calculated as the full width at the widest point of the tuning curve, while all other values were calculated as the full width at the half max.

Egocentric Coding

The head direction signals within the RSC can be integrated with visual, motor, and other cues to encode spatial information that is referenced to the animal rather than external cues within the environment (Alexander et al., 2020; Alexander and Nitz, 2015; Evans et al., 2016; Miller et al., 2019; Wang et al., 2020), establishing egocentric representations of space. Indeed, computational modeling of the larger spatial circuits in the brain predicts that the RSC serves to conjunctively encode egocentric views of space with allocentric location and direction information (Bicanski and Burgess, 2018; Byrne et al., 2007). This integration partly relies on the formation of a parietal egocentric representation and a separate parahippocampal allocentric boundary vector representation that then converge in the RSC (Bicanski and Burgess, 2018, 2016; Byrne et al., 2007). In support of these predictions, 39-45% of retrosplenial cells, located predominantly in RSD, are egocentric boundary vector cells (EBCs) which encode the location of boundaries relative to the egocentric position of the animal (Alexander et al., 2020; Laurens et al., 2019). A large proportion of these cells are also significantly tuned to HD and/or movement direction (Alexander et al., 2020; Laurens et al., 2019). Thus, these EBCs may represent a neuronal substrate within the RSC that is the result of the ego- and allocentric transformation predicted by computational models (Alexander et al., 2020; Bicanski and Burgess, 2018), as these cells provide an egocentric representation of otherwise allocentric cues (e.g., the wall is “behind the animal” rather than “near the chair”) and are directly modulated by visually acquired, direction signals (Alexander et al., 2020).

Such egocentric transformations may result from the integration of HD signals with visual and other landmark cues that converge in the RSC through both its afferent connections with directional and sensory regions (Alexander and Nitz, 2015; Bicanski and Burgess, 2018; Burgess et al., 2001; Robertson and Kaitz, 1981; van Groen and Wyss, 2003, 1992, 1990; Wyss and van Groen, 1992). The directional tuning of EBCs is biased such that EBCs with a rightward orientation were most often found in the left RSD and vice versa (Alexander et al., 2020; van Wijngaarden et al., 2020), a lateralization which has not been reported in directional coding of specialized cells in other regions. Thus, the unique convergence of widespread spatial and sensory inputs to the RSC facilitates the generation of complex spatial representations that conjunctively encode egocentric and allocentric spatial frames, a key navigational process attributed to the RSC (Alexander et al., 2020; Alexander and Nitz, 2015; Bicanski and Burgess, 2018; Miller et al., 2020; van Wijngaarden et al., 2020; Vedder et al., 2016).

Spatial and Contextual Coding

In addition to single, specialized neurons with spatial coding properties, the RSC also employs neuronal ensembles, or populations, that encode various spatial features. Distinct subpopulations of both RSD and RSG neurons increase their firing rates preferentially when the animal is turning left or right (Alexander and Nitz, 2017, 2015; Miller et al., 2019; Vedder et al., 2016), and these population codes improve with learning (Miller et al., 2019). Other population rate codes facilitate simultaneous encoding of full routes and sub-route positions of either the animal, positions of goal locations, and contextual features of the environment via the spatial up-modulation of

population and subpopulation firing rates (Alexander and Nitz, 2017; Miller et al., 2020, 2019). These population codes conjunctively provide a stable representation of both the entire route traversed as well as positions of interest within the route and can reliably distinguish between environmental contexts (Alexander and Nitz, 2017; Miller et al., 2020, 2019). Similar rate codes mapping location of the animal, goals, or rewards have been observed in the hippocampus and ventral striatum (Johnson and Redish, 2007; O'Keefe and Dostrovsky, 1971; van der Meer and Redish, 2009), but the simultaneous encoding of full route and sub-route spaces by one population is attributed more exclusively to the RSC and posterior parietal cortex (Alexander and Nitz, 2017; Nitz, 2006). This supports the consensus that the RSC distinctly contributes to conjunctive encoding of various spatial and egocentric features, facilitating path integration and contextual discrimination in the larger spatial circuit (Alexander and Nitz, 2017, 2015; Chrastil et al., 2015; Mao et al., 2017; Miller et al., 2019). Taken together, the presence of spatially modulated cells and populations across the RSC, a region whose outputs are necessary for successful spatial performance, establish the RSC as a critical component of the brain's navigational circuit.

Spatial Memory and Engrams

The RSC has also been heavily implicated in spatial memory and spatial memory engrams (Harker and Whishaw, 2004; Milczarek et al., 2018; Milczarek and Vann, 2020; Vann et al., 2003; Vann and Aggleton, 2002), which are formed by modifying synapses involved in memory acquisition or retrieval to create functionally linked ensembles of neurons (Milczarek and Vann, 2020). In RSD, such engrams have been visualized with longitudinal c-fos imaging (Czajkowski et al., 2014; Milczarek et al., 2018), and the

consistency of these engrams upon reactivation in repeated spatial behavior is positively correlated with performance on spatial memory tasks (Milczarek et al., 2018). Widespread inactivation of RSC, including both the granular and dysgranular subregions, significantly worsens performance on tasks that require spatial working memory as a result of losing this engram activity (Czajkowski et al., 2014; Keene and Bucci, 2009; Vann and Aggleton, 2002), demonstrating that these spatial engrams in the RSC are essential to successful spatial memory acquisition and consolidation.

Retrosplenial facilitation of contextual fear learning also provides evidence for its role in spatial memory (Kwapis et al., 2015; Lukoyanov and Lukoyanova, 2006; Sigwald et al., 2020; Travis P. Todd et al., 2017), as contextual fear conditioning relies on the proper encoding and storage of spatial memories that are linked with fear responses (Abel and Lattal, 2001; Kim and Cho, 2020; Lee, 2013). Both lesion and chemogenic studies that abolish retrosplenial activity at various stages in the fear learning process show that retrosplenial signaling, particularly excitatory synaptic transmission, is necessary for successful formation and retrieval of fear memories (Kwapis et al., 2015, 2014; Lukoyanov and Lukoyanova, 2006; Travis P Todd et al., 2017; Travis P. Todd et al., 2017). Optogenetic reactivation of retrosplenial engrams involved in either contextual fear or extinction learning is sufficient to establish systems-level consolidation of these two types of learning, resulting in significantly increased fear displays or full suppression of fear responses, respectively (De Sousa et al., 2019; Wang et al., 2019). These findings indicate that the RSC is necessary not only for generating accurate spatial representations to support successful navigation, but also

the consolidation and storage of these representations as spatial memory, reinforcing the importance of retrosplenial contributions to navigation.

1.2.4 Retrosplenial output to control external spatial coding and motor behavior

Retrosplenial output plays an important role in successful navigation, as its dense projections target many regions that are essential for spatial navigation (Sripanidkulchai and Wyss, 1987; van Groen and Wyss, 2003, 1992, 1990). To mediate these outputs, RSD projection neurons in layer 6 target the anterior, lateral, reticular, and reunions thalamic nuclei, while layer 5 neurons project to superior colliculus and ventral pontine nuclei (Figure 1-5; van Groen and Wyss, 1992). Layer 2 and 5 cells in RSD send projections to the anterior cingulate cortex, caudate putamen, layers 1-5 of ipsilateral RSG area a and posterior RSD, contralateral homotypic RSD, all layers of secondary motor cortex, layer 1 of visual cortex areas 17 and 18b, layers 1-4 of postsubiculum, and lateral entorhinal cortex via the cingulum bundle (Figure 1-5; van Groen and Wyss, 1992; Yamawaki et al., 2016). In contrast, the main cortical projections of RSG target layers 1-4 of the postsubiculum, medial entorhinal cortex, and all layers of ipsilateral and contralateral RSG and RSD (Figure 1-5; van Groen and Wyss, 2003, 1990; Wyss and van Groen, 1992). Subcortical projections from RSG layers 5 and 6 also target ADAV, laterodorsal thalamic nuclei, and rostral pontine nuclei (Figure 1-5; van Groen et al., 1993; van Groen and Wyss, 2003, 1990). These projections establish a widespread network of spatial, motor, and sensory regions whose spatial coding is likely influenced by retrosplenial output.

Disrupting retrosplenial output via either temporary inactivation of RSC neurons or localized lesions of RSC impairs the precision of spatial coding in several regions, such that hippocampal place fields show remapping (Cooper and Mizumori, 2001) and anterior thalamic HD cells exhibit broader tuning curves and lower direction information content (Clark et al., 2010). Similarly, inactivation of RSC projections to the superior colliculus significantly decreases the activity of neurons which encode the direction of a shelter (Vale et al., 2020). In the absence of these retrosplenial inputs, these superior colliculus neurons become less tuned to the direction of the shelter location, indicating that they are likely receiving and encoding goal-location signals from the RSC. Without these inputs, the animal takes significantly longer to reach the shelter when fleeing due to the use of indirect trajectories, reflecting an inefficient or incomplete representation of the goal location (Vale et al., 2020). These results indicate that the RSC provides necessary signals to its downstream targets that facilitate their spatial representations and the overall success of spatial navigation behaviors.

Notably, independent rhythmic activity of layer 5 retrosplenial cells, alone, is sufficient to induce widespread dissociation behaviors reflecting those seen after ketamine administration (Vesuna et al., 2020). When the distinct layer 5 RSC rhythms are blocked, ketamine administration is no longer sufficient to induce these dissociation behaviors (Vesuna et al., 2020), indicating that dissociative behaviors are tightly correlated with retrosplenial signaling. This suggests that there is global disruption in brain-wide functions when the RSC stops working as part of the network and instead follows its own rhythm.

Dense retrosplenial projections to the posterior secondary motor cortex also imply a role in the retrosplenial modulation of motor planning and output (Figure 1-5; Hooks et al., 2013; Shibata et al., 2004; Vogt and Miller, 1983; Yamawaki et al., 2016), and it has been hypothesized that these projections serve to relay dorsal hippocampal spatial information to neocortical motor networks (Shibata et al., 2004; Vogt and Miller, 1983; Yamawaki et al., 2016). However, this projection likely serves to provide far more than just indirect hippocampal input to M2, as M2-projecting neurons arise in superficial and deep layers of both retrosplenial regions (Yamawaki et al., 2016) that both receive and contain heterogeneous spatial codes (Alexander et al., 2020; Cho and Sharp, 2001; Miller et al., 2020; van Groen and Wyss, 2003, 1992, 1990). This provides an anatomical basis for the complex spatial representations of the RSC to inform and thus influence sensorimotor integration and motor output of M2, and reciprocal connections from M2 to RSD may in turn inform spatial memory encoding by providing updated motor planning information (Czajkowski et al., 2014; Yamawaki et al., 2016). Taken together, these findings corroborate the role of retrosplenial signaling in supporting the spatial coding and ultimate motor output of other navigationally relevant regions.

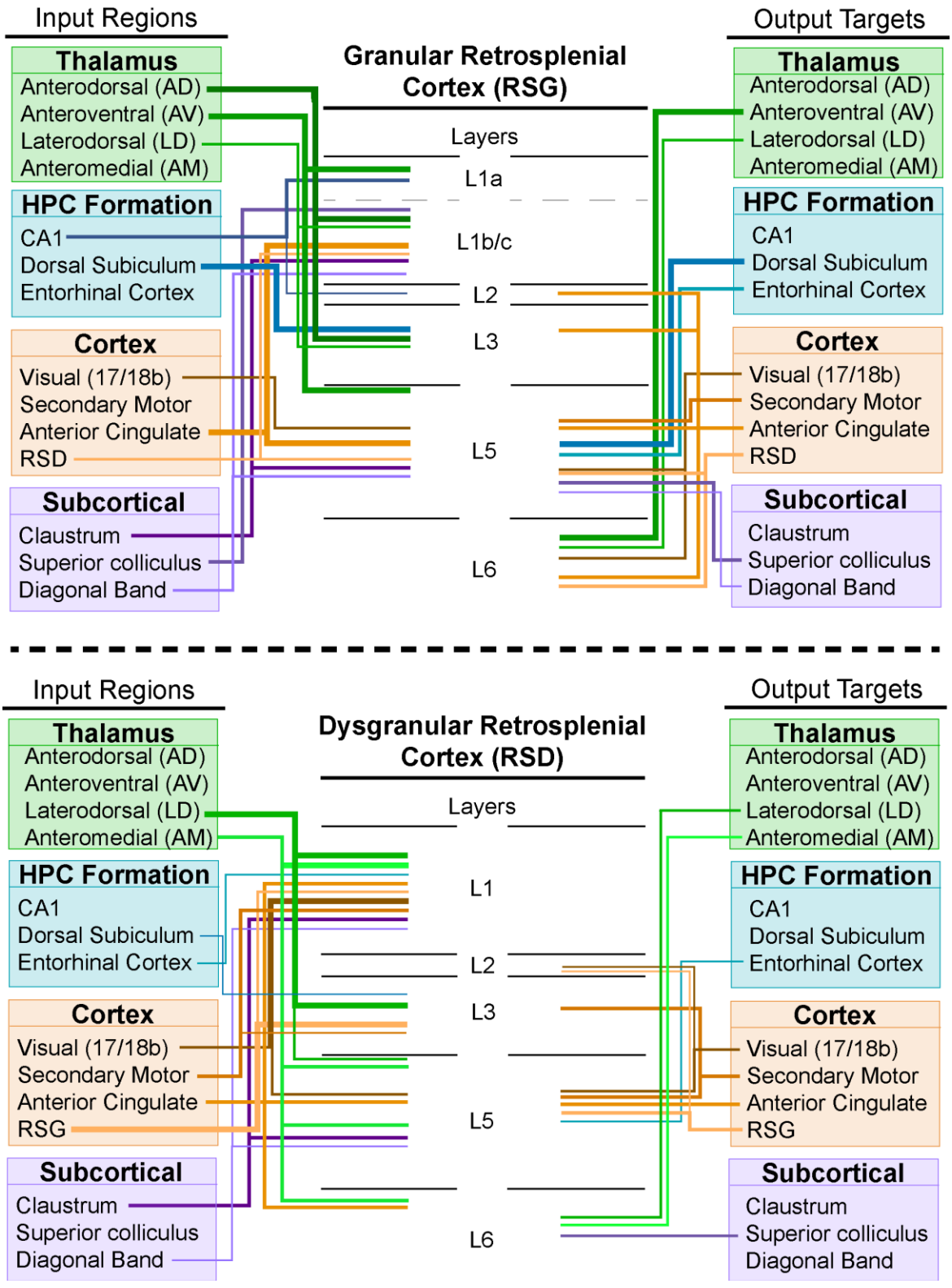

Figure 1-5. Key connectivity between the RSC and spatially relevant regions. Top shows a schematic of input-output connectivity with granular RSC, while bottom shows the same with respect to dysgranular RSC.

1.3 Conclusions

The RSC sits at the intersection between prominent spatial, motor, and sensory brain regions, integrating converging inputs to generate novel and complex representations of space (van Groen and Wyss, 2003, 1992, 1990; Whitesell et al., 2021; Alexander et al., 2020; Cho and Sharp, 2001; Miller et al., 2020; Olson et al., 2017). These retrosplenial representations and rate codes are necessary for successful navigation (Bottini et al., 1990; Harker and Whishaw, 2004; Heilman and Sypert, 1977; Ino et al., 2007; Osawa et al., 2007; Pothuizen et al., 2010; van Groen et al., 2004; Valenstein et al., 1987; Vann et al., 2003; Vann and Aggleton, 2005, 2002), providing outputs that support spatial coding of other key regions (Cooper and Mizumori, 2001; Clark et al., 2010; Vale et al., 2020) and inform motor planning (Hooks et al., 2013; Shibata et al., 2004; Vogt and Miller, 1983; Yamawaki et al., 2016). Mechanistic knowledge of these spatial codes provides the foundation for understanding how the RSC supports navigation, as well as key research targets that may help identify when and how these circuits become impaired in degenerative disease (Chen et al., 2017; Hou et al., 2020; Minoshima et al., 1997; Nestor et al., 2003; Pengas et al., 2010; Potvin-Desrochers et al., 2019). The majority of spatially tuned neurons and codes have been reported specifically in the dysgranular region of RSC (Alexander et al., 2020; Czajkowski et al., 2014; Jacob et al., 2017; Laurens et al., 2019; Milczarek et al., 2018; van Wijngaarden et al., 2020), leaving the question of the granular subregion's involvement in retrosplenial coding, as the RSG serves as the key target of hippocampal, anterior thalamic, and subicular projections (Nitzan et al., 2020; Wyss and

van Groen, 1992, 1993; Yamawaki et al., 2019b; Yamawaki et al., 2019a) that are likely to contain both egocentric and allocentric information. The superficial layers of RSG, in particular, remain severely understudied even though they are the main site of this spatial convergence in the RSC as a whole. The work presented in this dissertation aims to fill these gaps in the literature by identifying the superficial neurons of RSG and how cells across the layers of this region engage with converging spatial signals to form a mechanistic understanding of the RSG's contributions to navigation.

In Chapter 2, we identify and characterize a unique pyramidal neuron subtype localized to layers 2/3 of RSG that is hyperexcitable and computationally able to encode persistent direction signals, and we name these cells "Low-Rheobase (LR) neurons." In Chapter 3, we delve into the circuitry of layer 3 LR and neighboring regular-spiking (RS) neurons using channelrhodopsin-assisted circuit mapping and identify a double dissociation between local cell dendrite and afferent axon organization that facilitates parallel circuits in which LR neurons are optimized to encode spatial signals while RS neurons encode other inputs. We also find that the synaptic dynamics of anterior thalamic HD inputs to LR cells enable these neurons to simultaneously encode head direction and compute a novel head speed code. In Chapter 4, we switch gears and investigate the cholinergic modulation of neuronal activity in RSG and find that activity of LR neurons is not affected by cholinergic signaling, suggesting that their spatial codes are robust and independent of cholinergic tone. These findings collectively highlight the importance of the RSG, particularly LR neurons, in facilitating the navigational functions of the RSC as well as point out the need for more precise investigations of cell properties and connectivity across both RSG and RSD.

CHAPTER 2: Hyperexcitable Neurons Enable Precise and Persistent Information Encoding in the Superficial Retrosplenial Cortex

Ellen KW Brennan*, Shyam Kumar Sudhakar*, Izabela Jedrasiak-Cape, Tibin T John, & Omar J Ahmed

2.1 Abstract

The retrosplenial cortex (RSC) is essential for memory and navigation, but the neural codes underlying these functions remain largely unknown. Here, we show that the most prominent cell type in layers 2/3 (L2/3) of the mouse granular RSC is a uniquely excitable, small pyramidal cell. These cells have a low rheobase (LR), high input resistance, lack of spike-frequency-adaptation, and spike widths intermediate to those of neighboring fast-spiking (FS) inhibitory neurons and regular-spiking (RS) excitatory neurons. LR cells are excitatory but rarely synapse onto neighboring neurons. Instead, L2/3 is a feed-forward, not feedback, inhibition-dominated network with dense connectivity between FS cells and from FS to LR neurons. Biophysical models of LR but not RS cells precisely and continuously encode sustained input from afferent postsubicular head-direction cells. Thus, the unique intrinsic properties of LR neurons can support both the precision and persistence necessary to encode information over multiple timescales in the RSC.

2.2 Introduction

The retrosplenial cortex (RSC) plays a critical role in learning and memory. In humans, damage to the RSC via hemorrhage or tumor results in both anterograde and retrograde amnesia, often purging several years of recent memories (Ironside and Guttmacher, 1929; Heilman and Sypert, 1977; Valenstein et al., 1987; Todd and Bucci, 2015; Chrastil, 2018). Similar impacts on both anterograde and retrograde memory are also seen in monkeys when the RSC is lesioned (Buckley and Mitchell, 2016). In rodents, RSC lesions impair performance on both spatial learning and fear conditioning tasks (Vann et al., 2003, 2009; van Groen et al., 2004; Keene and Bucci, 2008b; Katche et al., 2013; Todd et al., 2015, 2017; Sigwald et al., 2016; Yamawaki et al., 2019b). Recent imaging studies in mice confirm that RSC neurons can display evidence of long-duration, persistent spatial memory engrams (Czajkowski et al., 2014; Milczarek et al., 2018; de Sousa et al., 2019; Hattori et al., 2019).

The RSC is also critical for spatial navigation (Maguire, 2001; Epstein, 2008). Human case studies show that damage to the RSC leads to disorientation in space in addition to memory impairments (Bottini et al., 1990; Takahashi et al., 1997; Ino et al., 2007; Osawa et al., 2007). Such patients can identify known scenes or locations but are unable to extract any orientation or location information from them and thus experience difficulties navigating even familiar environments (Bottini et al., 1990; Takahashi et al., 1997; Ino et al., 2007). A neuroimaging study identified the coding of head direction information in the RSC while participants navigated a novel virtual environment,

suggesting that the visual cues of orientation are processed in part by the RSC during navigation (Shine et al., 2016). Animal studies also report encoding of spatial information within the RSC, including that of head direction, position, and turning behavior (Cho and Sharp, 2001; Alexander and Nitz, 2015; Vedder et al., 2016; Mao et al., 2017, 2018; Miller et al., 2019).

How is the RSC uniquely suited to carry out these spatial memory and navigation computations? This is a fundamental but unsolved circuit input-output transformation problem. The RSC receives prominent spatial and memory-related inputs from the hippocampus, subicular complex, anterior thalamus, secondary motor cortex, and visual cortex, as well as the contralateral RSC (van Groen and Wyss, 1990, 2003; Wyss and van Groen, 1992; Miyashita and Rockland, 2007). Recent studies have started to document the functional nature of these inputs to the RSC (Yamawaki et al., 2016, 2019a, 2019b; Sempere-Ferràndez et al., 2018; Sempere-ferràndez et al., 2019). However, the precise properties of the RSC neuronal subtypes involved (Wyss et al., 1990; Sugar et al., 2011; Kurotani et al., 2013) is rarely studied and the local connectivity between RSC subtypes completely unknown. While attractor network models of RSC incorporating generic neurons exist (Bicanski and Burgess, 2016; Page and Jeffery, 2018), it is critical to discover the key intrinsic and local synaptic properties that allow RSC to perform its specialized functions. Without this information, it is impossible to develop biophysically-realistic models of RSC cells or circuits, which would in turn help to decipher the exact coding schemes being employed by the RSC.

Here, we investigate the intrinsic physiology, local synaptic connectivity, and computational abilities of cells within the superficial layers of granular retrosplenial

cortex (RSG). The majority of neurons within this region are a distinct subtype of small, highly excitable, non-adapting pyramidal neurons. We show, for the first time, that these cells are excitatory but, surprisingly, rarely excite their neighboring inhibitory or excitatory neurons. Instead, there is prevalent local inhibition from fast-spiking (FS) L2/3 neurons onto these highly excitable neurons and between pairs of FS cells, highlighting a network dominated by feedforward, not feedback, inhibition. We then use this information to construct biophysically-realistic computational models of RSC cell types and investigate how they process realistic, *in vivo* spike trains of incoming information. We find that these uniquely excitable principal neurons in the RSG are optimally suited to precisely and persistently encode the sustained head-direction input they receive from the postsubiculum. A smaller population of regular-spiking (RS) excitatory neurons in L2/3 show pronounced adaptation and are unable to maintain such sustained, high-frequency responses. Our results show that there are two complementary coding strategies operating in parallel in the superficial retrosplenial cortex.

2.3 Results

2.3.1 Low Rheobase cells are highly excitable neurons in the superficial RSG

We recorded from and parsed the intrinsic physiology of 167 cells in the superficial layers (L2/3) of the mouse retrosplenial granular cortex (RSG), with additional cells utilized for morphology (see Methods). Consistent with other cortical regions, fast-spiking (FS) interneurons were present in these RSG layers (Figure 2-1 A).

FS cells were identified by their unique spiking properties (Connors and Gutnick, 1990; Sempere-Ferràndez et al., 2018), including their narrow spike width and rapid, sharp AHPs. Regular-spiking (RS) pyramidal neurons were occasionally found, but far less often than in typical neocortex (Figure 2-1 B). A third population of cells was identified. For reasons investigated and explained in detail below, we refer to these unique neurons as Low Rheobase (LR) cells. Detailed analyses of physiological and intrinsic parameters revealed several distinctly unique properties of LR neurons. LR spike widths were between those of FS and RS cells (FS = 0.22 ± 0.05 ms, RS = 0.86 ± 0.05 ms, LR = 0.55 ± 0.02ms; $p<0.001$ for each comparison; Figure 2-1 D; Table 2-1). Additionally, these LR cells had uniquely high input resistance (402.69 ± 16.75 MΩ; $p<0.001$), low input capacitance (38.42 ± 1.32 pF; $p<0.001$), and low rheobase (91.79 ± 12.89 pA; $p<0.001$), suggesting they are a class of highly excitable neurons distinct from both FS and RS neurons (Figure 2-1 E-G; Table 2-1). LR cells did not differ in latency to first spike from FS ($p=0.09$) or RS ($p=0.11$) cells. LR cells also exhibited minimal spike frequency adaptation (ratio of 1.26 ± 0.06), far lower than the substantial spike frequency adaptation shown by RS cells (ratio of 3.42 ± 0.58; $p<0.001$), highlighting their potential ability to fire trains of action potentials at high frequencies with minimal adaptation (Figure 2-1 I; Table 2-1). LR cells also showed a dramatically higher slope in their frequency-current relationship (Figure 2-1 J). Additionally, 65% of LR neurons exhibited pronounced afterdepolarization (ADP; Figure 2-1 C) while the remaining 35% had no ADP (Table 2-1). The presence of ADP did not otherwise distinguish the LR cells from those where the ADP was absent. These groups did not differ on key intrinsic

properties such as input capacitance, rheobase, or input resistance (as verified using principal component analysis below).

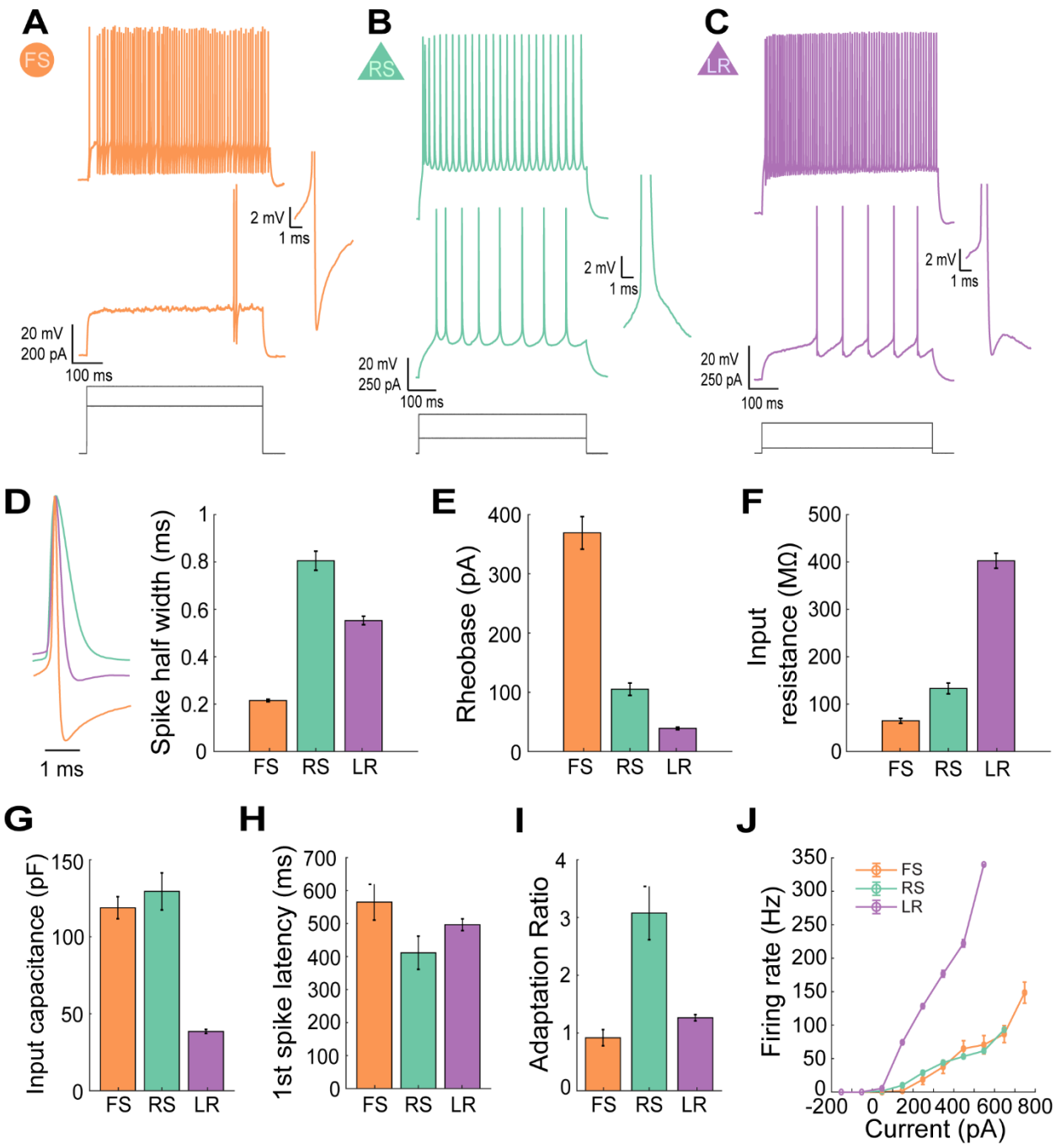

Figure 2-1. Low-Rheobase cells represent a highly excitable cell type in the superficial retrosplenial cortex.

A. Intrinsic physiological properties of an FS neuron in the superficial layers of the granular retrosplenial cortex. Top trace, Ability to fire sustained high frequency trains of action potentials with little or no spike frequency adaptation. Middle trace, A substantial delay to first spike after current onset during a near-threshold current step. Right inset is a zoomed-in view of the first spike in the middle trace. Bottom, injected current amplitudes for the voltage responses shown above.

B. Intrinsic physiological properties of an RS neuron in the superficial layers of the granular retrosplenial cortex. Top trace, Presence of spike frequency adaptation when firing at higher frequencies in response to large suprathreshold current steps. Middle trace, Minor delay to first spike after current onset during an at-threshold current step. Right inset is a zoomed-in view of the first spike in the middle trace. Bottom, injected current amplitudes for the voltage responses shown above.
C. Intrinsic physiological properties of an LR neuron in the superficial layers of the granular retrosplenial cortex. Top trace, Ability to fire sustained high frequency trains of action potentials with little spike frequency adaptation. Middle trace, Moderate delay to first spike after current onset during an at-threshold current step. Right inset is a zoomed-in view of the first spike in the middle trace. Bottom, injected current amplitudes for the voltage responses shown above.
D. Left, Representative traces from FS, RS, and LR cell action potentials overlaid to show differences in spike width. Right, Average spike widths showing that LR spike widths are intermediate to those of neighboring FS and RS [$p<0.001$ for each comparison; Wilcoxon rank sum test].
E. Average rheobase for FS, RS, and LR cells showing a markedly low rheobase for LR cells compared to that of FS and RS [$p<0.001$ for each comparison; Wilcoxon rank sum test].
F. Average input resistance (IR) for FS, RS, and LR cells showing a uniquely high IR for LR cells [$p<0.001$ for each comparison; two-tailed Wilcoxon rank sum test].
G. Average input capacitance (IC) for FS, RS, and LR cells showing a markedly low IC for LR cells compared to FS and RS [$p<0.001$ for each comparison; Wilcoxon rank sum test].
H. Bar graph of the average latency to first spike after onset of an at-threshold current injection for FS, RS, and LR cells [LR v FS, $p=0.09$; LR v RS, $p=0.11$; Wilcoxon rank sum].
I. Bar graph showing the average spike frequency adaptation ratio for FS, RS, and LR cells showing lack of adaptation in FS and LR cells [$p<0.001$ for each comparison; Wilcoxon rank sum test].
J. F-I curve for FS, RS, and LR neurons. Error bars for all represent standard error of the mean.

	FS	(n)	RS	(n)	LR	(n)
Postnatal age at time of recording (days)	25.93 ± 0.43	(42)	26.65 ± 0.52	(26)	27.37 ± 0.61	(115)
Resting potential (mV)	-61.17 ± 0.88	(42)	-65.12 ± 0.96	(26)	-66.27 ± 0.64	(115)
Input resistance (MΩ)	64.68 ± 5.04	(28)	133.09 ± 11.37	(18)	402.35 ± 15.92	(83)
Input capacitance (pF)	118.83 ± 7.19	(28)	129.46 ± 11.99	(18)	38.48 ± 1.33	(83)
Membrane time constant (ms)	7.16 ± 0.58	(28)	15.35 ± 0.86	(18)	14.28 ± 0.37	(83)
Action potential threshold (mV)	-40.73 ± 0.85	(35)	-40.93 ± 0.87	(26)	-40.83 ± 0.42	(100)
Action potential amplitude (mV)	56.86 ± 1.59	(35)	74.71 ± 2.39	(26)	64.29 ± 1.14	(100)
Action potential width (ms)	0.22 ± 0.05	(35)	0.80 ± 0.04	(26)	0.55 ± 0.02	(100)
Afterhyperpolarization amplitude (mV)	17.00 ± 0.54	(35)	9.74 ± 0.47	(26)	11.67 ± 0.31 (ADP)	(65)
					9.88 ± 0.57 (no ADP)	(35)
Afterhyperpolarization latency (ms)	0.60 ± 0.02	(35)	25.71 ± 2.74	(26)	1.39 ± 0.09 (ADP)	(65)
					9.25 ± 0.48 (no ADP)	(35)
Spike frequency adaptation ratio	0.92 ± 0.14	(35)	3.08 ± 0.46	(26)	1.26 ± 0.07	(100)
Latency to first spike (ms)	565.13 ± 54.30	(35)	411.53 ± 50.05	(26)	496.47 ± 19.36	(100)
Rheobase (pA)	363.70 ± 28.72	(31)	105.60 ± 9.62	(15)	40.45 ± 2.07	(80)

Table 2-1. Intrinsic cell properties reveal that LR cells have a uniquely low rheobase, high input resistance, low input capacitance, and low spike frequency adaptation, as well as a spike width between that of FS and RS cells. Values are mean ± SEM for each of the calculated intrinsic cell properties separated by cell group. Ns are reported individually for each property for each cell type. Details of the measurements are described in Methods. LR cells significantly differed from RS cells on the following measures: input resistance, input capacitance, spike width, spike frequency adaptation ratio, and rheobase ($p<0.001$). LR cells significantly differed from FS cells on the following measures: input resistance, input capacitance, membrane time constant, spike width, first spike latency, AHP amplitude, and rheobase ($p<0.001$). FS: Fast-Spiking; RS: Regular-Spiking; LR: Low Rheobase.

In order to determine whether the LR neurons are a truly distinct neuronal subtype, we sought to identify the physiological properties that can clearly distinguish them from other neurons in the superficial RSG. Specifically, using features such as rheobase, input capacitance, and spike width, we were able to isolate the LR cells from both FS and RS cells (Figure 2-2 A&B). LR cells cluster clearly and separately from FS and RS cells based on these intrinsic properties, suggesting they are a unique and distinct neuronal subtype compared to the others included in this study. To further verify this clustering, we conducted a principal components (PC) analysis. Upon plotting PC1 versus PC2 (which together account for 97.4% of variance), the three cell groups clearly separated into three distinct clusters (Figure 2-2 C). To examine whether the presence or absence of ADPs had any impact on LR classification, we labeled LRs with and without ADPs in separate colors. Both of these groups clustered together as part of the unified LR cluster, with no delineation observed between them. This strongly supports the assertion that LR neurons are one unique cell type (Figure 2-2 C).

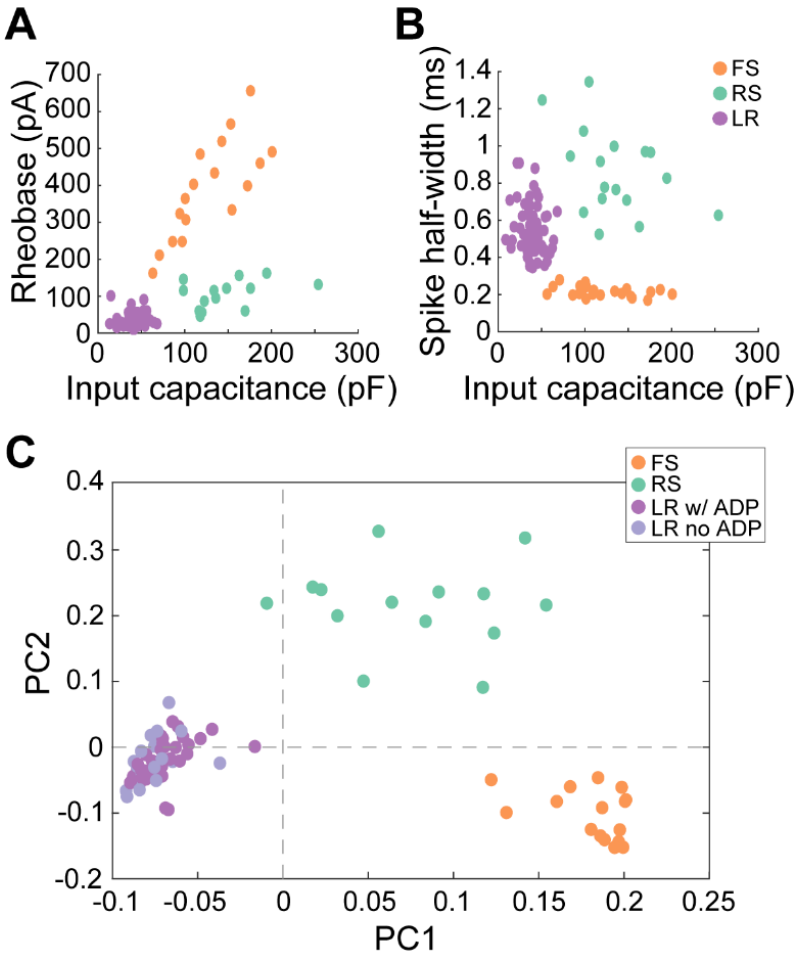

Figure 2-2. Low-Rheobase neurons are a distinct, unique cell type.
LR cells cluster clearly and separately from FS and RS cells when input capacitance is plotted against ***A.*** rheobase, and ***B.*** input resistance.
C. Principal component analysis results in three distinct clusters corresponding to LR, RS and FS cells. LR cells with and without ADPs cluster together in a single LR cluster.

2.3.2 Low Rheobase cells the dominant cell type in superficial retrosplenial granular cortex

LR neurons were the most commonly encountered cell type in L2/3 of RSG. To quantify the relative percentage of neurons in the superficial RSG, the recorded neurons were assigned to one of four groups based on their intrinsic physiological properties: FS, RS, LR, and unclassified. The unclassified group consisted of 10 neurons whose intrinsic and/or firing properties did not fall under any of the three defined groups (see Methods). We found that LR cells are the dominant cell type in both layers 2 and 3, accounting for 61% of the neurons in layer 2 and 59% in layer 3 (Figure 2-3). However, 0 out of 25 recordings in layers 5 and 6 were of LR cells and instead identified only RS and FS neurons, suggesting that LR neurons are restricted to the superficial layers of RSG (chi square test, $p<0.001$; data not shown). In the mouse lines with more than 20 cells recorded, greater than 50% were LR neurons in each line, confirming that LR cells are the dominant cell type in L2/3 of RSC regardless of mouse line. Surprisingly, the prevalence of RS cells in L2/3 of RSG was extremely low, representing only 26% of all layer 2 neurons and 10% of layer 3 neurons. As such, the proportion of LR neurons is in fact significantly greater than that of RS neurons in L2/3 (chi-square; $p<0.001$). The FS neuron probabilities are slightly skewed, as experiments detailed later in this manuscript specifically targeted FS interneurons. Thus, the FS neuron probability reported here is likely slightly larger than their true representation in the cortex. Nonetheless, it is clear that LR cells are the most prevalent cell type within the superficial layers of the granular retrosplenial cortex, being encountered 4.4 times more often than RS cells.

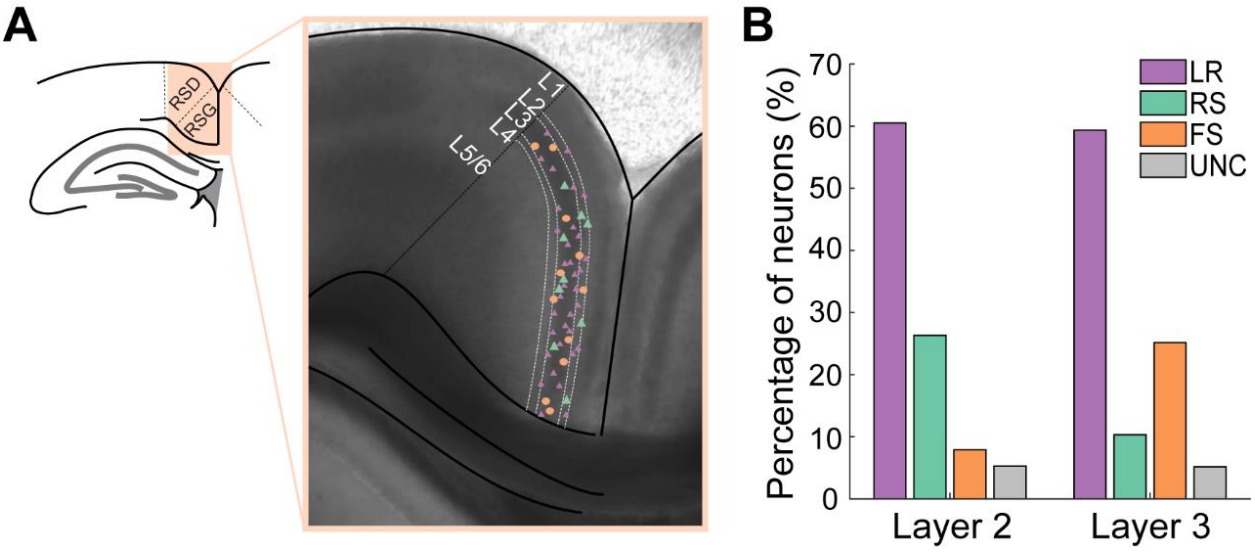

Figure 2-3. Low-Rheobase cells are the dominant cell type in layers 2/3 of the granular retrosplenial cortex.
(A.) Representative anatomy of the RSG and locations of a subset of patched neurons. The left panel shows the location of the retrosplenial cortex superior to the corpus callosum. Right panel shows a DIC image of a retrosplenial mouse brain slice with RSD and RSG separated by a black dotted line. The layers are demarcated by white dotted lines. Small purple triangles, large green triangles, and orange circles denote representative patch locations of a proportion of LR, RS, and FS cells patched in this study, respectively.
B. Percentage of each neuronal subtype patched in each layer of RSG. LR cells are the most prevalent cell type in each layer. UNC stands for unclassified. Layer 2: LR *n*=23 , RS *n*=10 , FS *n*=3 , UNC *n*=2. Layer 3: LR *n*=92 , RS *n*=16 , FS *n*=39 , UNC *n*=8.

2.3.3 Low Rheobase cells are found across the long-axis of the retrosplenial cortex and in both adolescent and adult male and female mice

The retrosplenial cortex is a large structure, spanning 4.38 mm rostracaudally in mice. In addition to LR cells being the most prevalent cell type, we also found that their expression is consistent across this entire long axis of the retrosplenial cortex (Figure 2-4 B). This suggests that the contribution of LR cells to retrosplenial circuit computations is likely to be similar across the long axis of the RSG.

LR cells are present in both adolescent and adult mice, suggesting this highly intrinsically excitable cell is not a transient developmental phenotype (Figure 2-4 A). LR cells are also found in both male and female mice (Figure 2-4 C). The properties of these neurons do not differ across these different locations, ages, or sex, further supporting their persistent existence as a single cell type (Table 2-2). Thus, these neurons are the dominant cell type in the superficial granular retrosplenial cortex, consistent across age, sex, and long-axis of the RSG.

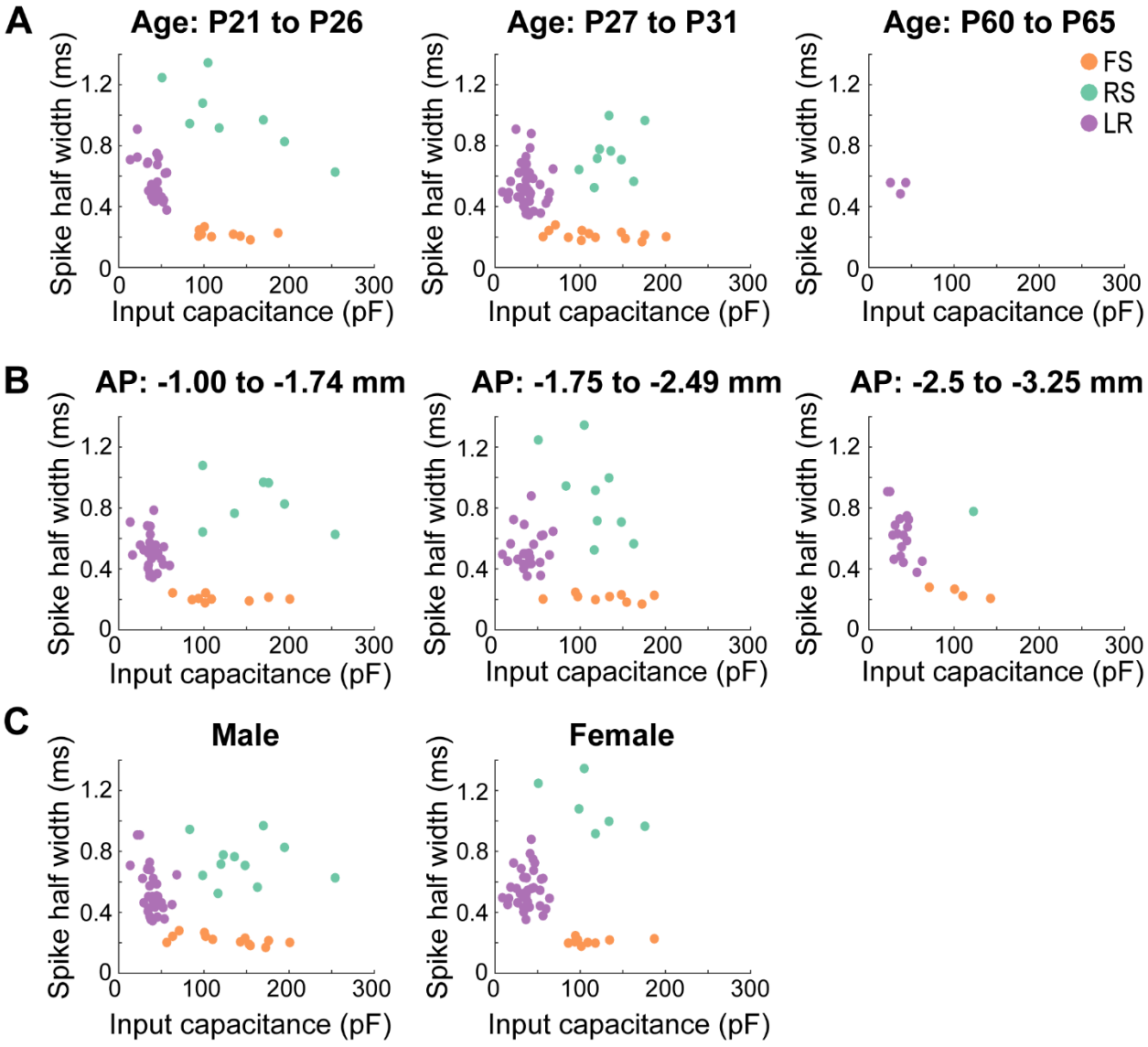

Figure 2-4. Low-Rheobase cells are consistent across age, sex, and long-axis of the RSG.

A. Scatterplots of the three cell types plotted as a function of spike width and input capacitance across different age groups. Left panel, Postnatal days 21-26 (FS: *n* = 9; RS: *n* = 8; LR: *n* = 24). Middle panel, Postnatal days 27-31 (FS: *n* = 13; RS: *n* = 9; LR: *n* = 45). Right panel, Postnatal days 60-65 (*n* = 3).

B. Similar to ***A***, now plotted across distinct anterior-posterior sections of the RSG. Left panel, -1 to -1.74 mm from bregma (FS: *n* = 9; RS: *n* = 7; LR: *n* = 29). Middle panel, -1.75 to -2.49 mm from bregma (FS: *n* = 9; RS: *n* = 9; LR: *n* = 26). Right panel, -2.5 to -3.25 mm from bregma (FS: *n* = 4; RS: *n* = 1; LR: *n* = 17).

C. Similar to ***A***, but now plotted across sex. All three cell types exist and cluster consistently in both male (FS: *n* = 13; RS: *n* = 11; LR: *n* = 34) and female (FS: *n* = 9; RS: *n* = 6; LR: *n* = 38) mice. Cell numbers in each panel reflect neurons with both the 600 ms current steps protocol and small negative current steps protocol (see Methods).

Category	P21-P26 *(n)*	P27-P31 *(n)*	P60-P65 *(n)*	AP -1 to -1.74 *(n)*	AP -1.75 to -2.49 *(n)*	AP -2.5 to -3.25 *(n)*	Male *(n)*	Female *(n)*
Input resistance (MΩ)	384.90 ± 25.61 *(33)*	416.01 ± 21.45 *(47)*	380.20 ± 52.80 *(3)*	397.06 ± 19.27 *(35)*	410.01 ± 31.99 *(30)*	399.85 ± 35.66 *(18)*	397.38 ± 22.92 *(38)*	406.54 ± 22.29 *(45)*
Input capacitance (pF)	41.28 ± 1.87 *(33)*	36.73 ± 1.89 *(47)*	35.07 ± 5.31 *(3)*	38.99 ± 1.64 *(35)*	38.96 ± 2.50 *(30)*	36.68 ± 3.27 *(18)*	39.65 ± 2.02 *(38)*	37.49 ± 1.76 *(45)*
Action potential width (ms)	0.60 ± 0.04 *(35)*	0.52 ± 0.02 *(62)*	0.53 ± 0.02 *(3)*	0.53 ± 0.02 *(44)*	0.54 ± 0.04 *(32)*	0.62 ± 0.03 *(24)*	0.55 ± 0.02 *(51)*	0.56 ± 0.03 *(49)*
Spike frequency adaptation ratio	1.42 ± 0.12 *(35)*	1.19 ± 0.04 *(62)*	0.99 ± 0.17 *(3)*	1.18 ± 0.04 *(44)*	1.25 ± 0.08 *(32)*	1.44 ± 0.18 *(24)*	1.24 ± 0.05 *(51)*	1.29 ± 0.09 *(49)*
Rheobase (pA)	39.40 ± 2.68 *(42)*	41.68 ± 3.36 *(36)*	40.44 ± 15.11 *(2)*	37.64 ± 2.79 *(39)*	40.62 ± 4.12 *(26)*	46.84 ± 4.21 *(16)*	41.84 ± 2.52 *(43)*	38.84 ± 3.41 *(37)*

Table 2-2. LR properties are consistent across age, AP, and sex. Key intrinsic properties calculated for LR neurons grouped by age, AP, and sex.

2.3.4 Low Rheobase cells are excitatory

In order to investigate whether LR neurons were excitatory or inhibitory, we next conducted whole-cell recordings coupled with optogenetic activation of channelrhodopsin in CaMKII+ cells. CaMKII-Cre x Ai32 mice (Jackson Laboratories 005359 and 024109 respectively, crossed in house) were used for these experiments. In these mice, cells containing the excitatory marker CaMKII express Cre, thus allowing for expression of a cre-dependent channelrhodopsin (ChR2) exclusively in CaMKII neurons (Figure 2-5 A). We then used 1 ms light pulses in a 10 Hz train to test ChR2 responses in the patched neurons. Of the LR cells tested, 85% (17/20) directly responded to the optogenetic light pulse, indicating that they were directly expressing ChR2 and thus were CaMKII positive (Figure 2-5 B&C). This suggested, but did not prove, that they may be excitatory neurons.

We then confirmed the excitatory nature of LR cells using paired recordings of layer 2/3 RSG neurons. Although connections were rare, when LR cells were connected to neighboring FS cells, they led to excitatory post-synaptic potentials (EPSPs) in the paired cell (Figure 2-6 D). This is the first demonstration that LR cells in RSG are indeed excitatory neurons.

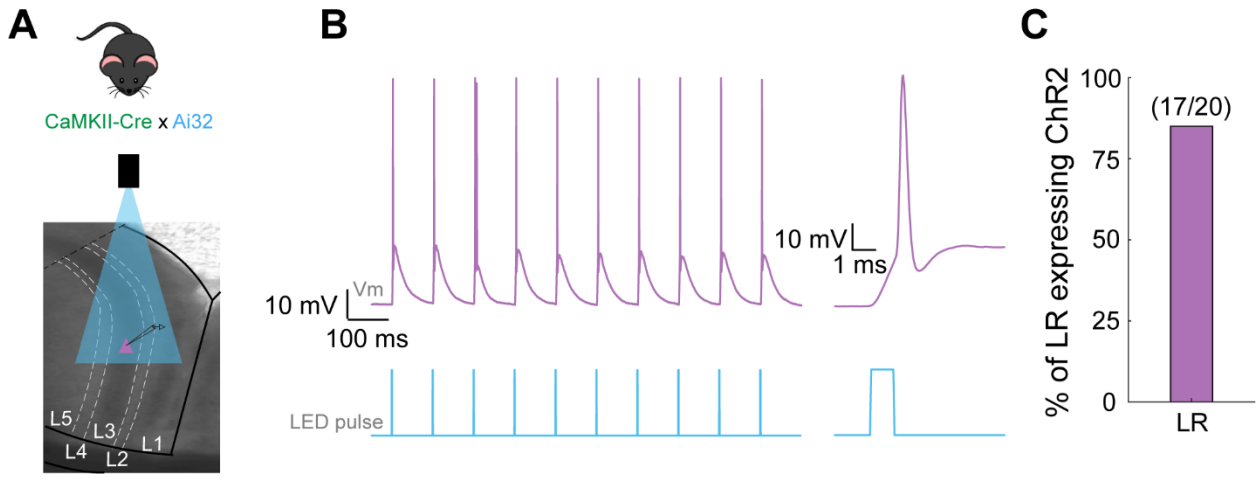

Figure 2-5. Low-Rheobase cells directly respond to ChR2 in CaMKII-Cre x Ai32 mice, indicating expression of CaMKII in this cell type.
A. Schematic showing the experimental set-up. Top panel, Mouse indicating the genetic cross of CaMKII-Cre (Jackson Laboratories, 005359) and Ai32 (Jackson Laboratories, 024109; crossed in house). Bottom panel, 10 Hz optical LED pulses were delivered to a whole-cell patched neuron in L2/3 of RSG while their responses were recorded.
B. Representative responses of LR cell to the 10 Hz optical pulses. Left traces show all 10 optical pulses (1ms each) over the span of one second and the patched LR cell response. Right trace is a zoomed in view of the first optical pulse and resulting spike from the LR cell. The almost instantaneous neuronal response to the light (<0.15 ms latency) is indicative of direct ChR2 expression.
C. Bar graph representing the percentage of LR cells tested that directly expressed ChR2 (85%, 17/20).

2.3.5 Dominant inhibition and rare local excitation in the superficial layers of RSG

Using paired whole-cell recordings, we sought to quantify the connectivity between these three major cell types in the superficial layers of RSG: LR and RS (both excitatory; E) and FS (the major inhibitory neurons in these layers; I). To our surprise, LR to FS connectivity was rare (17%), suggesting a lack of locally driven excitation of FS cells. On the other hand, FS cells were frequently connected to neighboring LR cells (52%; Figure 2-6 A). When all pairs were considered, the E→I connectivity was only 16%, whereas the I→E connectivity reached 53% (Figure 2-6 B). The difference in probability to observe I→E connections versus E→I connections was significant ($p<0.01$; two-tailed t-test), suggesting the superficial layers of the RSG represents an inhibition-dominated network, with feedforward inhibition far more likely than feedback inhibition. Additionally, we observed no LR→LR (0/30) or LR→RS connections (0/6), indicating a complete lack of E→E connectivity. In contrast, FS→FS connectivity was robust (100%; Figure 2-6 A).

The latency to onset of the evoked was similar between inhibition and excitation ($p=0.9273$; Wilcoxon rank sum test; Figure 2-6 E). However, the peak of the EPSP from LR onto FS cells was reached significantly faster than the peak of IPSPs from FS to LR ($p=0.0091$; Wilcoxon rank sum test; Figure 2-6 F). IPSPs from FS to LR cells exhibited clear short-term depression. This was seen in paired recordings (Figure 2-6 C&G) and also when recording from LR neurons during optogenetic stimulation of FS cells (data not shown). EPSPs from LR to FS cells did not clearly exhibit either depression or

facilitation (Figure 2-6 D). The circuit diagram for L2/3 of RSG is summarized in Figure 2-6 H and highlights the prominent role of inhibition in this circuit.

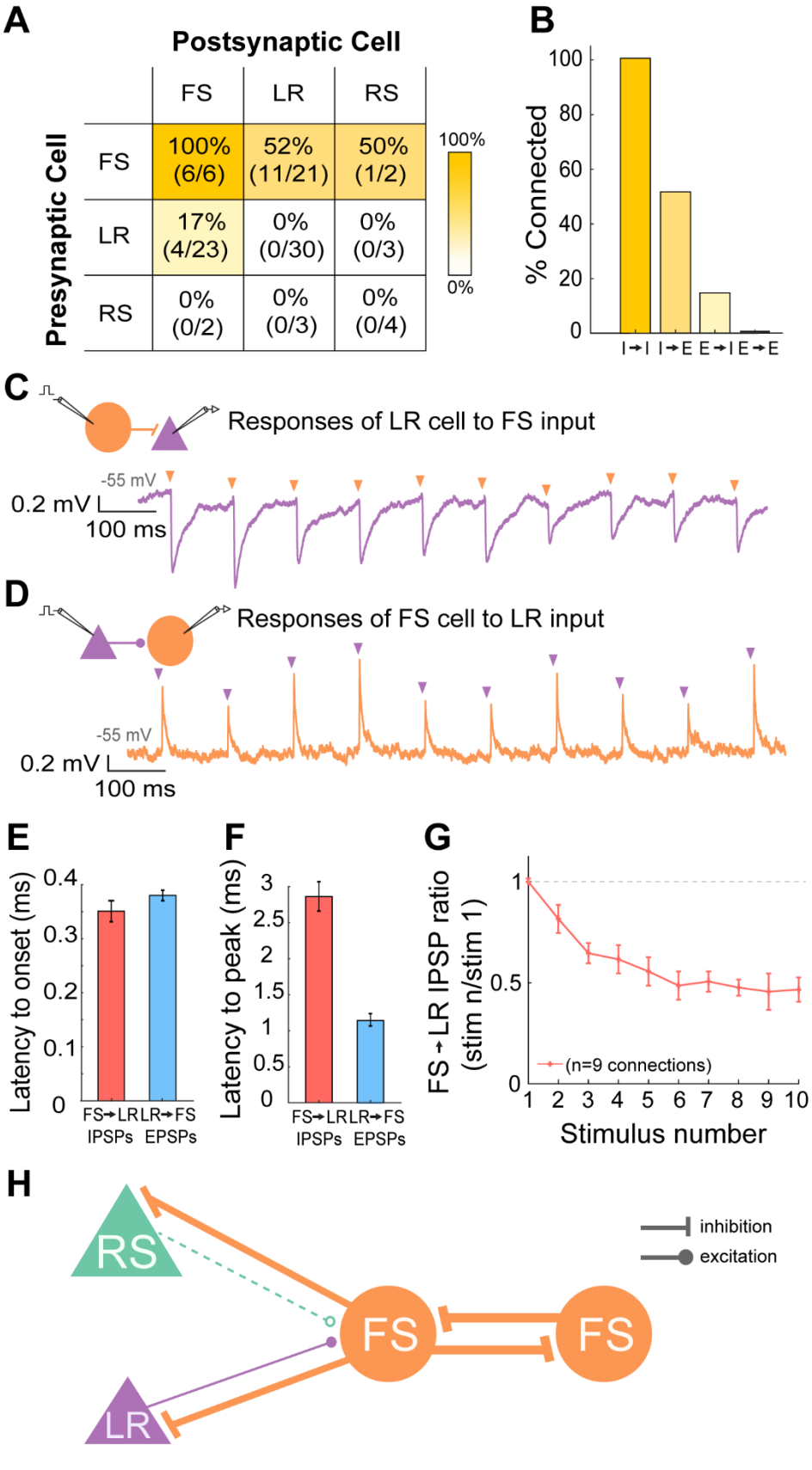
A
Postsynaptic Cell
FS
LR
RS
Presynaptic Cell
FS
100% (6/6)
52% (11/21)
50% (1/2)
LR
17% (4/23)
0% (0/30)
0% (0/3)
RS
0% (0/2)
0% (0/3)
0% (0/4)
100%
0%
B
% Connected
100
80
60
40
20
0
I→I
I→E
E→I
E→E
C
Responses of LR cell to FS input
-55 mV
0.2 mV
100 ms
D
Responses of FS cell to LR input
-55 mV
0.2 mV
100 ms
E
Latency to onset (ms)
0.4
0.3
0.2
0.1
0
FS→LR IPSPs
LR→FS EPSPs
F
Latency to peak (ms)
3
2.5
2
1.5
1
0.5
0
FS→LR IPSPs
LR→FS EPSPs
G
FS→LR IPSP ratio (stim n/stim 1)
1
0.5
0
(n=9 connections)
1 2 3 4 5 6 7 8 9 10
Stimulus number
H
RS
FS
FS
LR
inhibition
excitation

Figure 2-6. Dominant local inhibition in the superficial layers of the retrosplenial cortex.
A. Table indicating the percentage of connectivity between all types of pairs tested. The heat map indicates the probability of connections between the neuron types indicated in each cell of the table. For FS→FS, FS→LR and LR→LR ($p<0.01$, one-sample t-test).
B. Bar graph representing the total connectivity probability between all I→I directional pairs (100%), I→E directional pairs (52%), E→I directional pairs (16%), and E→E directional pairs (0%). Bootstrap resampling followed by a t-test revealed a significantly higher likelihood of observing I→E connections versus E→I connections.
C. Representative trace of the connection between a presynaptic layer 3 FS cell and a postsynaptic layer 3 LR cell (held at -55 mV). The neurons were 27 µm apart with the LR cell located superficial to the FS cell. Schematic shows the patched pair in which the FS cell is being stimulated to spike at 10 Hz, with postsynaptic potentials recorded in the LR cell. The purple trace is the response of the LR cell to a 10 Hz sequences of FS cell spikes (indicated by the orange arrows).
D. Similar to C, but now for a presynaptic LR to postsynaptic FS excitatory connection.
E. Bar graph showing the average latency to onset of the IPSPs recorded from the FS→LR pairs (red) and the EPSPs recorded from the LR→FS pairs (blue) [$p=0.9273$; Wilcoxon rank sum test]. Error bars are standard error.
F. Bar graph showing the average latency to peak of the IPSPs recorded from the FS→LR pairs (red) and the EPSPs recorded from the LR→FS pairs (blue) [$p=0.009$; Wilcoxon rank sum test; N=3 LR to FS connections; N=9 FS to LR connections]. Error bars are standard error.
G. Group synaptic dynamics for FS→LR connections (n=9). Inhibition onto LR cells exhibited strong short-term depression.
H. Schematic of the microcircuitry of FS, RS, and LR cells in the superficial layers of RSG.

2.3.6 Axons from Low Rheobase cells do not ramify locally but head to deeper layers and towards the corpus callosum

The rarity of connections from LR neurons onto their neighboring L2/3 cells suggested that LR axons have more distant targets. In order to investigate the projections of the LR cells, we used biocytin to fill cells for morphological consideration after characterizing their physiological properties and created 3D reconstructions of the neurons using Neurolucida. Three representative LR neurons whose cell body, dendrites, and axons were sufficiently filled are shown in Figure 2-7 All filled LR cells exhibited projections to the deeper layers of RSG (Figure 2-7 F-I). Axons often clearly entered and traveled within the corpus callosum (Figure 2-7 F,H,I). Additionally, LR neurons (unlike FS cells) had very few axonal ramifications within layers 2/3, matching their extremely low likelihood to synapse onto local neurons (Figure 2-7 A,F,G,I). Upon further examination of our four paired recordings in which LR cells directly excited the paired FS cell, we noted that all of these LR cells were located more superficially than their paired FS cell. Conversely, of the four pairs in which the FS cell was located more superficial to the LR cell, none exhibited connections from the LR to the FS cell. This supports the finding that LR axons immediately travel to deeper areas and do not ramify locally or superficial to their cell bodies. It also suggests that FS cells in L2, even more so than L3 FS cells, are likely to be completely devoid of local excitation from LR cells.

Since LR neurons are pyramidal, we also sought to compare their morphology to neighboring pyramidal RS neurons which exhibit extremely different electrophysiological properties. Sholl analysis revealed distinct dendritic morphologies of the two pyramidal

cell types, with RS neurons having significantly more intersections up to 150 μm from the soma (Figure 2-7 B). To further investigate these differences, we measured key morphological characteristics and found that RS cells were indeed significantly larger than LR neurons, having larger cell bodies, longer dendrites, and a greater number of dendritic branches (Figure 2-7 C-E). These morphological differences between RS and LR cells reinforce their physiological differences and further support the characterization of LR cells as a unique cell type.

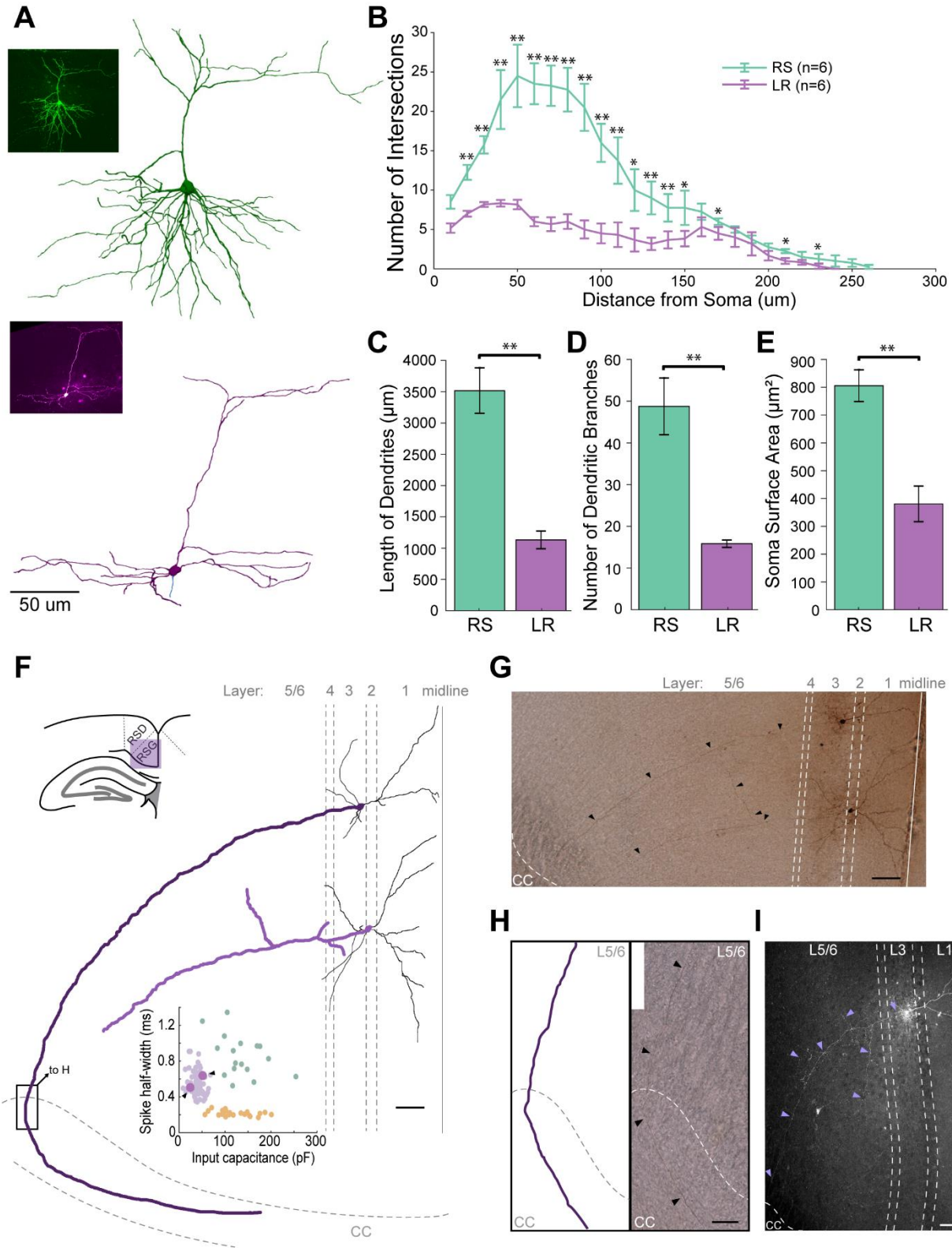
A
B
Number of Intersections
Distance from Soma (um)
RS (n=6)
LR (n=6)
50 um
C
Length of Dendrites (µm)
D
Number of Dendritic Branches
E
Soma Surface Area (µm²)
RS
LR
F
Layer: 5/6 4 3 2 1 midline
RSD
RSG
to H
Spike half-width (ms)
Input capacitance (pF)
CC
G
Layer: 5/6 4 3 2 1 midline
CC
H
L5/6
CC
I
L5/6
L3
L1
CC

Figure 2-7. Low-Rheobase axons do not ramify locally and instead project to deeper layers and the corpus callosum.
A. Fluorescent fills and subsequent Neurolucida reconstructions of an example RS (green) and LR (purple) neuron. Scale bar indicates 50 um.
B. Sholl analysis of the total dendrites of RS (green) and LR (purple) neurons in layers 2/3 of RSG (*p<0.05; **p<0.01; Wilcoxon rank sum test).
C. Bar graph comparing the total length of dendrites of RS (green) and LR (purple) neurons (**p<0.01; Wilcoxon rank sum test).
D. Same as **C** for number of dendritic branches (**p<0.01; Wilcoxon rank sum test).
E. Same as **C** for soma surface area (**p<0.01; Wilcoxon rank sum test).
F. Schematic of the axonal ramifications of two L2/3 LR neurons. Top left shows the location of the RSC within the -1.82 mm AP slice in a P25 mouse. Layers and corpus callosum (CC) are demarcated by grey dashed lines, with the midline of the brain demarcated as a solid line. Scale bar represents 50 um. Dendrites are in black, and cell bodies/axons are in purple. Axons project clearly to deeper layers, often entering the corpus callosum. Minimal axonal ramifications are observed in L2/3. Inset is identical to that in Figure 2-2 B with the two LR cells referenced here in larger purple dots, indicated by the arrows.
G. Biocytin fill used to create the schematic in A. Arrows are placed periodically along the axon for visualization. Scale bar represents 50 µm.
H. Zoomed in view of the indicated box in A. Left shows a schematic of the axon projecting through L5/6 before entering and traveling within the CC. Right shows biocytin fill image. Arrows are placed periodically along the axon for visualization. Scale bar represents 50 µm.
I. Fluorescent fill of an LR cell with axonal projection to the corpus callosum. Arrows are used to visualize the projecting axon and minor ramifications in deeper layers. Layers and corpus callosum are demarcated by dashed lines; a solid line indicates the midline. Scale bar represents 100 µm.

2.3.7 Low Rheobase neurons support high fidelity, sustained responses to persistent head direction inputs

We next created biophysically realistic models of both RS and LR cells (see Methods). The morphology of both the RS and LR neuron models were based on anatomical reconstructions of their experimental counterparts (Figure 2-8 A&E). Experimental physiological properties were accurately reproduced in each model (Figure 2-8 B&F), with the LR neuron model having a higher input resistance, minimal spike frequency adaptation, and narrower spike width than the RS neuron model (Figure 2-8 C&G). Frequency-current responses and latency-current response of the neuron models also closely corresponded to the experimental data for each neuronal subtype (Figure 2-8 D&H).

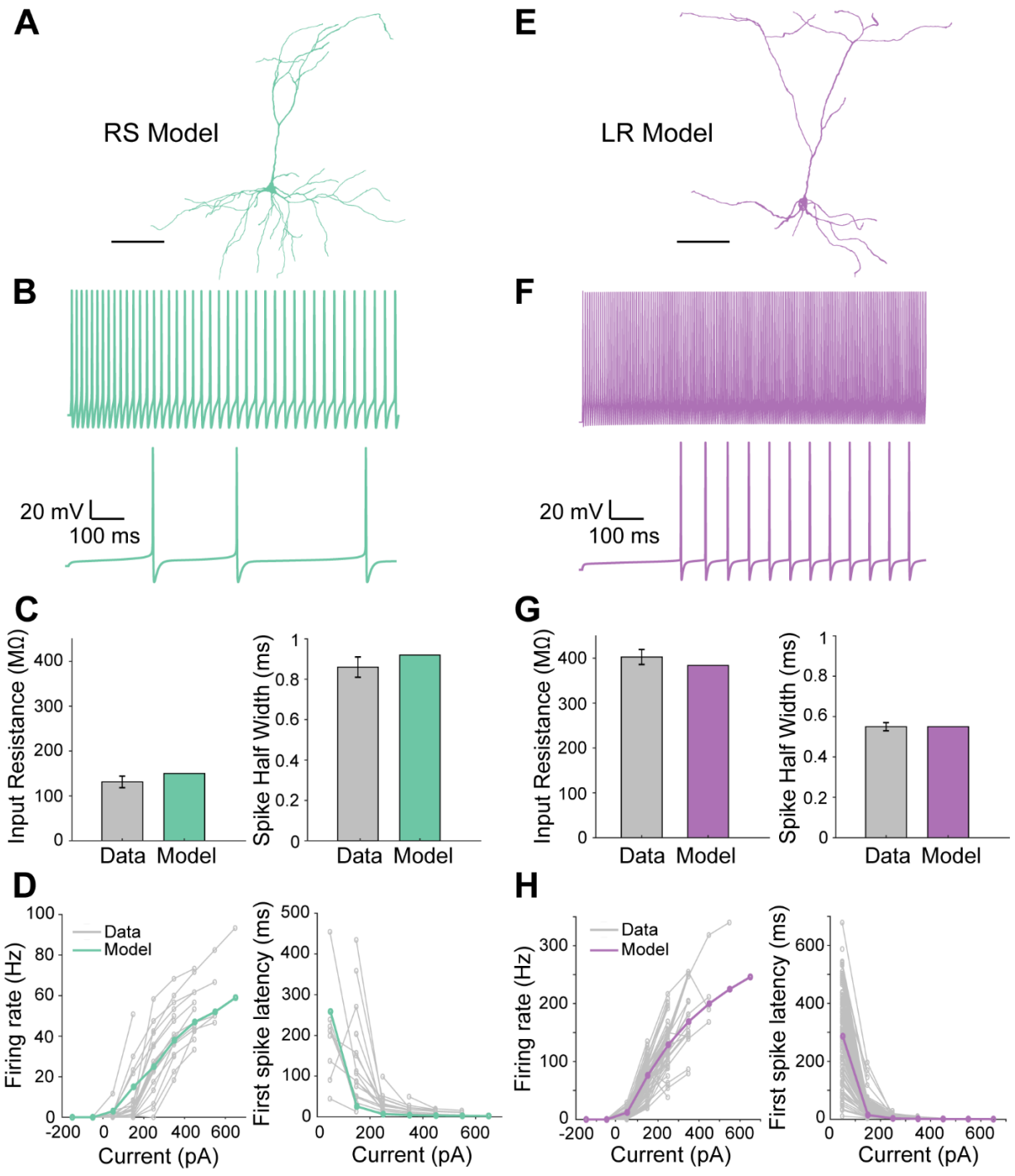

Figure 2-8. Computational models of low-rheobase and regular-spiking neurons accurately replicate the physiological and morphological properties of the respective neuronal subtypes.

A. Morphology of the corresponding RS neuron model. Scale bar indicates 50 µm.

B. Response of the RS neuron model to a low (50 pA) and high (400 pA) current injection.

C. Left, Input resistance of the RS neuron model (green; 150 MΩ) compared to the average input resistance of the physiologically recorded RS cells (grey; 131.27 MΩ). Right, Bar graph representing the spike width of the RS neuron model (green; 0.87 ms) compared to the average spike width of the physiologically recorded RS cells (grey; 0.86 ms).
D. Left, Similar Frequency-Current (F-I) relationships for the model (green) and physiologically recorded (grey) RS cells. Right, Latency to first spike-Current (L-I) relationship for the model (green) and physiologically recorded (grey) RS cells.
E. Morphology of the LR neuron model. Scale bar indicates 50 μm.
F. Modeled LR cell response to a low (50 pA) and high (400 pA) current injection.
G. Left, Input resistance of the LR neuron model (purple; 441 MΩ) compared to the average input resistance of the physiologically recorded LR cells (grey; 402.69 MΩ). Right, Bar graph representing the spike width of the LR neuron model (purple; 0.49 ms) compared to average spike width of physiologically recorded LR cells (grey; 0.55 ms).
H. Left, Similar F-I relationship for the model (purple) and physiologically recorded (grey) LR cells. Right, L-I relationship for the model (purple) and physiologically recorded (grey) LR cells.

We next used these biophysically realistic models to understand the information processing capabilities of LR versus RS neurons. The subdivisions of the subicular complex provide some of the most prominent sources of input to the superficial layers of the RSC (Wyss and van Groen, 1992; van Groen and Wyss, 2003; Yamawaki et al., 2019a). Many cells in the postsubiculum fire selectively when an animal is facing a particular direction and are hence called head-direction (HD) cells (Taube et al., 1990). These postsubicular HD cells are bursty, firing a series of rapid spikes at a rate of 150-250 Hz (Funahashi and Stewart, 1997; Peyrache et al., 2015). The same postsubicular HD cells also fire long-duration, persistent trains of action potentials (Taube and Bassett, 2003; Yoshida and Hasselmo, 2009; Peyrache et al., 2015). This persistent firing is thought to be critical for maintaining a sense of orientation when the animal is not moving, but instead continuously facing a particular direction (Taube and Bassett, 2003; Yoshida and Hasselmo, 2009; Peyrache et al., 2015).

We sequentially examined how these important properties of postsubicular inputs are processed by RS versus LR neurons. First, 200 Hz bursts consisting of 5 spikes were input into both RS and LR cell models (Figure 2-9 A&B). The RS cell response to each of the constituent spikes within the burst was characterized by a low probability of firing and imprecisely timed action potentials (high jitter). LR cells, on the other hand, responded with high reliability and more precisely timed action potentials with little jitter across trials (Figures 2-9 C-F), as would be expected based on their much higher input resistance. LR cell spikes were significantly more reliable and more precise (less jitter) than RS cell spikes in response to the burst input ($p<0.001$; two-tailed t-test), showing that LR neurons are capable of higher fidelity burst encoding with superior spike timing

coding capabilities than their neighboring RS neurons. Qualitatively similar results were obtained when the g_{max} of synaptic inputs was halved in strength (data not shown).

We next examined the ability of LR and RS neurons to respond to persistent inputs of varying durations. First, we utilized a continuous input spike train of 200 Hz over progressively longer durations. LR cells were able to respond with high probability and high precision for all durations examined (Figure 2-9 G). RS cells, on the other hand, had average response probabilities under 0.4, even when we removed the adaptation current from the RS cell model. Signal-to-noise ratio (SNR) analyses (see methods) showed that the LR cell response was characterized by high SNR to prolonged 200 Hz inputs (Figure 2-9 H). RS cells, with and without adaptation, showed several fold lower SNR for both short and long durations (Figure 2-9 H). The ratio of SNR_{LR} to SNR_{RS} progressively increased at higher input durations (Figure 2-9 H, inset), indicating the progressive failure of RS cells to reliably encode longer duration inputs with enough spikes. When we removed the adaptation current from the RS cell model, the ratio SNR_{LR} to $SNR_{RS\text{-}No\text{-}Adap}$ remained very high but did not progressively increase as a function of increasing input durations (Figure 2-9 H, inset), indicating that the spike frequency adaptation of RS neurons prevents reliable transmission of long duration, persistent inputs to its postsynaptic targets. These results suggest that a combination of passive and active properties enable LR neurons to have higher fidelity, sustained SNR at high input durations. The SNR results held true even when we increased the stimulation frequency of background synaptic inputs to 10 or 20 Hz (Figure 2-10), suggesting our results were robust to variations in these model parameters. The spike

frequency adaptation of RS neurons amplifies the SNR disadvantage of RS neurons at longer durations.

Finally, we validated our models' predictions by utilizing realistic input spike trains recorded from head direction cells in the postsubiculum (Figure 2-9 I; Peyrache and Buzsaki, 2015). As expected, this dataset included epochs of persistent, long-duration firing when the animal faced a given cell's preferred head direction. A typical postsubicular neuron had an intra-burst frequency of ~100 Hz, based upon the inter-spike-interval (ISI) histogram (Figure 2-11 A). The LR neuron model exhibited higher probability of firing and greater spike timing precision compared to the RS neuron model when stimulated with spike trains corresponding to this peak firing rate in this dataset, further affirming the superior encoding capabilities of the LR neuron model (Figure 2-11 B-D). We found that LR neurons encoded this postsubiculum HD input with higher SNR at all input durations. The ratio of SNR_{LR} to SNR_{RS} again increased dramatically at higher input durations (when the animal faced the same direction for long periods of time; Figure 2-9 J), indicating the inability of RS neurons to faithfully encode persistent, long duration inputs coming from the postsubicular HD cells.

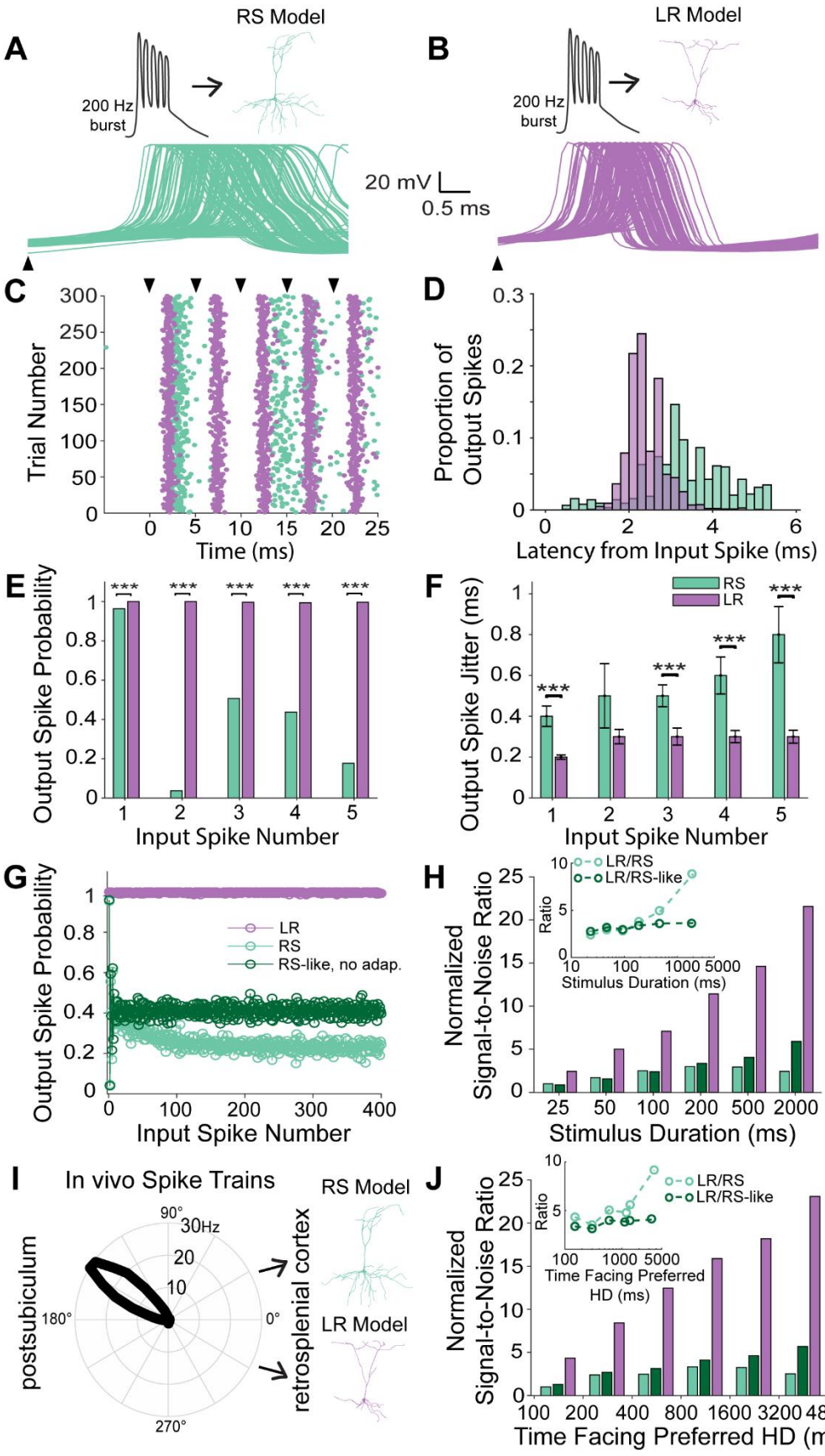
A
RS Model
200 Hz burst
20 mV
0.5 ms
B
LR Model
200 Hz burst
C
Trial Number
Time (ms)
D
Proportion of Output Spikes
Latency from Input Spike (ms)
E
Output Spike Probability
Input Spike Number
***
F
Output Spike Jitter (ms)
RS
LR
Input Spike Number
G
Output Spike Probability
LR
RS
RS-like, no adap.
Input Spike Number
H
Normalized Signal-to-Noise Ratio
LR/RS
LR/RS-like
Ratio
Stimulus Duration (ms)
I
In vivo Spike Trains
postsubiculum
retrosplenial cortex
30Hz
RS Model
LR Model
J
Normalized Signal-to-Noise Ratio
LR/RS
LR/RS-like
Ratio
Time Facing Preferred HD (ms)

Figure 2-9. Unique properties of low-rheobase neurons enable high fidelity, sustained transmission of persistent head-direction input.
A. Top, Schematic of a 200 Hz, 5-spike burst input to the RS neuron model. Bottom, Membrane potential traces of the RS neuron in response to first spike of the burst input across 300 trials.
B. Top, Similar to ***A***, but now for the LR neuron model.
C. Raster plot of the firing of RS and LR neuron models in response to the burst input. The RS model response is characterized by low-reliability and lack of spike timing precision, whereas the LR model fires with high reliability and high spike timing precision.
D. Distribution of spike latencies of the RS (green) and LR (purple) models for all five spikes within the burst input, highlighting the precise timing of LR responses.
E. Output spike probability of the RS (green) and LR (purple) models to each individual spike within the burst. The LR model has a significantly higher probability of responding to each spike within the burst compared to the RS model (*** $p<0.001$; Pearson chi-square test).
F. Spike timing precision computed as the jitter in the output spikes for the RS (green) and LR (purple) models to each individual spike within the burst. LR model is characterized by high spike timing precision compared to the RS model (*** $p<0.001$; two-tailed t-test).
G. Output spike probability of the LR model and two models of RS cells (a standard model and a second model without spike frequency adaptation) as a function of input spike number for a 2s continuous stimulation. Note the diminished spike probability on both RS models, compared to the highly reliable LR responses.
H. Signal to noise ratio (SNR) of RS (with and without spike frequency adaptation) and LR neuron models as a function of the duration of the input stimulus. Inset represents the ratio of SNR of the LR neuron model to the SNR of the RS neuron model (with and without spike frequency adaptation).
I. Schematic of *in vivo* head direction input from the postsubiculum (from dataset: (Peyrache and Buzsaki, 2015)) to the modeled RS and LR neurons. The polar plot shows the *in vivo* head-direction tuning of the input postsubiculum head-direction cell.
J. Same as ***H***, but now in response to realistic *in vivo* spike trains of the postsubiculum head-direction cell shown in ***I***. Similar to continuous burst stimulation, the RS neuron model's SNR declines rapidly with increase in stimulus duration due to spike frequency adaptation, highlighting the ability of LR, but not RS, neurons to respond to persistent head-direction input.

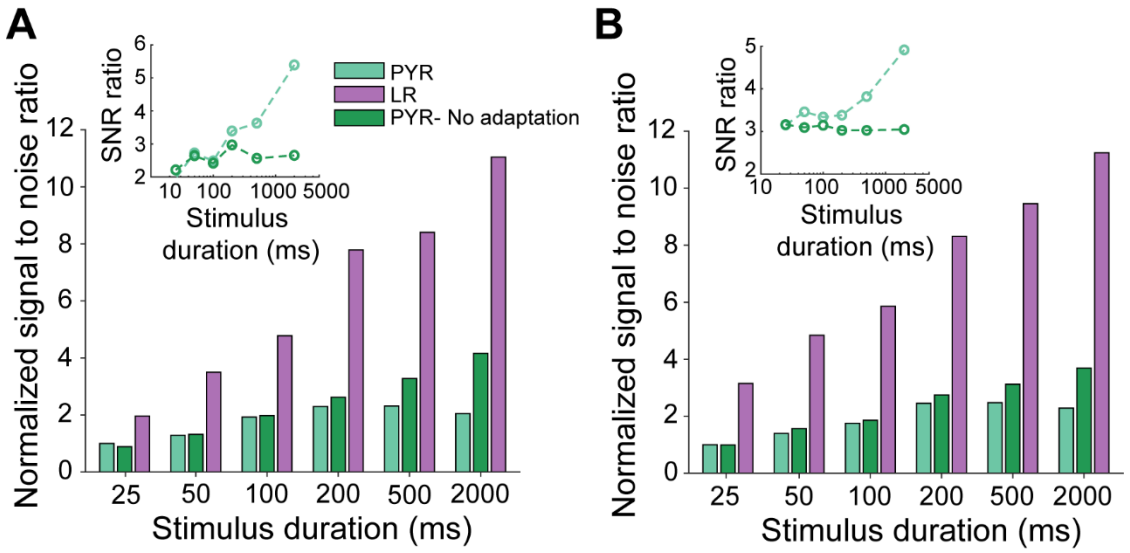

Figure 2-10. SNR of the RS and LR neuron models to inputs of various durations when the background firing frequency is increased to 10 and 20 Hz.
A. SNR of the RS and LR neuron models to 200 Hz input of varying durations when background firing frequency is 10 Hz.
B. Same as ***A*** with background firing frequency increased to 20 Hz.

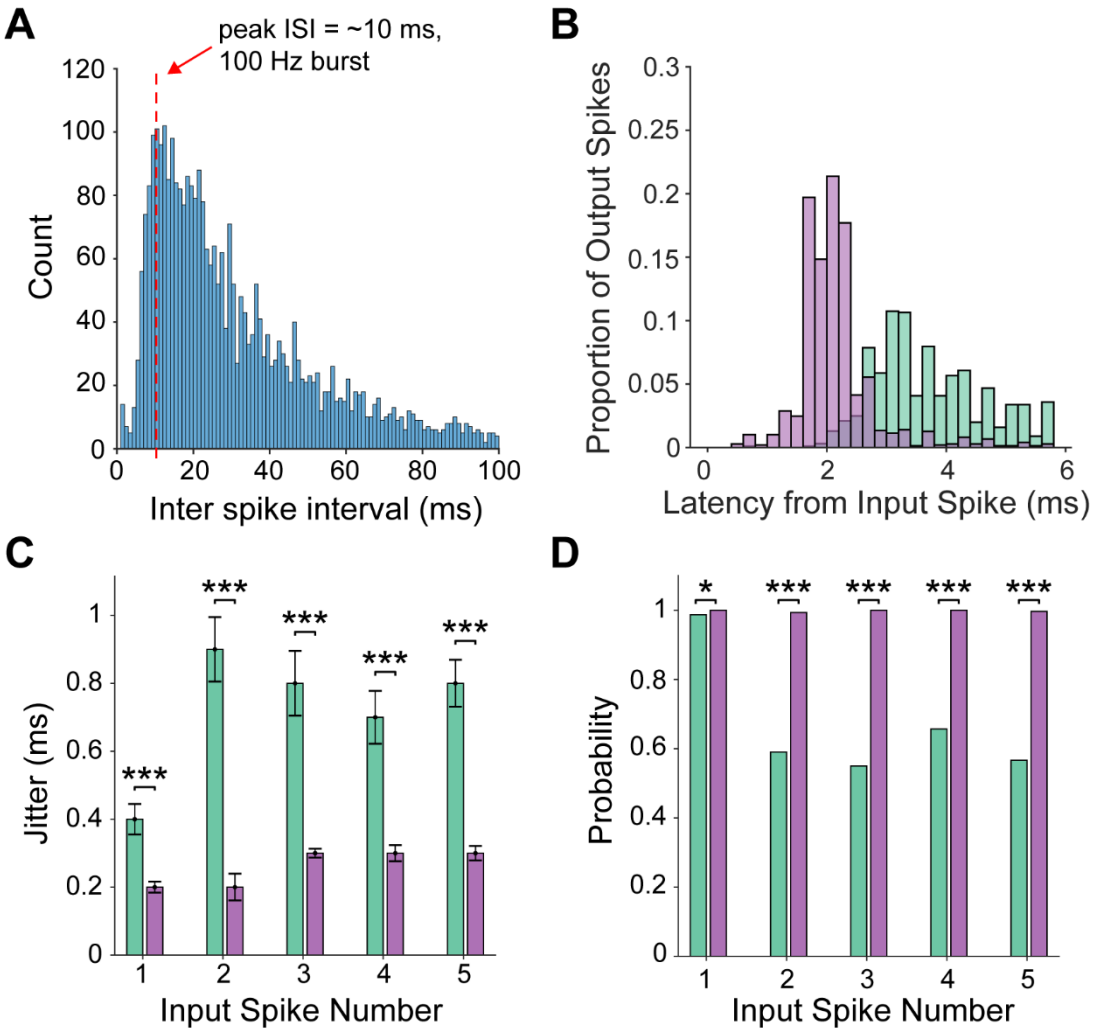

Figure 2-11. Response of the RS and LR neuron models to *in vivo* like spike trains.

A. ISI distribution of *in vivo* spike trains showing peak firing rate at ~100 Hz.

B. Distribution of spike latencies of the RS and LR neuron models when stimulated with 100 Hz spike trains for 2 seconds.

C. Spike timing precision of the RS and LR neuron models in response to each spike of the burst input (*** p<0.001; two-tailed t-test).

D. Spike probability of the two models to each individual spike within the burst input (*** p<0.001, * p<0.05; Pearson chi-square test).

LR and RS neurons are characterized by different dendritic morphologies and branching patterns in terms of number of branches and total branch length (Fig 2-7 B-D). As a result, synaptic inputs can undergo differential filtering, as inputs arriving at apical portions of the dendritic tree are filtered more at the soma compared to proximal inputs (Häusser, 2001). In order to ensure that the differences in SNR between the LR and RS neuron models are not due to their differential dendritic filtering properties, we normalized the synaptic inputs such that their location dependence was eliminated. Even after normalizing the synaptic inputs, the LR neuron model had superior SNR compared to the RS neuron model, and the difference became larger when the input duration was increased (Figure 2-12). The same result was observed when the two models were stimulated with realistic *in vivo* input spike trains (Figure 2-12). These results indicate that SNR differences between the two neuronal subtypes are primarily due to differences in their intrinsic properties and not due to morphological differences. Thus, LR neurons are better suited to encode persistent inputs, such as those involved in long-duration head-direction signaling, than RS neurons.

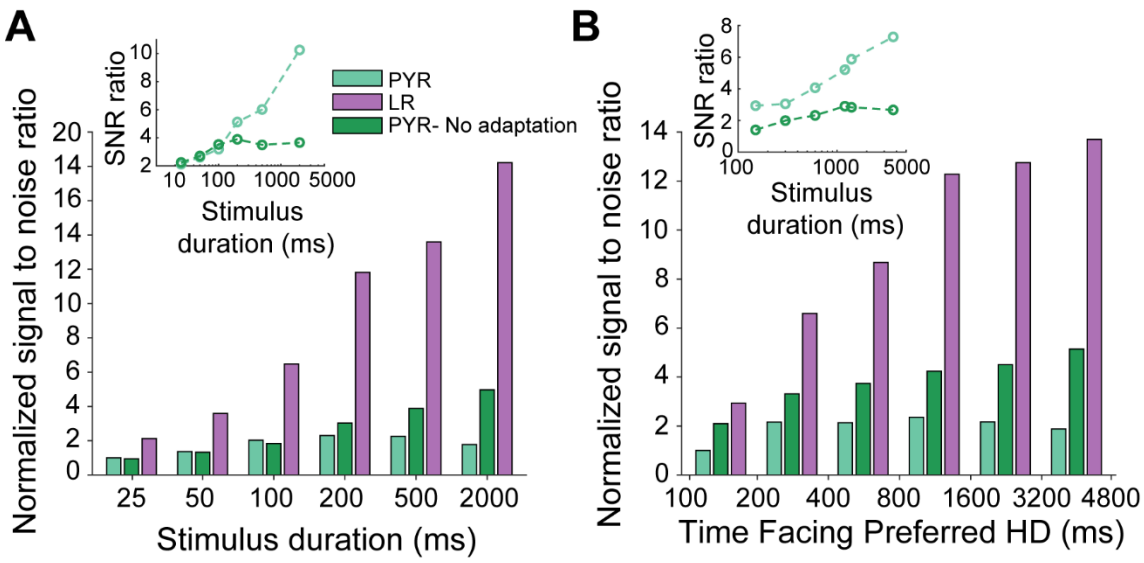

Figure 2-12. SNR of the RS and LR neuron models when location dependence of dendritic synaptic inputs was removed.
A. SNR of the RS and LR neuron models in response to 200 Hz burst input of varying durations. Synaptic inputs were normalized to get rid of the dendritic location dependence. LR neurons have superior SNR compared to RS neurons. The difference in SNR increases with stimulus duration due to the spike frequency adaptation of RS neurons (inset).
B. Same as ***A***, when both RS and LR neuron models were stimulated with realistic *in vivo* spike trains from the postsubiculum head-direction cell as shown in Fig. 2-7 I. Therefore, even when dendritic location dependence of synaptic inputs was eliminated, the LR neuron model is characterized by superior SNR compared to the RS neuron model.

2.4 Discussion

The unique cytoarchitecture of the retrosplenial cortex has long been appreciated by neuroanatomists (Rose, 1927; van Groen and Wyss, 2003; Wyss et al., 1990; Wyss and van Groen, 1992; Ichinohe and Rockland, 2002). The granular division of the retrosplenial cortex, in particular, has two geometric features that appear to set it apart from many other cortical regions: 1) uniquely small pyramidal neurons that cluster most densely in layers 2 and 3 (Wyss et al., 1990; Kurotani et al., 2013); 2) the bundling of apical dendrites emanating from these L2/3 pyramidal neurons (Wyss et al., 1990; Ichinohe and Rockland, 2002). Thus, a thorough understanding of granular RSC function would greatly benefit from an in depth understanding of these unique L2/3 neurons.

Here, we have characterized the detailed intrinsic properties, connectivity, and computational capabilities of these small pyramidal cells, as well as their neighboring, larger, more familiar RS cells, revealing a number of key differences. We call these small pyramidal cells “Low Rheobase” (LR) neurons based upon the ease with which they can be excited and made to fire (due, in large part, to their high input resistance). In addition to their high excitability, these cells also have spike widths that are much narrower than RS cells, and show minimal spike frequency adaptation, again in sharp contrast to RS neurons (Figure 2-1; Table 2-1). We also found that all three cell types examined had a tendency to spike late during a near threshold current injection, consistent with high levels of Kv1.1 or Kv1.2 ion channel expression in the RSC (Kurotani et al., 2013). There was no significant difference in the first spike latency of LR

versus RS cells (Figure 2-1; Table 2-1). Thus, the key, unique computational features of LR cells are their hyperexcitability and lack of spike-frequency adaptation.

How do the distinct passive and active properties of LR vs RS neurons impact their input-output transformations and information-coding capabilities? We used biophysically-realistic models to investigate this question. On the short time-scale, the higher excitability and shorter spike widths of LR cells enables them to spike with a higher probability and lower jitter in response to incoming bursts of spikes (Figure 2-9 A-F), such as those generated by afferent postsubicular cells during active behaviors (Simonnet and Brecht, 2019). On the long time-scale, the almost complete lack of spike-frequency adaptation helps LR cells maintain sustained (and still precise) responses to incoming persistent inputs (Figure 2-9 G-J). This encoding of persistent information appears critical to the function of the RSC. Recent imaging evidence suggests that RSC neurons (generically defined, irrespective of subtype) have a unique ability to encode long-duration, history-dependent value signals (Hattori et al., 2019). Of even more direct relevance is the persistent nature of the navigational information being processed by the superficial RSC. The subicular complex, including the postsubiculum, represents one of the key functional inputs to RSC L2/3 cells (Wyss and van Groen, 1992; Yamawaki et al., 2019b, 2019a). Postsubicular neurons display a strong preference for particular orientations and are thus called head direction (HD) cells (Taube et al., 1990). When an animal faces a particular direction for long durations, postsubiculum HD cells keep spiking persistently, likely contributing to the maintenance of the sense of orientation in the absence of ongoing vestibular changes (Taube et al., 1990; Yoshida and Hasselmo, 2009). The unique properties of LR cells suggest they are ideally suited to respond to

this persistent postsubicular input (Figure 2-9 I-J), enabling the retrosplenial circuit to utilize this valuable head-direction input to help generate a sense of orientation regardless of how long an animal has been facing the same direction. In fact, our results suggest that the longer an animal faces a postsubicular cell's preferred direction, the better the signal-to-noise ratio with which LR neurons can encode this information (due to the accumulation of high-rate signal spikes over time), potentially helping to increase the behavioral certainty of the current orientation and helping to recall orientation-relevant memories. Indeed, a sense of spatial disorientation is one of the key deficits after RSC damage in humans (Bottini et al., 1990; Takahashi et al., 1997; Ino et al., 2007; Osawa et al., 2007).

The presence of two distinct, neighboring principal neurons is seen in several structures that are important for spatial navigation and memory. Recent work has shown that granule and mossy cells in the dentate gyrus differentially encode spatial information (Scharfman, 1992, 2019; GoodSmith et al., 2017; Senzai and Buzsáki, 2017), resolving several previously confusing data points regarding the nature of the sparse code used by granule cells (Leutgeb et al., 2007). Similarly, neighboring deep versus superficial CA1 pyramidal cells have been shown to have differential spatial and temporal firing properties, as well as distinct local and distant connectivity (Mizuseki et al., 2011; Lee et al., 2014; Danielson et al., 2016; Soltesz and Losonczy, 2018). In the subiculum, the cells show two distinct patterns of bursting as well as differences in VGlut1 versus VGlut2 expression (Simonnet and Brecht, 2019; Yamawaki et al., 2019a). Thus, the notion of parallel coding schemes implemented by distinct populations of principal neurons is of clear importance in regions involved in memory

and navigation. In the superficial RSC, our results show that such parallel neural codes are likely to be implemented by the distinct properties of LR and RS neurons. The respective intrinsic properties of LR and RSC cells are likely to make them better suited to encode persistent vs rapidly-changing inputs, respectively. We thus hypothesize that RS cells in L2/3 of RSG are likely to better encode information during active head rotations and movement, whereas LR cells may be better suited to integrating long-duration persistent head direction and position information when the animal is not moving (as shown in Figure 2-9). Indeed, our results predict that the longer an animal faces a particular direction, the higher the signal-to-noise with which LR neurons can encode this information. Thus, LR neurons may contribute heavily to retaining the current directional bearing when initiating the next movement. In addition to the postsubiculum, the RSC receives inputs from several other regions, including directional information from the anterior thalamus (Taube, 1995; Peyrache et al., 2015) and positional and route-based information from the dorsal subiculum and posterior parietal cortex (Sharp and Green, 1994; Sharp, 1999; Nitz, 2006; Kim et al., 2012; Stewart et al., 2014; Wilber et al., 2014; Cullen and Taube, 2017; Olson et al., 2017; Simonnet and Brecht, 2019). Regardless of the precise content of the information being conveyed by these sources, our results indicate the LR neurons are more suited to integrating this information over longer timescales, potentially helping the retrosplenial cortex encode a sense of long-duration spatial orientation and bearing – a sense that manifests itself as confidently knowing where one is and which way one is looking.

Our paired recordings provide the first direct proof that LR neurons are indeed excitatory (Figure 2-6). Although LR cells are the most prevalent cell type in L2/3

(Figure 2-3), they make few local connections (Figure 2-6), instead sending their axons into the deeper layers and corpus callosum (Figure 2-7). LR cells receive prominent inhibitory inputs from the neighboring L2/3 FS cells (Figure 2-6), with the probability of FS-to-LR connectivity reaching 52%, somewhat higher than that reported in many other regions of the neocortex (Beierlein et al., 2003; Yoshimura and Callaway, 2005; Packer and Yuste, 2011; Jiang et al., 2015). This, coupled with the complete lack of local excitatory connections onto LR cells (Figure 2-6) and the dense FS-FS connectivity (Figure 2-6), indicates that the superficial layers of the RSG are a network dominated by local inhibition. The inhibition from FS to LR neurons showed similar short-term depression to that seen from FS to RS cells in many other cortical structures (Figure 2-6 G; Beierlein et al., 2003). Our study had a low number of RS-FS pairs sampled, and their connectivity will be precisely quantified in future work. While we did not explicitly model feedforward inhibition in our simulations, this depression is likely to further aid in the long-duration firing of LR neurons in response to persistent postsubicular inputs by curtailing the strength of feedforward inhibition over time. Of importance to network computations, the strong FS-FS and FS-LR connectivity is also likely to allow the RSC circuit to implement high frequency oscillations that are generated by the interneuron-gamma (ING) mechanism, instead of, or in addition to, oscillations generated via the pyramidal-interneuron-gamma (PING) mechanism (Koike et al., 2017; Alexander et al., 2018). Future large-scale circuit models of the superficial RSC incorporating LR, RS, and FS cells based on the intrinsic properties and connectivity principles described here will help to understand the network computations performed by this unique retrosplenial circuit (Figure 2-6 H).

2.5 Materials and Methods

2.5.1 Experimental model and subject details

All housing of animals and procedures were approved by the University of Michigan Institutional Animal Care and Use Committee. Multiple mouse lines were used in this study, including PV-IRES-Cre (Jackson Laboratories, 008069), CaMKII-Cre (Jackson Laboratories, 005359), Ai32 (Jackson Laboratories, 024109), Ai14 (Jackson Laboratories, 007914), PV-IRES-Cre x Ai14 (crossed in house), PV-IRES-Cre x Ai32 (crossed in house), CaMKII-Cre x Ai32 (crossed in house), and NTSR1-Cre (MMRRC, 030648-UCD). All mice excluding the NTSR1-Cre line were on a C57Bl6 background, while the NTSR1-Cre mice had a mixed C57Bl6/ICR background. Mice of both sexes between the ages of P21-31 and P60-65 were included in the experiments.

2.5.2 Physiological Experimental Methods

Slice preparation

A total of 167 recordings used for intrinsic physiology analyses are included in this study from the following mouse lines: PV-IRES-Cre (55), CaMKII-Cre (15), Ai32 (3), PV-IRES-Cre x Ai14 (3), PV-IRES-Cre x Ai32 (64), CaMKII-Cre x Ai32 (20), and NTSR1-Cre (7). No differences in cell type properties were observed across mouse lines, while both age and sex were explicitly analyzed in terms of their relationship to cell type properties (see Results).

Mice underwent deep isoflurane anesthesia before decapitation. Brains were removed within one minute of decapitation and placed in an ice-cold high-sucrose slicing solution that had been saturated with carbogen gas for at least 30 minutes prior to use. Coronal slices (300um) were cut using a Leica 1200 VT vibratome. Slices were allowed to rest in the slicing solution for about 2 minutes before being placed in a carbogen-saturated high-magnesium artificial CSF (ACSF) solution to incubate at body temperature (32°C) for 20 minutes. The entire bubbling bath was then removed from the heater, allowing the slices to gradually cool to room temperature. Slices rested an additional 30 minutes at room temperature before use.

Slices were submerged in a recording chamber with a constant flow of ACSF containing 126 mM NaCl, 1.25 mM NaH2PO4, 26 mM NaHCO3, 3 mM KCl, 10 mM dextrose, 1.20 mM CaCl2, and 1 mM MgSO4. Recordings were done between 29-31°C with an ACSF flow rate of 2 mL per minute. All recordings were done within 8 hours of slicing to ensure reputable health of the cells. Patch pipettes with 2-3 µm diameter and resistances of 3-6 MΩ were filled with a potassium gluconate internal solution containing 130 mM K-gluconate, 2 mM NaCl, 4 mM KCl, 10 mM HEPES, 0.2 mM EGTA, 0.3 mM GTP-Tris, 14 mM phosphocreatine-Tris, and 4 mM ATP-Mg (pH 7.25, ~290 mOsm).

Whole-cell recordings

Slices were visualized using an Olympus BX51WI microscope equipped with Olympus 5x and 60x water immersion lens and the Andor Neo sCMOS camera (Oxford Instruments, Abingdon, Oxfordshire, UK). In most cases, neurons were patched randomly within layers 2/3 of RSG with the exception of experiments in which PV

neurons were targeted for patching based on their expression of either an eYFP tag (PV-IRES-Cre x Ai32 cross) or a tdTomato tag (PV-IRES-CRE x Ai14 cross). All recordings were done under current clamp conditions using the Multiclamp 700B and Digidata 1440A (Molecular Devices). Neurons were adjusted for series resistances and held at a resting potential of -65 mV (unless otherwise stated) using a constant holding current injection. Recordings were not corrected posthoc for liquid junction potential. In order to characterize the different neuron types, intrinsic and firing properties of recorded neurons were calculated using the Clampfit and Matlab software packages.

Synaptic connections between neurons were tested using paired whole-cell recordings. 1 ms current pulses were delivered to the presynaptic neuron at 10 Hz for a total of 1 second (10 pulses). The synaptic responses of the postsynaptic neuron were simultaneously recorded, while holding the postsynaptic cell at -55 mV.

Optogenetic testing of CaMKII expression

Optogenetic verification of CaMKII expression was conducted using CaMKII-Cre x Ai32 mice (Jackson Laboratories 005359 and 024109 respectively, crossed in house) in which channelrhodopsin is expressed in CaMKII-Cre-expressing neurons. Slices were visualized with the Olympus BX51WI equipped with Olympus 5x and 60x water immersion lens. Expression of channelrhodopsin was marked by fluorescence of the eYFP tag. Neurons were recorded in the same manner as described above with at least one additional protocol to verify functional expression of the channelrhodopsin. One millisecond optogenetic light pulses with a 5,500K white LED (Mightex; maximum power of 14.47 mW measured at the slice focal plane) were delivered at 10 Hz while the

neuronal responses were recorded. Direct expression was verified by responses to the light pulses under 0.15 ms.

Morphological investigations with biocytin

An additional 12 cells were characterized for their morphology. To determine patched cells' morphology, 5mg/ml of biocytin was added to the internal solution of recording electrodes. Cells were filled with biocytin (Sigma, cat. no. B4261) throughout the recording session, and the pipette was left attached to the cell for at least 20 min. At the end of the recording, cells were "zapped" with fifteen 1 Hz pulses of 3-4 nA current to improve the diffusion of biocytin into the axon (Jiang et al., 2015). Slices were left to recover in the recording chamber for 30 min before further processing. A detailed description of the biocytin labelling and processing is available elsewhere (Marx et al., 2012). Briefly, slices were filled with biocytin as described above, placed in 4% paraformaldehyde (PFA; Acros Organics, cat no. B0144942) for 12-15 hours, and then transferred to phosphate buffer solution (PBS). After 24-48 hours in the PBS, slices were incubated in avidin-biocytin (ABC Elite kit, VectaShield) for 12 hours and then treated with peroxidase to reveal cell morphology. Finally, slices were mounted on microscope slides with Mowiol-based embedding medium and allowed to dry for at least 12 hours. Cells were visualized using a Leica DM4000B light microscope equipped with a Leica DMC 6200 CMOS camera.

Morphological investigations with Alexa-Fluor

To investigate cell morphology using fluorescence, biocytin (5mg/ml, Sigma cat no. B4261) was added to the internal solution. Cells were filled with biocytin for a total of 20-30 min each, and the slices were then moved to 4% PFA (Fisher Scientific, cat no.

50-980-494) for overnight incubation. Afterwards, the slices were washed in PBS, permeabilized in 0.2% Triton-X (Sigma, X-100) and incubated for 48 hours in either streptavidin conjugated Alexa Fluor 488, 594, or 647 (1mg/1ml diluted to 1:1000, Thermo Fisher Scientific S11223, S11227, or S21374 respectively). Slices were mounted on glass slides using Fluoromout-G mounting medium (SouthernBiotech, cat no. 0100-01) and glass coverslips and visualized with Leica 6000B microscope equipped with a 10x objective and QImaging Retiga-SRV Fast 1394 camera.

Morphological reconstructions

For morphological analysis, z-stacks of filled cells were taken with the Leica SP5 confocal microscope using a 40x dry objective. Reconstructions from z-stacks were performed using user-guided mode in Neurolucida software and analysed in Neurolucida Explorer.

2.5.3 Computational Modeling Methods

Model motivation

Biophysical modeling was utilized to study in detail the computational properties of LR and RS neurons and the possible coding mechanisms by which they could contribute to the spatial navigation functions of the RSC. To this end, we constructed multi-compartmental, biophysically-realistic models of the two neuronal subtypes based on anatomical reconstructions and tuned the model parameters so that their intrinsic properties closely match their experimental counterparts. The following section explains in detail the active and passive properties of the LR and RS neuron models. Both LR

and RS neuron models will be uploaded to ModelDB (http://modeldb.yale.edu/260192). Unlike the experimental data, where junction potential was not adjusted for, all membrane potential values listed below for the computational model should be considered adjusted for the junction potential.

2.5.3a LR neuron model

Morphology and passive properties

To further elucidate the computational properties of LR neurons, we constructed a biophysically realistic model based on their anatomical reconstruction and physiological properties. The model's morphology (Figure 2-8 E) was imported in NEURON using the import3D tool (M.L Hines and N.T.Carnevale, 2001). The model has an input resistance and input capacitance of 384 MΩ and 37.2 pF, respectively, closely matching the experimental values of LR neurons. The membrane time constant of the model is 14.29 ms. The resting membrane potential of the model is -77.8 mV.
Both LR and RS neuron models were simulated at a temperature of 30°C, and a q10 value of 3 (Bertil Hille, 2001) was used to scale the temperature dependence of ion channel kinetics. The number of segments in each compartment was calculated using the d-lambda rule (Hines and Carnevale, 2001). The axial resistivity for both models is 200 Ω-cm (Vierling-Claassen et al., 2010).

Active properties

Three voltage-gated ion channels were simulated for the LR neuron model: Fast sodium current (I_{Na}), delayed rectifier potassium current (I_{Kdr}), and K_v1 current (I_d). In addition, a phenomenological mechanism (I_{adap}) for spike frequency adaptation was also modeled (Treves, 1993; Fuhrmann et al., 2017). The properties of these currents

are described in detail in the following sections. The LR neuron model has a spike half-width of 0.55 ms and a spike threshold of -53.9 mV. The model exhibits very little spike frequency adaptation, with an adaptation ratio of 1.1, as seen in the experimental data. For both models, the reversal potential of sodium (E_{Na}) and potassium ions (E_K) were set to +50 mV and -96 mV, respectively.

Fast sodium current

The fast sodium current (I_{Na}) responsible for action potential generation was modeled based on Hodgkin Huxley formulation (Hodgkin and Huxley, 1952) using the experimental gating properties of transient sodium current found in RS neurons (Martina and Jonas, 1997). The channel was modeled with 3 activation gates and an inactivation gate. The channel was distributed in all the 8 compartments of the model, and their respective maximal channel conductance (g_{max}) is tabulated in Table 2-3. The channel equations and parameters (Martina and Jonas, 1997; voltage dependence of steady state activation/inactivation (m_∞, h_∞), the time constants of activation and inactivation gates (τ_m, τ_h), channel current (I_{Na})) is given below.

$$m_\infty = \frac{1}{\left(1 + exp\left(-\left(\frac{v - \theta\_m}{\sigma\_m}\right)\right)\right)} \tag{2-1}$$

$$h_\infty = \frac{1}{\left(1 + exp\left(-\left(\frac{v - \theta\_h}{\sigma\_h}\right)\right)\right)} \tag{2-2}$$

$$\tau_m = \left(\left(0.022 + \frac{3.6}{\left(1 + exp\left(\frac{(v + 27.9)}{7.6}\right)\right)}\right) \times \left(0.009 + \frac{1.9}{\left(1 + exp\left(\frac{-(v - 1.3)}{12.7}\right)\right)}\right)\right)$$

(2-3)

$$\tau_h = \left(0.31 + \frac{14}{\left(1 + exp\left(\frac{(v + 60)}{12}\right)\right)}\right)$$

(2-4)

where $\theta_m = -22.8\,mV,\ \sigma_m = 11.8\,mV,\ \theta_h = -62.9\,mV, \sigma_h = -10.7\,mV.$

$$I_{Na} = g_{max} \times m^3 \times h \times (V_m - E_{Na})$$

(2-5)

Delayed rectifier potassium current

Delayed rectifier potassium currents (I_{Kdr}) are known to contribute to action potential repolarization in numerous neuronal subtypes of the brain (Locke and Nerbonne, 1997; Murakoshi and Trimmer, 1999; Guan et al., 2007; Liu and Bean, 2014). We modeled this current in the LR neuron model using the channel gating properties of delayed rectifier potassium currents found in RS neurons (Liu and Bean, 2014). The channel model consists of 2 activation gates (Golomb et al., 2007) and no inactivation gates. The channel's activation time constant (Liu and Bean, 2014) was tuned such that the model's spike half width matches the experimentally obtained values. The channel was distributed in all 8 compartments of the model, and their g_{max} values are given in Table 2-3. The equations for voltage dependence of steady state activation (n_∞) and the activation time constant (τ_n) of the channel is described below.

$$n_\infty = \frac{1}{\left(1 + exp\left(-\left(\frac{v - \theta\_n}{\sigma\_n}\right)\right)\right)} \tag{2-6}$$

$$\tau_n = \left(\left(0.087 + \frac{3.4}{\left(1 + exp\left(\frac{(v + 3.6)}{9.6}\right)\right)}\right) \times \left(0.087 + \frac{3.4}{\left(1 + exp\left(\frac{-(v - 1.3)}{18.7}\right)\right)}\right)\right) \tag{2-7}$$

where $\theta_n = -20\ mV,\ \sigma_n = 10.4\ mV$

$$I_{Kdr} = g_{max} \times n \times n \times (V_m - E_K) \tag{2-8}$$

<u>K_v1 current</u>

The K_v1 current (also known as the d-current,(I_d)) is a potassium current that is widely known to cause a delay to first action potential in many neuronal subtypes (Storm, 1988; Goldberg et al., 2008; Kurotani et al., 2013). We modeled this current to capture the late spiking property of LR neurons that is observed in our physiological data. Similar to the fast sodium and delayed rectifier currents, this current was modeled using the Hodgkin Huxley formalism (Hodgkin and Huxley, 1952). Based on experimental data (Wu and Barish, 1992) and a previously published model (Golomb et al., 2007), the K_v1 channel was modeled with 3 activation gates with faster kinetics and a slowly inactivating gate. This channel was distributed only in the somatic compartment of the neuron. The channel's g_{max} is given in Table 2-3. The voltage dependence of steady state activation/inactivation (a_∞, b_∞) and their respective time constants (τ_a, τ_b) of the channel are given below.

$$a_\infty = \frac{1}{\left(1 + exp\left(-\left(\frac{v - \theta\_a}{\sigma\_a}\right)\right)\right)}$$

(2-9)

$$b_\infty = \frac{1}{\left(1 + exp\left(-\left(\frac{v - \theta\_b}{\sigma\_b}\right)\right)\right)}$$

(2-10)

$$\tau_a = 1.4\, ms,\ \tau_b = 150\, ms$$

(2-11)

where $\theta_a = -50\, mV,\ \sigma_a = 20\, mV,\ \theta_b = -70\, mV, \sigma_b = -6\, mV.$

$$I_d = g_{max} \times a^3 \times b \times (V_m - E_K)$$

(2-12)

Adaptation current

Spike frequency adaptation was modeled using a linear mechanism (I_{adap}) as described in previous studies (Treves, 1993; Fuhrmann et al., 2017). I_{adap} was modeled using the following equations (Treves, 1993).

$$I_{adap} = g(t) * (V_m - E_K)$$

(2-13)

$$\frac{dg}{dt} = -\frac{g}{\tau_g} + g_{adap} \times \delta\left(t - t_{spike}\right)$$

(2-14)

Briefly, when a cell fires an action potential, $g(t)$ is increased by g_{adap}, which decays to zero with a time constant of τ_g. t_{spike} is the time at which the neuron spikes, and E_K is the potassium reversal potential. $g_{adap} = 10\,pS$ and $\tau_g = 500\,ms$ (Liu and Wang, 2001).

2.5.3b RS neuron model

Morphology and passive properties

The RS neuron model in our study is based on the biophysical and anatomical properties of RS neurons in layers 2/3 of RSG. The morphology of the model is based on anatomical reconstructions of its experimental counterpart (Figure 2-8 A). The model's input resistance is 148 MΩ and input capacitance is 96.6 pF. The model has a membrane time constant of 14.29 ms. The model's resting membrane potential is -74.95 mV. Thus, the model's passive properties accurately replicate those of RS neurons in layer 2/3 of RSG. The model's ion channels and active properties are described in detail below.

Active properties

Similar to the LR neuron model, the RS neuron model has 3 voltage gated currents and a current for spike frequency adaptation (I_{adap}). The voltage gated currents incorporated in the RS neuron model are fast sodium current (I_{Na}), delayed rectifier potassium current (I_{Kdr}) and K_v1 current (I_d). The model has a spike half width of 0.92 ms and a spike threshold of -54.12 mV. The spike frequency adaptation ratio of the model is 2.5, closely matching the experimental values.

Fast sodium current

The fast sodium current of the RS neuron model was modeled using Hodgkin Huxley's equations (Hodgkin and Huxley, 1952). The channel's voltage dependence of steady state activation/inactivation and their time constants were modeled using equations 1-5 (Martina and Jonas, 1997). The channel was distributed both in the somatic and dendritic compartments whose g_{max} values are described in Table 2-3.

Delayed rectifier potassium current

The delayed rectifier potassium current (I_{Kdr}) was modeled based on the channel gating properties of K_v2 currents found in RS neurons (Liu and Bean, 2014). Similar to the LR neuron model, the channel consists of 2 activation gates and does not exhibit any inactivation (Liu and Bean, 2014). Compared to LR neurons, the activation kinetics of I_{Kdr} was slower to account for the larger spike width of RS neurons. The kinetics of this current was chosen to account for the spike width differences between the two neuronal subtypes as delayed rectifier potassium current play a vital role in controlling the spike width of many central neurons (Erisir et al., 1999). The channel was placed in the somatic and dendritic compartments of the model (see Table 2-3 for g_{max} values). The channel equations are given below.

$$n_{\infty} = \frac{1}{\left(1 + exp\left(-\left(\frac{v - \theta\_n}{\sigma\_n}\right)\right)\right)} \tag{2-15}$$

$$\tau_n = \left(\left(0.087 + \frac{17.4}{\left(1 + exp\left(\frac{(v + 3.6)}{9.6}\right)\right)}\right) \times \left(0.087 + \frac{25.4}{\left(1 + exp\left(\frac{-(v - 1.3)}{18.7}\right)\right)}\right)\right) \tag{2-16}$$

where $\theta_n = -20\,mV$, $\sigma_n = 10.4\,mV$

$$I_{Kdr} = g_{max} \times n \times n \times (V_m - E_K) \quad \text{(2-17)}$$

K_v1 current

In order capture the observed late spiking behavior of layer 2/3 RS neurons of the RSC, I_d was also modeled in the RS neuron model. The channel's gating mechanisms were modeled using equations 9-12 (Golomb et al., 2007). I_d was distributed only in the somatic compartment of the model (see Table 2-3 for g_{max} values).

Adaptation current

The spike frequency adaptation in the RS neuron model was modeled using the same schema (I_{adap}) as described for LR neurons (equations 13-14; Treves, 1993; Fuhrmann et al., 2017). The following parameters were used for this current: $g_{adap} = 800\,pS$ and $\tau_g = 500\,ms$. In a subset of simulations (Figure 2-10) the adaptation current in RS cells was explicitly removed to study the contributions of adaptation to RS input-output transformations.

2.5.3c Modeled inputs

Synaptic inputs

The LR and RS neuron models received background and burst synaptic inputs. Briefly, the synaptic inputs were simulated in the following way: 40 AMPA synapses and 40 GABA synapses were uniformly distributed throughout the dendritic tree of both neuron models. Each of the background and burst inputs was randomly assigned to one of the AMPA synapses in the dendritic tree of the LR and RS neuron models. The

properties of background and burst inputs are described in detail below. Similarly, each of the background GABAergic inputs discussed below was randomly assigned to one of the GABAergic synapses.

Background inputs

The RS and LR neuron models received 50 AMPAergic background inputs. The time course of synaptic conductance of these background inputs is given by the following equation (Sterratt et al., 2011),

$$G(t) = g_{max} \times S \times \left[\exp\left(\frac{-t}{\tau_{\text{decay}}}\right) - \exp\left(\frac{-t}{\tau_{\text{rise}}}\right)\right] \quad (2\text{-}18)$$

where τ_{decay} and τ_{rise} represent decay and rise time constant, respectively. g_{max} is the maximal synaptic conductance, and S is a normalization factor that equalizes the maximum of $G(t)$ to g_{max}. The values of τ_{rise} and τ_{decay} were 0.5 ms and 2.5 ms, respectively. The AMPAergic background inputs were modeled as Poisson spike trains with a frequency of 5 Hz and reversal potential of 0 mV (E_{AMPA}).

Similarly, phasic GABAergic inputs (50 inputs) were simulated for both models using equation 18. The τ_{rise} and τ_{decay} values for these inputs are 0.88 ms and 9.4 ms, respectively (Neymotin et al., 2011). Similar to excitatory background inputs, inhibitory inputs were simulated at a frequency of 5 Hz and reversal potential of -80 mV (E_{GABA}). The g_{max} values of the excitatory and inhibitory background inputs were chosen to capture the low background firing rates of pyramidal neurons observed *in vivo* and the ratio of excitatory-inhibitory (E-I) synaptic input strength (Xue et al., 2014) of neurons in the superficial layers of the cortex. For the LR neuron model, the g_{max} values of phasic

excitatory and inhibitory background inputs were set to 0.2 nS and 1.2 nS, thereby maintaining an E-I ratio that is seen in experiments (Xue et al., 2014). Similarly, for the RS neuron model, the g_{max} values of phasic excitatory and inhibitory background inputs were set to 0.6 nS and 3.6 nS, respectively. The LR and RS neuron models have a background firing rate of ~1 Hz (Dégenètais et al., 2002; Koga et al., 2010; Nakamura et al., 2012).

Burst inputs

In addition to receiving background synaptic inputs, the models also received synchronous and identical burst inputs of various durations (25 ms, 50 ms, 100 ms, 200 ms, 500 ms, 2000 ms). The LR and RS neuron models received stimulation from 20 synchronous AMPAergic burst inputs. These inputs were jittered over a time period of 2 ms and had a spiking probability which was varied from 0.1 to 1. The jitter and probability were varied across trials. The time course of synaptic conductance of burst inputs were modeled using equation 18. The τ_{decay} and τ_{rise} of these inputs was set to 0.5 ms and 2.5 ms, respectively. The strength of burst inputs (g_{max}) were set to 1200 pS for both models. For each burst condition (duration), the models were run for 300 trials.

Parameter Description	RS neuron model		LR neuron model	
	Soma	Dendrites	Soma	Dendrites
Specific membrane resistance (kΩcm²)	14.29	14.29	14.29	14.29
Specific membrane capacitance (μF/cm²)	1	1	1	1
Membrane time constant (ms)	14.29	14.29	14.29	14.29
Axial resistivity (Ω-cm)	200	200	200	200
I_{Na} g_{max} (S/cm²)	2	0.5	5.5	0.81
I_{Kdr} g_{max} (S/cm²)	0.02	0.008	0.07	0.006
I_d g_{max} (S/cm²)	0.0125	0	0.075	0
I_{adap}, g_{adap} (pS)	600	0	10	0

Table 2-3. Model parameters. The table lists the values of various model parameters and distribution of ion channel conductances in the somatic and dendritic compartments of the LR and RS neuron models.

In vivo dataset related modeling

In order to determine if LR and RS neuron models can sustain continuous firing as would be expected from the firing of head direction neurons in the preferred direction during motionless conditions, we stimulated the LR and RS neuron models with input spike trains of neurons recorded from the postsubiculum that had one preferred head-direction angle (head-direction cells) of awake mice (Peyrache et al., 2015). Spike data was downloaded from the website of CRCNS (Peyrache and Buzsaki, 2015) and given as input to the neuron models. Briefly, the LR and RS neuron models were stimulated with 20 synchronous input spike trains of head direction neurons recorded from postsubiculum. Similar to the 200 Hz input simulations, the *in vivo* spikes were also jittered (2 ms) and had a spiking probability that was varied from 0.1 to 1. Simulations were run for one entire awake epoch in the th-1 dataset, 1200 seconds in duration (Peyrache and Buzsaki, 2015).The simulations were repeated for 30 trials each. SNR was calculated according to equation 19 below. The resulting SNR was binned and plotted as a function of stimulus duration.

2.5.4 Experimental Analysis and Statistics

Neuronal analysis and statistics

From the whole-cell recordings, the following intrinsic neuronal properties were calculated: resting membrane potential, spike threshold, spike amplitude, spike width, input resistance (R_{in}), membrane time constant (τ_m), capacitance (C_{in}), afterhyperpolarization (AHP) amplitude, AHP latency, spike frequency adaptation ratio,

and rheobase. Resting membrane potential was recorded within 2 minutes of break-in. Cells with severely depolarized break-in potentials (> -55 mV) were not included in this study. Spike threshold, amplitude, width, AHP amplitude, and AHP latency were calculated by averaging all spikes in the first sweep of a 600 ms current step protocol that elicited a firing rate of at least 5 Hz. Spike threshold is calculated from the peak of the third derivative of membrane potential (Cruikshank et al., 2012). Spike amplitude was measured as the voltage change from the spike threshold to the peak of the action potential. Spike width was calculated as the full-width at half-max of the spike amplitude. AHP amplitude was calculated as the voltage change from spike threshold to the peak negativity of the AHP, and AHP latency as the time from peak of the spike to peak negativity of the AHP. Input resistance (R_{in}), membrane time constant (τ_m), and input capacitance (C_{in}) were calculated from a series of small negative current steps ranging from -5 pA to -30 pA, creating a deflection in membrane potential of -2 to -4 mV. R_{in} was calculated using Ohm's law, as the mean voltage change divided by mean current amplitude. τ_m was calculated by fitting a single exponential to the average of the initial 60 ms voltage response, ignoring the first 20 ms. C_{in} was then calculated from those two parameters using the formula $\tau_m = R_{in} \times C_{in}$. Spike frequency adaptation ratio was calculated from the first sweep of the 600ms current step protocol that elicited a firing rate of at least 10Hz (6 spikes per 600ms) using the equation ISI_{last} / ISI_{first}. Rheobase was calculated from 1 sec current pulses increasing in steps of 1-5 pA as the minimum current required to elicit at least one action potential.

To visualize this high-dimensional dataset including 10 electrophysiological properties for each recorded cell (input resistance, input capacitance, membrane time

constant, rheobase, adaptation ratio, action potential amplitude, action potential width, action potential threshold, AHP amplitude, and AHP latency), we applied Principal Component Analysis (PCA) to find the most informative dimensions of the data. The loadings of each cell onto the first two principal components were plotted to visualize variation in nearly all properties in a dimensionally reduced space. Cells were grouped into three defined groups (Low Rheobase, Fast Spiking, and Regular Spiking) as confirmed by the existence of distinct clusters in principal component space.

Cells which did not fall under the three defined categories were grouped as “unclassified”. This group consists of 10 cells with the following characteristics: 4 cells that had very distinct intrinsic physiology, likely corresponding to other inhibitory subtypes, 3 cells with uncharacteristically broad spike widths > 1.6 ms, 2 cells with hybrid LR-like and RS-like characteristics, and 1 cell with FS-like characteristics but with surprisingly broad action potentials.

A two-tailed Wilcoxon rank sum test was used to compute the statistical significance between the intrinsic properties of various neuronal subtypes. To establish the statistical significance between the probability of E→I and I→E connections, a bootstrap resampling (1000 bootstrap samples) method was used to generate a distribution of connectivity probabilities (Sudhakar et al., 2017). Briefly, a connectivity matrix was generated which consists of a pre-synaptic label (E or I), post-synaptic label (E or I) and an observation (0 or 1) saying whether this pair is connected or not. This matrix was bootstrapped (n =1000) and a distribution of E→I and I→E connectivity probabilities was thus formed. Statistical significance was then computed using a two-tailed t-test (Henseler et al., 2009) with a confidence interval of 95%. Significance in the

number of LR neurons in layer 2/3 versus layer 5/6 was established by Pearson chi-square test (Alan Agresti, 2007) . The same statistical test was used to establish whether the proportion of LR neurons in layer 2/3 was significantly different from that of RS neurons.

Connectivity analysis and statistics

When analyzing connected pairs, latency to onset of an IPSP or EPSP was calculated as the time from the peak of the presynaptic action potential to the onset of the postsynaptic IPSP or EPSP. Latency to peak was calculated as the time from the peak of the presynaptic action potential to the peak of the postsynaptic IPSP or EPSP.

To test if the connectivity between different neuronal populations are significantly different from chance, we randomly shuffled the pre-synaptic, post-synaptic labels and the observation (whether the pair is connected) for 1000 trials. By doing this, we established the distribution of chance probabilities for each connectivity pairs. We then utilized one-sample t-test (two-tailed, 95% confidence interval) to determine if the experimentally observed connectivity probabilities differed significantly from their chance distributions.

Morphological analysis and statistics

For morphological comparisons, cell body surface, number and length of dendrites, and Sholl analysis (at 10 µM intervals) were extracted directly from Neuron Summary, Sholl– dendrites, and Sholl – apical dendrites analysis results in Neurolucida Explorer. Apical and basal dendrites were added together for all calculations and data was plotted in MATLAB using custom scripts. Statistical differences were calculated using a two-tailed Wilcoxon rank sum test for all morphological comparisons.

2.5.5 Computational Analysis and Statistics

The models were simulated using NEURON 7.5 simulation environment (M.L Hines and N.T.Carnevale, 2001) with an integration time step of 0.025 ms. Simulation output was written into binary files and analyzed using custom programs written in MATLAB (R2018b) software. Spike threshold, spike half width, input resistance, membrane time constant and input capacitance of the models were calculated using the same method that was used for experimental data.

Signal to noise ratio (SNR) in response to the burst input was computed by calculating the number of spikes in response to the burst input and comparing it with the background response for the same duration as the burst response. SNR in our study is calculated using the following formula (Duguid et al., 2012),

$$SNR = \frac{S_{burst} - S_{back}}{\sqrt{0.5 \times (Var_{burst} + Var_{back})}} \quad (2\text{-}19)$$

S_{burst} is the average number of spikes in 'x' ms post burst onset, where x = burst duration+125 ms. S_{back} is the average number spikes per 'x' ms from 4000 ms to 8000 ms post burst onset. Var_{burst} and Var_{back} are the corresponding variances of the number of spikes during those two time intervals.

The spike timing precision (jitter) in response to the burst input was computed by calculating the median absolute deviation of spike latencies from all trials. Bootstrapped resampling was then used to compute a distribution of jitter values, and significance between the jitter of LR and RS neurons was established by 2-tailed t-test (95% confidence interval; Sudhakar et al., 2015). Significance in the probability of spiking

between LR and RS neurons was established by Pearson chi-square test (Alan Agresti, 2007; 95% confidence interval).

For simulations related to Figure 2-12, location dependence of different synaptic inputs along the dendritic tree of LR and RS neuron models was eliminated using the following equation,

$$g_{max_{scaled}} = g_{max} + (g_{max} * dist * m) \quad (2\text{-}20)$$

where the value of g_{max} is 1200 pS as mentioned before, 'dist' is the Euclidean distance between the location of the synaptic input on the dendritic tree and the model's somatic location. The scaling factor, 'm' was tuned until the location dependence of synaptic input was removed/normalized.

2.5.6 Data Code and Availability

Further information and requests for resources and reagents should be directed to and will be fulfilled by the Lead Contact, Dr. Omar J Ahmed (ojahmed@umich.edu). This study did not generate new unique reagents. The NEURON models (LR and RS neuron models) and the code files used in this study will be uploaded to ModelDB (http://modeldb.yale.edu/260192). The experimental data sets that were used in this study are available on request to the corresponding author.

2.6 Acknowledgements

We thank Barry Connors, Scott Cruikshank, Wayne Aldridge, and Vaughn Hetrick for their comments on the manuscript and Vaughn Hetrick for his technical assistance. This work was supported by grants to OJA from the NIH (R03MH111316), the American Epilepsy Society Junior Investigator Award, the Massey Foundation and the MICDE Catalyst Award.

2.7 Author Contributions

Conceptualization, Dr. Omar J Ahmed, Ellen KW Brennan, Dr. Shyam Kumar Sudhakar; Methodology, Dr. Omar J Ahmed, Ellen KW Brennan, Dr. Shyam Kumar Sudhakar; Investigation, Ellen KW Brennan, Dr. Shyam Kumar Sudhakar, Izabela Jedrasiak-Cape; Software, Dr. Shyam Kumar Sudhakar, Dr. Omar J Ahmed; Formal Analysis, Ellen KW Brennan, Dr. Shyam Kumar Sudhakar; Visualization, Ellen KW Brennan, Dr. Shyam Kumar Sudhakar, Izabela Jedrasiak-Cape, Dr. Omar J Ahmed; Writing – Original Draft, Dr. Omar J Ahmed, Ellen KW Brennan; Writing – Review & Editing, Dr. Omar J Ahmed, Ellen KW Brennan, Dr. Shyam Kumar Sudhakar, Izabela Jedrasiak-Cape; Funding Acquisition, Dr. Omar J Ahmed; Supervision, Dr. Omar J Ahmed.

CHAPTER 3: Thalamus and Claustrum Control Parallel Layer 1 Circuits in Retrosplenial Cortex

Ellen KW Brennan*, Izabela Jedrasiak-Cape*, Sameer Kailasa*, Sharena P Rice, Shyam Kumar Sudhakar, & Omar J Ahmed

3.1 Abstract

The granular retrosplenial cortex (RSG) is critical for both spatial and non-spatial behaviors, but the underlying neural codes remain poorly understood. Here, we use optogenetic circuit mapping in mice to reveal a double dissociation that allows parallel circuits in superficial RSG to process disparate inputs. The anterior thalamus and dorsal subiculum, sources of spatial information, strongly and selectively recruit small low-rheobase (LR) pyramidal cells in RSG. In contrast, neighboring regular-spiking (RS) cells are preferentially controlled by claustral and anterior cingulate inputs, sources of mostly non-spatial information. Precise sublaminar axonal and dendritic arborization within RSG layer 1, in particular, permits this parallel processing. Observed thalamocortical synaptic dynamics enable computational models of LR neurons to compute the speed of head rotation, despite receiving head direction inputs that do not explicitly encode speed. Thus, parallel input streams identify a distinct principal

neuronal subtype ideally positioned to support spatial orientation computations in the RSG.

3.2 Introduction

Activity in the granular retrosplenial cortex (RSG) is correlated with a wide variety of behaviors, including spatial navigation, learning, memory, fear conditioning, imagination, and planning for the future (Alexander et al., 2020; Alexander and Nitz, 2017; Chang et al., 2020; Chrastil, 2018; Hinman et al., 2018; Mao et al., 2018; Miller et al., 2020, 2019). The RSG is also among the most densely connected regions of the brain, integrating inputs from a bevy of cortical and subcortical sources and serving as part of the default mode network (Greicius et al., 2009; Kaboodvand et al., 2018; Liu et al., 2019; Whitesell et al., 2021). While these anatomical connections are well-documented (van Groen and Wyss, 2003, 1990; Whitesell et al., 2021; Wyss and van Groen, 1992), few studies have examined their functional nature (Nitzan et al., 2020; Yamawaki et al., 2019b, 2019a, 2016a), and cell-type specificity has yet to be sufficiently explored. Such knowledge is critical to develop a mechanistic understanding of how the RSG integrates information from multiple sources to carry out its spatial and non-spatial functions.

Cortical regions, including the RSG, receive inputs from one or more thalamic nuclei (Herkenham, 1986, 1980; Jones, 2001, 1998; Peters, 1979; van Groen and Wyss, 1995). Thalamic relay cells (Clascá et al., 2012) are grouped into three distinct classes: core, intralaminar, and paralaminar/ventral midline (matrix) nuclei (Hanbery

and Jasper, 1953; Herkenham, 1986; Jones, 2001, 1998; Morison and Dempsey, 1941; Rubio-Garrido et al., 2009). Thalamic matrix nuclei project predominantly to layer 1 of many cortical regions (Herkenham, 1986, 1980), resulting in subtype-specific activation of cortical inhibitory (Anastasiades et al., 2021; Cruikshank et al., 2012; Delevich et al., 2015) and excitatory neurons (Collins et al., 2018; Cruikshank et al., 2012; Guo et al., 2018; Rodriguez-Moreno et al., 2020; Rubio-Garrido et al., 2009; Van Der Werf et al., 2002; Yamawaki et al., 2019b). Matrix thalamocortical (TC) inputs from the anterior thalamus, which contains the highest proportion of head direction cells in the brain (Taube and Bassett, 2003), influence layer 5 pyramidal cells in RSG (Yamawaki et al., 2019b). However, potential subtype specific responses and their functional impact on the encoding of directional information in RSG have yet to be examined.

The cortex, including the RSG, also receives widespread inputs from the densely connected claustrum (Brown et al., 2017; Crick and Koch, 2005; Goll et al., 2015; Jackson et al., 2018; Kim et al., 2016; Narikiyo et al., 2020; Wang et al., 2017; White and Mathur, 2018). As with TC signaling, the claustrum innervates both excitatory (Da Costa et al., 2010; Narikiyo et al., 2020) and inhibitory (Jackson et al., 2018; Narikiyo et al., 2020; Salerno et al., 1984) neurons via precise laminar targeting (Wang et al., 2017) and projects to many of the same cortical regions as the thalamus (Burman et al., 2011). Claustrocortical (ClaC) projections are thought to regulate complex functions (Crick and Koch, 2005; Goll et al., 2015; Jackson et al., 2018; Kitanishi and Matsuo, 2017; Narikiyo et al., 2020; Renouard et al., 2015; Smith et al., 2012; White and Mathur, 2018), including the coordination and amplification of correlated signals across cortical regions (Kim et al., 2016; Smith et al., 2012; Smythies et al., 2012). Surprisingly, the

RSG is one of few regions that does not return reciprocal connections to the claustrum (Zingg et al., 2018). Despite the unique unidirectional nature of this connection, no studies have investigated the functional nature or subtype-specificity of ClaC inputs to RSG neurons.

Each cortical region also receives inputs from select other cortical areas. The RSG receives direct innervation from the secondary motor cortex (Yamawaki et al., 2016a), contralateral RSG (Sempere-Ferràndez et al., 2018; Wyss et al., 1990), and anterior cingulate cortex (ACC; van Groen and Wyss, 2003, 1990), among others. The RSG and ACC, in particular, have been implicated in several shared limbic and cognitive functions, including fear conditioning (Frankland et al., 2004; Han et al., 2003; Yamawaki et al., 2019a, 2019b), but the cellular targets of ACC inputs to RSG have not been identified.

Thalamic, claustral, and cortical inputs all converge in the RSG, but whether they do so via parallel or integrative control of target excitatory neurons remains unknown. Within the RSG, the superficial layers contain two subtypes of principal excitatory pyramidal neurons that have strikingly distinct physiology, morphology, and computational capabilities: the low-rheobase (LR) neuron and the regular-spiking (RS) neuron (Brennan et al., 2020; Kurotani et al., 2013; Yousuf et al., 2020). Here, we use channelrhodopsin (ChR2)-assisted circuit mapping (CRACM) to study the subtype-specific circuits formed by anterior thalamic, claustral, anterior cingulate, and dorsal subicular inputs to the RSG. Our results reveal a double dissociation in the precise organization of afferent axons and principal cell dendrites that can support parallel processing in superficial RSG. Specifically, we find that anterior thalamus and dorsal

subiculum preferentially control LR neurons, whereas claustrum and anterior cingulate control RS cells. We show that the synaptic dynamics of thalamic inputs allow for the robust encoding of angular speed by LR cell models, even though these inputs only explicitly contain information about head direction, not speed. Together, our results suggest that LR neurons are ideally positioned to contribute to the initial spatial orientation computations performed in superficial RSG.

3.3 Results

3.3.1 Cell-type specific thalamic control of layer 3 pyramidal cells in granular retrosplenial cortex

Layer 3 of the granular retrosplenial cortex (RSG) contains two types of principal pyramidal neurons: the low-rheobase (LR) neuron and the regular-spiking (RS) neuron (Brennan et al., 2020; Kurotani et al., 2013; Yousuf et al., 2020). Using whole-cell patch clamp recordings, we again distinguished LR from RS neurons by their unique intrinsic properties, predominantly the low rheobase, high input resistance, lack of adaptation, and narrow spike width (Figure 3-1 A-C, Supplemental Figure 3-1S, Supplemental Table 3-1S, Supplemental Table 3-2S; Brennan et al., 2020). We used channelrhodopsin-assisted circuit mapping (CRACM) to interrogate inputs to these two cell types. Consistent with previous studies (Odagiri et al., 2011; van Groen and Wyss, 2003, 1990; Yamawaki et al., 2019b), virus injections into the anterodorsal and anteroventral thalamic nuclei (ADAV) resulted in ChR2-eYFP expression in

thalamocortical (TC) axons and terminals predominantly in layer 1a (L1a; the most superficial part of layer 1) and in layer 3 (L3) of superficial RSG (Figure 3-1 D). To test whether these thalamocortical inputs target the LR and RS neurons in layer 3, we stimulated the thalamic axons and terminals with 1 ms LED pulses at a 10 Hz frequency for 1 second at high LED power over the cell body of the patched neurons (Figure 3-1 E; see Methods). From resting membrane potentials of approximately -65 mV, LR neurons were strongly driven past spike threshold by these thalamic inputs while RS neurons exhibited far smaller EPSPs (Figure 3-1 F). To quantify the impact of TC inputs on LR and RS spike rates, we next depolarized the cells until they were spiking at 10-25 Hz and delivered a single LED pulse (see Methods). To rule out effects of feed-forward inhibition in these experiments, the $GABA_A$ antagonist, picrotoxin (50 µM), was added to the bath. Compared to their baseline activity, this stimulation evoked a significant increase in spiking in LR neurons ($p = 0.002$, Wilcoxon rank sum test) but not RS neurons ($p = 0.19$, Wilcoxon rank sum test; Figure 3-1 G). The LR neurons thus had a significantly larger increase in spike rate evoked by the optical pulse than RS neurons ($p = 0.0012$, Wilcoxon rank sum test; Figure 3-1 H). This suggests that LR neurons receive stronger activation from TC inputs than their neighboring L3 RS neurons.

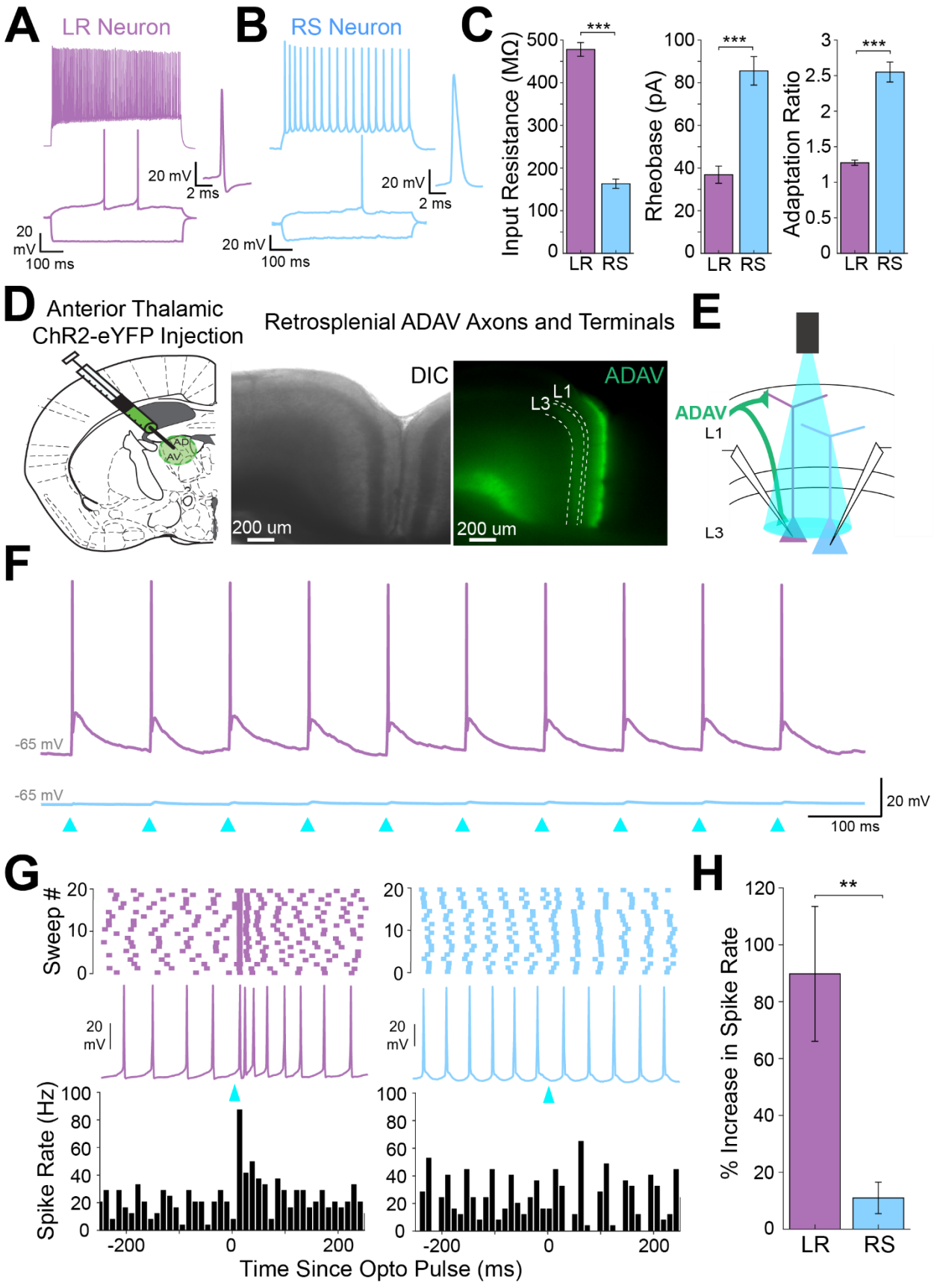
A
LR Neuron
20 mV
2 ms
20 mV
100 ms
B
RS Neuron
20 mV
2 ms
20 mV
100 ms
C
Input Resistance (MΩ)
***
LR RS
Rheobase (pA)
***
LR RS
Adaptation Ratio
***
LR RS
D
Anterior Thalamic
ChR2-eYFP Injection
AD
AV
Retrosplenial ADAV Axons and Terminals
DIC
200 um
ADAV
L1
L3
200 um
E
ADAV
L1
L3
F
-65 mV
-65 mV
20 mV
100 ms
G
Sweep #
20 mV
Spike Rate (Hz)
-200
0
200
Time Since Opto Pulse (ms)
H
% Increase in Spike Rate
**
LR RS

Figure 3-1. Anterior thalamic input controls LR, but not RS, neurons in superficial granular retrosplenial cortex.

A. Representative example of the firing properties of LR neurons. Top trace: sustained high-frequency firing of action potentials with little spike frequency adaptation at high current inputs in response to 200 pA current injection. Bottom trace: Delay to first spike at threshold current inputs (50 pA) and little to no sag when hyperpolarized (-100 pA). Right inset is a zoomed in view of the first spike in response to a near-threshold current input. Cell is held at -65 mV resting potential.

B. Same as ***A,*** but for a representative RS neuron. Note the spike frequency adaptation with high current inputs, delay to first spike at near-threshold current inputs, and sag potential seen with hyperpolarization. Cell is held at -65 mV resting potential.

C. Population data comparisons between LR and RS neurons of the following intrinsic properties: input resistance ($p = 1.31e-26$; Wilcoxon rank sum), rheobase ($p = 1.24e-17$; Wilcoxon rank sum), and adaptation ratio ($p = 2.94e-24$; Wilcoxon rank sum). Error bars are standard error of the mean (SEM).

D. Left: Schematic showing the injection of optogenetic viral construct into the anterodorsal/anteroventral (ADAV) nuclei of the anterior thalamus. Middle: DIC image of RSG. Right: EYFP fluorescence image of RSG showing expressing anterior thalamic axons and terminal arbors.

E. Schematic of optogenetic stimulation of TC axons and terminal arbors over the patched cell body in RSG L3.

F. LR (purple) and RS (blue) cell responses to 10 Hz light pulses (see Methods) at maximum LED power. LR cell shows spiking responses, while the RS cell has very small EPSPs. Both cells were held at -65 mV before stimulation. Blue triangles indicate light pulses.

G. Optogenetic activation of thalamic axons in RSG increases the firing rate of the LR (purple) but not RS (blue) neuron in a simultaneously patched pair. Neurons were held in ACSF+picrotoxin at a constant firing rate of 10-30 Hz via a 2 s current injection, and a 1 ms LED pulse was delivered 500 ms into the spike train (see Methods). Top: Raster plots for all sweeps of a representative LR (purple) and RS (blue) example. Middle: Firing trace of one sweep for that same LR and RS pair. Bottom: PSTH plots evaluating all sweeps for the same LR and RS example cells.

H. Population analysis of the spike ratio for all tested LR (n=7) and RS (n=6) cells showing a significant increase in firing rate post-LED pulse in LR cells compared to RS cells ($p = 0.0012$; Wilcoxon rank sum test). Error bars are SEM.

3.3.2 Precise overlap of anterior thalamic afferents with LR, but not RS, apical dendrites

LR neurons are morphologically distinct from their neighboring RS neurons (Brennan et al., 2020; Kurotani et al., 2013; Yousuf et al., 2020). Given the precise laminar pattern of anterior thalamic inputs to RSG (Figure 3-1 D and Figure 3-2 B), we next investigated the overlap between anterior thalamic afferents and the dendritic morphologies of reconstructed LR (n = 10) and RS (n = 5) cells (see Methods). Apical dendrites of LR neurons were most densely localized to L1a, with basal dendrites remaining confined to L3 (Figure 3-2 C). In contrast, RS apical dendrites rarely entered L1a, instead existing in the deeper subdivisions of layer 1 (L1b/c), with basal dendrites primarily in upper layer 5 (L5; Figure 3-2 D). Projection density analysis showed localization of ADAV axons and terminal arbors in L1a and weakly in L3 (Figure 3-2 C&D). Thus, dendrites of LR, but not RS, cells selectively co-localize within layers 1a and 3 with ADAV TC afferents (Figure 3-2 C&D). This anatomical colocalization of LR, but not RS, dendrites with TC axons coupled with the increase in LR, but not RS, spiking in response to TC optical stimulation indicates that the anterior thalamic-retrosplenial circuit at least partially obeys Peters' rule, which states that neuronal populations with anatomically overlapping axonal and dendritic arbors are more likely to show functional connectivity (Peters, 1979; Peters and Feldman, 1976).

To further verify this, we examined the responses of L3 LR and RS neurons to ADAV input at L1a, where the highest projection density of ADAV inputs exist (see Methods). When delivering 1 ms high LED power light pulses, we indeed found that LR neurons had a significantly larger excitatory postsynaptic potential (EPSP) amplitude in

response to the L1a LED stimulation compared to RS cell responses ($p = 0.0185$, Wilcoxon rank sum test; Figure 3-2 E). Notably, in response to layer 1 stimulation, LR cells also showed significantly larger EPSP amplitudes compared to L5 RS neurons (Supplemental Figure 3-2S), which have been previously shown to respond to TC input (Yamawaki et al., 2019b). This suggests that LR neurons, rather than layer 3 or 5 RS neurons, are the predominant RSG cell type receiving and processing head direction inputs from the anterior thalamus.

To further examine the effects of lamination of anterior thalamic inputs to LR and RS neurons on their resulting responses, we conducted a high-resolution protocol that used minimum thresholded LED power to optically stimulate every 20-30 μm along the neuron's longitudinal axis (Figure 3-2 F; see Methods). We found that LR neurons have the largest EPSP amplitude when the LED pulse is targeting layer 1a, corresponding with the peak projection density of ADAV axons and terminal arbors at this lamina. LR response amplitude then decreases as the LED moves away from the pia before reaching no response at the layer 1/2 border. As LED stimulation entered layer 3, the LR EPSP amplitude increased, consistent with the increase in projection density of the ADAV axons and terminal arbors, before again decreasing until their response amplitude reached 0 mV in layer 5 (Figure 3-2 F). In contrast, the RS neuron showed much smaller EPSP amplitude with no significant variation in response across the layers (Figure 3-2 F&G). To verify this functional sublaminar correlation between thalamocortical axons and pyramidal cell dendrites, we ran a population analysis comparing the EPSP amplitudes within LR and RS cell groups from all layers relative to L1/2, which represents our minimum projection density of ADAV inputs in the superficial

layers. We found that within the LR cell population, LR cells have significantly larger responses at L1a ($p = 0.00001$) and cell body ($p = 0.0006$) compared to L1/2 (paired t-test; Figure 3-2 G). This lamination of functional responses in the LR population precisely aligns with the lamination of ADAV axons and terminal arbors within these superficial layers. When stimulating in layer 5, there was no significant difference between EPSP amplitude at L1/2 and $L5_{sup}$ ($p = 0.420$), while $L5_{dp}$ responses were significantly smaller than those at L1/2 ($p = 0.0462$; Figure 3-2 G), as would be expected given the complete lack of LR dendrites in L5. In contrast, RS EPSP amplitudes at layers 1a, cell body, $L5_{sup}$, and $L5_{dp}$ did not differ from responses at L1/2 ($p > 0.05$ for all; paired t-test), indicating that there is no significant lamination of functional responses to thalamic inputs in the RS population, likely due to their relative lack of response to these inputs in general (Figure 3-2 G). These relationships persisted when inhibition blocker picrotoxin (50 µM) or sodium channel blocker TTX (1 µM) + 4-AP (100 µM) were added to the bath (data not shown; see Methods). Thus, the connectivity between anterior thalamic TC arbors and L3 principal neurons in RSG highlights a circuit that depends on the precise sublaminar colocalization of both local principal cells' dendrites and incoming thalamocortical axons. This demonstrates that LR neurons are uniquely anatomically adapted to respond to incoming inputs from the anterior thalamus, where ~60% of neurons are head direction cells (Taube, 1995; Taube and Bassett, 2003), due to a precise overlap of their apical dendrites with the dense thalamic axons and terminals in the uppermost sublamina of L1 (L1a).

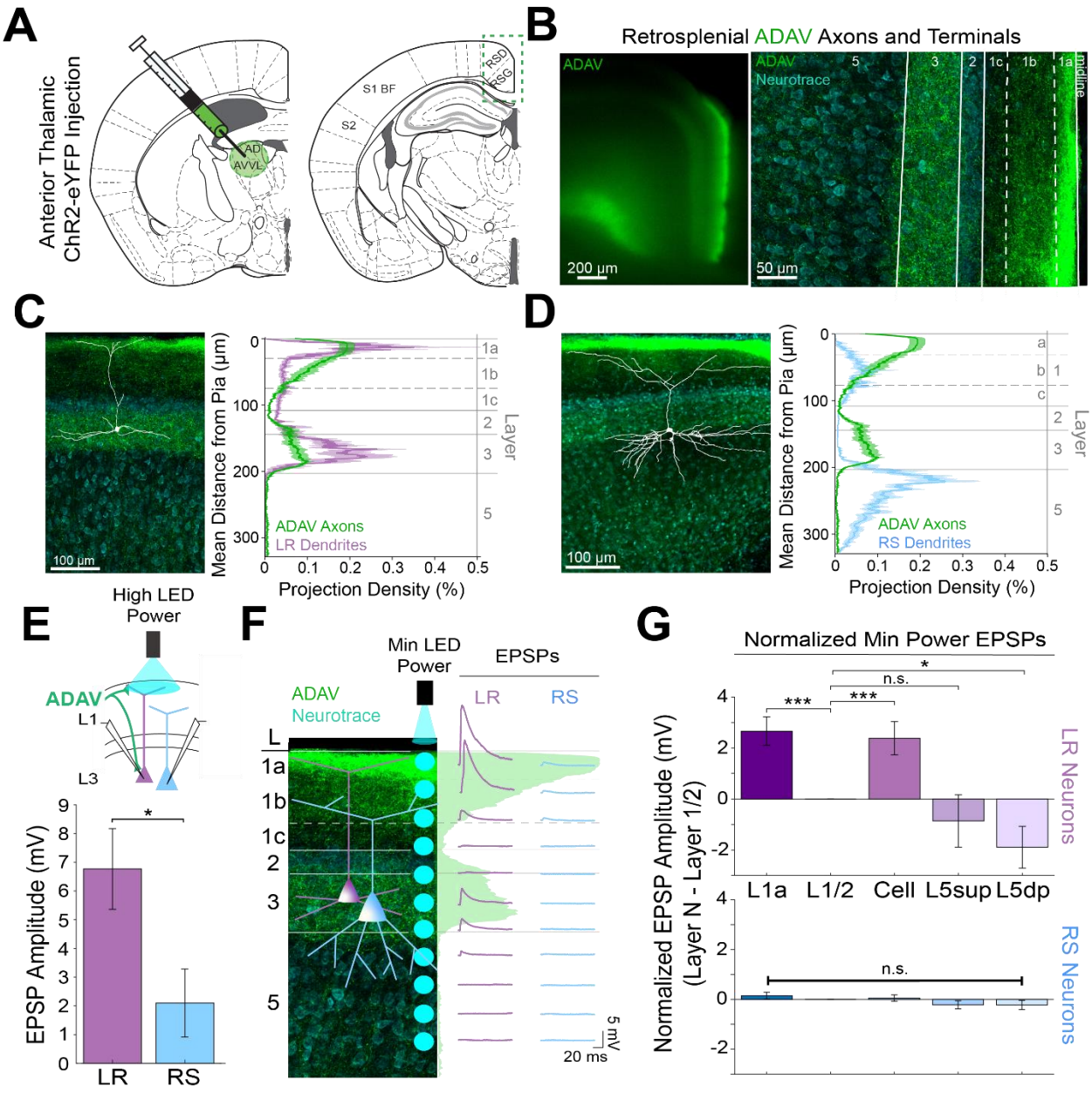

Figure 3-2. Thalamic control of LR neurons is explained by precise convergence of LR dendrites and anterior thalamic axons in layer 1a of granular retrosplenial cortex.

A. Schematic of channelrhodopsin injection into anterior thalamus (left) and RSG target recording region (right).

B. Left: epifluorescent image of the retrosplenial cortex showing expression of anterior thalamic axons and terminal arbors in green. Right: confocal image of layers 1-5 of RSG showing lamination of anterior thalamic axons and terminal arbors (green) and cell membrane marker, NeuroTrace (cyan).

C. Left: LR reconstruction superimposed on patch location in an RSG slice with thalamic projections (green) and NeuroTrace (cyan). Right: Projection density

plot showing density of LR dendrites (n = 10; mean ± SEM shaded) in purple and density of ADAV axon expression (n = 5; mean ± SEM shaded) in green plotted as distance from the pia (µm).

D. Same as ***C*** for RS cells with dendrites (n = 5) plotted in blue.

E. Top: Schematic of L1a-targeted optogenetic stimulation. Bottom: Significantly larger EPSP amplitude at high LED power for LR (n = 15) cells compared to RS (n = 8) cells (p = 0.0185; Wilcoxon rank sum test). Error bars are SEM.

F. Left: Confocal image of RSG slice with anterior thalamic axons and terminal arbors (green). Layers are demarcated, and schematic LR and RS neurons are placed in their representative locations within the superficial layers. Blue circles indicate targeting of minimum LED power stimulations, beginning at midline and extending into layer 5, stimulating every 20-30 µm (see Methods). Right: Representative trace examples of an LR (purple) and RS (blue) neurons' responses to the LED stimulation at each location. Green shading is representative of the projection density of thalamic axons and terminal arbors across the shown layers.

G. Population analysis for LR and RS cells' normalized EPSP responses to minimum LED power optogenetic stimulations at L1a, L1/2 boundary, cell body in L3, superficial L5 ($L5_{sup}$), and deep L5 ($L5_{dp}$) locations. Top: LR cells have significantly larger responses at L1a (n = 58, p = 0.00001, paired t-test) and cell body (n = 53, p = 0.0006) compared to L1/2 (n = 59). Responses at $L5_{dp}$ (n = 10, p = 0.0462) are significantly smaller than L1/2, and responses at $L5_{sup}$ (n = 12, p = 0.420) do not significantly differ from L1/2. Bottom: EPSP amplitude in RS cells does not significantly differ at any stimulation location compared to L1/2 stimulation (L1a: n = 27, p = 0.289; cell body: n = 25, p = 0.702; $L5_{sup}$: n = 12, p = 0.197; $L5_{dp}$: n = 11, p = 0.261; L1/2: n = 27). Error bars are SEM. The paired t-test was used for all statistical comparisons.

3.3.3 Claustrum and anterior cingulate selectively control retrosplenial RS cells while avoiding LR cells

Two other main sources of input to RSG are the claustrum (CLA; van Groen and Wyss, 2003, 1990) and anterior cingulate cortex (ACC; Shibata and Naito, 2007; van Groen and Wyss, 2003, 1990). Both claustrocortical (ClaC) and ACC corticocortical (CC) projections have been anatomically shown to exhibit distinct laminar organization within its target cortical layers (van Groen and Wyss, 2003; Vogt and Miller, 1983; Wang et al., 2017), but the precise functional targets of claustral and cingulate inputs to superficial RSG have, to our knowledge, never been examined. To address this, we next used CRACM, this time to examine CLA inputs to RSG LR and RS neurons and then compared these projections to RSG thalamic inputs. ChR2 injections into CLA (Figure 3-3 A) resulted in expression of CLA axons and terminals in layers 1c, 2, and 5 (Figure 3-3 B). This expression pattern is distinct from the thalamic expression localized to layers 1a and 3 (Figure 3-2 B-D). Dendritic lamination plots of LR and RS dendrites and projection density plots of CLA axons and terminal arbors show that RS, but not LR, apical dendrites anatomically overlap with CLA arbors in superficial layers 1c and 2 and upper layer 5 (Figure 3-3 D). Using the same targeted optogenetic stimulation approach as previously described (see Methods), we found that RS neurons have significantly larger responses to CLA input compared to LR neurons when stimulated at layer 1/2 ($p = 0.0000035$, Wilcoxon rank sum test; Figure 3-3 E), the area of the strongest superficial projection density of CLA arbors. Similarly, layer 5 RS neurons exhibited significantly larger EPSP amplitudes in response to CLA inputs compared to LR cells

(Supplemental Figure 3-2S). This again indicates that while LR neurons may be optimally positioned to receive thalamic input, RS neurons in both RSG L3 and L5 are instead the primary recipients of CLA inputs.

To further examine the lamination of ClaC inputs to LR and RS neurons and their resulting responses, we again conducted the high-resolution CRACM protocol using minimum LED power (Figure 3-3 F; see Methods). We found that RS neurons have the largest EPSP amplitude when the LED pulse is stimulating both layer 1c and 5_{sup} and weakest EPSP amplitude at layer 1a, corresponding with, respectively, the strongest and the weakest projection density of CLA afferents at these laminar locations. In contrast, the complementary LR cell had no response to LED stimulation at any of the laminar locations (Figure 3-3F). Population analysis showed that within the RS cell population, RS cells have significantly larger responses at L1/2 ($p = 0.00725$) and $L5_{sup}$ ($p = 0.0301$) compared to those at L1a (paired t-test; Figure 3-3 G). This lamination of functional responses in the RS cell precisely aligns with the lamination of ClaC axons and terminal arbors within these layers. In contrast, LR EPSP amplitudes across all layers were much lower in magnitude and did not differ from responses at L1a ($p > 0.05$ for all; paired t-test; Figure 3-3 G), indicating no significant lamination of functional responses to ClaC inputs in the LR population. These relationships persisted when inhibition blocker picrotoxin (50 µM) or sodium channel blocker TTX (1 µM) + 4-AP (100 µM) were added to the bath (data not shown; see Methods).

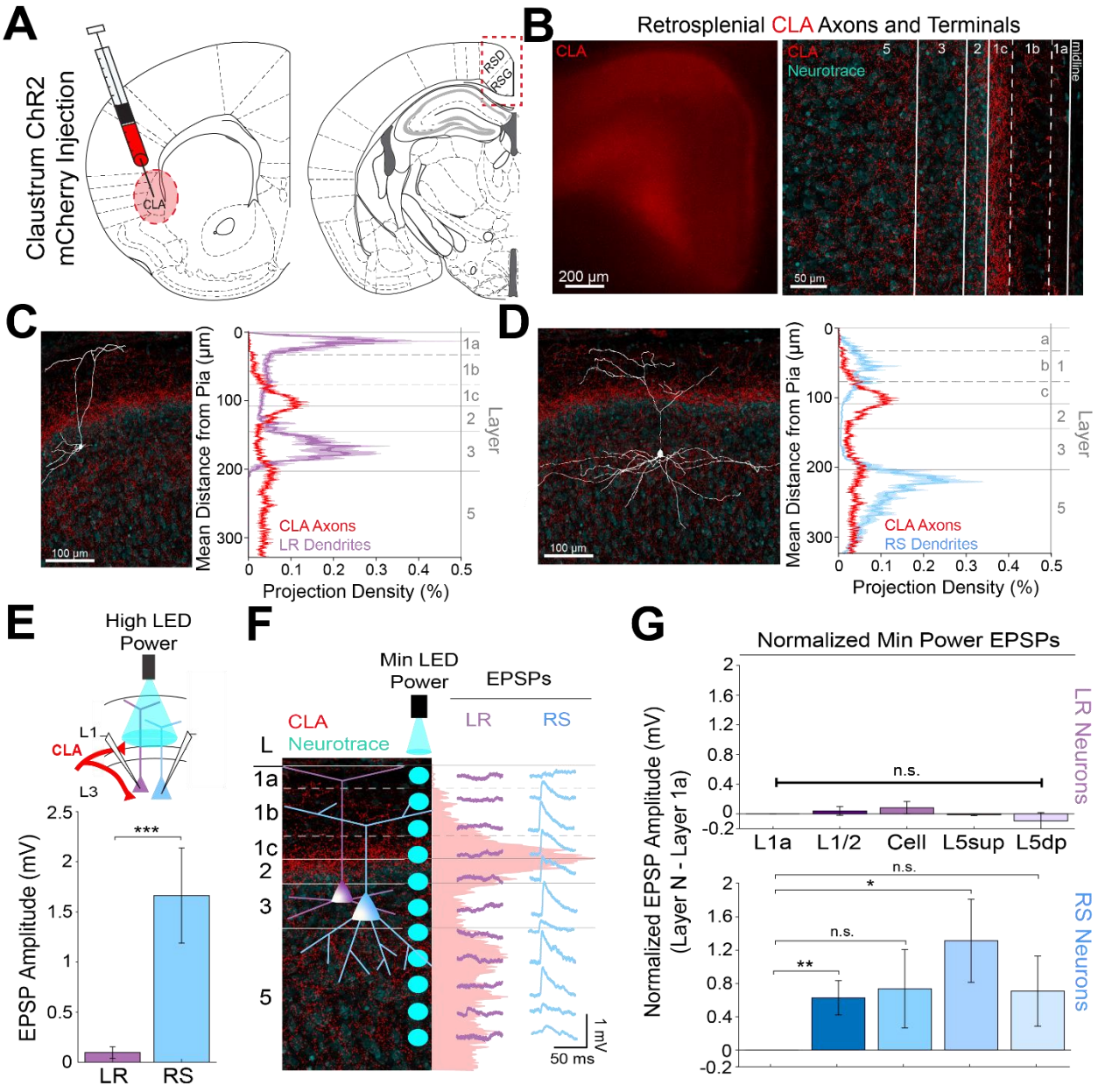

Figure 3-3. Claustral inputs to RSG selectively drive RS, not LR, neurons, consistent with stronger anatomical overlap of RS neuron dendrites with claustral axons.

A. Schematic of channelrhodopsin injection into claustrum (CLA; left) and target recording region, RSG (right; see Methods).

B. Left: Epifluorescent image of the RSG brain slice showing expressing ClaC arbors in red. Right: confocal image of layers 1-5 of RSG showing lamination of claustral axons and terminal arbors (red) and NeuroTrace (cyan).

C. Left: LR reconstruction superimposed on patch location in an RSG slice with claustral projections (red) and NeuroTrace (cyan). Right: Projection density plot showing density of LR dendrites in purple (n = 10; mean ± SEM shaded) and

density of CLA axon expression in red (n = 6; mean ± SEM shaded) plotted as distance from pia (μm).

D. Same as ***C*** for RS cells with dendrites (n = 5) plotted in blue.

E. Top: Schematic of L1/2-targeted optogenetic stimulation. Bottom: Significantly larger EPSP amplitude at high LED power for the RS (n = 16) cells compared to LR (n = 26) cells (p = 0.0000035; Wilcoxon rank sum test). Error bars are SEM.

F. Left: Confocal image of RSG slice with CLA axons and terminal arbors (red) and NeuroTrace (cyan). Layers are demarcated, and schematic LR and RS neurons are placed in their representative locations within the superficial layers. Blue circles indicate targeting of the minimum LED power stimulations, beginning at midline and extending into layer 5, stimulating every 20-30 μm (see Methods). Right: Representative trace examples of an LR (purple) and RS (blue) neurons' responses to the LED stimulation at each location. Red shading is representative of the projection density of CLA axons and terminal arbors across the layers.

G. Population analysis for LR and RS normalized EPSP responses to minimum LED power stimulations at L1a, L1/2, cell body, $L5_{sup}$, and $L5_{dp}$ locations. Top: EPSP amplitude in LR cells does not significantly differ at any stimulation location compared to L1a stimulation (L1/2: n = 24, p = 0.5151; L3: n = 23, p = 0.3276; $L5_{sup}$: n = 10, p = 0.3434; $L5_{dp}$: n = 7, p = 0.4348; L1a: n = 24). Bottom: RS cells have significantly larger responses at L1/2 (n = 18, p = 0.00725) and $L5_{sup}$ (n = 9, p = 0.0301) compared to L1a (n = 18), while normalized response amplitudes at cell body (n = 17, p = 0.1377) and $L5_{dp}$ (n = 8, p = 0.1355) did not differ from responses at L1a. The paired t-test was used for all statistical analyses. Error bars are SEM.

Using the same CRACM approach to examine ACC inputs to RSG (Figure 3-4 A), we found that corticocortical inputs from the anterior cingulate target L1b/c and, to a lesser extent, L5 (Figure 3-4 B), partially resembling the laminar pattern seen with CLA arbors (Figure 3-3 B) and overlapping precisely with RS, but not LR, dendrites (Figure 3-3 C&D). Indeed, when stimulating ACC arbors at L1/2, RS cells had significantly larger EPSP amplitudes compared to LR cells ($p = 0.0019$). When examining the lamination of these inputs with higher spatial resolution, we found that RS cells have the largest EPSP response to ACC inputs at L1/2, while the same minimum LED stimulation power elicits no response in layer 1a (Figure 3-4 F). Population analysis of RS cells revealed significantly larger responses to optogenetic stimulation of ACC inputs at the L1/2 ($p = 0.000037$) and cell body ($p = 0.000525$) compared to L1a stimulation (Figure 3-4 G), reflecting the precise overlap of ACC arbors and RS dendrites. In contrast, the much smaller LR EPSP amplitudes across all layers did not differ from responses at L1a ($p > 0.05$ for all; paired t-test; Figure 3-4 G). Again, the same results were seen when inhibition blocker picrotoxin (50 µM) or sodium channel blocker TTX (1 µM) + 4-AP (100 µM) were added to the bath (data not shown; see Methods). Thus, both claustrocortical and corticocortical inputs to RSG target RS apical dendrites at the lower divisions of L1 (L1c and L1b/c, respectively), whereas thalamocortical inputs preferentially target the apical dendrites of LR cells in upper L1 (L1a). This again indicates that parallel circuits in RSG process TC versus ClaC and CC information, and this parallel processing is enabled by precise sublaminar organization of afferent axons and layer 3 principal cell apical dendrites.

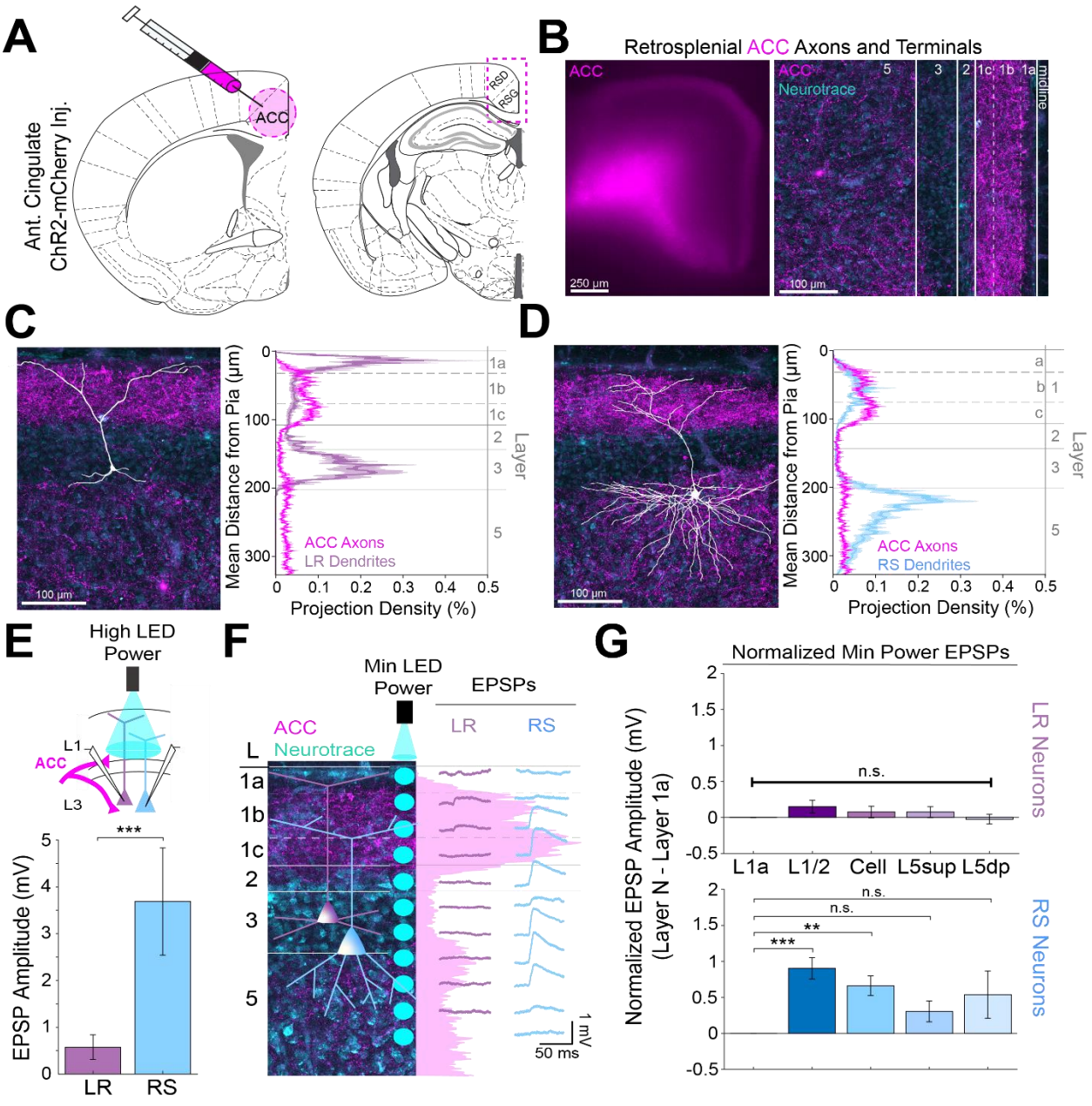

Figure 3-4. Anterior cingulate inputs to RSG selectively drive RS, not LR, neurons, consistent with anatomical overlap of RS neuron dendrites with anterior cingulate axons.

- ***A.*** Schematic of channelrhodopsin injection into anterior cingulate (ACC; left) and target recording region, RSG (right; see Methods).
- ***B.*** Left: Epifluorescent image of the RSG brain slice showing expressing ACC arbors in magenta. Right: confocal image of layers 1-5 of RSG showing lamination of cingulate axons and terminal arbors (magenta) and NeuroTrace (cyan).
- ***C.*** Left: LR reconstruction superimposed on patch location in an RSG slice with ACC projections (magenta) and NeuroTrace (cyan). Right: Projection density plot

showing density of LR dendrites (n = 10; mean ± SEM shaded) in purple and density of ACC axon expression (n = 4; mean ± SEM shaded) in magenta plotted as distance from the pia (µm).

D. Same as ***C*** for RS cells with dendrites (n = 5) plotted in blue.

E. Top: Schematic of L1/2-targeted optogenetic stimulation. Bottom: Significantly larger EPSP amplitude at high LED power for the RS (n = 10) cells compared to LR (n = 16) cells (p = 0.0019; Wilcoxon rank sum test). Error bars are SEM.

F. Left: Confocal image of RSG slice with ACC axons and terminal arbors (magenta) and NeuroTrace (cyan). Layers are demarcated, and schematic LR and RS neurons are placed in their representative locations within the superficial layers. Blue circles indicate targeting of the minimum LED power stimulations, beginning at midline and extending into layer 5, stimulating every 20-30 µm (see Methods). Right: Representative trace examples of an LR (purple) and RS (blue) neurons' responses to the LED stimulation at each location. Magenta shading is representative of the projection density of ACC axons and terminal arbors across the layers.

G. Population analysis for LR and RS normalized EPSP responses to minimum LED power stimulations at L1a, L1/2, cell body, $L5_{sup}$, and $L5_{dp}$ locations. Top: EPSP amplitude in LR cells does not significantly differ at any stimulation location compared to L1a stimulation (L1/2: n = 19, p = 0.1126; cell body: n = 19, p = 0.35; $L5_{sup}$: n = 13, p = 0.3423; $L5_{dp}$: n = 13, p = 0.7166; L1a: n = 19). Bottom: RS cells have significantly larger responses at L1/2 (n = 14, p = 0.000037) and cell body (n = 14, p = 0.000525) compared to L1a (n = 14) and did not significantly differ at $L5_{sup}$ (n = 11, p = 0.0607) or $L5_{dp}$ (n = 10, p = 0.1340) compared to L1a. The paired t-test was used for all statistical analyses. Error bars are SEM.

3.3.4 Dorsal subiculum selectively controls LR, but not RS, cells

The dorsal subiculum (DS), which serves to transmit allocentric information such as axis cell and boundary vector signals (Derdikman, 2009; Olson et al., 2017; Simonnet and Brecht, 2019; Bicanski & Burgess, 2020), also precisely targets layer 2/3 neurons in RSG (Nitzan et al., 2020; Yamawaki et al., 2019a). These inputs overlap with LR cell bodies and basal dendrites and have been shown to evoke larger responses in superficial compared to layer 5 cells (Nitzan et al., 2020; Yamawaki et al., 2019a). This suggests DS projections to RSC may be targeting LR cells. However, it remains unknown whether LR or layer 3 RS cells are the primary target of these DS projections. To investigate this, we repeated our CRACM protocols and examined responses of LR and layer 3 RS cells to DS inputs (Figure 3-5 A&B). We found that DS afferents precisely overlap with LR basal and, to a lesser degree, proximal apical dendrites (Figure 3-5 C) but not RS basal dendrites (Figure 3-5 D). LR neurons responded with larger EPSPs compared to RS neurons when DS inputs were stimulated at the cell body in layer 3 ($p = 0.004$; Figure 3-5 E). Our high-resolution protocol and population analysis also confirmed that LR cells had significantly larger responses at layers 1/2 and 3 compared to L1a (L1/2 $p = 0.0132$, L3 $p = 0.0135$; Figure 3-5 F&G), suggesting the possibility of integration of synchronous anterior thalamic and dorsal subicular inputs by LR neurons. In contrast, RS cells showed no significant laminal differences in response to DS input ($p > 0.05$ for all; Figure 3-5 G). Thus, inputs from both the dorsal subiculum and anterior thalamus target LR cells, reflecting their precise overlap with LR dendrites, while the claustrum and anterior cingulate cortex instead target RS cells.

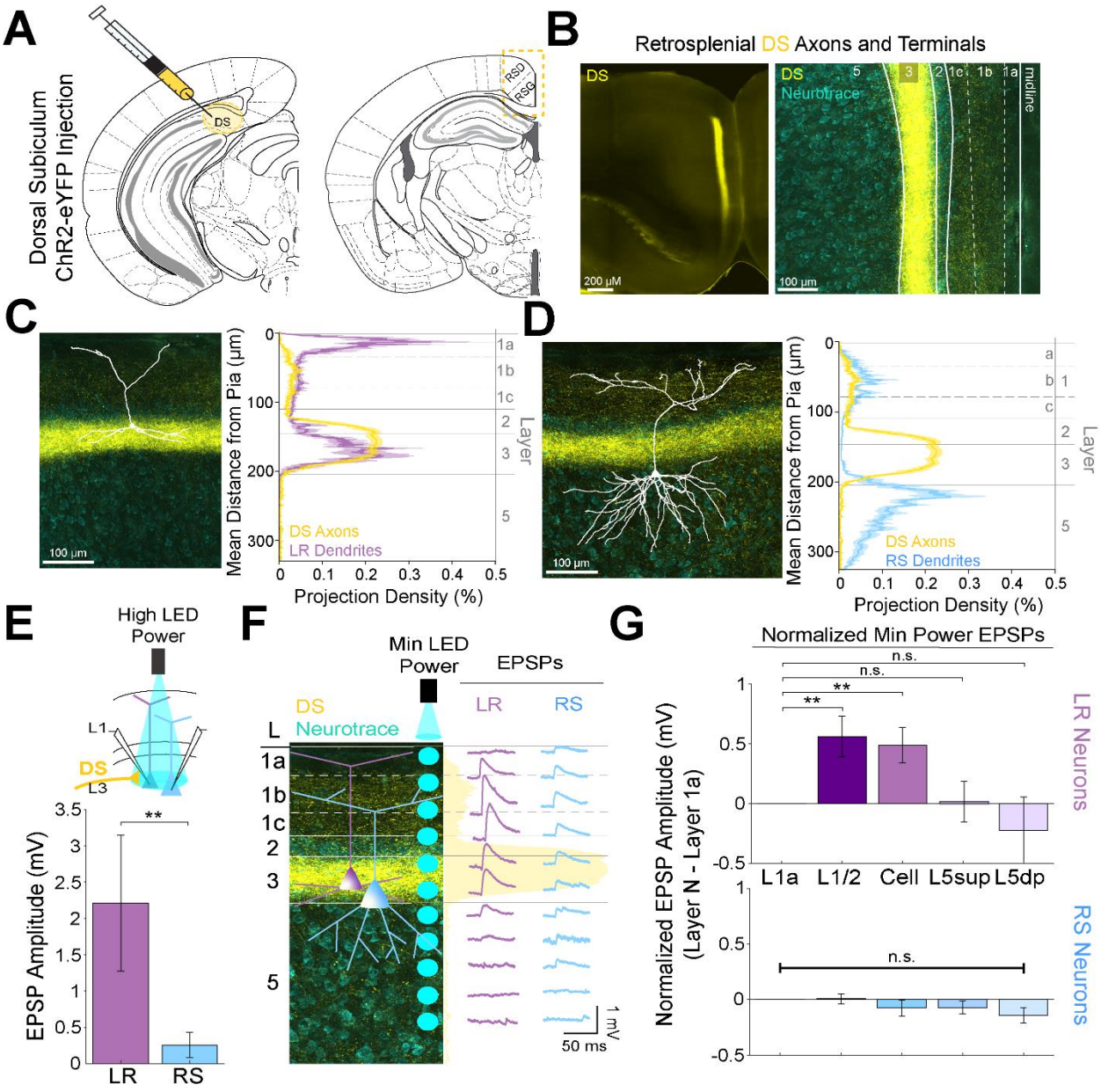

Figure 3-5. Dorsal subiculum inputs to RSG selectively drive LR, not RS, neurons, consistent with anatomical overlap of LR neuron dendrites with subicular axons.

A. Schematic of channelrhodopsin injection into dorsal subiculum (DS; left) and target recording region, RSG (right; see Methods).

B. Left: Epifluorescent image of the RSG brain slice showing expressing DS arbors in yellow. Right: confocal image of layers 1-5 of RSG showing lamination of DS axons and terminal arbors (yellow) and NeuroTrace (cyan).

C. Left: LR reconstruction superimposed on patch location in an RSG slice with DS projections (yellow) and NeuroTrace (cyan). Right: Projection density plot showing density of LR dendrites (n = 10; mean ± SEM shaded) in purple and density of DS axon expression (n = 4; mean ± SEM shaded) in yellow plotted as distance from the pia (µm).

D. Same as ***C*** for RS cells with dendrites (n = 5) plotted in blue.

E. Top: Schematic of cell body-targeted optogenetic stimulation at high LED power (see Methods) conducted in standard ACSF. Bottom: Bar graph showing significantly larger EPSP amplitude at high LED power for the LR (n = 9) cells compared to RS (n = 8) cells (p = 0.004; Wilcoxon rank sum test). Error bars are SEM.

F. Left: Confocal image of RSG slice with DS axons and terminal arbors (yellow) and NeuroTrace (cyan). Layers are demarcated, and schematic LR and RS neurons are placed in their representative locations within the superficial layers. Blue circles indicate targeting of the minimum LED power stimulations, beginning at midline and extending into layer 5, stimulating every 20-30 µm (see Methods). Right: Representative trace examples of an LR (purple) and RS (blue) neurons' responses to the LED stimulation at each location. Yellow shading is representative of the projection density of DS axons and terminal arbors across the layers.

G. Population analysis for LR and RS normalized EPSP responses to minimum LED power stimulations at L1a, L1/2, cell body, $L5_{sup}$, and $L5_{dp}$ locations. Top: LR cells have significantly larger responses at L1/2 (n = 8, p = 0.0132) and cell body (n = 8, p = 0.0135) compared to responses at L1a (n = 8), while responses at $L5_{sup}$ (n = 8, p = 0.9146) and $L5_{dp}$ (n = 7, p = 0.4902) do not differ from those at L1a. Bottom: EPSP amplitude in RS cells does not significantly differ at any stimulation location compared to L1a stimulation (L1/2: n = 7, p = 0.8811; cell body: n = 7, p = 0.3304; $L5_{sup}$: n = 7, p = 0.2260; $L5_{dp}$: n = 6, p = 0.0816; L1a: n = 7). The paired t-test was used for all statistical analyses. Error bars are SEM.

3.3.5 Precise anatomical overlap of LR versus RS dendrites with distinct incoming axons facilitates parallel circuits in superficial RSG

We next extended our physiological examination of superficial RSG circuits to include correlational analyses and dual injection experiments (Figure 3-6 A). We found that LR dendrites are strongly and significantly positively correlated with both ADAV ($r = 0.88$, $p < 0.001$) and DS ($r = 0.69$, $p = 1.41e-254$) axons. In contrast, RS dendrites are strongly correlated with CLA ($r = 0.29$, $p = 4.82e-36$) and ACC ($r = 0.43$, $p = 5.73e-82$) axons. Notably, LR dendrites are significantly negatively correlated with both CLA ($r = -0.49$, $p = 1.16e-110$) and ACC ($r = -0.15$, $p = 1.00e-10$) axons, and RS dendrites are negatively correlated with ADAV ($r = -0.55$, $p = 2.47e-145$) and DS ($r = -0.44$, $p = 7.74e-85$) axons (Figure 3-6 B&C). These anatomical results mirror our functional findings that LR neurons are preferentially driven by both ADAV and DS inputs, while RS neurons are targeted by CLA and ACC inputs.

We also compared laminar expression of afferents from the 4 input regions and found that ADAV and DS inputs to RSG, which both at least in part target layer 3, were significantly positively correlated with one another ($r = 0.55$, $p = 2.93e-143$). Similarly, CLA and ACC inputs, which both target the lower divisions of L1 as well as L5, were also significantly positively correlated ($r = 0.23$, $p = 2.3e-23$). However, ADAV and DS inputs were significantly negatively correlated with both CLA and ACC inputs, confirming that these two streams target separate sublayers within RSG (Figure 3-6 B&C). Dendrite-dendrite correlations of LR and RS cell populations were also strongly anti-correlated ($r = -0.65$, $p = 3.00e-215$; Figure 3-6 C), highlighting the distinct

anatomical organization of these two neighboring principal cell types. Taken together, these axon-axon, dendrite-dendrite, and axon-dendrite correlations indicate that precise, fine-grained laminar organization of LR and RS dendrites and afferent axons creates a parallel circuit in which LR neurons are selectively optimized to integrate incoming spatial information (Figure 3-6 D).

Supplemental examination of contralateral RSG (cRSG) inputs to RSG showed lamination and resulting cell type specific targeting resembling that of projections from CLA and ACC (Supplemental Figure 3-3S). Specifically, cRSG inputs targeted L1c, L2, and L5, resulting in strong activation of RS cells, with almost no responses in LR cells (Supplemental Figure 3-3S). This again suggests that inputs from CLA, ACC and cRSG follow a structured pattern by which these inputs preferentially control RS cells, while ADAV and DS projections target LR cells. Importantly, laminar dichotomies similar to those seen here in RSG also exist between TC and ClaC/corticocortical projections to other cortical regions such as the medial prefrontal cortex (Cruikshank et al., 2012), as also revealed by our examination of anatomical datasets from the Allen Brain Institute (Supplemental Figure 3-4S). Thus, our findings may also highlight a more universal framework by which other cortical regions integrate and process thalamic versus claustral and cortical inputs.

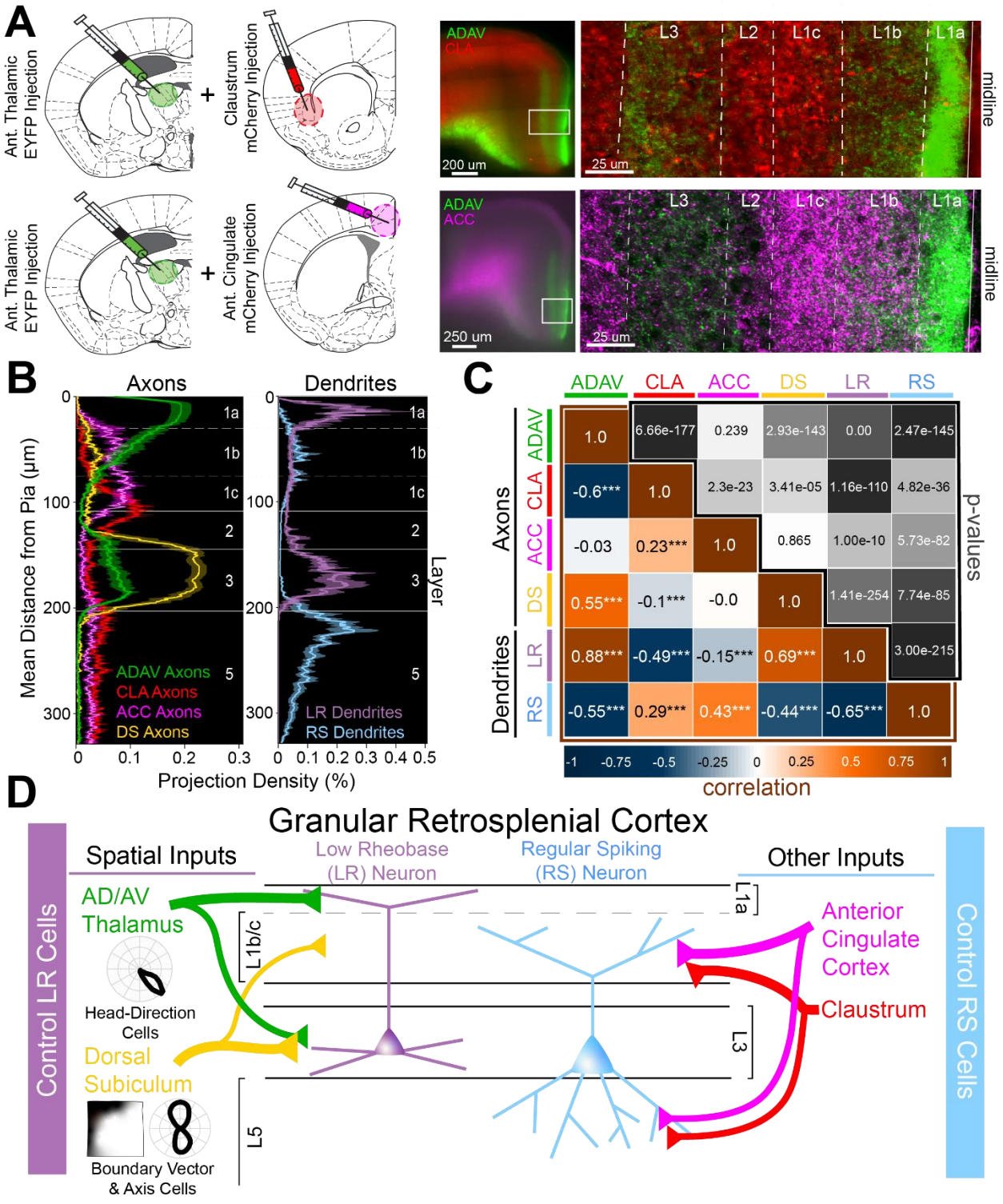

Figure 3-6. Two parallel circuits in superficial granular retrosplenial cortex.

A. Left: Schematics of dual injections into anterior thalamus (ADAV) and claustrum (CLA; top) or anterior cingulate (ACC; bottom). Right: Resulting dual expression

of ADAV (green) and CLA (red; top) or ACC (magenta; bottom) axons with zoomed-in confocal view of layers, demarcated by white lines.

B. Left: Projection density of anterior thalamus (ADAV; green; n = 5), claustrum (CLA; red; n = 6), anterior cingulate (ACC: magenta; n = 4), and dorsal subiculum (DS; yellow; n = 4; mean ± SEM shaded for all) axons and terminal arbors in RSG. Note distinct sublaminar distribution of axons from ADAV, ACC, and CLA in layer 1. Right: Projection density of LR (purple; n = 10) and RS (blue; n = 5; mean ± SEM shaded for all) neurons. Note the distinct difference between LR and RS dendrite lamination across the layers.

C. Correlation matrix of means for all axon-axon, axon-dendrite, and dendrite-dendrite comparisons. Note that LR dendrites are significantly positively correlated with ADAV and DS axons but negatively correlated with CLA and ACC axons, while RS dendrites are significantly positively correlated with CLA and ACC axons but negatively correlated with ADAV and DS axons.

D. Summary schematic showing selective control of LR neurons by inputs from ADAV and DS, including head direction signals. In contrast, RS neurons are preferentially controlled by inputs from the CLA and ACC. This precise organization of principal cell dendrites and afferent axons forms two parallel circuits in superficial RSG.

3.3.6 Anterior thalamic input to LR neurons is uniquely depressing

To investigate the functional implications of these parallel circuits, we next examined the short-term dynamics of each input onto the RSG principal cells. LR short-term dynamics were examined in response to ADAV and DS inputs, while RS short-term dynamics were examined in response to CLA and ACC inputs (see Methods). In contrast to previously documented thalamocortical matrix inputs to both superficial pyramidal cells and interneurons (Anastasiades et al., 2021; Cruikshank et al., 2012), 10 Hz anterior thalamic inputs from ADAV to RSG LR neurons were uniquely and significantly depressing ($p = 1.02e-5$, Wilcoxon rank sum test; Figure 3-7 A&B). In contrast, 10 Hz DS inputs to LR neurons were not depressing and exhibited weak facilitation (Figure 3-7 A&B). Both CLA and ACC inputs to RS cells were also weakly facilitating (Figure 3-7 C&D). Thus, the synaptic depression of anterior thalamic inputs to LR neurons is unique among the inputs examined here and also distinct from anterior thalamic inputs to superficial principal neurons in PFC and ACC (Cruikshank et al., 2012). As expected, we found that ADAV inputs to LR cells do not show synaptic depression at the much slower stimulation frequency of 0.1 Hz (Supplemental Figure 3-5S panel C), but 40 Hz inputs resulted in stronger depression than 10 Hz ($p = 0.0022$, Wilcoxon rank sum test; Supplemental Figure 3-5S panel B).

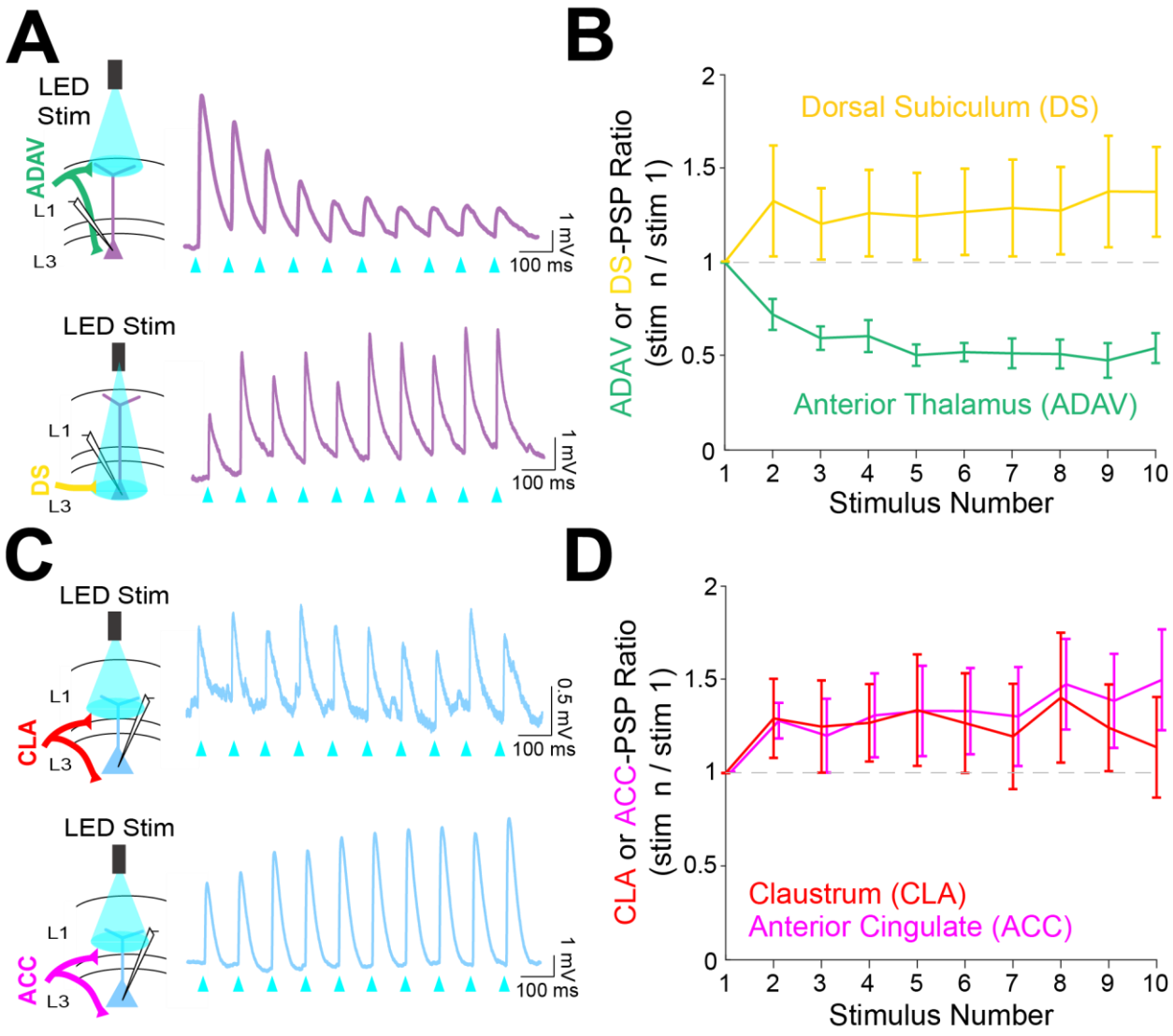

Figure 3-7. Anterior thalamic inputs to LR cells evoke robust synaptic depression.

A. Top: Schematic showing anterior thalamic (ADAV) inputs to an LR neuron being optically stimulated at L1a (left). Example trace from a representative LR cell in response to 10 Hz ADAV stimulation shows clear synaptic depression (purple). Blue triangles represent light pulses (right). Bottom: As above, but now for dorsal subicular (DS) input. LR responses to DS input are weakly facilitating.

B. Group synaptic dynamics for LR neurons in response to ADAV (green; n = 9) and DS (yellow; n = 9) inputs. ADAV synapses are strongly depressing, while DS synapses are weakly facilitating.

C. Same as ***A*** but for RS responses to claustral (CLA; top) and anterior cingulate (ACC; bottom) inputs. Both inputs to the RS neurons are weakly facilitating.

D. Group synaptic dynamics for RS neurons in response to CLA (red; n = 8) and ACC (magenta; n = 7) inputs. Both CLA and ACC synapses are weakly facilitating.

3.3.7 Short-term depression of anterior thalamic inputs enables encoding of angular head speed by LR cells

We next used computational modeling to elucidate the functional role of synaptic depression in this circuit, especially with respect to the processing of head direction input (Taube, 1995; Taube and Bassett, 2003). Up to 60% of cells in the anterior thalamus are classical head direction (HD) cells (Taube and Bassett, 2003). Each HD cell has a unique preferred direction at which its firing rate is highest when the head is facing that direction. The preferred directions of all cells in the HD ensemble span the full range of compass directions (Taube, 1998). Our modeling setup consisted of a postsynaptic RSG LR cell receiving input from an ensemble of 7500 presynaptic HD cells via depressing synapses (for full details, see Methods). In the initial simulations shown in Figure 3-8, the morphologically realistic model LR cell (Brennan et al., 2020) received uniform inputs (all HDs being equally likely) via depressing synapses with Tsodyks-Markram short-term dynamics (Tsodyks et al., 1998). The synaptic parameters were fit to match the experimentally observed response of LR cells to optogenetic stimulation of thalamic afferents reported above (Figure 3-7).

We found that the firing rate of the postsynaptic LR cell receiving HD input via depressing synapses was strongly correlated with angular head speed, giving rise to symmetrical angular head velocity tuning (Figure 3-8 B&C). Identical HD inputs transmitted via non-depressing synapses resulted in LR firing rates that were uncorrelated with angular head speed (Figure 3-8 B,E-F). It is important to note that in our model, firing rates of input HD cells were not explicitly modulated by angular head

velocity; therefore, the observed speed tuning resulted strictly from the depressing synaptic dynamics. For the parameter set whose results are depicted, LR cell firing rate was optimally correlated with head speed 24 milliseconds in the past, confirmed by both cross-correlation and mutual information analyses (Figure 3-8 E&F). We obtained the same results when modeling an ensemble of only 2500 presynaptic HD cells, indicating that our results are robust to the size of the presynaptic population (Supplemental Figure 3-6S). Taken together, these results suggest that synaptic depression of HD ensemble inputs introduces an angular head speed signal into the LR population, producing neurons that are more responsive during faster head turns, and potentially supporting the spatial orientation encoding functions attributed to the RSG (Epstein, 2008; Ino et al., 2007; Milczarek et al., 2018; Miller et al., 2019).

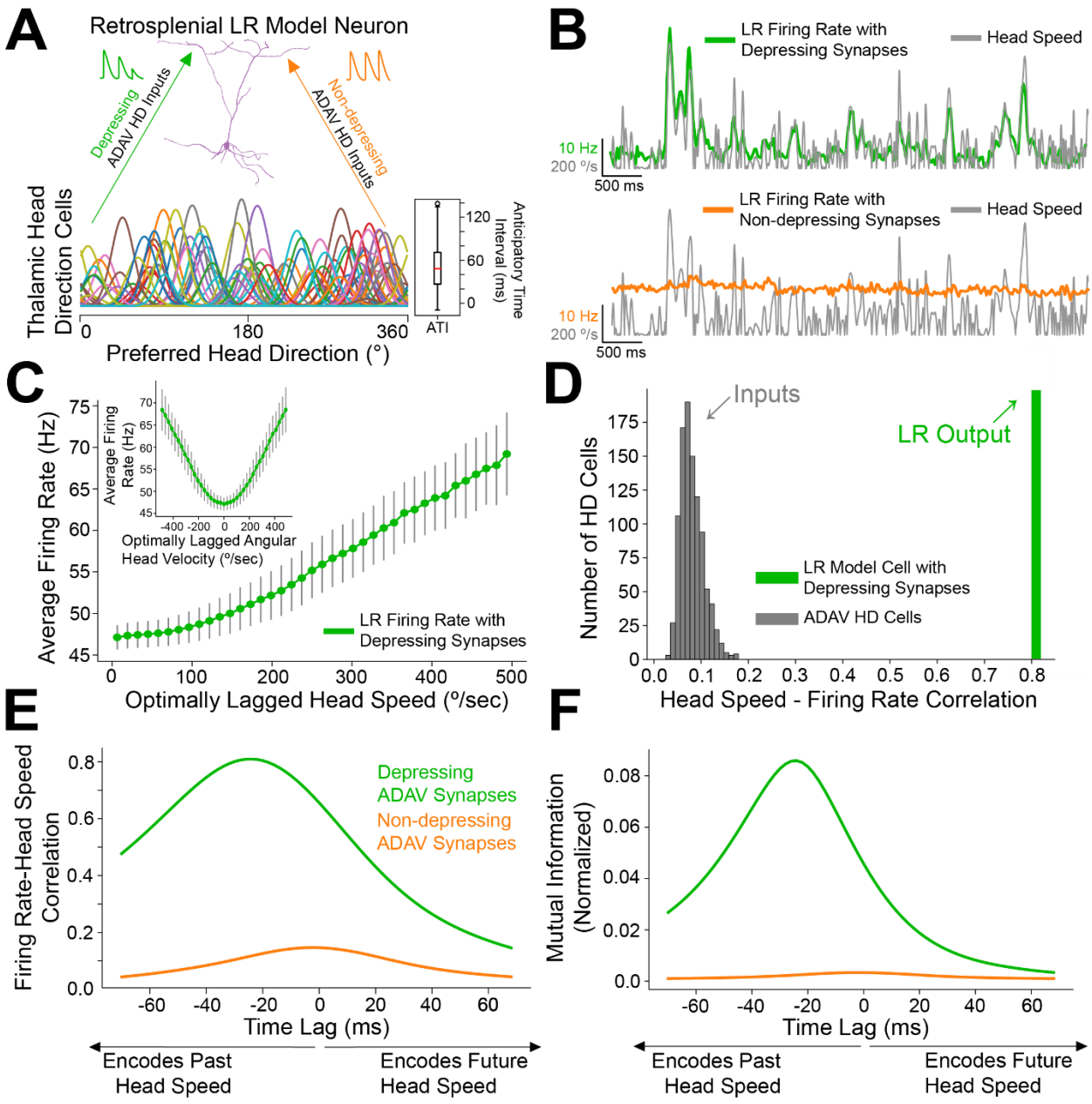

Figure 3-8. Depressing thalamocortical synapses allow LR cells to compute head speed from directional inputs.

A. We modeled a heterogeneous population of HD cells providing input to a single LR neuron via either depressing (green) or non-depressing (orange) synapses. Presynaptic HD cells varied in their tuning width, maximum firing rate, background firing rate, and anticipatory time interval (ATI). Tuning curves of a randomly selected subset of 100 (out of 7500) HD cells in the simulated ensemble are depicted here. Boxplot on the right depicts the empirical distribution of ATIs of all HD cells in the presynaptic population, with the mean ATI chosen as 50 ms in accordance with Taube (2010).

B. Sample traces spanning ten seconds of simulation time. Green: firing rate of postsynaptic LR cell receiving HD input via depressing synapses; Orange: firing rate of postsynaptic LR cell receiving HD input via non-depressing synapses; Grey: head turning speed. Note that for the non-depressing inputs, the firing rate of the LR cell remains approximately constant throughout. In contrast, depressing synapses produce a firing rate whose fluctuations visibly reflect fluctuations in the angular head speed.

C. Firing rate of postsynaptic LR cell plotted against head speed 24 ms in the past shows a clear monotonic relationship. A similar relationship exists between firing rate and current angular head speed (see panels ***E***, ***F***). The inset shows firing rate as a function of angular head velocity. The error bars indicate the standard deviation of all firing rates in each AHV bin; note that these variabilities are low, emphasizing the consistency and reliability of this code.

D. The grey histogram depicts the correlations between input HD cell firing rate and angular head speed during active (>10 Hz firing) windows. Since presynaptic firing rate was only explicitly modulated by head direction and not head speed, these values are low, with a mean value of 0.08. The green bar depicts correlation between postsynaptic firing rate and head speed at the optimal time lag (24 ms, see panels ***E***, ***F***). Hence, LR cells can utilize depressing inputs from HD cells to compute de novo head speed.

E. Cross-correlation between LR cell firing rate and head speed. We computed the Pearson correlation between the firing rate of the postsynaptic LR cell and the head speed L ms in the future for varying values of L, ranging from -70 to 70 ms. Postsynaptic firing rate was maximally correlated with head speed 24 ms in the past.

F. Same as ***E*** but for cross-mutual information. Cross-mutual information identifies the same optimal lag as cross-correlation.

3.3.8 Anticipatory firing of thalamic head direction cells improves postsynaptic speed encoding by retrosplenial LR neurons

Anterior thalamic HD cells display anticipatory firing (Blair et al., 1997), a phenomenon where an HD cell becomes most active at a fixed time interval before the animal is facing that cell's preferred direction (Figure 3-9 A). This temporal offset associated with each cell is called its anticipatory time interval (ATI). In anterior thalamus, the mean ATI has been reported as 25-50 ms (Taube, 2010). In our initial simulations, shown in Figure 3-8, we drew the ATI of each HD cell randomly from distributions matching these known *in vivo* ranges. To more systematically understand if and how the ATI of HD cells influences angular head speed coding by LR neurons, we next performed a series of simulations using various fixed ATI values for the entire HD population (Figure 3-9 A) and analyzed the resulting postsynaptic LR response.

Increasing ATI from 0 ms (no anticipation by the HD cell) to higher values (HD cell firing prior to facing the preferred HD) improved the lag between LR firing rate and angular head speed, with larger ATIs resulting in shorter latency between the head movement and LR coding of that angular head speed (Figure 3-9 C). Remarkably, larger ATIs also improved the angular head speed tuning of LR neurons independent of lag, as quantified by the maximum value (over the full range of lags) of cross-correlation or cross-mutual information (Figure 3-9 B). Thus, anticipatory firing of HD cells may constitute a powerful coding principle in the thalamo-retrosplenial circuit, helping LR cells to not only encode the current head speed with minimal lag, but also better encode the head speed independent of the lag.

In order to better understand this surprising effect, as well as how speed tuning generally arises, we analytically studied a simplified mean-field model of this thalamo-retrosplenial circuit (Supplemental Figure 3-7S). Our analysis allowed us to mathematically derive that LR activity should encode head speed with depressing synapses from simplified HD cells (see *Mean-Field Model Analysis*). Moreover, the analysis showed that anticipatory firing compensates for the lag introduced by integration time, leading to a theoretical parameter regime for which postsynaptic speed coding can be essentially perfect (where LR firing rate reflects head speed exactly with minimal latency). The observed improvement in quality of speed coding with increases in ATI corresponds to moving closer to this regime. Finally, our analysis showed that postsynaptic activity, at least at lower rotational speeds, is proportional to the square of head speed, thereby explaining the concave-up, parabolic shape of the speed-firing rate curve (Figure 3-8 C & Supplemental Figure 3-8S). Thus, both the simulations and the analytical theory show that synaptic depression of HD cell input onto LR cells should result in angular speed coding in the LR cell firing rate, and that anticipatory firing improves both the precision and quality of this coding.

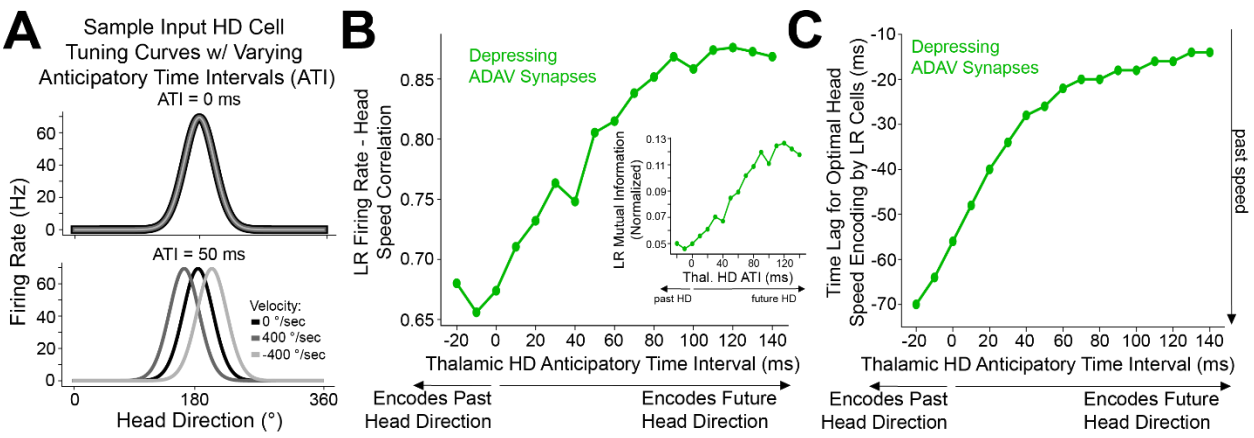

Figure 3-9. Encoding of future head direction in thalamus helps to better encode present head speed in retrosplenial LR cells.

A. The schematic depicts tuning curves for an HD cell with a preferred direction of 180 degrees. Top: the tuning curves of this cell if it displayed no anticipatory firing (ATI = 0 ms). Note that clockwise and counterclockwise turns produce identical tuning curves in this case. Bottom: the tuning curves of this cell if it had an ATI = 50 ms. Note that now, during head turns in either direction, the cell will fire 50 ms prior to when the animal faces 180 degrees. Our convention takes positive angular head velocity to denote counterclockwise turning.

B. Anticipatory firing of presynaptic HD cells improves speed coding in the postsynaptic LR cell. To quantify strength of speed coding independent of latency between head speed and postsynaptic firing rate, we used the maximum correlation between head speed and postsynaptic firing rate across all time lags. Inset shows a similar relationship, now for the maximum of cross-mutual information.

C. Anticipatory firing of presynaptic HD cells improves the latency between current head speed and postsynaptic firing rate, enabling more temporally precise speed coding.

3.3.9 Non-uniform head direction inputs can allow LR neurons to encode both head direction and speed, with a tradeoff

In the simulations above, we utilized a uniform distribution of HD inputs to each LR cell, such that each preferred direction was equally represented. However, in practice, it is likely that there will be heterogeneity in the preferred HDs of the cells providing inputs to any given retrosplenial LR cell. To study the extent to which speed coding persists under these conditions, we simulated a population of 200 LR cells, each of which received inputs from a randomly selected distribution of preferred directions for the presynaptic HD cells (Figure 3-10 Ai,Bi,Ci). We then analyzed the information content of each LR cell's firing rate, assessing the correlation and mutual information with both head direction and speed. We found that single cell activity in the LR population could encode both head direction and head speed (Figure 3-10 Aii,Bii,Cii), but there was a clear tradeoff between the two types of information.

This tradeoff between directional versus speed encoding was explained by the level of heterogeneity in the presynaptic preferred direction distribution (Figure 3-10 D-F), making intuitive sense. If an LR cell receives inputs that represent each HD equally, then it is not biased towards any one HD and encodes direction poorly. However, it encodes head speed very strongly in this case because it is able to sample the speed across all directions—there are no directional blind spots where the LR cell cannot detect the speed of head rotation from its presynaptic inputs. On the other hand, consider an LR cell that, by chance, gets inputs from a higher proportion of HD cells encoding a direction around 180 degrees. Now, the output of this LR cell is better

correlated with direction, acting as a broadly tuned HD cell itself and preferring 180 degrees, but also firing at most other directions. However, this LR cell's encoding of head speed gets worse because it under-samples many of the head directions faced by an animal. Thus, non-uniform HD inputs via depressing thalamocortical synapses represent a simple mechanism by which LR cells can conjunctively encode both head direction and head speed. Overall, our results predict *in vivo* LR neuronal spike trains that are likely to correlate with both the head direction and rotational speed of an animal, with a tradeoff between direction versus speed coding seen across individual LR cells (Figure 3-10 E).

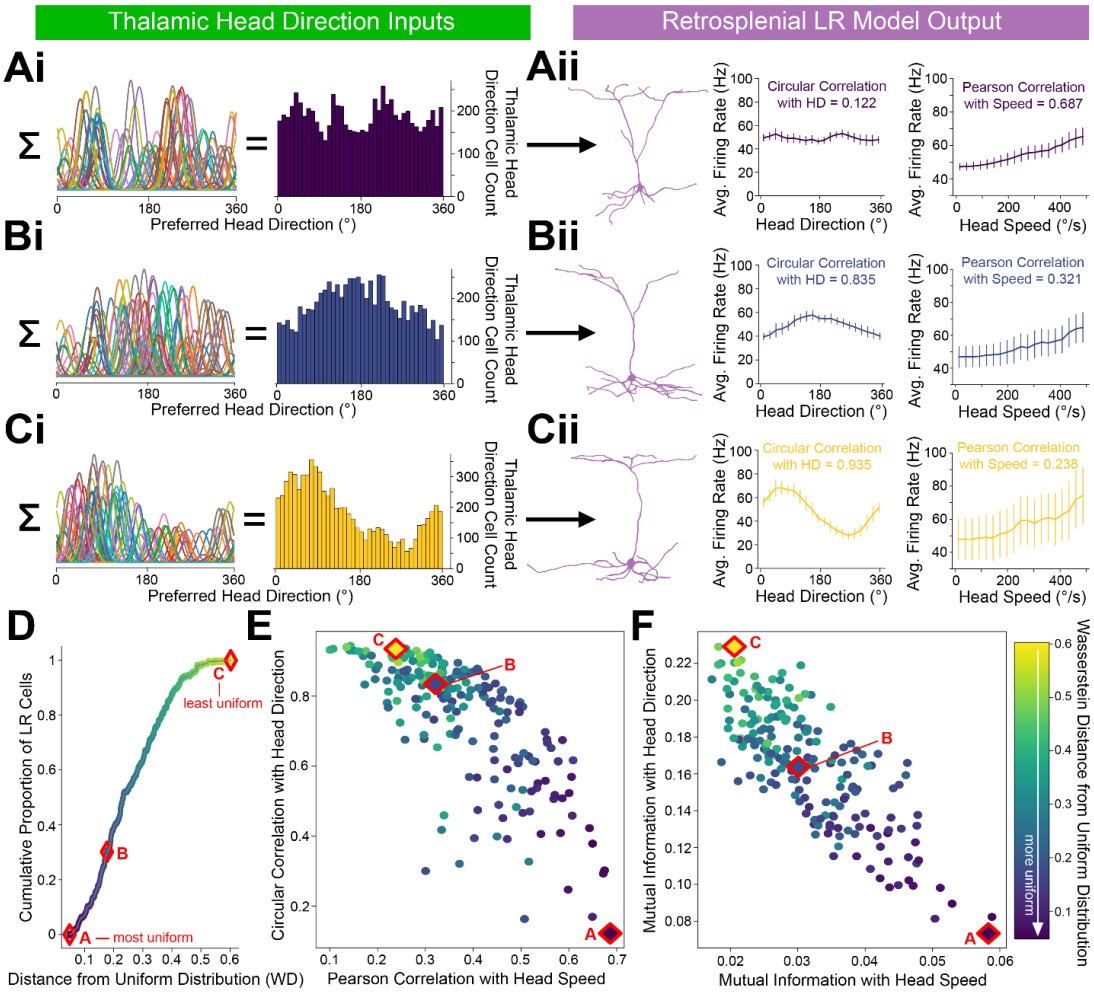

Figure 3-10. LR cells can conjunctively encode both head direction and speed, with a tradeoff.

i. Sample presynaptic preferred HD distributions for three simulated LR cells with distinct heterogeneity among their inputs. A is most uniform, and C is least uniform. Left: schematic depiction of the tuning curves of HD cells synapsing onto the LR cell. Right: calculated histogram of preferred directions of all HD cells synapsing onto the given LR cell.

ii. Response properties of the 3 LR cells whose preferred direction distributions are depicted in ***Ai,Bi,Ci***. As the preferred direction distribution becomes less uniform (from A to C), directional encoding improves (left graph) while speed coding becomes less precise (right graph).

D. For each simulated LR cell, we quantified the heterogeneity of its input HD distribution using the standard metric for this measure (Wasserstein distance from a uniform distribution; WD). Plot shows the cumulative distribution of WD values over the entire simulated LR population. Markers A,B,C correspond to the three example LR cells shown above.

E. Scatterplot showing each LR cell's correlation with angular head speed versus its correlation with head direction. The color-coded WD is also shown for each cell.

F. Same as ***E*** but for mutual information.

3.4 Discussion

We have identified a circuit that supports parallel processing of information as it first reaches the superficial granular retrosplenial cortex. Layer 3 of RSG contains two distinct pyramidal neuronal subtypes: small, excitable low rheobase (LR) neurons and regular spiking (RS) cells (Brennan et al., 2020). Here, we show that LR cells are driven by inputs from the anterior thalamus and dorsal subiculum but are essentially unresponsive to inputs from the claustrum, anterior cingulate, and contralateral retrosplenial cortex. (Figures 3-1 through 3-6, Supplemental Figure 3-3S). RS cells show precisely the opposite relationship: they are strongly driven by claustral, anterior cingulate, and contralateral retrosplenial inputs, but very weakly activated by anterior thalamic or dorsal subicular inputs (Figures 3-1 through 3-6, Supplemental Figures 3-2S and 3-3S). This dichotomy can be explained in large part by the precise overlap of LR versus RS apical dendrites with distinct afferent axons, including clear sublamination of both axons and dendrites within layer 1 (Figure 3-6). Anterior thalamic and dorsal subicular cells show robust directional and spatial modulation (Barry et al., 2006; Olson et al., 2017; Stewart et al., 2014; Taube, 1998; Taube and Bassett, 2003). Thus, the parallel circuit described here allows LR cells to selectively process this spatially relevant information and makes them ideally suited to support the spatial orientation computations carried out by the RSG.

3.4.1 LR cells are morphologically and computationally unique

The small, excitable LR cells are unique among pyramidal cells in RSG, and there is no evidence, to our knowledge, for such cells in any other cortical regions (Brennan et al., 2020; Holmgren et al., 2003; Jiang et al., 2015; Kurotani et al., 2013; Wyss et al., 1990). Indeed, the “granular” in granular retrosplenial cortex refers to the appearance of these dense small cell bodies in superficial RSG (Sripanidkulchai and Wyss, 1987; Vogt and Peters, 1981). Thus, LR cells are the defining morphological feature of RSG.

The distinct electrophysiological properties of LR neurons, specifically, play an integral role in the RSG’s unique capacity to process anterior thalamic head direction inputs. We have previously reported that the low rheobase and lack of spike frequency adaptation of these neurons are their defining computational features (Brennan et al., 2020). For this reason, we refer to them as low-rheobase (LR) neurons. They have also been called late-spiking (LS) neurons (Kurotani et al., 2013; Yousuf et al., 2020), but we argue this name is not optimal for several reasons. First, many other neurons in superficial RSG are also late spiking (Brennan et al., 2020), with L2/3 fast-spiking (FS) interneurons and also some RS neurons exhibiting a substantial delay to first spike, likely due to increased Kv1.1 or 1.2 channel expression in this region compared to other cortical areas (Kurotani et al., 2013). Thus, late-spiking is neither a distinctive feature of LR neurons nor excitatory neurons in this region. Second, the name “late-spiking (LS) neuron” is already the accepted and widely used nomenclature referring to a distinct inhibitory neuronal subtype, the neurogliaform cells that are located throughout the cortical layers in many regions of the brain, including within layer 1 of RSG (Cruikshank et al., 2012; Hestrin and Armstrong, 1996; Kawaguchi and Kubota, 1997; Overstreet-

Wadiche and McBain, 2015). Instead, the defining computational feature of the small pyramidal cells in L2/3 of the RSG is their low rheobase, and this nomenclature serves to provide an unambiguous name for these hyperexcitable cells (Brennan et al., 2020).

3.4.2 LR cells respond most strongly to inputs from spatially relevant regions

Previous work has reported TC-evoked responses in layer 5 RS neurons at their apical dendrites (Yamawaki et al., 2019b), with some variation in the magnitude of responses across cells. Our results reproduce these observations (Supplemental Figure 3-2S). Layer 5 is not a homogenous layer, often divided into sublayers 5A and 5B (Sempere-ferràndez et al., 2019; Sempere-Ferràndez et al., 2018; Sigwald et al., 2020; Sripanidkulchai and Wyss, 1987; Yamawaki et al., 2016a), and contains a variety of pyramidal cells, including the thin-tufted and thick-tufted neurons who have been shown to exhibit different responses to external inputs (Sempere-Ferràndez et al., 2018; Wyss et al., 1990). Further work is needed to determine whether any particular subtype of layer 5 pyramidal neurons may exhibit substantial TC-evoked responses, but our results, reporting significantly larger responses to TC input by LR neurons, suggest LR cells are the predominant spatial information-encoding subtype within RSG.

The dorsal subiculum, which serves to transmit allocentric spatial information such as axis and boundary vector signals (Lever et al., 2009; Derdikman, 2009; Olson et al., 2017; Simonnet and Brecht, 2019; Bicanski & Burgess, 2020), also precisely targets LR neurons via projections predominantly to layer 3 of RSG (Figure 3-5; Nitzan et al., 2020; Yamawaki et al., 2019a). These inputs overlap with LR cell bodies, basal

dendrites, and apical dendrites in L1b/c and evoke larger excitatory postsynaptic currents in superficial cells compared to layer 5 pyramidal neurons (Figure 3-5; Nitzan et al., 2020; Yamawaki et al., 2019a). Thus, the distinct morphology and intrinsic properties of LR neurons make them ideally suited to integrate head direction input from the thalamus and spatial inputs from the hippocampal formation via the dorsal subiculum. Indeed, this integration of various types of directional and distance information is often stated as the key computational function of the retrosplenial cortex as a whole (van Wijngaarden et al., 2020; Burgess et al., 2001; Byrne et al., 2007; Epstein, 2008; Ichinohe et al., 2003; Maguire, 2001), further highlighting the defining role that LR cells are likely to serve in the RSG.

3.4.3 Thalamic inputs to LR cells show short-term depression: implications for angular head velocity and head direction coding in RSG

We have shown that thalamocortical synapses onto LR cells are depressing (Figure 3-7). Our modeling results demonstrate that such depressing synapses allow LR neurons to compute angular head speed from head direction input, leading to robust encoding of angular speed in the postsynaptic LR firing rate (Figure 3-8). This result is in line with previous studies (Abbott et al., 1997; de la Rocha and Parga, 2008; Puccini et al., 2007) that use synaptic depression to implement neural circuits that perform rate of change computations. We also find that LR encoding of angular head speed is improved by the fact that input HD cells display anticipatory firing (Figure 3-9; Blair et al., 1997). This improvement not only allows LR cells to encode current head speed with

a shorter time lag (Figure 3-9 C), but also strengthens the correlation with head speed regardless of lag (Figure 3-9 B). This proposed mechanism by which depressing synapses compute head speed is fully generalizable, and thus may also be of relevance to other brain circuits employing HD-like population codes (Maunsell and Van Essen, 1983). Furthermore, we have shown that this thalamocortical synapse can support conjunctive encoding of both head direction and angular head speed by individual LR cells (Figure 3-10).

Our results make specific predictions about the coding properties of LR cells that can be tested with *in vivo* recordings. First, based on their intrinsic properties (Supplemental Figure 3-1S; Brennan et al., 2020), LR cells in superficial RSG are likely to show high firing rates and spike widths intermediate to the standard “broad/narrow” criteria currently used to distinguish putative RS and FS cells in most cortical recordings. Thus, future recordings will need a large sampling of cells in L2/3 of RSG to provide enough data to identify the predicted three distinct clusters of spike shapes (RS/LR/FS). Second, we expect LR cell activity to be correlated with angular head speed with a relatively small lag (Figures 3-8, 3-9). Third, we predict that the experimentally observed head velocity tuning curves will be concave up and exhibit approximately quadratic scaling at low rotational speeds, as our analytical work suggests (Figure 3-8; *Mean-Field Model Analysis*). Fourth, we anticipate a significant proportion of LR cells will show conjunctive encoding, where both angular head speed and direction are encoded. A key aspect of this conjunctive encoding, as predicted by our simulations (Figure 3-10), is that individual cells will show a tradeoff between directional and speed encoding. As a population, this is likely to allow LR cells to

comprehensively encode conjunctive speed and directional information and provide this information to downstream targets, helping with spatial orientation computations within RSG. This predicted conjunctive encoding will also necessitate that the test of predictions 2 and 3 be carried out in a head-direction delimited manner.

3.4.4 Downstream targets of LR cells and potential role of RS neurons in retrosplenial spatial computations

LR neurons do not synapse onto neighboring excitatory neurons within layers 2/3 (Brennan et al., 2020), and no (0/9) pairs tested in this study between LR and layer 5 RS cells exhibited connectivity (data not shown). Thus, LR cells likely do not provide any substantial input to other LR cells or any RS cells located in layers 2-5 of ipsilateral RSG. Instead, LR neurons send their axons into the corpus callosum and may likely target homotopic regions of contralateral RSG (Brennan et al., 2020; Kurotani et al., 2013). Indeed, retrograde injections into one RSG hemisphere have been shown to predominantly label small contralateral L2/3 cells (Sripanidkulchai and Wyss, 1987; van Groen and Wyss, 2003), most likely corresponding to the LR cells that constitute the majority of cells in L2/3 (Brennan et al., 2020). Our supplementary results (Supplemental Figure 3-3S) show that inputs from contralateral RSG preferentially and strongly target RS neurons, with almost no recruitment of LR neurons. This is consistent with the observed distribution of afferent axons from contralateral RSG: these axons and terminals avoid L1a and L3 where all LR dendrites are located (Supplemental Figure 3-3S). Thus, we propose the following hypotheses for LR downstream targets

and possible function: LR neurons in one hemisphere receive unilateral inputs from directional cells in the anterior thalamus (Figure 3-1, 3-2, & 3-6). These inputs are utilized to encode information about both the speed and direction of head rotations and are subsequently transmitted to RS cells in contralateral, but not ipsilateral, RSG (Supplemental Figure 3-3S). Thus, LR cells may serve to perform a hemispheric switch of rotational speed and direction information. Given the known bidirectional connectivity between secondary motor cortex and RSG (Yamawaki et al., 2016a), RS cells may be able to utilize inputs from contralateral LR cells to perform comparisons of the actual head speed and direction signal with motor efference signals, helping to sharpen the code for spatial orientation in the RSG. However, extensive future investigations of this contralateral circuit are needed to explore these hypotheses.

3.4.5 Potential role of claustral and anterior cingulate inputs

In contrast to thalamic and DS inputs to RSG, projections from both the claustrum and anterior cingulate cortex avoid laminar overlap with LR apical dendrites, instead projecting to the lower divisions of L1/2 and L5 to target RS apical and basal dendrites (Figures 3-3, 3-4, & 3-6). Both the CLA and ACC are heavily implicated in a range of non-spatial behaviors often described as being “cognitive” or “mnemonic” in function (Botvinick, 2007; Brown and Braver, 2005; Carter et al., 1998; Devinsky et al., 1995; Kim et al., 2016; Mohanty et al., 2007; Smith et al., 2012; Smythies et al., 2012; Stevens et al., 2011), but there is also evidence that these regions exhibit some degree of spatial information processing (Guterstam et al., 2015; Jankowski and O’Mara, 2015;

Sutherland et al., 1988; Whishaw et al., 2001). Indeed, 7-15% of cells in the claustrum were found to encode place or boundary-related information (Jankowski and O'Mara, 2015), though this percentage is relatively low compared to the 60% of anterior thalamic (Taube, 1998) and 61% of dorsal subicular (Kitanishi et al., 2021) neurons that are known to clearly encode elemental direction, place, and other spatial features. Regardless, retrosplenial RS neurons may be receiving direct spatial inputs from the CLA and ACC in addition to the cognitive and mnemonic information relayed by these two regions. We also speculate that retrosplenial RS neurons may receive directional and spatial information that has already been heavily integrated by LR neurons in the contralateral hemisphere (Supplemental Figure 3-3S), as discussed above. This convergence of disparate signals onto RS cells could then serve to support functions that require both spatial and non-spatial integration, such as contextual fear conditioning, a key function attributed to the RSC (de Sousa et al., 2019; Keene and Bucci, 2008a, 2008b; Kwapis et al., 2015; Yamawaki et al., 2019a).

Indeed, a recent study reported that selective ablation of putative retrosplenial RS cells located near the boundary and within upper layer 5 resulted in contextual fear amnesia (Sigwald et al., 2020), indicating that these cells are involved in the fear-related functions of the retrosplenial cortex (Lukoyanov and Lukoyanova, 2006; Yamawaki et al., 2019a, 2019b). The laminar location of these cells corresponds well to the position of the RS cells recorded in our study that we show to preferentially receive CLA and ACC inputs. Both the CLA (Cho et al., 2017; Ipser et al., 2013; Vakolyuk et al., 1980; Vetere et al., 2017; Zingg et al., 2018) and ACC (Frankland et al., 2004; Han et al., 2003; Steenland et al., 2012) have been heavily implicated in fear-associated

behaviors, suggesting again that CLA and ACC inputs to L3 RS cells help to support the role of these neurons in contextual fear conditioning. Future work that selectively inactivates CLA versus ACC axon terminals in RSC will be necessary to causally confirm the role of each of these synapses in fear conditioning.

3.4.6 Conclusions

In summary, our results highlight a superficial retrosplenial circuit enabled by the precise sublaminar organization of distinct principal neuronal subtypes and axonal afferents. LR neurons receive directional and spatial inputs from the anterior thalamus and dorsal subiculum. The synaptic dynamics of thalamic inputs to LR cells can give rise to rate coding of angular head speed in LR cells. In contrast, neighboring RS neurons in RSG respond very weakly to these directional inputs, as their apical and basal dendrites distinctly avoid laminar overlap with anterior thalamic and subicular afferents. Instead, RS neurons respond to claustrocortical and anterior cingulate inputs. Determining how these two parallel streams of information are integrated in downstream neurons within both the ipsilateral and contralateral granular and dysgranular retrosplenial cortices is the next critical step towards a mechanistic understanding of retrosplenial computations.

3.5 Materials and Methods

3.5.1 Animals

All procedures and use of animals were approved by the University of Michigan Institutional Animal Care and Use Committee. The following mouse lines were used for the CRACM experiments: Ai14 (Jackson Laboratories, 007914), Ai32 (Jackson Laboratories, 024109), C57BL6 wildtypes (Charles River, stock #027), *Camk2α*^{Cre} (Jackson Laboratories, 005359), *Grp*-KH288^{Cre} (RRID:MMRRC 037585-UCD), *Pvalb*^{Cre} (PV-IRES-Cre; Jackson Laboratories, 008069), and *Pvalb*^{Cre} x Ai14 (crossed in house). A combined total of 70 mice of both sexes between the ages of P41–P184 were used in this study.

3.5.2 Experimental Procedures

Surgical procedures

Surgical anesthesia was induced via isoflurane inhalation at 4% and then maintained on a surgical anesthetic plane at 2-3% isoflurane. Upon induction, atropine was injected subcutaneously at 0.05 mg/kg. A Physitemp (Clifton, New Jersey, USA) controller monitored and maintained body temperature at 37ºC. Ophthalmic ointment was placed on the eyes. The incision site was prepared using 1:40 Nolvasan followed with isopropyl alcohol before being subcutaneously injected with 1% lidocaine. The skull was then leveled, and bregma was identified. Using a digital stereotaxic coordinate

system, the following injection target sites were identified: right anterodorsal thalamic nucleus (AP = -0.6 mm, ML = +0.78 mm, DV = -2.5, -3.25 mm), right claustrum (AP = +1.25 mm, ML = +2.6 mm, DV = -3.3 mm), right dorsal subiculum (AP = -3.0 mm, ML = +1.5 mm, DV = -1.5, -1.8 mm), right anterior cingulate cortex (AP = +0.3 mm, ML = +0.3 mm, DV = -0.7, -1.0 mm), and contralateral RSG (see Supplemental Figure 3-3S; AP = -2.25 mm, ML = -0.2 mm, DV = -0.7 mm). Burr holes were then drilled through the skull at the identified sites, and dura removed. Micropipettes were lowered under stereotaxic guidance into the target injection site containing the ChR2 viral construct (AAV2-EF1a-DIO-hChR2(h134R)-eYFP for *Grp*^{Cre} mice and AAV2-hsyn-ChR2(H134R)-eYFP or AAV2-hsyn-ChR2(H134R)-mCherry for all other lines, UNC Gene Therapy Vector Core). For dual injection surgeries, the ChR2 viral construct was injected into the functional target, and a fluorescent tag (AAV2-hsyn-mCherry or AAV2-hsyn-eYFP) was injected into the other region for comparison of various afferent axonal and terminal arborizations within the same animal.

Injections of 0.5 µL total virus volume at each depth were given via a picospritzer at 0.05-0.07 µL/min with a 5-minute pause between injecting the more dorsal and ventral DV coordinates, when applicable. After a region was injected, there was a 10-minute period before removing the micropipette from the brain. Enrofloxacin was administered at 8.0 mg/kg after injections. Burr holes were sealed with bone wax, and the incision was closed with VetBond with antibiotic ointment placed under skin edges. Isoflurane was tapered down prior to removal. After removal from isoflurane, carprofen was administered at 5 mg/kg. The mice were kept warm through an artificial heat source

during the recovery period. Mice then recovered for 2-14 weeks post-injection before being used for slice experiments.

Slice preparation

Slices were prepared as described previously (Brennan et al., 2020). Briefly, mice were deeply anesthetized using isoflurane before decapitation. Brains were removed and placed in a carbogen-saturated ice-cold high-sucrose slicing solution within 30 seconds of decapitation. Using a Leica 1200VT or Leica 1000S vibratome, 300 µm coronal slices were cut and placed in a high-magnesium artificial cerebrospinal fluid (ACSF) solution at 32ºC. After resting in this solution for 20 minutes, the entire bath was moved to room temperature where the slices rested for the remainder of the experiment.

Whole-cell recordings

During whole-cell recordings, slices were submerged in a recording chamber with a 2 mL/minute flow of body-temperature ACSF (126 mM NaCl, 1.25 mM NaH2PO4, 26 mM NaHCO3, 3 mM KCl, 10 mM dextrose, 1.20 mM CaCl2, and 1 mM MgSO4). They were visualized using an Olympus BX51WI microscope, Olympus 60x water immersion lens, and Andor Neo sCMOS camera (Oxford Instruments, Abingdon, Oxfordshire, UK). Patch pipettes had a diameter of 2-4 µm and resistances between 2-5 MΩ. The potassium gluconate internal solution used in these experiments contained 130 mM K-gluconate, 2 mM NaCl, 4 mM KCl, 10 mM HEPES, 0.2 mM EGTA, 0.3 mM GTP-Tris, 14 mM phosphocreatine-Tris, and 4 mM ATP-Mg and had a pH of 7.25 and osmolarity of 290 mOsm.

Current-clamp recordings were conducted using the Multiclamp 700B and Digidata 1550B (Molecular Devices). Patched neurons were adjusted for series resistances and held at resting potentials around -65 mV. Recordings were not corrected post hoc for liquid junction potential. Resting membrane potential, defined as recorded potential within 30 seconds of break-in, was recorded, and cells with resting potentials more depolarized than -50 mV were not included in this study. Intrinsic neuronal properties were calculated using a set of protocols detailed below and measured with either Clampfit or simple custom MATLAB routines. Pharmacological agents were prepared prior to experiments as outlined by the manufacturer and added to the ACSF. Agents were applied for at least 10 minutes before conducting experiments, and verification of effect was visualized (no spiking for strong, suprathreshold current injections for TTX-4AP; no feedforward inhibition for picrotoxin).

Channelrhodopsin-assisted circuit mapping

Channelrhodopsin-assisted circuit mapping (CRACM) experiments (Yamawaki et al., 2016b) were conducted under the same rig set-up as described above while using a 5,500K white light-emitting diode (LED; Mightex; maximum power of 14.47 mW measured at the slice focal plane). Synaptic responses to optical stimulation of the ChR2-expressing axons were measured from postsynaptic retrosplenial neurons recorded under whole-cell current-clamp conditions.

To examine the effect of afferent axonal input to retrosplenial neurons, two optogenetic stimulation protocols were used. First, a targeted optogenetic stimulation approach was used to examine the distribution of afferent axons and terminal arbors across the cortical layers in which the postsynaptic retrosplenial neurons resided. The

main areas of interest included layer 1a (L1a; defined as the top 1/3 of L1 adjacent to the midline), layer 1/2 boundary (L1/2; defined as the border between the sparse L1 and densely-packed L2), the location of the patched cell body (all patched cells were located in layers 3 or 5), upper layer 5 ($L5_{sup}$: defined as 100 µm from the L3/5 boundary), and deep layer 5 ($L5_{dp}$; defined as 200 µm from the L3/5 boundary). For LED-based stimulation over L1a, the objective was centered approximately 30 µm from the pia in L1. For LED-based stimulation over L1/2, the objective was centered over the border between L1 and L2. For LED-based stimulation over the cell body, the objective was centered on the patched cell body at its widest diameter. For $L5_{sup}$, the objective was centered 100 µm into L5, and for $L5_{dp}$, the objective was centered 200 µm into L5. All LED-based stimulations were aligned in the cortical column with the patched cell body. LED intensity was kept constant at each stimulation location and was set at the minimum intensity necessary to evoke the smallest visible response when stimulating at the minimum location (see below). For most cells, this minimal response was between 0.25-5 mV, while strongly activated cells had larger responses with the smallest possible LED intensity. The minimum location for ADAV experiments was L1/2, while the minimum location for CLA, ACC, and DS experiments was L1a, corresponding with the lowest projection density of inputs within the superficial layers of RSG. All layer test optogenetic stimulation protocols consisted of a 1 second 10 Hz train of 1 ms LED pulses. For short-term dynamics analyses, an additional optogenetic stimulation protocol was used that consisted of a 1 second 40 Hz train of 1 ms LED pulses.

Second, a current step protocol was used to examine the effect of thalamic input on the postsynaptic retrosplenial neurons' spike trains. In this protocol, a 2 sec current

step was delivered to the postsynaptic cell that elicited a 10-30 Hz spike train with a 1 ms LED pulse delivered at 500 ms into the current step. The objective for this protocol was centered directly over the cell body.

Morphological investigations and reconstructions

To analyze the morphology of the cells, biocytin (5mg/ml) was added to the recording solution immediately before recording. Biocytin was allowed to diffuse into the cell for no less than 20 min. Shortly before removing the patch pipette from the neuron, ten current pulses (1-3nA at 1Hz) were applied to aid the diffusion process (Jiang et al., 2015). After the fill process was complete, the patch pipette was retracted from the cell slowly to allow the membrane resealing. 1-4 cells were filled per slice, and then the slice was transferred from the recording chamber to 4% PFA for overnight fixation. The next day, slices were washed in PBS and incubated for 24-48 hours in streptavidin conjugated Alexa Fluor (488, 594 or 647) with 0.2% TritonX added to permeabilize the cells. For a subset of cells, fluorescent nissl stain, NeuroTrace, was added to the Alexa Fluor incubation step (at 1:200 dilution). After this incubation, slices were washed in PBS, mounted on slides, and cover slipped using Fluoromount-G.

Z-stacks of each filled cell were acquired using the Leica SP5 confocal microscope with a dry 40x lens or the Zeiss Axio Image M2 confocal microscope with 20x lens. Reconstructions from z-stacks were performed using NeuroLucida software in user-guided mode or NeuTube software (Feng et al., 2015). Additional reconstructions previously generated were also added to the analyses described below (Brennan et al., 2020).

Imaging of slice expression

Representative images of axonal projection to RSG were obtained from mice injected with anterograde AAV2 into ADAV, CLA, ACC, DS, and cRSG. Slices were prepared as for electrophysiology recordings. After use, slices with ADAV, DS, and cRSG expression from AP range -1.7 to -2.06 mm were fixed overnight in 4% PFA and then stained with the fluorescent Nissl stain, NeuroTrace 435-455, to aid laminar demarcation. ACC and CLA slices underwent an additional signal amplification protocol. Those slices were first incubated overnight in PBS containing appropriate normal blocking serums with 0.2% TritonX. On the following day, anti-GFP (for eYFP) or anti-mCherry primary antibodies (Abcam ab13970 and ab167453 respectively, diluted 1:2000) were added and slices were incubated at 4°C on a shaker for up to 24h. Next, slices were washed in PBS and incubated on a shaker for 3 hours at room temperature in PBS containing 2% bovine serum albumin (BSA), 0.2% TritonX and biotin-conjugated secondary antibodies (Jackson ImmunoResearch AB_2313596 and AB_2340593, dilution 1:300) then again washed in PBS. Finally, slices were incubated on a shaker in PBS with 0.2% TritonX and streptavidin-conjugated Alexa Fluor (488 for eYFP and 594 for mCherry amplification, dilution 1:300) and NeuroTrace 435-455 (dilution 1:200) for another 3 hours at room temperature, and then washed in PBS. All slices were then mounted on slides using Fluoromount-G and allowed to dry overnight at room temperature. Z-stack images (7 µm at 0.5 µm z-steps) of the slices were obtained the following day using confocal microscope Zeiss Axio Image M2 with 20x dry objective.

3.5.3 Experimental Quantification and Statistical Analysis

Neuronal analysis and statistics

Multiple intrinsic neuronal properties were calculated as previously reported (Brennan et al., 2020). Briefly, spike threshold, spike amplitude, spike width, spike frequency adaptation ratio, latency to first spike, rheobase, input resistance (R_{in}), input capacitance (C_{in}), and membrane time constant (τ_m) were measured. Spike amplitude, threshold, and width were calculated from the average of all spikes in a 600 ms current step that elicited a 5 Hz spike train. Amplitude was calculated as the voltage difference from threshold to the peak of the spike, threshold from the peak of the third derivative of membrane potential (Cruikshank et al., 2012), and width as the full width at half-maximum spike amplitude. Spike frequency adaptation ratio was calculated from the same 600 ms current step protocol using the first sweep that elicited a 10 Hz spike train using the equation ISI_{last}/ISI_{first}. Latency to first spike and rheobase were measured using a 1 sec current step protocol that began below threshold and increased by 1-5 pA steps until at least 3 sweeps post-threshold. Latency to first spike was calculated as the time from the onset of the current step to the peak of the first spike. Rheobase was measured as the minimum current needed to cause at least one spike in the 1 sec current step. Lastly, input resistance (R_{in}), input capacitance (C_{in}), and membrane time constant (τ_m) were all measured from a protocol that delivered a series of small negative current steps resulting in ~4 mV deflection in membrane potential. R_{in} was calculated using Ohm's law, mean voltage change divided by mean current. τ_m was measured by fitting a single exponential to the average of the initial 60 ms of the negative voltage

deflection, ignoring the first 20 ms. Lastly, C_{in} was calculated using the formula $\tau_m = R_{in} \times C_{in}$. Statistical significance of the differences in intrinsic properties between the retrosplenial neuronal subtypes was calculated using the Wilcoxon rank sum test.

ChR2-assisted circuit mapping analysis and statistics

To quantify the effect of TC and ClaC input across the layers, the amplitude of the resulting postsynaptic responses from each laminar location of LED stimulation (L1a, L1/2, and cell body) were measured with Clampfit and Matlab. The average of the response to the first pulse in the 10 Hz train was calculated for each cell at each LED laminar location. Significant differences between cell types and/or laminar locations were calculated using the Wilcoxon rank sum test. From the current step protocol, raster plots and PSTHs were plotted for each cell in MATLAB. The percent increase in spike rate was calculated by subtracting the number of spikes in a 100 ms window after the LED pulse from the number of spikes in a 100 ms window before the LED pulse, then dividing this value by the number of spikes in the 100 ms window before the LED pulse. Significant differences between spike count pre- and post-stimulation for both LR and RS cells and LR and RS percent increase in spike rates were calculated using the Wilcoxon rank sum test.

Short-term dynamics were calculated from 10 Hz or 40 Hz LED pulses protocols (see Channelrhodopsin-assisted circuit mapping subsection of the Experimental Procedures section of Methods). To analyze 0.1 Hz short-term dynamics, the first response to the first pulse of each sweep from the 10 Hz protocols was used. Average response amplitudes of each pulse were measured for each cell. Amplitudes were then normalized using the equation stimulus n / stimulus 1, and normalized postsynaptic

ratios were plotted. Cells with first pulse responses greater than 0.5 mV but not spiking were included. Significance of resulting short term synaptic depression of LR neuron responses to 10 Hz and 40 Hz thalamic stimulation were calculated using the Wilcoxon rank sum test.

Morphological analysis and statistics

All z-stack images of axonal projections and their corresponding NeuroTrace channel were first collapsed in ImageJ (using Z project option with max intensity). A section of image spanning layers 1 to 6 from each image was chosen to serve as a representative sample of expression pattern in that image. In each sample, boundaries of retrosplenial layers 1, 2, 3, and 5 were measured as distance from pia based on NeuroTrace expression, and the information was saved. L1 was distinguished by a low cell density, L2 by a thin, densely packed band of small pyramidal cell bodies, L3 by a lower density (compared to L2) of small pyramidal neurons, L5 as having larger cell bodies relative to L3, and L6 as having smaller cell bodies. Images of fills of the reconstructed cells underwent a similar process (with the exception of LR neurons, which only had layers 1, 2, and 3 boundaries measured, and the average layer width for L5 was applied to them by default). After all images (both cell reconstructions and sample projections into RSG) were measured and processed, they were turned into binary black and white thresholded versions using ImageJ. For the images of reconstructed cells, cell bodies were removed from the black and white images to allow the analysis of dendrites only.

Dendrites and axons were analyzed as a function of cortical depth (Yamawaki et al., 2014). White pixels in every image (axonal expression or reconstructed cell) were

counted, and their total counts per row were divided by the total numbers of white pixels in the image, resulting in a projection density distribution vector along the layers of RSG. Average layer widths were calculated from the previously acquired measurements and used to set the number of bins per layer to uniformly represent layers. Density plots were then visualized from the adjusted distribution vectors using the following Python modules: pandas, matplotlib, scipy, and Seaborn. For correlation analysis, area from pia to layer 5A, corresponding to the end of RS basal dendrites), was chosen. Spearman's correlation matrices were created using the pandas and scipy Python modules and plotted as a heatmap. Images of axonal projection patterns to prefrontal cortex (PFC) (Supplemental Figure 3-4S) were obtained from the Allen Mouse Brain Connectivity Atlas (https://connectivity.brain-map.org; Oh et al., 2014).

3.5.4 Modeling Methodology

Our model circuit consists of an RSG LR cell receiving input from an ensemble of N thalamic HD cells, via synapses exhibiting short-term depression.

3.5.4a Modeling the presynaptic head direction population

Throughout, let $\theta_T(t) \in [0,2\pi]$ denote the head direction at time t ms. Each HD cell has a preferred angle (PA) at which its firing rate is maximized. The firing rate at time t of an HD cell with PA θ takes the form

$$r(\theta, t) = f\big(\theta - \theta_T(t)\big)$$

where f is a fixed function describing the shape of the cell's tuning curve. In all simulations, we utilize a Gaussian tuning curve

$$f(\theta) = \left(f_{max} - f_{bg}\right) \cdot e^{\epsilon(\cos(\theta)-1)} + f_{bg}$$

Here f_{bg} is the background firing rate, f_{max} is the maximum firing rate, and ϵ sets the tuning curve width. We draw these parameters from Beta distributions with statistics in accordance with the ADN HD cell statistics reported in (Taube, 2010); see Supplemental Table 3-3S for exact quantities. The spike train of a single HD cell with PA θ follows an inhomogeneous Poisson process, with intensity given by $r(\theta, t)$ at time t. We additionally impose a post-spike refractory period of 4 ms.

We draw these parameters from Beta distributions with statistics in accordance with the ADN HD cell statistics reported in Taube, 2010 (see Supplemental Table 3-3S for exact quantities). The probability density function of the Beta distribution with parameters $(a, b,$loc,scale$)$ is given by $p((x - \text{loc})/\text{scale})$ with

$$p(x) = \frac{\Gamma(a+b)x^{a-1}(1-x)^{b-1}}{\Gamma(a)\Gamma(b)},$$

where Γ denotes the standard Gamma function.

Finally, the spike train of a single HD cell with PA θ follows an inhomogeneous Poisson process, with intensity given by $r(\theta, t)$ at time t. We additionally impose a post-spike refractory period of 4 ms.

Anticipatory Firing

Thalamic HD cells exhibit an *anticipatory time interval*, or ATI: for each cell, there exists some constant duration A ms such that the cell tends to spike A ms prior to when the animal's heading equals the preferred direction of the cell. We define this notion

more precisely following a previous study (Blair et al., 1997). Restrict attention to a specific HD cell, with ATI A ms, and let θ denote its PA when the angular head velocity is zero. The ATI is defined via the property that when angular head velocity equals ω, the PA of this cell shifts from θ to $\theta - \omega A$. Equivalently, we can think of HD cell PAs as static and instead say anticipatory firing effectively transforms the heading trajectory itself: if $\theta_T(t)$ describes the true angular trajectory, the effective trajectory experienced by our chosen HD cell is

$$\theta_A(t) = \theta_T(t) + A \cdot \acute{\theta}_T(t)$$

In Vivo Head Direction Recordings

To simulate the angular trajectory $\theta_T(t)$, we employ *in vivo* mouse head tracking recordings from the data set CRCNS-th1 (Peyrache et al., 2015). These *in vivo* heading recordings were originally sampled at a relatively low rate of approximately 40 Hz; in order to facilitate use of this data at the finer time scale of HD cell spiking, we linearly interpolated the raw data. Angular head velocity was computed using the standard centered approximation to the derivative:

$$\acute{\theta}_T(t_i) \approx \frac{\theta_T(t_{i+1}) - \theta_T(t_{i-1})}{t_{i+1} - t_{i-1}}$$

3.5.4b Modeling short-term synaptic plasticity

In the Tsodyks-Markram (TM) model (Tsodyks et al., 1998) of short-term synaptic plasticity, each synapse has a finite pool from which it releases vesicles into the cleft upon arrival of a presynaptic spike. The state of the synapse at any moment in time is characterized by the triple (x, u, g), specified as

- $x(t)$: fraction of vesicles remaining in the pool at time t
- $u(t)$: fraction of pool released into cleft upon presynaptic spike arrival at time t (i.e. release probability)
- $g(t)$: synaptic conductance at time t

Here t is measured in milliseconds, g in umho, and the variables x and u are dimensionless. Depression results from depletion of x due to a spike train, followed by slow recovery of the vesicle pool; facilitation results from increase in u due to a spike train, followed by slow decay of this release probability. Formally, these dynamical variables satisfy the system.

$$\frac{dx}{dt} = \frac{1-x}{\tau_d} - u^+ x^- \delta\left(t - t_{sp}\right)$$

$$\frac{du}{dt} = \frac{-u}{\tau_f} + U(1-u^-)\delta\left(t - t_{sp}\right)$$

$$\frac{dg}{dt} = \frac{-g}{\tau_g} + Au^+ x^- \delta\left(t - t_{sp}\right)$$

Here t_{sp} denotes an arbitrary presynaptic spike time, and the δ term specifies a discontinuous modification to the variable upon arrival of a presynaptic spike. We use the notation $f^{\pm}(t) = \lim_{h \to 0^{\pm}} f(t+h)$, and thus u^+ and u^- satisfy the relation $u^+ = u^- + U(1-u^-)$. The parameters τ_d, τ_f, and τ_g set the timescale of depression recovery, facilitation decay, and synaptic conductance decay, respectively. Note that $u^+ \geq U$ always, so U represents the minimum fraction of x contributing to the conductance on each presynaptic spike arrival. Finally, the parameter A is just a tunable synaptic weight (with units of umho).

In the regime of $\tau_d \gg \tau_f$, depression dominates the synaptic dynamics; conversely, in the regime of $\tau_f \gg \tau_d$, facilitation dominates. Accordingly, the limits $\tau_f \to 0$ and $\tau_d \to 0$ describe *depression-only* and *facilitation-only* dynamics, respectively. On the other hand, when τ_f and τ_d are on the same order of magnitude, the synapse may exhibit combined depressing-facilitating dynamics.

Synapse Implementation and Parameter Choices

We utilized an implementation of the Tsodyks-Markram model as a NEURON mechanism, freely available for download from Model DB (https://senselab.med.yale.edu/ModelDB/showmodel.cshtml?model=3815). For all simulations, we use the parameters

$$\tau_d = 270\text{ms}, \tau_f = 40\text{ms}, U = 0.28$$

in the TM model. We obtained this parameter set by fitting the TM model response to recorded EPSP amplitudes evoked via thalamocortical stimulation of RSG LR cells with a 10 Hz pulse train (Figures 3-2 & 3-7). This was accomplished by searching parameter space exhaustively for the parameter set minimizing a least-squares loss function. The resultant TM dynamics were moderately depressing, in accordance with the experimental results. Non-depressing synapses were modeled as standard exponential synapses with instantaneous rise time.

3.5.4c Modeling the postsynaptic LR population

We model the postsynaptic LR cell using the morphologically detailed model originally presented in Brennan et al. (2020). This model, implemented in NEURON (Carnevale and Hines, 2006), consists of Hodgkin-Huxley conductances representing a

fast sodium current, a delayed rectifier potassium current, and a Kv1.1-mediated slow potassium current. We place each HD input → LR synapse at a random location on a distal apical dendrite of the LR cell; varying this synaptic placement does not qualitatively change results (data not shown).

PA Distribution of a Postsynaptic Cell

Each postsynaptic cell receives input from N presynaptic HD cells, each of which has a unique PA. When studying postsynaptic speed coding, we initially drew the PA of each HD cell uniformly at random from $[0,2\pi]$. Later on, we examined the effect of introducing nonuniform PA distributions. In this case, we assumed that the PA distribution of each LR cell was continuous as a function of angle, and thus modeled the PA distribution probability densities randomly as resulting from Brownian bridge processes (to ensure 2π-periodicity of the density). We then used inverse transform sampling to draw from the generated distributions.

3.5.4d Data analysis

To quantify the extent to which postsynaptic activity reflects head turning speed, we utilized two similarity measures M: Pearson correlation and mutual information. In fact, we used the time-lagged counterparts of these measures: for a pair of time series x_t, y_t, their l-lagged similarity measure is $M(x_t, y_{t-l})$. Varying l, we obtain the cross-correlation and cross-mutual information between the two variables. Throughout the paper, when referring to an instance of measure M between time series x_t, y_t, we either report the function $l \mapsto M(x_t, y_{t-\ell})$ or just the maximum value of the function

$$\max_l M(x_t, y_{t-l})$$

In order to compute mutual information, we discretized the time series for head turning speed and postsynaptic firing rate into 40 bins each and calculated the mutual information between these discrete proxies.

3.5.5 Mean-Field Model Analysis

In order to better understand the observed speed tuning effects, we study an analytically tractable mean-field model of the simulation circuit. We show for this model that the aggregate postsynaptic activity does indeed reflect head turning speed – in fact, at low speeds it is proportional to the squared head speed. Moreover, we show that anticipatory firing compensates for lag introduced by the depression recovery timescale, enabling sharper and lower latency speed encoding. Finally, we briefly comment on model predictions when the HD synaptic input exhibits facilitating or combined facilitating-depressing dynamics.

Let $\theta_T(t)$ denote the true head direction at time t. For our mean-field analysis, we model all HD cells sharing preferred angle (PA) θ as a lumped subpopulation, whose firing rate at time t is given by $r(\theta, t) = f\big(\theta - \theta_T(t)\big)$ for the tuning curve function

$$f(\theta) = \big(f_{max} - f_{bg}\big) \cdot 1_{(-\epsilon,\epsilon)}(\theta) + f_{bg}$$

(Equation 3-1)

where 1_I denotes the indicator function of the interval I. Note that this is not the same tuning function as utilized in simulations; here, the subpopulation of HD cells with PA θ is active precisely at times t when the current head direction $\theta_T(t)$ is within ϵ of θ. This simplification, in which HD cell tuning curves are discontinuous step functions rather

than continuous Gaussians, gives qualitatively analogous results to the Gaussian case (data not shown). In the mean-field model, we further assume the background firing rate f_{bg}, maximum firing rate f_{max}, and tuning curve width ϵ are constants independent of θ.

The synapses follow simplified Tsodyks-Markram (TM) dynamics (Tsodyks et al., 1998), in which the dynamical quantities represent population-averaged values of the standard TM synaptic variables (see *Methods* for details of the standard TM model) over all synapses corresponding to HD cells having a particular θ. In what follows, we explicitly model synaptic depression only, although similar equations describe the full TM model with combined depression and facilitation. Thus, we are interested in the quantity $x(\theta, t)$, representing the average value of the depression variable x for all synapses corresponding to HD cells with PA θ, at time t. The dynamics of x are given by the equation:

$$\frac{dx(\theta,t)}{dt} = \frac{1 - x(\theta,t)}{\tau} - Ux(\theta,t)r(\theta,t)$$

(Equation 3-2)

Here τ denotes the time constant of recovery from depression, and U represents the synaptic release probability. When $x(\theta, t) \approx 0$, the HD cells with PA θ are very depressed; when the firing rate $r(\theta, t)$ lets up, x recovers to its steady-state value of 1. Similarly, $g(\theta, t)$ denotes the average conductance of all synapses corresponding to HD cells with PA θ, at time t. We consider the limit in which the timescale of synaptic decay is much shorter than the depression recovery timescale τ, and thus we can make the approximation $g(\theta, t) = x(\theta, t) \cdot r(\theta, t)$.

Now, let $p(\theta)$ denote the density function of the presynaptic PA distribution. We are interested in dynamics of the θ-averaged quantities

$$\overline{x}(t) = \int_0^{2\pi} x\,(\theta, t)p(\theta)d\theta$$

$$\overline{g}(t) = \int_0^{2\pi} g\,(\theta, t)p(\theta)d\theta$$

(Equation 3-3)

In particular, $\overline{g}$ is proportional to the sum of g over all θ, i.e. the total conductance of the postsynaptic cell, and thus reflects the activity level of the postsynaptic cell.

Equation for Dynamics of $\overline{g}$

In this section, we derive an explicit equation for the dynamics of $\overline{g}$ in the limit of low background firing ($f_{bg} \to 0$). Crucially, the choice of step function tuning enables us to close the relevant system of ODEs to obtain low-dimensional dynamics. Although we will not study this case in any further depth, we note that when f_{bg} is nonneglible, the quantities $\overline{x}$ and $\overline{g}$ form a coupled planar system.

Proposition. *In the limit of low background firing ($f_{bg} \to 0$), the mean synaptic conductance $\overline{g}$ satisfies the equation*

$$\frac{d\overline{g}}{dt} = \frac{b_g(t) - \overline{g}}{\tau_g} + f_{max}\acute{\theta}_T(t)\alpha(t)$$

(Equation 3-4)

where

$$\alpha(t) = x(\theta_T(t) + \epsilon, t)p(\theta_T(t) + \epsilon) - x(\theta_T(t) - \epsilon, t)p(\theta_T(t) - \epsilon)$$

(Equation 3-5)

$$b_g(t) = \frac{\overline{r}(t)}{1 + \tau U f_{max}}$$

(Equation 3-6)

and

$$\tau_g = \frac{\tau}{1+\tau U f_{max}}$$

with $\overline{r}$ *defined as the average firing rate of a presynaptic HD cell at time* t*, i.e.*

$$\overline{r} = \int_0^{2\pi} r(\theta, t)p(\theta)d\theta = \left(f_{max} - f_{bg}\right)\int_{\theta_T(t)-\epsilon}^{\theta_T(t)+\epsilon} p(\theta)d\theta + f_{bg}$$

Proof. From the defining equation (Equation 2) for x, we see that $\overline{x}$ satisfies

$$\frac{d\overline{x}}{dt} = \frac{1-\overline{x}}{\tau} - U\overline{g}$$

We have for fixed θ that

$$\frac{dg}{dt} = \frac{dx}{dt}r + \frac{dr}{dt}x = \frac{r-g}{\tau} - Uxr^2 + x\frac{dr}{dt}$$

For our specific choice of step function r, we have $r^2 = \left(f_{max} + f_{bg}\right)r - f_{max}f_{bg}$. Setting $C = f_{max} + f_{bg}$ and $D = f_{max}f_{bg}$, we thus have

$$\frac{dg}{dt} = \frac{r-g}{\tau} - UCxr + UDx + x\frac{dr}{dt} = \frac{r-g}{\tau} - UCg + UDx + x\frac{dr}{dt}$$

Now averaging over θ gives

$$\frac{d\overline{g}}{dt} = \frac{\overline{r}-\overline{g}}{\tau} - UC\overline{g} + UD\overline{x} + \int_0^{2\pi} x\,p\frac{dr}{dt}d\theta = \frac{\overline{r}/(1+\tau UC) - \overline{g}}{\tau/(1+\tau UC)} + UD\overline{x} + \int_0^{2\pi} x\,p\frac{dr}{dt}d\theta$$

Setting $b_g = \overline{r}/(1+\tau UC)$ and $\tau_g = \tau/(1+\tau UC)$, we can rewrite this as

$$\frac{d\overline{g}}{dt} = \frac{b_g - \overline{g}}{\tau_g} + UD\overline{x} + \int_0^{2\pi} x\,p\frac{dr}{dt}d\theta$$

$$\frac{dr}{dt} = -\dot{\theta}\frac{dr}{d\theta} = -E\dot{\theta}\left(\delta(\theta - \theta_T(t) + \epsilon) - \delta(\theta - \theta_T(t) - \epsilon)\right)$$

where δ denotes the Dirac delta function and $E = f_{max} - f_{bg}$. It follows that

$$\int_0^{2\pi} x\, p \frac{dr}{dt} d\theta = E\dot{\theta}\big(x(\theta_T(t)+\epsilon,t)p(\theta_T(t)+\epsilon) - x(\theta_T(t)-\epsilon,t)p(\theta_T(t)-\epsilon)\big) = E\dot{\theta}\alpha$$

Now setting $f_{bg} = 0$ gives the proposition.

Analyzing Contributions to $\overline{g}$

In the $f_{bg} \to 0$ limit, the mean conductance $\overline{g}$ is driven by fluctuations in $\dot{\theta}\alpha$, between which it relaxes to the value b_g with time constant τ_g. Accordingly, to understand the behavior of $\overline{g}$ we should study the behavior of b_g and α. For all of what follows, we assume $f_{bg} = 0$.

Baseline Activity: b_g

When $\dot{\theta}_T = 0$, i.e. the true head direction is not changing, we have $\overline{g} = b_g$ following a transient. Thus, we can interpret b_g as the baseline activity level of the postsynaptic cell. In the case $p(\theta) = 1/(2\pi)$, i.e. that of a uniform presynaptic PA distribution, the baseline activity b_g is constant in time, since

$$b_g \propto \overline{r} \propto \int_{\theta_T(t)-\epsilon}^{\theta_T(t)+\epsilon} p\,(\theta) d\theta = \frac{\epsilon}{\pi}$$

by (Equation 6). On the other hand, if $p(\theta)$ is nonuniform, then the integral defining $\overline{r}$ is not constant in time, taking larger values when $\theta_T(t)$ is at angles around which the PA distribution p has more mass. Since $b_g \propto \overline{r}$, b_g exhibits the same effect, thereby explaining the observed modulation of baseline firing rate by head direction.

Contribution of Depression: α

We now assume in all of what follows that the PA distribution is uniform, i.e. $p(\theta) = 1/(2\pi)$. In this case, the function α reduces to

$$\alpha(t) = \frac{1}{2\pi}\big(x(\theta_T(t)+\epsilon,t) - x(\theta_T(t)-\epsilon,t)\big)$$

We can interpret α as the contribution of synaptic depression to $\overline{g}$, since it is the only term in the equation for $\overline{g}$ that incorporates any effect of the depression variable x. To understand the behavior of α, we differentiate to obtain

$$\frac{d\alpha}{dt} = \acute{\theta}_T \beta - \frac{\alpha}{\tau_\ell}$$

(Equation 3-7)

where $\beta(t) = x_\theta(\theta_T(t) + \epsilon, t) - x_\theta(\theta_T(t) - \epsilon, t)$ and

$$\tau_\ell = \frac{\tau}{1+\tau U f(\epsilon)}$$

(Equation 3-8)

Note that for our step function tuning, $f(\epsilon)$ is not actually defined. However, we can treat f as if it is continuous at ϵ. One way to justify this is to imagine f has been replaced with a continuous function h that is close to f in the sense that

$$\max_{x\in[0,2\pi]} |f(x) - h(x)|$$

is small; it is always possible to make this quantity arbitrarily small with a suitable choice of continuous h.

The equation above further reduces the problem of understanding α to that of understanding β, which distorts the velocity information $\acute{\theta}_T$ appearing in (Equation 7). To proceed, we make the approximation $\beta(t) \approx M$, where $M > 0$ is the time-average of β. This approximation will be valid if β is typically positive and not too variable about its mean. Indeed, at each moment t in time, we have a depression profile $\theta \mapsto x(\theta, t)$ describing, for PA $\theta \in$, the average depression of synapses from the HD subpopulation having PA θ. The graph of this profile has a well-like shape, centered close to $\theta_T(t)$. At low speeds, the slope $x_\theta(\theta_T(t) + \epsilon, t)$ will be positive, and the slope $x_\theta(\theta_T(t) - \epsilon, t)$ will

be negative; it follows that the difference β is itself typically positive, becoming smaller only during high speed head turns. For now, we assume β also has low variability, and that therefore the approximation $\beta \approx M$ holds; later on, we will discuss the validity of this assumption. Continuing with the approximation, we have the simplified equation

$$\frac{d\alpha}{dt} = M\acute{\theta}_T - \frac{\alpha}{\tau_\ell}$$

(Equation 3-9)

It follows that α tracks the variable $M\acute{\theta}_T$, i.e, we have the approximate relation $\alpha \propto \acute{\theta}_T$. Since $\overline{g}$ is driven by the product $\acute{\theta}_T\alpha$, it follows that approximately $\acute{\theta}_T\alpha \propto \acute{\theta}_T^2$. Thus, when the approximation for β is valid, we conclude the postsynaptic conductance $\overline{g}$ is proportional to the square of angular head speed.

However, these proportionality relations are only approximate, and are degraded by the integration times τ_ℓ in (Equation 9) and τ_g in (Equation 4). In the next section, we will see that anticipatory firing compensates for these lags and sharpens speed coding.

Anticipatory Firing Improves Speed Coding

As mentioned above, the lags τ_ℓ and τ_g degrade the approximate relation $\overline{g} \propto \acute{\theta}^2$. Indeed, as shown in Figure 3-10, at ATI = 0 the postsynaptic activity is not especially informative about head speed, relative to the ATI = 50 ms and ATI = 100 ms cases. Intuitively, a positive ATI compensates for these lags; to make this statement precise, we note the following lemma, for which we omit the straightforward proof.

Lemma. *Let F be a differentiable function with $F(0) = 0$. If $C = \tau$, then the solution y to the initial value problem $\frac{dy}{dt} = F(t) + CF'(t) - \frac{y}{\tau}\, y(0) = 0$ has the property that $y(t) = \tau F(t)$ following a transient (more precisely, $y - \tau F \to 0$ exponentially fast as $t \to \infty$)*

Recall that introducing an ATI of A ms is equivalent to replacing the true angular trajectory $\theta_T(t)$ with the effective trajectory $\theta_A(t) = \theta_T + A\acute{\theta}_T$. Applying the lemma to (Equation 9) with $C = A = \tau_\ell$ and $F = \theta_T$, we see that when the ATI equals τ_ℓ ms, the relation $\alpha \propto \acute{\theta}_T$ becomes *exact* (with a proportionality constant $M\tau_l$). Moreover, in this case, the equation for $\overline{g}$ simplifies to

$$\frac{d\overline{g}}{dt} = \frac{b_g - \overline{g}}{\tau_g} + f_{max}\acute{\theta}_A\alpha = \frac{b_g - \overline{g}}{\tau_g} + f_{max}M\tau_\ell\left(\acute{\theta}_T + A\acute{\theta}_T\right)\cdot\acute{\theta}_T$$

Since we have assumed $p(\theta)$ is uniform, and hence b_g is constant in time, we can apply the lemma again taking $F(t) = \left(b_g/\tau_g\right) + f_{max}C\tau_\ell\acute{\theta}_T^2$. If we assume $C = A = 2\tau_g$, then there is the exact equality

$$\overline{g} = b_g + f_{max}M\tau_\ell\tau_g\acute{\theta}_T^2$$

Thus, the condition for exact speed coding is

$$A = \tau_\ell = 2\tau_g$$

Finally, we note that in (Equation 8), the most parsimonious assumption to make is that $f(\epsilon) \approx f_{max}/2$; this amounts to assuming we have replaced the step function tuning f with a continuous function $\acute{f}$ whose steepest portions are centered at ϵ and $-\epsilon$. It follows that indeed $\tau_\ell \approx 2\tau_g$, and therefore it is possible to be in the regime of exact speed coding. This analysis shows that the ATI optimizing speed coding in our model is $2\tau_g$. For the parameter set used in simulations ($\tau = 270$ ms, $U = 0.28$, $f_{max} = 0.07$ spikes/ms), we find that

$$\tau_g = \frac{\tau}{1 + \tau U f_{max}} \approx 43\text{ms}$$

Accordingly, the optimal ATI is $2\tau_g \approx 86\text{ms}$. Indeed, simulations utilizing the above parameter set and step-function tuning curves exhibit optimal speed coding at an ATI of precisely 85 ms, thereby validating the analysis (Supplemental Figure 3-6S).

Scaling of Postsynaptic Activity with Speed

As mentioned earlier, validity of the approximation $\beta(t) \approx M$ depends on the variability of β about its mean. When this approximation is valid, we have the scaling $\overline{g} \propto \acute{\theta}_T^2$. Before describing the empirical validity of this approximation, we first note that even when β is fairly variable, the function α remains strongly correlated with $\acute{\theta}_T$, and consequently the analysis of ATI in the previous section remains approximately valid. Indeed, in the case of step-function tuning, we find that β is actually fairly variable (CV = 0.6), but postsynaptic activity is still very strongly correlated with speed at the optimal ATI computed by the formula above (Supplemental Figure 3-8S). However, the distortion by β of the velocity information in α results in a speed-postsynaptic activity relation whose best-fit power law exponent is approximately 1.5-1.7, instead of the predicted value of 2. Thus, for step function tuning, the quadratic scaling does not hold.

On the other hand, for Gaussian tuning curves, the approximation $\beta(t) \approx M$ is valid. Although the above derivations have assumed step-function tuning, we may heuristically imagine that the equations are approximately valid even with Gaussian tuning, for some suitable choice of tuning curve width ϵ. Proceeding as such, we find that with Gaussian tuning, β is relatively invariable about its mean (CV = 0.2), especially for low head speeds. We note that the tuning curve shape directly affects the shape of the depression profile $\theta \mapsto x(\theta, t)$, and consequently affects the variability of β. This suggests that for low speeds and Gaussian tuning, the scaling $\overline{g} \propto \acute{\theta}_T^2$ will be accurate.

Mean-field simulation results do yield that for low speeds, the best-fit power law exponent is approximately 1.9-2.1.

This raises the question of whether this scaling is observable in data from simulations of our spiking model, since spiking simulations utilize the Gaussian tuning, which is more accurate to the experimentally observed shape of HD cell tuning curves. We fit results from the spiking model (postsynaptic firing rates binned by head speed) to a power law when including data points in the speed-firing rate curve only up to y deg/s, for varying values of y (Supplemental Figure 3-7S). We found that best-fit residuals were lowest for low speeds and that the best-fit exponents plateaued in a neighborhood of 2 before falling off as the considered range of speeds widened, suggesting that the approximate quadratic scaling is likely to be visible in experimental data in this circuit and others utilizing the same synaptic-depression-based mechanism for computing rate of change.

3.5.6 Data and Software Availability

The LR neuron model utilized here is available on ModelDB (***https://modeldb.yale.edu/260192***), and the implementation of the Tsodyks-Markram model utilized here is also available from ModelDB (https://senselab.med.yale.edu/ModelDB/showmodel.cshtml?model=3815). Reconstructions will be available at ***http://neuromorpho.org/KeywordSearch.jsp*** and can be found by searching for the “Ahmed” archive.

3.6 Acknowledgements

We would like to thank Scott Cruikshank, Roger Albin, and Clare Weiland for their comments on the manuscript, Vaughn Hetrick for his technical assistance, Michael Roberts for his help with the NeuroLucida software, Victoria Booth for her assistance with the modeling work, and Danny Siu for his assistance with MATLAB-based analyses. This work was supported by lab startup funds from the University of Michigan, a grant from the Whitehall Foundation, NIH grant NS121745, and pilot funds from the NIH/NIA funded Michigan Alzheimer's Disease Research Center 5P30AG05376 to OJA, as well as NIH T-32-NS076401 and NSF graduate research fellowship to EKWB.

3.7 Author Contributions

Conceptualization, Dr. Omar J Ahmed, Ellen KW Brennan, Izabela Jedrasiak-Cape, Sameer Kailasa; Methodology, Dr. Omar J Ahmed, Ellen KW Brennan, Izabela Jedrasiak-Cape, Sameer Kailasa; Investigation, Ellen KW Brennan, Izabela Jedrasiak-Cape, Sameer Kailasa; Software, Sameer Kailasa, Dr. Shyam Kumar Sudhakar, Izabela Jedrasiak-Cape, Ellen KW Brennan, Dr. Omar J Ahmed; Formal Analysis, Ellen KW Brennan, Izabela Jedrasiak-Cape, Sameer Kailasa; Visualization, Ellen KW Brennan, Izabela Jedrasiak-Cape, Sameer Kailasa, Dr. Omar J Ahmed; Writing – Original Draft, Ellen KW Brennan, Dr. Omar J Ahmed; Writing – Review & Editing, Dr. Omar J Ahmed, Ellen KW Brennan, Izabela Jedrasiak-Cape, Sameer Kailasa; Funding Acquisition, Dr. Omar J Ahmed; Supervision, Dr. Omar J Ahmed.

3.8 Supplemental Figures and Tables

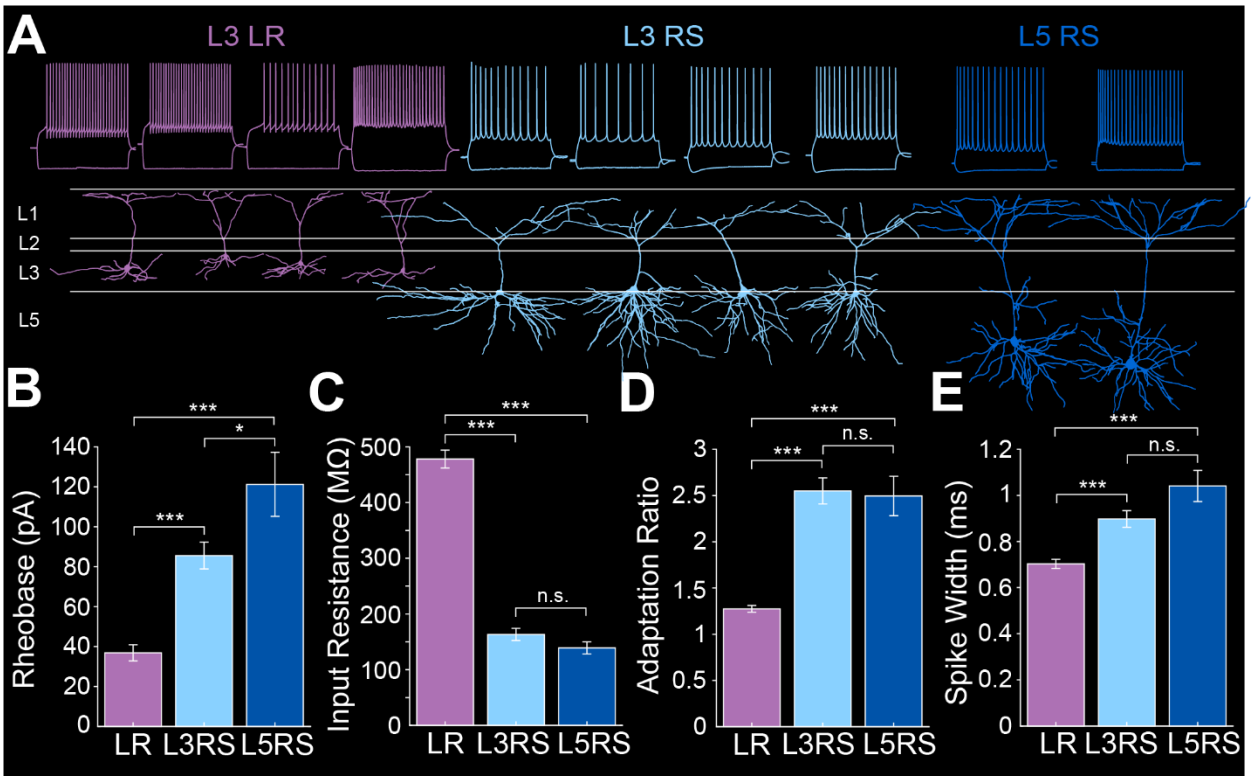

Supplemental Figure 3-1S. Intrinsic properties of RSG layer 3 LR, layer 3 RS, and layer 5 RS neurons.

- ***A.*** Top row shows intrinsic firing properties of layer 3 low-rheobase (LR) neurons (purple), layer 3 regular-spiking (RS) neurons (light blue), and layer 5 RS neurons (dark blue). Bottom row shows the matching reconstructions.
- ***B.*** Average rheobase for LR, L3 RS, and L5 RS neurons. Note the significantly lower rheobase in LR neurons compared to L3 RS (p = 1.24e-17; Wilcoxon rank sum test) and L5 RS (p = 9.33e-12; Wilcoxon rank sum test) neurons. Rheobase of L3 and L5 RS neurons significantly differs (p=0.0312; Wilcoxon rank sum test).
- ***C.*** Average input resistance (IR) for LR, L3 RS, and L5 RS neurons. Note the significantly larger IR in LR neurons compared to L3 RS (p = 1.31e-26; Wilcoxon rank sum test) and L5 RS cells (p = 3.07e-18; Wilcoxon rank sum test).
- ***D.*** Average adaptation ratio for LR, L3 RS, and L5 RS neurons. Note the significantly lower adaptation ratio in LR cells compared to L3 RS (p=2.94e-24; Wilcoxon rank sum test) and L5 RS cells (p=6.24e-15; Wilcoxon rank sum test).
- ***E.*** Average spike half-width for LR, L3 RS, and L5 RS neurons. Note the significantly narrower spike width in LR neurons compared to L3 RS (p = 3.71e-06; Wilcoxon rank sum test) and L5 RS cells (p = 1.25e-06; Wilcoxon rank sum test), while L3 and L5 RS cells do not differ (p = 0.0914; Wilcoxon rank sum test). Error bars are SEM for all.

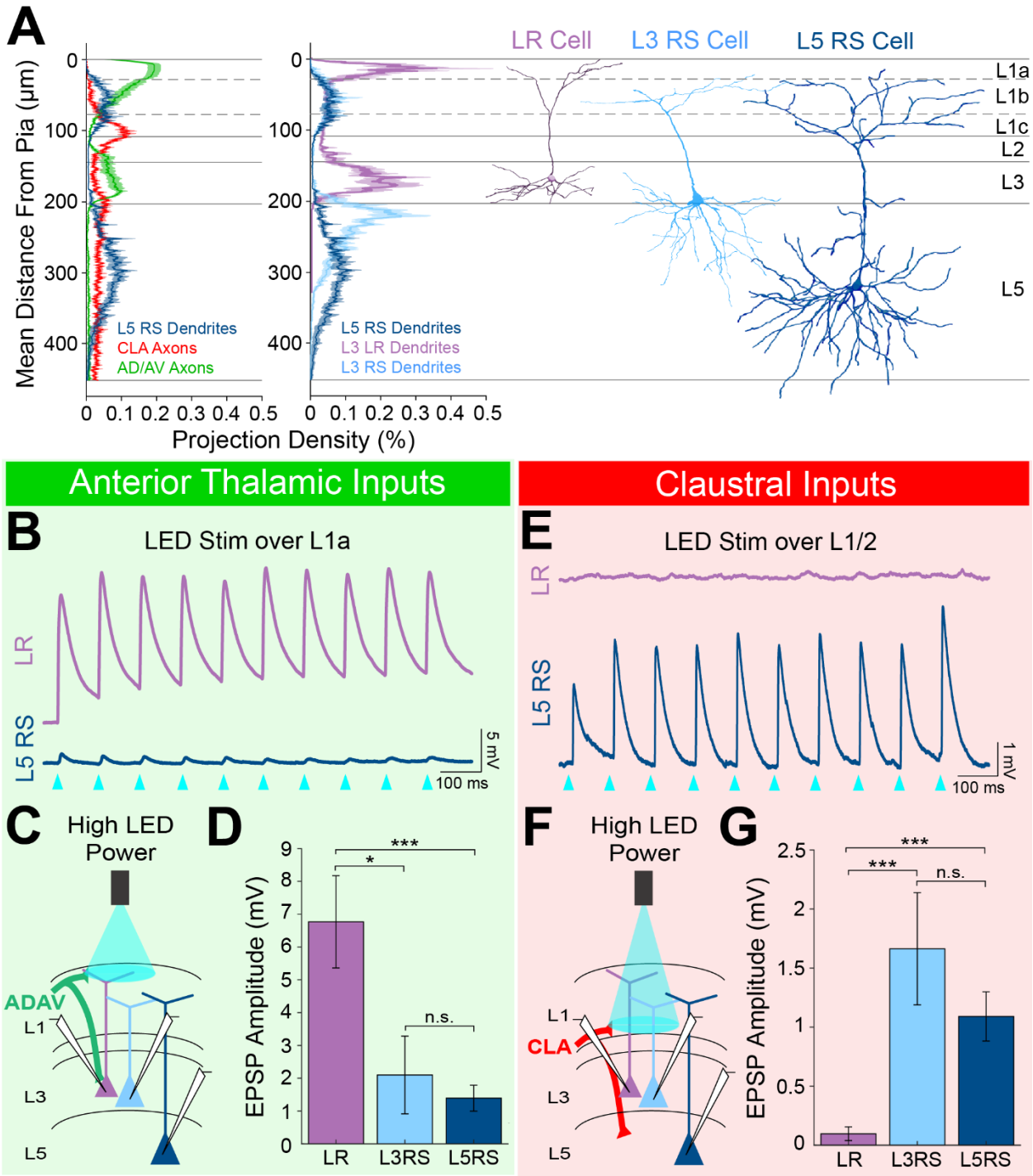

Supplemental Figure 3-2S. LR neuron responses to anterior thalamic and claustral inputs differ significantly from those of L5 RS cells.

A. Left: Projection density plot of ADAV arbors (green, n = 5), CLA arbors (red, n = 6), and L5 RS neuron dendrites (navy, n = 5). Right: Projection density plot of LR (purple, n = 10), L3 RS (light blue, n = 5), and L5 RS neuron dendrites (navy, n = 5) showing an overlap in apical dendrites between L3 RS and L5 RS cells. Plots

are mean ± SEM shaded. Representative reconstructions of LR (purple), L3 RS (blue), and L5 RS (navy) neurons are aligned in the cortical layers.

B. Trace example of a simultaneously patched LR (purple) and L5RS (navy) neuron pair showing responses to 10 Hz train of 1 ms wide optogenetic LED pulses. Blue triangles indicate each LED pulse. Cells were held at -65 mV.

C. Schematic showing TC inputs from ADAV to patched LR, L3 RS, and L5 RS neurons. LED stimulation is focused on L1a.

D. Bar graph of the population data for LR, L3 RS, and L5 RS neuron responses to TC input at L1a. LR responses are significantly larger than both L3 RS and L5 RS, while L3 RS and L5 RS responses do not differ. LR vs L3 RS: $p = 0.0185$, LR vs L5 RS: $p = 0.00072$, L3 RS vs L5 RS: $p = 0.9335$; Wilcoxon rank sum test. Error bars are SEM.

E. Trace example of a same-slice sequential pair of LR (purple) and L5RS (navy) neurons showing responses to 10 Hz train of 1 ms wide optogenetic LED pulses. Blue triangles indicate each LED pulse. Cells were held at -65 mV.

F. Schematic showing CLA inputs to patched LR, L3 RS, and L5 RS neurons. LED stimulation is focused on L1/2 boundary.

G. Bar graph of the population data for LR, L3 RS, and L5 RS neuron responses to CLA input at L1/2. LR responses are significantly smaller than both L3 RS and L5 RS, while L3 RS and L5 RS responses do not differ. LR vs L3 RS: $p = 0.00000353$, LR vs L5 RS: $p = 0.00000233$, L3 RS vs L5 RS: $p = 0.7989$; Wilcoxon rank sum test. Error bars are SEM.

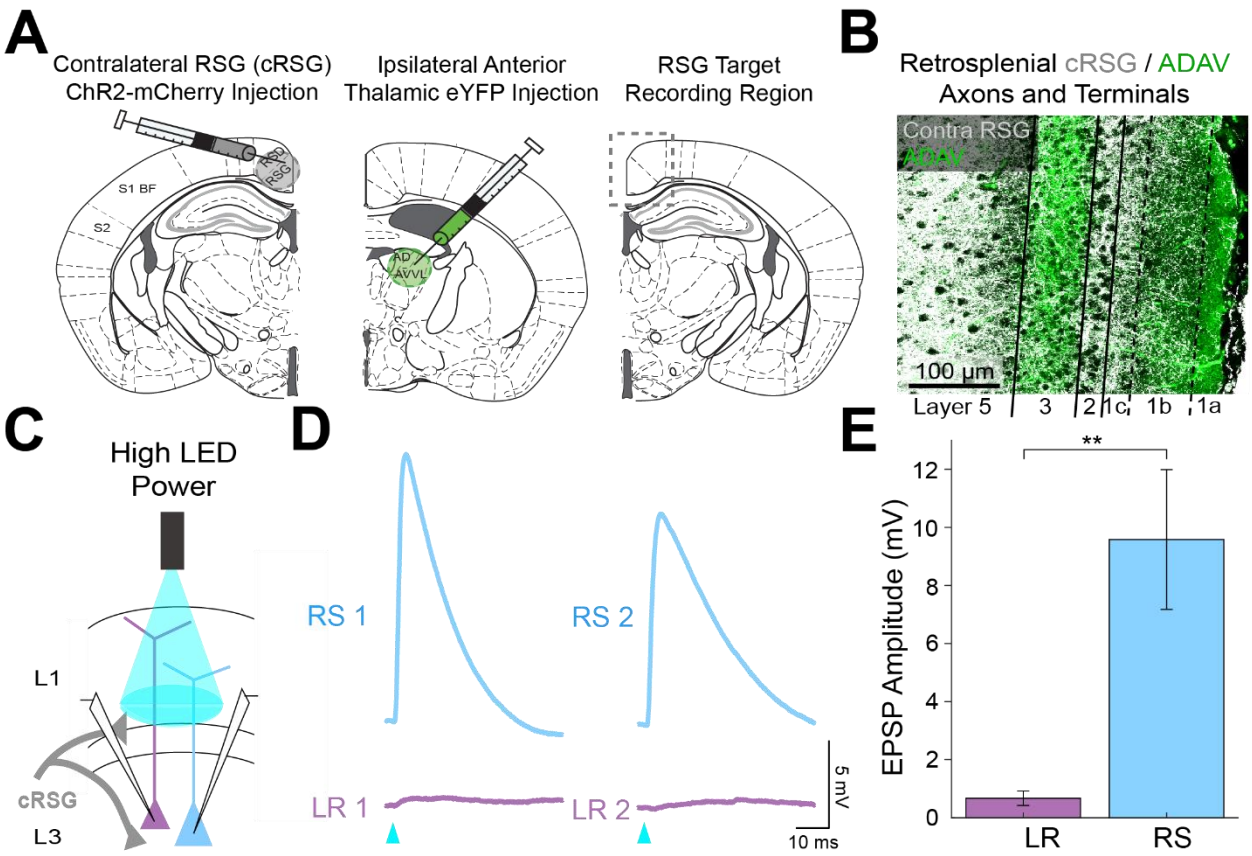

Supplemental Figure 3-3S. Contralateral RSG projections drive RS, but not LR, neurons.

- ***A.*** Left: Schematic of contralateral RSG (cRSG) ChR2-mCherry injection (opposite hemisphere compared to recordings). MCherry is pseudo colored as grey. Middle: Schematic of ipsilateral ADAV eYFP injection (same hemisphere as recordings). Right: Schematic of target recording region in RSG.
- ***B.*** Confocal image of dual-injection expression with cRSG axons and terminal arbors in grey and ADAV axons and terminal arbors in green. Layers are demarcated by black lines. Note the precise targeting of L1c, L2, and L5 by cRSG axons and terminal arbors (grey) in contrast to the L1a and L3 targeting of anterior thalamic arbors (green).
- ***C.*** Schematic showing cRSG inputs to patched LR and RS neurons being stimulated at L1/2 boundary.
- ***D.*** Example traces of two sequential pairs of RS (blue) and LR (purple) neuron responses to the high power LED pulse.
- ***E.*** Significantly larger EPSP amplitudes in RS (n = 5) cells compared to LR (n = 7) cells (p = 0.0051; Wilcoxon rank sum test). Error bars are SEM.

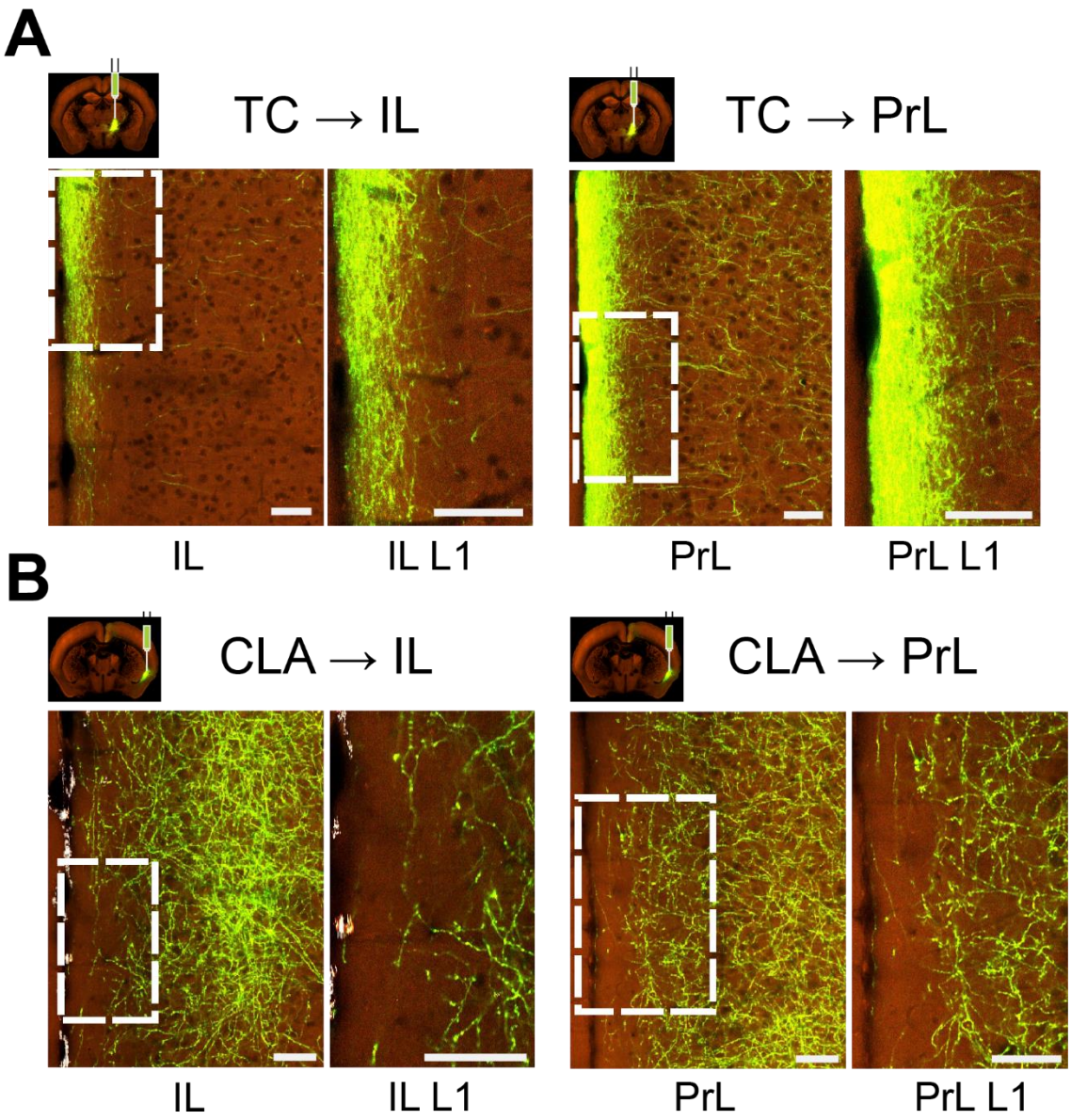

Supplemental Figure 3-4S. Sublaminar differences in thalamic vs claustral projections to medial prefrontal cortex. Each panel shows overview of expression in a cortical area (left) and its layer 1 (right), with images obtained from the Allen Mouse Brain Connectivity Atlas (https://connectivity.brain-map.org; Oh et al., 2014). The following images, as numbered in high resolution image viewer, were used: for TC, ventromedial nucleus (VM; experiment #127797441), image #69 for injection and #36 for PrL/IL; for CLA (experiment #485903475), image #56 for injection and #31 for PrL/IL. Abbreviations: PrL - prelimbic cortex and IL - infralimbic cortex. Scale bar is 70 μm.

- ***A.*** Axonal projection expression in infralimbic and prelimbic cortices from anterograde injection into ventromedial thalamus. Projections show strong preference for superficial parts of layer 1.
- ***B.*** Axonal projection expression in infralimbic and prelimbic cortices from anterograde injection into claustrum. Higher density of projections can be observed at deep layer 1, while very few axons reach superficial-most parts.

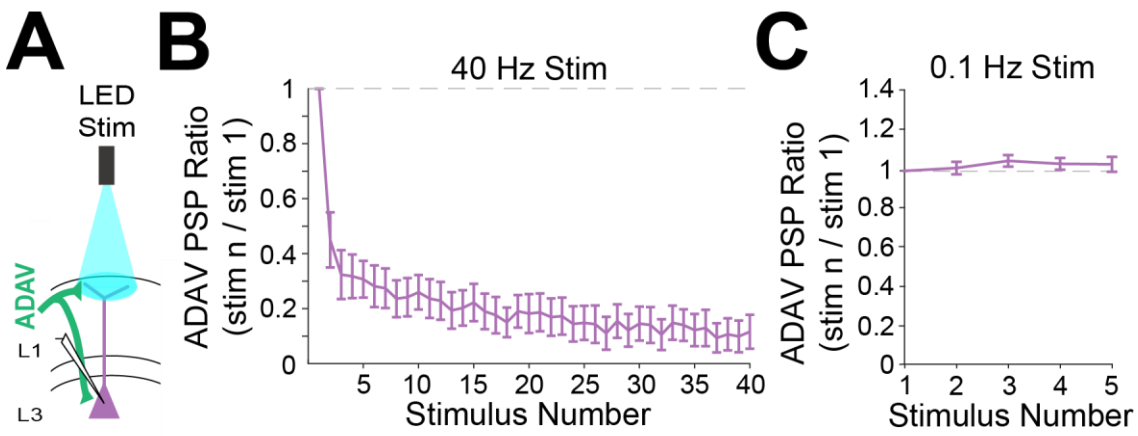

Supplemental Figure 3-5S. Anterior thalamic inputs to LR neurons are strongly depressing at higher frequencies.

- ***A.*** Schematic showing anterior thalamic (ADAV) inputs to a patched LR neuron. Thalamic axons and terminal arbors are being stimulated by the LED at L1a.
- ***B.*** Group synaptic dynamics for LR neurons (n = 8) in response to 40 Hz ADAV inputs show synaptic depression.
- **C.** Group synaptic dynamics for LR neurons (n = 9) in response to 0.1 Hz ADAV inputs do not show synaptic depression.

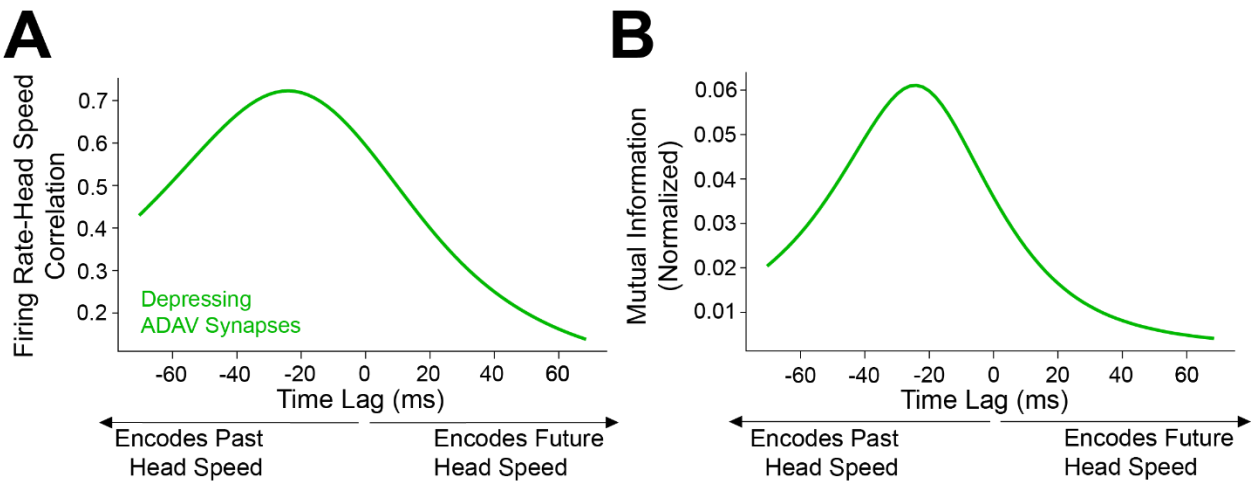

Supplemental Figure 3-6S. Angular head speed coding by LR cells is robust regardless of presynaptic thalamic head direction cell count.
Speed tuning of postsynaptic LR cells is robust to the number of inputs they receive from thalamic HD cells. In these plots, we depict the mean correlation (***A***) and MI values (***B***) of LR firing rate and head speed from simulations using only 2500 presynaptic HD inputs.

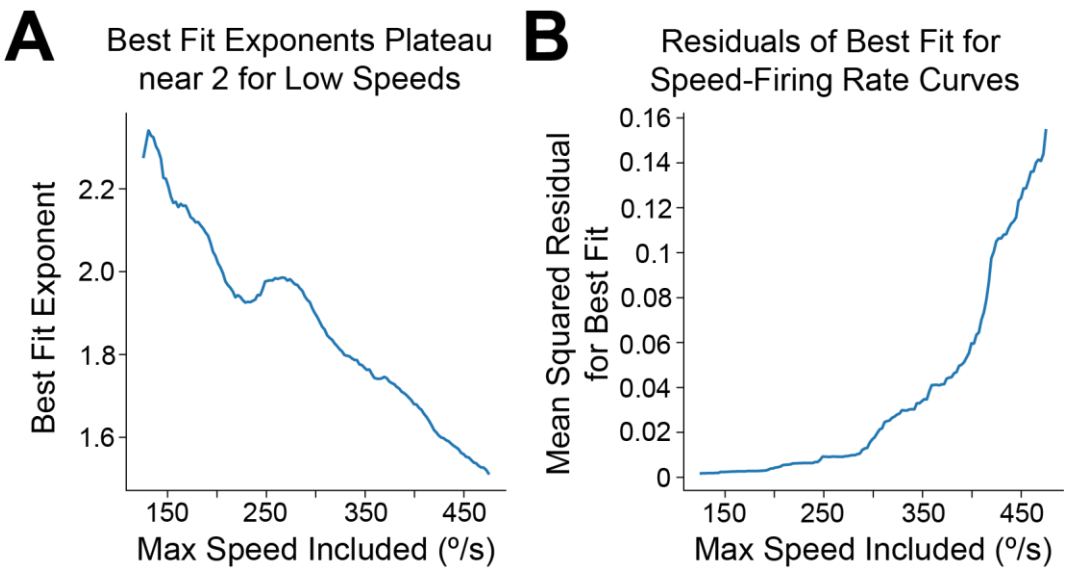

Supplemental Figure 3-7S. LR firing rate exhibits approximately quadratic scaling for low speeds.

A. Using data from the spiking simulations, we binned the speed-postsynaptic firing rate curve at high resolution (2.5 º/bin) and computed, for varying values of *y*, the best-fit power law exponent when considering only data points corresponding to speeds less than or equal to *y* deg/s. For values of *y* less than 300 deg/s, we find exponents in the range 1.8-2.2, approximately matching the analytical prediction of quadratic scaling at low speeds for Gaussian tuning curves.

B. Same as ***A*** but mean squared residuals of the best-fit power law for each value of *y*. Smallest residuals are obtained with the approximately quadratic fits for *y* less than 300 deg/s. The fits become increasingly poor when including higher speeds, suggesting that at high speeds the scaling exponent changes; this is apparent visually in Figure 3-8 C and expected from our analysis.

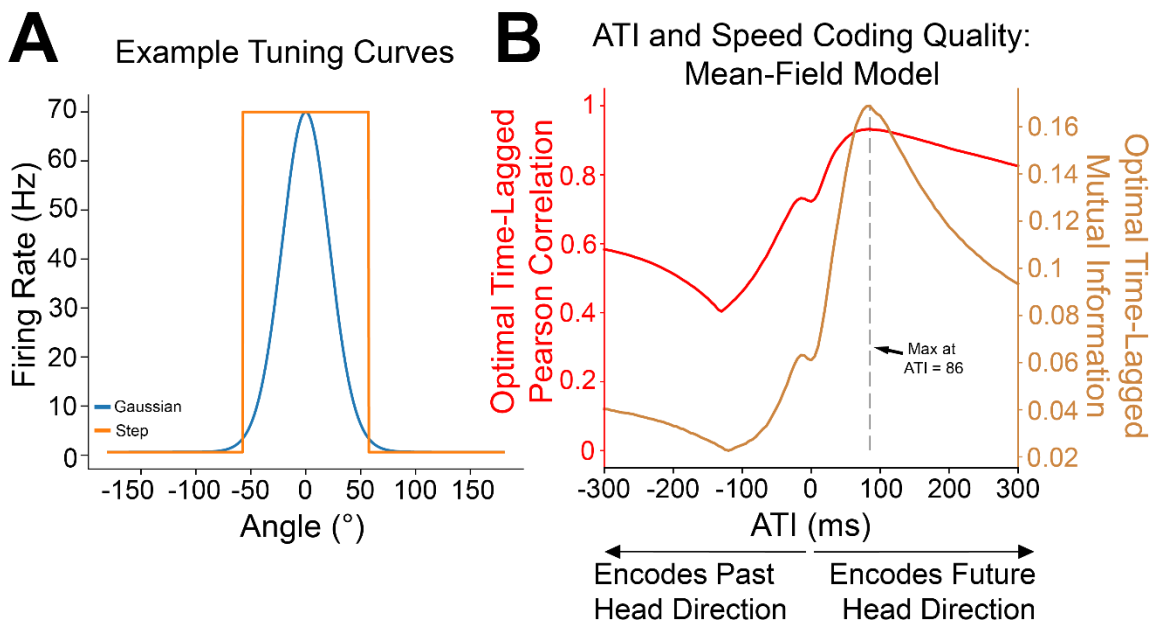

Supplemental Figure 3-8S. Analytical calculations independently confirm the improvement of head speed coding with anticipatory firing of head direction inputs.

A. Simulations utilized the continuously varying Gaussian tuning curves, but our mean-field analysis employed the more analytically tractable, but discontinuous, step-function tuning curves.

B. The mean-field model replicates the behavior observed in the spiking simulations, including improvement of postsynaptic speed coding with the introduction of anticipatory firing. Moreover, analytical calculations enabled us to compute the optimal value of anticipatory time interval (ATI) for this parameter set, which came out to 86 ms; the dotted grey line shows that mean-field simulation results indeed agree with the calculation.

Supplemental Table 3-1S. Intrinsic cell properties.

	LR	*n*	L3 RS	*n*	L5 RS	*n*
Postnatal age at time of recording (days)	**70.32** ± 3.65	*132*	**78.00** ± 6.06	*80*	**79.74** ± 7.37	*42*
Input resistance (MΩ)	**478.10** ± 16.09	*122*	**163.31** ± 10.81	*78*	**139.07** ± 10.83	*37*
Input capacitance (pF)	**32.10** ± 1.20	*122*	**95.53** ± 3.17	*78*	**107.65** ± 5.73	*37*
Membrane time constant (ms)	**14.13** ± 0.36	*122*	**13.78** ± 0.52	*78*	**13.42** ± 0.75	*37*
Action potential threshold (mV)	**-40.16** ± 0.33	*120*	**-40.89** ± 0.33	*78*	**-38.78** ± 0.75	*38*
Action potential amplitude (mV)	**62.97** ± 0.82	*120*	**76.77** ± 0.91	*78*	**73.16** ± 1.92	*38*
Action potential width (ms)	**0.70** ± 0.02	*120*	**0.90** ± 0.04	*78*	**1.04** ± 0.07	*38*
Spike frequency adaptation ratio	**1.27** ± 0.04	*120*	**2.55** ± 0.14	*78*	**2.50** ± 0.21	*38*
Latency to first spike (ms)	**497.90** ± 22.57	*104*	**227.54** ± 24.99	*70*	**179.11** ± 34.26	*24*
Rheobase (pA)	**36.88** ± 4.02	*104*	**85.58** ± 6.7	*70*	**121.20** ± 16.01	*24*

Supplemental Table 3-1S. Intrinsic cell properties.
Values are mean ± SEM. Ns are reported individually for each intrinsic property and cell type. All p-values for intrinsic property comparisons are reported immediately below in Supplemental Table 3-2S.

Supplemental Table 3-2S. P-values for intrinsic property comparisons across cell types.

	LR v. L3 RS p-values	LR v. L5 RS p-values	L3 RS v. L5 RS p-values
Postnatal age at time of recording (days)	0.5583	0.2345	0.5892
Input resistance (MΩ)	1.31e-26 ***	3.07e-18 ***	0.2798
Input capacitance (pF)	1.43e-30 ***	6.11e-19 ***	0.1321
Membrane time constant (ms)	0.3732	0.3506	0.7533
Action potential threshold (mV)	0.1873	0.1521	0.0250 *
Action potential amplitude (mV)	4.82e-20 ***	9.18e-07 ***	0.1742
Action potential width (ms)	3.71e-06 ***	1.25e-06 ***	0.0914
Spike frequency adaptation ratio	2.94e-24 ***	6.24e-15 ***	0.5387
Latency to first spike (ms)	4.19e-15 ***	1.37e-09 ***	0.1748
Rheobase (pA)	1.24e-17 ***	9.34e-12 ***	0.0312 *

Supplemental Table 3-2S. P-values for intrinsic property comparisons across cell types.
All p-values for statistical significance between cell types for the intrinsic properties calculated and reported in Supplemental Table 3-1S. Wilcoxon rank sum test was used for all comparisons.

Supplemental Table 3-3S. HD Cell Parameter Distributions

Beta Distribution Parameters	a	b	**Location**	**Scale**	**Mean**	**St. Dev.**
f_{max}	2	3	0	175	70	40
f_{bg}	.6	150	0	150	0.6	0.8
ATI	2	3	-10	150	50	30
ϵ	2	2	3	8	7	1.6

Supplemental Table 3-3S. Head direction cell parameter distributions. Parameter distributions for head direction cells that can be utilized with the scipy.stats.beta python function.

CHAPTER 4: Cell-Type-Specific Cholinergic Control of Persistent Activity in Retrosplenial Cortex

Izabela Jedrasiak-Cape*, Ellen KW Brennan*, & Omar J Ahmed

4.1 Abstract

Acetylcholine release is correlated with active spatial navigation. At the cellular level, cholinergic activation induces persistent firing of principal neurons in multiple regions involved in navigation, potentially helping to support path integration. The granular retrosplenial cortex (RSG) is a key region involved in spatial navigation, and it contains multiple subtypes of computationally distinct principal cells that differentially support its spatial functions, including low-rheobase (LR), regular-spiking (RS), and intrinsically-bursting (IB) neurons. However, no studies have examined the effect of acetylcholine on retrosplenial neurons. Here, we show that RS and IB neurons across all layers of RSG exhibit robust persistent firing when exposed to cholinergic agonists. In stark contrast, LR neurons do not show any features of persistent activity, suggesting a complete lack of cholinergic modulation specific to this neuronal subtype. Previous work has identified that LR neurons can encode persistent spatial inputs with high precision to conjunctively encode head direction and compute head speed, and the findings presented here suggest that the LR cells employ acetylcholine-independent

mechanisms to support such persistent encoding. Thus, unlike the majority of principal neurons in navigationally-important brain regions, retrosplenial LR neurons are likely to perform similar spatial orientation computations when animals are standing still and actively navigating.

4.2 Introduction

Acetylcholine (ACh) influences neuronal excitability, circuit dynamics, synaptic transmission and plasticity across the brain (Picciotto et al., 2012; Rasmusson, 2000; Sarter and Lustig, 2020). Cholinergic transmission is important for attention and goal-directed behaviors (Arnold et al., 2002; Hasselmo, 2006; Luchicchi et al., 2014; Sarter et al., 2014, 2005), including spatial navigation (Hamlin et al., 2013; Solari and Hangya, 2018; Stancampiano et al., 1999; Whishaw, 1985; Winkler et al., 1995; Zannone et al., 2018). To aid in successful navigation, ACh levels increase throughout brain regions involved in spatial computations (Anzalone et al., 2009; Giovannini et al., 2001; Sarter et al., 2005) to induce cortical synaptic plasticity (Kilgard and Merzenich, 1998; Pinto et al., 2013; Rasmusson, 2000; Zannone et al., 2018), increase sensitivity to behaviorally relevant cues (Parikh et al., 2007; Pinto et al., 2013; Sarter et al., 2005), and facilitate sensorimotor gating (Jin et al., 2019; Luntz-Leybman et al., 1992; Sarter et al., 2005). Indeed, blocking cholinergic transmission in areas like the hippocampus and cortex result in significantly impaired performance on spatial tasks (Berger-Sweeney et al., 1994; Hamlin et al., 2013), highlighting the key role cholinergic inputs play in navigation.

At the cellular level, ACh is known to induce persistent firing of principal neurons in spatially relevant brain regions, including the entorhinal cortex (Jochems et al., 2013; Tahvildari et al., 2007; Yoshida et al., 2008), CA1 (Knauer et al., 2013; Yamada-Hanff and Bean, 2013), CA3 (Bianchi and Wong, 1994; Jochems and Yoshida, 2013) dorsal subiculum (Kawasaki et al., 1999; Yoshida and Hasselmo, 2009), motor cortex (Rahman and Berger, 2011), anterior cingulate cortex (ACC; Ratté et al., 2018; Zhang and Seguela, 2010), primary visual and somatosensory cortices (Rahman and Berger, 2011), and prefrontal cortex (Dembrow et al., 2010; Thuault et al., 2013). In many cortical areas, cholinergic induced persistent activity is seen across layers, in both superficial (Navaroli et al., 2012; Ratté et al., 2018; Tahvildari et al., 2007; Yoshida et al., 2008; Zhang and Seguela, 2010) and deep (Egorov et al., 2002; Fu et al., 2019; Rahman and Berger, 2011; Thuault et al., 2013) pyramidal neurons, likely due to the widespread expression of cholinergic terminals across the cortical layers (Eckenstein et al., 1988; Levey, 1993; Vogt, 1984).

The basal forebrain (BF) is one of the main sources of cholinergic neurons in the brain (Mesulam et al., 1983) and sends widespread projections to the cortex to influence cortical function (Hsieh et al., 2000; Kawaguchi, 1997; Sarter et al., 2005; Sarter and Lustig, 2020; Verhoog et al., 2016). One key target of these projections is the retrosplenial cortex (RSC), a navigationally important region which receives cholinergic inputs in both superficial and deep layers from various regions of the BF (Gyengesi et al., 2013; Saper, 1984; van Groen and Wyss, 2003, 1992, 1990). The granular region of the RSC (RSG) serves as the main target of navigationally-important regions including the hippocampus (Opalka and Wang, 2020; Wyss and van Groen,

1992; Yamawaki et al., 2019b), anterior thalamus (Brennan et al., 2021; Yamawaki et al., 2019a), and dorsal subiculum (Brennan et al., 2021; Nitzan et al., 2020; Yamawaki et al., 2019a), and shows a larger increase in concentration of ACh during navigation compared to both RSD and the hippocampus (Anzalone et al., 2009), suggesting a relative increase in cholinergic modulation of spatial signaling in RSG compared to other regions. The RSG also contains multiple principal cell types (Brennan et al., 2020), including a low-rheobase neuron that receives preferential innervation from both anterior thalamic and dorsal subicular spatial inputs and has been hypothesized to simultaneously encode direction and compute head speed (Brennan et al., 2021). However, despite the convergence of multiple spatial sources onto RSG cells and the dramatic increase in ACh release within RSG during navigation, it remains unknown how ACh directly impacts the activity of RSG neurons.

Here, we used whole-cell patch clamp with pharmacology to explore the influence of cholinergic agonists on both superficial and deep layer principal neurons in RSG. We found that regular-spiking (RS) and intrinsically-bursting (IB) neurons exhibit persistent firing when exposed to cholinergic agonists, regardless of their laminar location or morphology. However, LR neurons do not exhibit any indicators of persistent activity. These results highlight cell-type-specific responses to cholinergic signaling in the RSG. Surprisingly, the neurons which selectively receive the strongest directional and spatial inputs—LR neurons—do not directly respond to cholinergic stimulation, suggesting that their spatial orientation computations are relatively consistent across brain states and independent of cholinergic release.

4.3 Results

4.3.1 Cholinergic agonists induce persistent activity in RS, but not LR, neurons in granular retrosplenial cortex

Using whole-cell patch clamp recordings, we recorded from and identified previously recognized pyramidal cell types in the granular retrosplenial cortex (RSG; Brennan et al., 2021, 2020; Yousuf et al., 2020). As in previous work (Brennan et al., 2020, 2021) the distinct cell-types were identified by their unique intrinsic, spiking, and anatomical properties: layer 3 low-rheobase (LR) neurons, layer 3 regular-spiking (L3 RS) neurons, layer 5 RS (L5 RS) neurons, and layer 5 intrinsically bursting (L5 IB) neurons. Specifically, LR neurons exhibited significantly lower rheobase, higher input resistance, and lower spike frequency adaptation ratio values compared to RS cells, and L5 IB cells displayed prominent bursts at just-threshold current injections (Figure 4-1A; Table 4-1). Sparse dendritic branching and small soma size of LR neurons also distinguished these cells from L3 RS and L5 cells (Figure 4-1A; Brennan et al., 2021, 2020).

To examine how RSG neurons may be impacted by increased cholinergic tone seen during navigation, we combined whole-cell recordings with bath application of the nonselective muscarinic receptor agonist, carbachol (CCh; 40 µM), to measure cholinergically-induced changes in neuronal activity (Figure 4-1B; see Methods). We found that 83-100% of RS and IB neurons fired persistently when exposed to CCh (Figure 4-1D-G). Responses returned to baseline upon washout of CCh. In stark

contrast, 0 out of 12 LR neurons tested fired persistently (Figure 4-1C&G). These results indicate that increased cholinergic tone differentially affects RSG neurons, such that the LR cell is the only pyramidal subtype examined in RSG layers 1-5 that does not exhibit persistent activity.

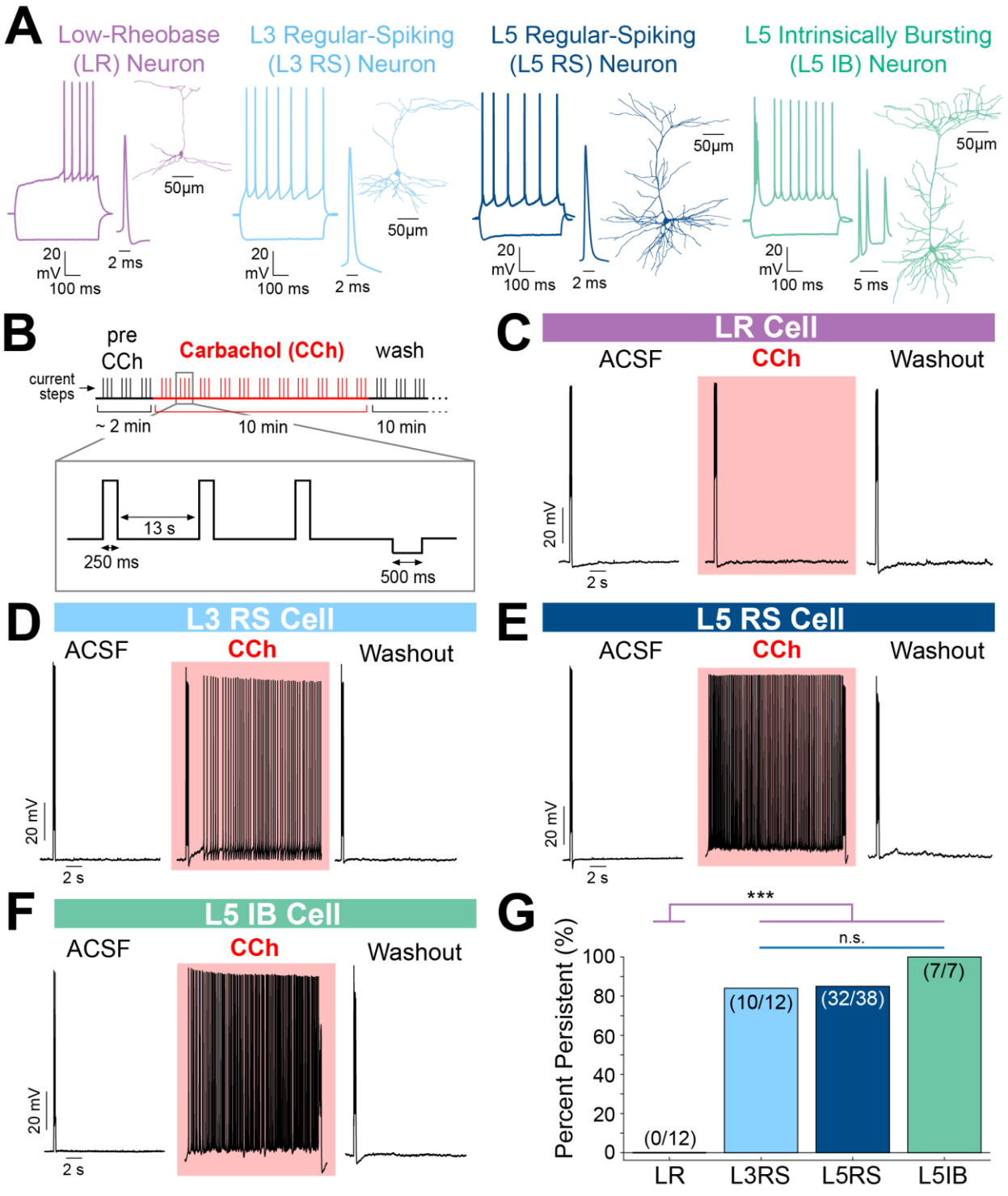

Figure 4-1. Persistent firing is a cell type-specific activity present in both superficial and deep layers of the RSG.

A. Representative reconstructions and firing properties of LR (purple; left), L3 RS (light blue; middle left), L5 RS (navy; middle right), and L5 IB (teal; right) neurons.

B. Schematic of the full recording protocol with an inset showing a single sweep. See Methods for details.

C. Responses from a representative LR neuron (shown in ***A***). Left: Baseline trace of LR activity in normal ACSF. Middle: Trace showing lack of persistent firing after 10 minutes of exposure to CCh. Right: Trace of baseline activity after washout of CCh with normal ACSF.

D. Responses from a representative L3 RS neuron (shown in ***A***). Left: Baseline trace of L3 RS activity in normal ACSF. Middle: Trace of persistent firing after 9 minutes of exposure to CCh. Right: Trace of the return baseline activity after washout of CCh with normal ACSF.

E. Same as ***D*** but for a representative L5 RS neuron in ACSF (left) and after 5 minutes exposure to CCh (middle).

F. Same as ***D*** but for a representative L5 IB neuron in ACSF (left) and after 7 minutes exposure to CCh (middle).

G. Population analysis of the percentage of neurons within each cell type that exhibited persistent firing showing a significantly smaller percentage of LR neurons fire persistently compared to the other 3 cell types (LR v L3 RS: $X^2(1, n = 24) = 17.14$, p = 3.467e-05; LR v L5 RS: $X^2(1, n = 50) = 28.07$, p = 1.170e-07; LR v L5 IB: $X^2(1, n = 19) = 19.00$, p = 1.307e-05; chi-squared test for all). L3 RS, L5 RS, and L5 IB cell persistent percentages did not significantly differ (L3 RS v L5 RS: $X^2(1, n = 50) = 0.01$, p = 0.042; L3 RS v L5 IB: $X^2(1, n = 19) = 1.30$, p = 0.2535; L5 RS v L5 IB: $X^2(1, n = 45) = 1.28$, p = 0.259; chi-squared test for all).

Table 1. Intrinsic cell properties

Intrinsic Values	LR *(n = 12)*	L3RS *(n = 12)*	L5RS *(n = 38)*	IB *(n = 7)*
Postnatal age (days)	34.08 ± 2.31	30.75 ± 1.11	31.63 ± 1.00	36.00 ± 4.36
Resting potential (mV)	-64.42 ± 1.22	-63.00± 1.46	-61.37 ± 0.53	-62.71 ± 1.43
Input resistance (MΩ)	537.75 ± 48.11	171.73 ± 21.89	106.31 ± 11.38	234.54 ± 60.95
Input capacitance (pF)	33.69 ± 1.77	125.22 ± 11.90	136.97 ± 8.66	114.09 ± 23.00
Membrane time constant (ms)	17.28 ± 0.83	19.27 ± 1.55	12.38 ± 0.74	18.88 ± 2.83
Action potential threshold (mV)	-39.70 ± 0.59	-43.55 ± 0.77	-43.05 ± 0.42	-40.95 ± 1.07
Action potential amplitude (mV)	63.2 ± 2.44	87.07 ± 9.92	80.15 ± 1.45	73.05 ± 3.49
Action potential width (ms)	0.69 ± 0.07	1.10 ± 0.05	0.71 ± 0.03	1.20 ± 0.21
Spike frequency adaptation ratio	1.09 ± 0.03	2.08 ± 0.16	3.99 ± 0.90	9.32 ± 3.37
Latency to first spike (ms)	773.09 ± 43.98	201.90 ± 22.27	219.11 ± 32.02	229.33 ± 48.97
Rheobase (pA)	29.68 ± 3.02	67.34 ± 16.20	132.36 ± 12.81	90.77 ± 34.24

Table 4-1. Intrinsic cell properties of LR, L3 RS, L5 RS, and L5 IB neurons. LRs significantly differed from L3RS cells on: $p<0.001$ - input resistance, input capacitance, adaptation ratio, spike width, spike amplitude, and latency to first spike; $p<0.01$ - spike threshold and rheobase; LRs significantly differed from L5RS cells on: $p<0.001$ - input resistance, input capacitance, adaptation ratio, spike amplitude, spike threshold, latency to first spike, and rheobase; $p<0.01$ - membrane time constant. LRs significantly differed from IB cells on: $p<0.001$ - input capacitance and latency to first spike; $p<0.01$ - adaptation ratio and input resistance; $p<0.05$ – spike width, and spike amplitude. L3RS cells significantly differed from L5 RS cells on: $p<0.001$ membrane time constant, spike width, and rheobase; $p<0.01$ - input resistance; $p<0.05$ - spike amplitude. L3RS cells significantly differed from IB cells on: $p<0.05$ - spike amplitude. L5RS cells significantly differed from IB cells on: $p<0.01$ - spike width; $p<0.05$ - membrane time constant and spike amplitude.

4.3.2 Slow afterdepolarization is the hallmark of persistent activity and is absent in LR cells

Neurons that exhibit cholinergic-induced persistent activity first show a gradual build-up of a slow afterdepolarization potential (sADP) that precedes persistent firing (Haj-Dahmane and Andrade, 1998; Navaroli et al., 2012). To more closely examine the persistent activity of the four RSG cell types, we next analyzed sADP amplitudes of all tested neurons. We found that 0/12 LR neurons showed any sADPs, regardless of time exposed to CCh (Figure 4-2A&F). In contrast, 92% of L3 RS, 95% of L5 RS, and 100% of L5 IB cells exhibited clear sADPs in the sweeps preceding persistent firing (Figure 4-2B-D&F). Even for the few L3 RS, L5 RS, and L5 IB cells that did not fire persistently, a clear trend toward sustained depolarization was observed in the form of sADP. The lack of sADP in LR neurons was significantly different compared to sADP occurrence in the other 3 cell groups ($p < 0.001$ for all, chi-squared test; Figure 4-2F), but there was no difference in the number of L3 RS, L5 RS, and L5 IB cells which expressed sADPs or their amplitude (chi-squared test; Figure 4-2E&F). These results show that this hallmark of persistent firing is ubiquitous across RS and IB neurons in RSG but uniquely absent from LR neurons.

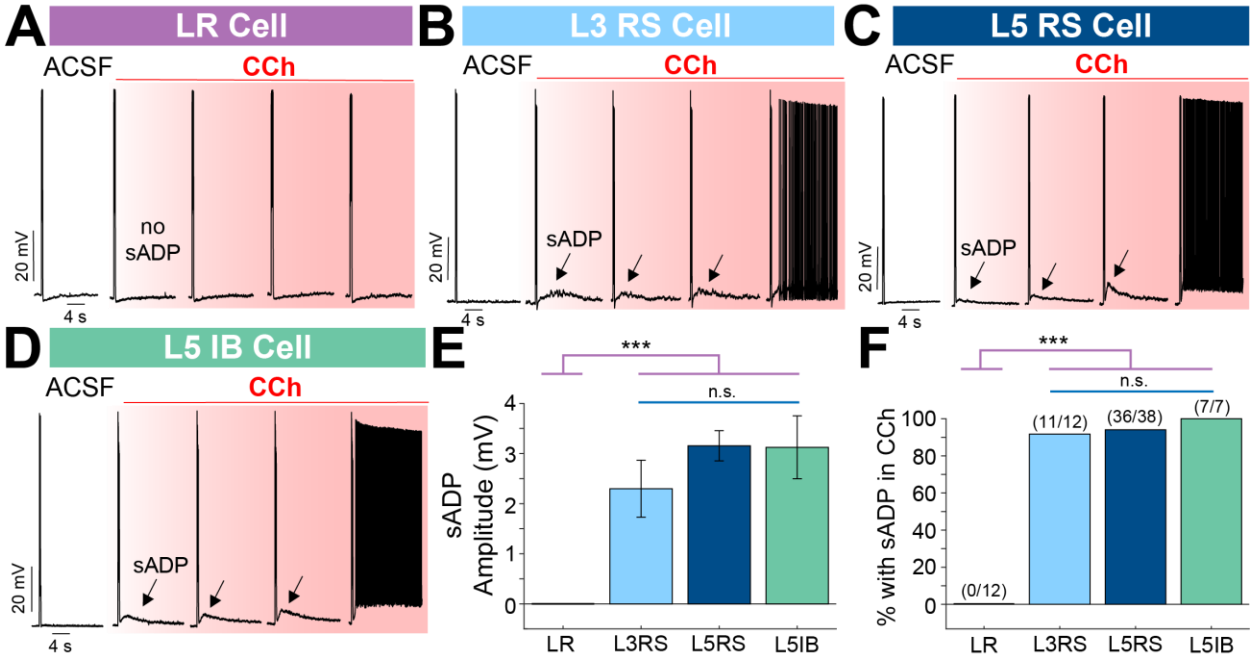

Figure 4-2. Slow ADP is a hallmark of persistence and absent in LR neurons.

A. Responses from a representative LR neuron. Left: Single baseline trace of LR activity in normal ACSF. Right traces: 3 subsequent traces after 10 minutes of exposure to CCh showing complete lack of sADP.

B. Responses from a representative L3 RS neuron. Left: Single baseline trace of L3 RS activity in normal ACSF. Right traces: 3 subsequent traces after 8 minutes of exposure to CCh showing the slow build-up of sADP that immediately preceded persistent firing (sweep not shown).

C. Same as ***B*** but for a L5 RS neuron in ACSF and after 4 min of exposure to CCh.

D. Same as ***B*** but for a L5 IB neuron in ACSF and after 6 min of exposure to CCh.

E. Population analysis of sADP amplitudes across the four cell types. LR neurons had significantly smaller sADPs (0 mV) compared to all other cell types (LR v L3 RS: p = 6.7477e-05; LR v L5 RS: p = 1.7793e-06; LR v L5 IB: p = 6.2846e-05; rank sum test). In contrast, sADP amplitude did not significantly differ between L3 RS, L5 RS, or L5 IB cells (L3 RS v L5 RS: p = 0.1043; L3 RS v L5 IB: p = 0.1956; L5 RS v L5 IB: p = 0.9875; rank sum test).

F. Population analysis of sADP occurrence across the four cell types. LR neurons had a significantly lower percentage of cells exhibiting sADPS (0%) compared to the other cell types (LR v L3 RS: $X^2(1, n = 24) = 20.31$, p = 6.594e-06; LR v L5 RS: $X^2(1, n = 50) = 40.60$, p = 1.867e-10; LR v L5 IB: $X^2(1, n = 19) = 19.00$, p = 1.307e-05; chi-squared test for all). In contrast, percentage of cells exhibiting sADPs did not differ between L3 RS, L5 RS, or L5 IB cells (L3 RS v L5 RS: $X^2(1, n = 50) = 0.15$, p = 0.6962; L3 RS v L5 IB: $X^2(1, n = 19) = 0.616$, p = 0.4326; L5 RS v L5 IB: $X^2(1, n = 45) = 0.3856$, p = 0.5436; chi-squared test for all).

4.3.3 Persistent firing in RSG is dependent on M1 receptor activity via an ICAN pathway

We next used a series of pharmacological channel blockers to determine the mechanism supporting persistent activity in RS and IB cells. Following the same protocol as previously described (Figure 4-1B), layer 5 cells were exposed to CCh to induce persistent activity. Once the cell was firing persistently, we first tested whether persistent activity in RSG was dependent on synaptic activity by applying synaptic blockers—NMDA receptor antagonist, APV, AMPA/kainite receptor antagonist, CNQX, and GABA receptor antagonist, picrotoxin—to the bath (see Methods). Application of these synaptic blockers did not affect persistent firing in any of the cells tested (0/5; Figure 4-3A), indicating that persistent activity in RSG does not rely on synaptic activity. We then verified that the CCh induced persistent firing was indeed an effect of cholinergic signaling by adding the nonselective muscarinic receptor antagonist, atropine, to the bath in order to block the receptors CCh would otherwise activate. As expected, application of atropine blocked persistent firing (4/4; Figure 4-3B), indicating that persistence is an effect of muscarinic receptor activity induced by CCh. Using the M1-selective receptor blocker, pirenzepine, we again observed a complete cessation of persistent firing in all tested neurons (4/4; Figure 4-3B), indicating that persistent activity in RSG is dependent on m1 receptor activity. Lastly, we applied flufenamic acid, a blocker of the calcium-activated nonselective cation current (I_{CAN}), and found that persistent activity was blocked in the vast majority of cells tested (7/8; Figure 4-3B). These results are consistent with observations in other brain regions that exhibit persistent firing (Navaroli et al., 2012; Yan et al., 2009), suggesting that cholinergic

induced persistent activity in the RSG follows the same mechanisms. However, the cell type-specificity among pyramidal neurons in RSG is unique compared to the more ubiquitous expression of persistent activity in other regions.

A Persistence is **not** dependent on glutamate or GABA receptors

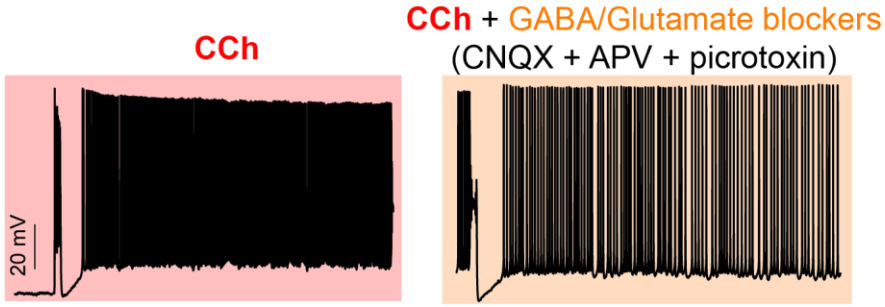

B Persistence depends on the m1 AChR via an ICAN pathway

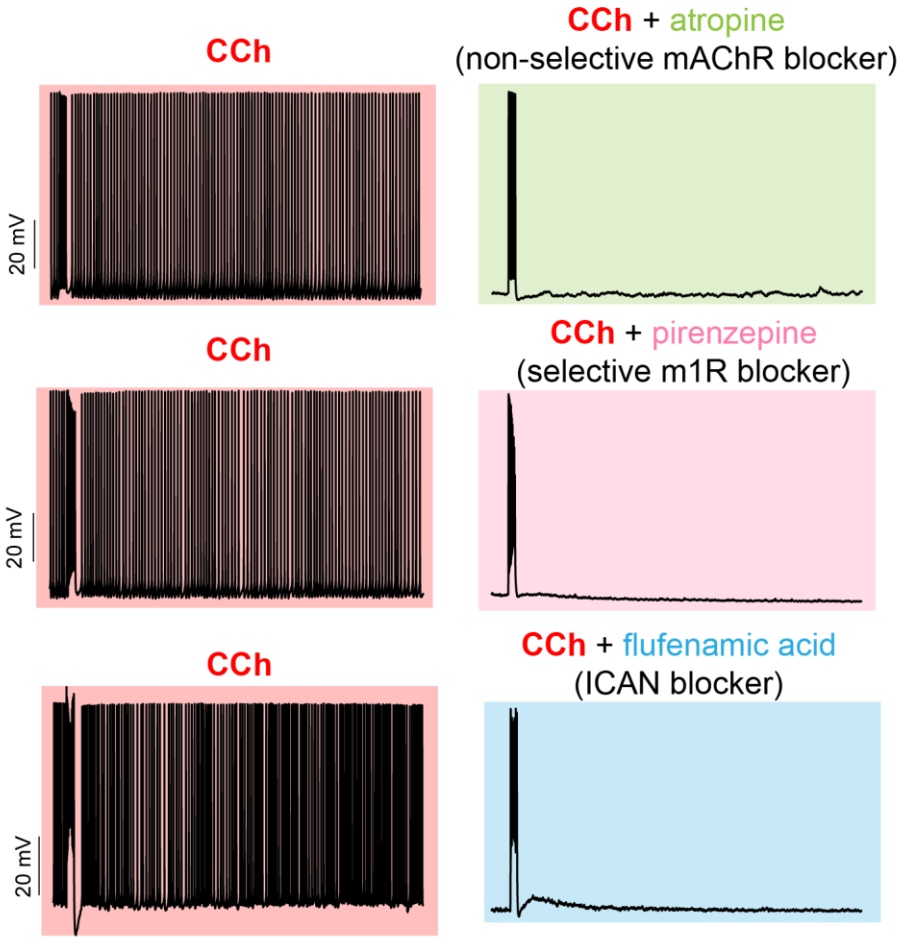

C % cells blocked from firing persistently

Glu/GABA blockers	atropine	pirenzepine	flufenamic acid
0% (0/5)	100% (4/4)	100% (4/4)	87.5% (7/8)

Figure 4-3. Persistence is independent of glutamatergic and GABAergic activity and dependent on the M1 receptor via the ICAN pathway.

A. Left: Trace of persistent firing after exposure to CCh from a representative L5 RS neuron. Right: Trace from the same neuron after synaptic blockers APV, CNQX, and picrotoxin were added to the bath. Note that application of these blockers did not block persistent activity.

B. Same as ***A*** but for the nonselective muscarinic receptor antagonist, atropine. Application of atropine completely blocked persistent activity.

C. Same as ***A*** but for the selective m1 receptor antagonist, pirenzepine. Application of pirenzepine completely blocked persistent activity.

D. Same as ***A*** but for the ICAN blocker, flufenamic acid. Application of flufenamic acid completely blocked persistent activity.

E. Table reporting the percent of cells with persistent activity blocked by the various pharmacological interventions reported in the previous panels.

4.4.4 Persistent activity is universal across layer 5 cells, regardless of anatomical or morphological features

Layer 5 is not a homogenous layer, with principal cells exhibiting a wide variety of morphological features and spiking profiles (Hattox and Nelson, 2007; Sempere-ferràndez et al., 2019; Sempere-Ferràndez et al., 2018; Tsiola et al., 2003; Wyss et al., 1990). Our results indicate that physiological differences between layer 5 cells do not influence persistence, as there was no difference in proportion of RS and IB cells which fired persistently (chi-square test; Figure 4-1G). To determine whether the heterogenous anatomical profiles of L5 RSG cells influence their propensity to fire persistently, we created reconstructions of a subset of the tested layer 5 cells, including both L5 RS and L5 IB neurons, and analyzed their morphologies (Figure 4-4A). We found that the location of the neuron within layer 5, analyzed as soma distance from the L3/5 boundary, was independent of the cell's likelihood to fire persistently (Figure 4-4B; chi-squared test). We next analyzed the apical and basal dendritic morphology of the reconstructed layer 5 cells and again found that proportion of persistently firing cells was independent of both apical and basal dendritic branching (Figure 4-4C&D; chi-squared test). We also examined potential sex differences in persistent activity and found that the proportion of cells which fired persistently did not significantly differ between male and female mice (chi-squared test, $X^2(1, n = 45) = 1.38$, $p = 0.2393$; data not shown). Taken together, these results indicate that persistent activity is a ubiquitous feature of all layer 5 pyramidal subtypes, regardless of anatomical, morphological,

physiological, or sex differences. Thus, LR neurons remain the only principal cell subtype within RSG layers 1-5 that do not exhibit cholinergic induced persistent activity.

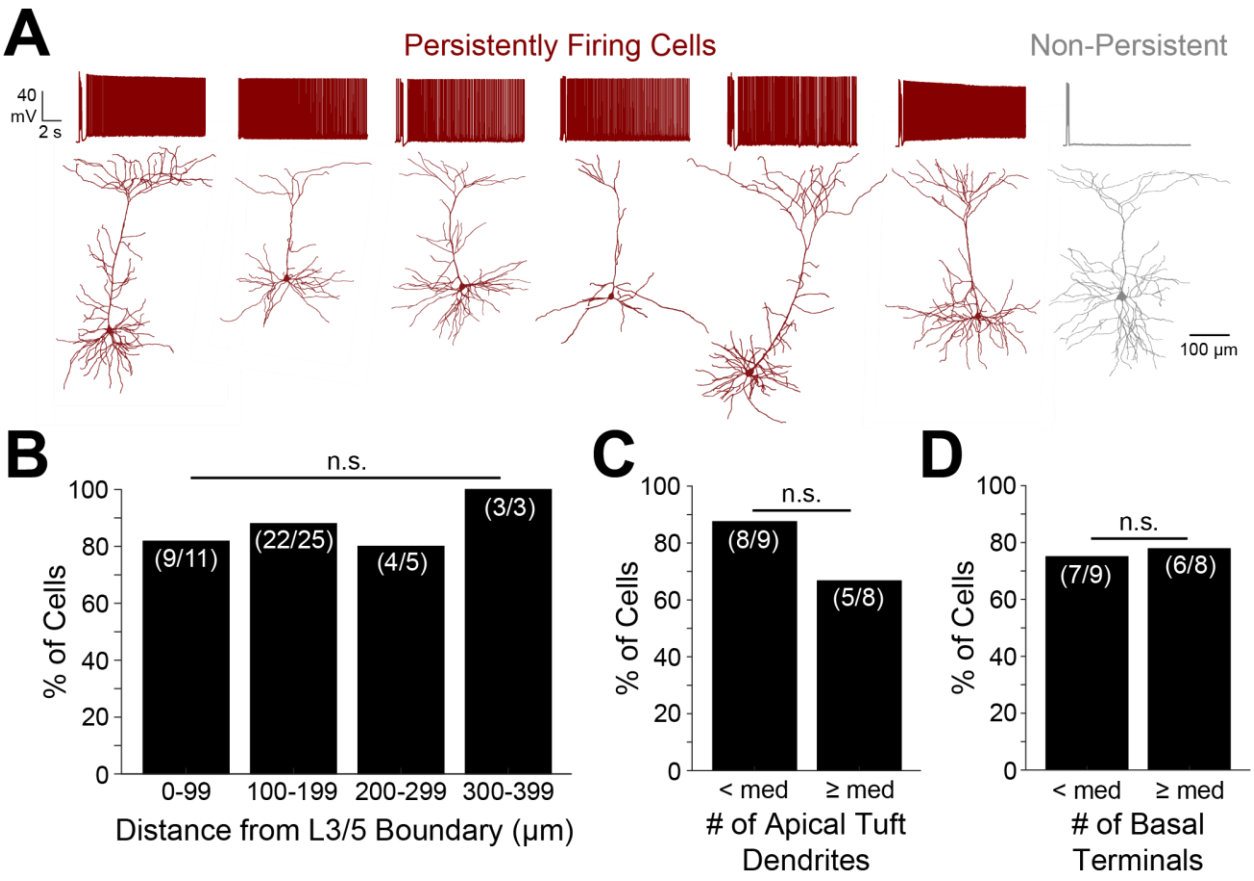

Figure 4-4. Persistent activity in layer 5 RSG neurons is independent of anatomical and morphological features.

A. Representative reconstructions of a subset of layer 5 neurons which either did (red) or did not (grey) fire persistently. Traces of the shown cell's response in CCh are shown above each reconstruction.

B. Population analysis of proportion of reconstructed cells which fired persistently plotted against soma distance from the L3/5 boundary. There is no significant difference in propensity to fire persistently across the cortical depth (0-99 v 100-199: $X^2(1, n = 36) = 0.24$, p = 0.6213; 0-99 v 200-299: $X^2(1, n = 16) = 0.01$, p = 0.9312; 0-99 v 300-399: $X^2(1, n = 14) = 0.64$, p = 0.4250; 100-199 v 200-299: $X^2(1, n = 30) = 0.23$, p = 0.6310; 100-199 v 300-399: $X^2(1, n = 28) = 0.40$, p = 0.5254; 200-299 v 300-399: $X^2(1, n = 8) = 0.69$, p = 0.4076; chi-squared test for all).

C. Population analysis of proportion of reconstructed cells which fired persistently plotted against number of apical tuft dendrites with bins split by median. There is no significant difference in propensity to fire persistently across the two groups ($X^2(1, n = 17) = 1.02$, p = 0.3121; chi-squared test).

D. Same as ***C*** but for number of basal terminals. There is no significant difference in propensity to fire persistently across the two groups ($X^2(1, n = 17) = 0.02$, p = 0.8928; chi-squared test).

4.4 Discussion

Here, we have provided the first examination of the direct effects of cholinergic neurotransmission onto granular retrosplenial (RSG) neurons at the cellular level. We found that regular-spiking (RS) and intrinsically-bursting (IB) cells across the superficial and deep layers fired persistently when exposed to the nonselective muscarinic receptor agonist, carbachol (CCh). In layer 5 RS and IB cells, this persistence was independent of the cell's physiological, morphological, anatomical, and sex characteristics, indicating that persistent activity is a ubiquitous feature of these neurons. Surprisingly, we found that low-rheobase (LR) cells, which have recently been identified as a key, selective recipient of directional and spatial inputs to RSG (Brennan et al., 2021, 2020), do not exhibit any markers of persistent activity in response to increased cholinergic neurotransmission.

To the best of our knowledge, features of cholinergic induced persistent activity have been found across principal cell types in all brain regions investigated so far. Persistent firing and/or sADPs in response to cholinergic agonists has been reported in layer 5 cells in primary sensory and motor cortices (Fu et al., 2019; Rahman and Berger, 2011) as well as both superficial and deep cells in medial entorhinal cortex (MEC), anterior cingulate cortex (ACC), postsubiculum, and prefrontal cortex (PFC) (Egorov et al., 2002; Jochems et al., 2013; Magistretti et al., 2004; Ratté et al., 2018; Seamans et al., 2003; Yan et al., 2009; Yoshida et al., 2008; Yoshida and Hasselmo, 2009; Zhang and Seguela, 2010). Similarly, we observed both sADPs and persistent firing in superficial principal neurons recorded in both the ACC and prelimbic cortices

(Supplemental Figure 4-1S). Taken together, these findings suggest that cholinergic induced persistent activity is ubiquitous among cortical principal cells. Persistent activity is also seen in multiple subcortical regions such as CA1, CA3, and subiculum (Bianchi and Wong, 1994; Jochems and Yoshida, 2013; Kawasaki et al., 1999; Yamada-Hanff and Bean, 2013), indicating that it is not just a feature of cortical cells but rather a more widespread property of principal neurons. Thus, the lack of both sADPs and persistent firing in LR neurons is a unique feature of these cells compared to other principal neurons across the brain.

LR neurons are the main retrosplenial target of converging directional & spatial inputs from the anterior thalamus (ADAV) and dorsal subiculum (Brennan et al., 2021). Computational modeling has also shown that LR cells can conjunctively encode head direction and compute head speed (Brennan et al., 2021), with their encoding exhibiting improved signal-to-noise the longer a persistent HD input is received (Brennan et al., 2020), such as when the animal is standing still. Under these awake, stationary conditions, cortical cholinergic tone is low (Solari and Hangya, 2018), so LR neurons must encode this persistent direction signal without the influence of cholinergic inputs. In contrast, when the animal is actively navigating a space or moving their head in an exploratory manner, cortical cholinergic tone is high via increased basal forebrain neurotransmission (Anzalone et al., 2009; Szymusiak et al., 2000). Our results indicate that LR encoding of direction as well as computation of head speed should be similar under this ambulatory and high cholinergic input condition, as cholinergic transmission does not directly impact LR activity at the cellular level. Thus, LR neurons are likely to

be optimized to encode a similar sense of orientation regardless of the animal's current behavioral state.

Even though cholinergic inputs do not impact LR firing directly, ACh may have indirect effects that influence LR spatial computations via modulation of their ADAV synaptic inputs. Cholinergic neurotransmission in other regions impacts thalamocortical signaling by modulating pre- and postsynaptic signals through the activation of muscarinic receptors, which can enhance or suppress postsynaptic response amplitudes, and nicotinic receptors, which often enhance response amplitudes (Arroyo et al., 2014, 2012; Kimura, 1999; Luchicchi et al., 2014; Picciotto et al., 2012). A key function attributed to increased cortical cholinergic tone is gain modulation (Ferguson and Cardin, 2020; Minces et al., 2017), as ACh can amplify relevant sensory signals to increase the gain of relevant inputs over background signals or pre-established firing patterns (Donoghue and Carroll, 1987; Kimura, 1999; Pinto et al., 2013; Polack et al., 2013; Soma et al., 2013, 2012). Indeed, simultaneous selective suppression of corticocortical signaling and enhancement of thalamocortical signaling across the cortex by cholinergic neurotransmission has been suggested to serve as a focusing mechanism to increase the signal-to-noise of external, thalamic inputs for signal detection by diminishing the influence cortical inputs (Picciotto et al., 2012). This suggests that ACh in RSG may amplify relevant spatial signals, like the HD inputs from ADAV, at the synaptic level, supporting LR spatial coding during conditions of increased cholinergic tone. Indeed, expression of acetylcholinesterase, which is localized at the postsynaptic junction of cholinergic synapses (Bigl et al., 1982; McKinney et al., 1983; Tengelsen et al., 1992), is highest in layer 1a and lower layer 3 in RSG (Tengelsen et

al., 1992), precisely overlapping with ADAV HD inputs that also preferentially target these same sublayer areas (Brennan et al., 2021). This suggests a convergence of HD and ACh inputs that may enable ACh to affect thalamic inputs to LR cells at the presynapse. Thus, future work should combine optogenetic techniques with pharmacological interventions to directly measure changes in LR neuron synaptic responses to spatially relevant inputs under varying cholinergic conditions.

While our findings emphasize the possibility of LR spatial coding in RSG that is independent of cholinergic release, what could be the function of persistent activity in RSG RS and IB neurons? Persistent activity is thought to support path integration (Hasselmo, 2008; McNaughton et al., 2006; Yoshida et al., 2012), which involves the maintenance of spatial representations through the combination of external and self-motion cues (McNaughton et al., 2006, 1991). Computational modeling suggests that path integration in the MEC is facilitated by integration of direction and speed signals that changes the firing rate of persistent neurons to provide a rate code for the current position of the animal relative to target locations in their environment (Hasselmo, 2008). The RSG has also been heavily implicated in path integration (Chrastil et al., 2017, 2015; Cooper and Mizumori, 1999; Elduayen and Save, 2014; Sherrill et al., 2013), and blocking cholinergic neurotransmission in RSC significantly worsens performance on navigational tasks that require use of learned representations via path integration but not visually guided navigation that is independent of path integration (Riekkinen et al., 1995). Thus, it is possible that persistent activity as a result of increased ACh in RSG during navigation (Anzalone et al., 2009) in RS and IB neurons may support the path integration functions of this region, but RS and IB neurons would need to be receiving

HD and speed signals in order to follow the same rate code mechanisms proposed to be employed by the MEC (Hasselmo, 2008). It has been predicted that retrosplenial RS neurons receive inputs from contralateral LR neurons, likely containing their direction and speed code (Brennan et al., 2021), but LR neurons have not yet been verified as the source of these contralateral projections. While extensive future work is needed to determine the functional and computational benefits of persistent RS and IB activity in the RSC, the findings presented here provide necessary foundational knowledge of subtype-specific cholinergic effects on retrosplenial cells.

4.5 Materials and Methods

4.5.1 Experimental Model and Subject Details

All animal use and housing were approved by the University of Michigan Institutional Animal Care and Use Committee. Multiple mouse lines were used in this study: Ai32 (Jackson Laboratories, 024109), *Camk2α*^{Cre} (Jackson Laboratories, 005359), *Camk2α*^{Cre} x Ai32 (crossed in house), C57Bl6-wildtype (Charles River, stock #027), Ai14 (Jackson Laboratories, 007914), *Grp*-KH288^{Cre} (RRID:MMRRC 037585-UCD), *Pvalb*^{Cre} (PV-IRES-Cre; Jackson Laboratories, 008069), *Pvalb*^{Cre} x Ai32 (crossed in house), Tg(Sla-cre)KJ303 (MGI:4940648), Tg(Sla-cre)KJ319 (MGI:4847420) x Ai32 (crossed in house), and *Grp*-KH288^{Cre} x Ai32 (crossed in house).

4.5.2 Slice Electrophysiology Experimental Methods

Slice preparation

Detailed description of slice preparation is available elsewhere (Brennan et al, 2020). Briefly, mice were deeply anesthetized using isoflurane and decapitated. The brain was rapidly removed and placed in an ice cold, carbogen-saturated high sucrose solution. 300 µm thick slices were cut using Leica 1200VT or 1000S vibratomes and transferred into high magnesium artificial cerebrospinal fluid (ACSF) kept at 32 °C. After 20 min, the recovery chamber containing the slices was moved to room temperature. Experimental recordings started 45min after the additional room temperature recovery.

Whole-cell recordings

Slices were placed in a submerged recording chamber continuously perfused at 2 mL/min with body temperature ACSF containing: 126 mM NaCl, 1.25 mM NaH2PO4, 26 mM NaHCO3, 3 mM KCl, 10 mM dextrose, 1.20 mM CaCl2, and 1 mM MgSO4. Cells were visualized using an Olympus BX51WI microscope with Olympus 60x water immersion lens and Andor Neo sCMOS camera (Oxford Instruments, Abingdon, Oxfordshire, UK). Patch pipettes were pulled using a horizontal puller and had resistances between 4-7 MΩ. Recordings were done using a potassium gluconate intracellular solution containing: 130 mM K-gluconate, 2 mM NaCl, 4 mM KCl, 10 mM HEPES, 0.2 mM EGTA, 0.3 mM GTP-Tris, 14 mM phosphocreatine-Tris, and 4 mM ATP-Mg (pH 7.25, osmolarity 290 mOsm).

Patch clamp recordings were obtained with Multiclamp 700B and Digidata 1440A (Molecular Devices). Neurons from layers 2, 3, and 5 were randomly chosen based on

their pyramidal or oval soma shape, and recordings were done in the current clamp mode. Only the cells with resting membrane potential of -55 mV or lower were used for the analysis. Cells were adjusted for series resistances and held at -65 mV for all but the persistence protocol recordings. Recordings were not liquid junction potential corrected. Each recorded cell was first characterized for intrinsic and firing properties (see Brennan et al., 2020, 2021 for detailed protocols) and subsequently tested for persistence.

Pharmacology

After the cells were characterized (see Methods above), the persistence protocol was started (see Figure 1B for schematic). The protocol consisted of repetitive sweeps of 3 current injections, each at an intensity at least twice that which was required to reach firing threshold, meant to evoke persistent firing. These current injections were followed by a small negative step (same intensity and length as for input resistance characterization; see Brennan et al., 2020, 2021) to monitor the input resistance changes. From that point until the end of the experiment, the resting membrane potential was not adjusted. Cells were recorded for about 2 minutes in ACSF before the non-selective muscarinic receptor agonist, carbachol (40 uM; CCh), was added to the bath, and responses were recorded for 10 min. CCh was then washed out using standard ACSF for 5 min, or until no persistent activity was observed for at least 1 min.

In order to evaluate the nature of persistent firing, blockers were added to the recording chamber. AP-5 (50 µM), CNQX (10 µM), flufenamic acid (100 uM) and pirenzepine (1 µM) were added from frozen stock solutions, while picrotoxin (100 µM) and atropine (1 µM) were added fresh. Drugs entered the bath about 2 min after the

persistence was first observed and were either applied to the perfusate (when persistent activity was continuous) or directly to the recording chamber (when persistence was intermittent).

4.5.3 Quantification and statistical analysis

Electrophysiological measurements and analysis

Cells were characterized based on their spike threshold, spike amplitude, spike width, spike frequency adaptation ratio, latency to first spike, rheobase, input resistance (Rin), input capacitance (Cin), and membrane time constant (τm), as described elsewhere (Brennan et al., 2021), and all measurements were obtained using Clampfit analysis and MATLAB scripts.

Distance from layer 3 was measured in µm using Andor Solaris software and defined as the distance between the boundary between layers 3 and 5 and the tip of the recording pipette.

Slow afterdepolarization (sADP) was measured in Clampfit as the highest amplitude of the membrane potential within 1.5 s after the end of the current injection, relative to 0.5 s baseline before the current step for three consecutive steps, and the average of those steps was reported. Initial sADP was measured from the first three step currents in the persistence protocol, while onset sADP was measured from 3 steps immediately preceding persistent firing. For 3 cells' measurements, those time points were slightly offset due to either nonstandard protocol (1 cell) or EPSPs being too high to reliably measure the sADP at the typical time points (2 cells). In those cases, first

reliable step currents immediately adjacent to the standard ones were used. For cells that did not fire persistently, CCh sADP was measured from three consecutive current steps starting 5 min after carbachol entered the bath. If no sADP was observed, the sADP was reported as 0 mV.

Neurons were classified as persistently firing if it exhibited at least 6 spikes within 13 s after the termination of the current injection (modified from Jochems et al., 2013, to account of the different current step interval) in at least two of three consecutive step currents.

4.5.4 Morphological reconstructions

Biocytin (5 mg/ml) was added to the intracellular recording solution to aid morphological analysis. During whole-cell recordings, biocytin diffused into cells for at least 30 min. At the end of each recording, an additional zap protocol (15 1-4 nA current injections at 1 Hz) was applied to improve the diffusion process (Jiang et al., 2015). After the recording ended, the patch pipette was carefully withdrawn from the cell and the slice was left to rest in the recording chamber for 10 min before being transferred to 4% PFA solution for 24-72 h fixation. Afterward fixation, the slices were washed in phosphate buffer solution (PBS) and incubated in PBS containing 0.4% triton and 1:1000 streptavidin conjugated Alexa Fluor 647 for another 48 h. Slices were then again washed in PBS and mounted on slides using FluoromountG mounting medium and left to set for at least 24 h before imaging.

Fluorescent fills were imaged with Zeiss Axio Image M2 confocal microscope with 20x lens as z-stacks with z-step of 0.5 µm. Neurons were then reconstructed from these files using NeuTube software.

Morphological analysis

17 (13 firing persistently and 4 not) reconstructed neurons (in the .swc format) were quantified using the NeuroM python module. The number of basal dendrite terminations was counted using python scripts, and the number of apical tuft terminations was counted by hand, to avoid including oblique dendrites.

4.6 Acknowledgements

We would like to thank Izabela Jedrasiak-Cape for her exceptional experimental work collecting the data that informed this chapter. We would also like to thank Danny Siu for his advice and assistance with MATLAB based statistical and data visualization procedures. This work was supported by lab startup funds from the University of Michigan (OJA), a grant from the Whitehall Foundation (OJA), NIH grant NS121745 (OJA), NIH T-32-NS076401 (EKWB), NSF graduate research fellowship (EKWB), and by a Rackham Predoctoral Fellowship (EKWB).

4.7 Author Contributions

Conceptualization, O.J.A, I.J-C, E.K.W.B; Methodology, O.J.A., I.J-C; Investigation, I.J-C.; Software, I.J-C., E.K.W.B.; Formal Analysis, I.J-C., E.K.W.B.;

Visualization, E.K.W.B., I.J-C., O.J.A.; Writing – Original Draft, E.K.W.B., I.J.C., O.J.A.; Writing – Review & Editing, O.J.A., E.K.W.B., I.J-C.; Funding Acquisition, O.J.A.; Supervision, O.J.A.

4.8 Supplemental Figures

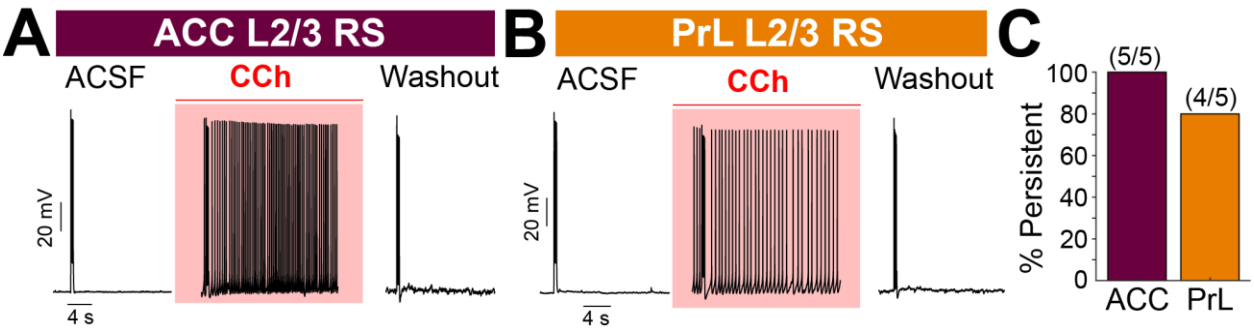

Supplemental Figure 4-1S. Principal cells in the superficial layers of ACC and PrL exhibit both sADPs and persistent firing.

- ***A.*** Responses from a representative L2/3 RS neuron in ACC. Left: Baseline trace of neuron activity in normal ACSF. Middle: Trace showing persistent firing after exposure to CCh. Right: Trace of baseline activity after washout of CCh with normal ACSF.
- ***B.*** Same as ***A*** but for a representative L2/3 RS neuron in PrL which also showed persistent firing in the presence of CCh.
- ***C.*** Population analysis of the percentage of neurons within each region that exhibited persistent firing.

CHAPTER 5: Discussion and Future Directions

5.1 Abstract

The work presented in this dissertation provides multiple novel findings and insights regarding mechanisms underlying spatial navigation in the granular retrosplenial cortex (RSG). By identifying the neuronal subtypes and computations supporting navigation in the RSC, we have provided new avenues for research regarding orientation in both health and disease. Through a combination of whole-cell patch clamp, imaging, pharmacological interventions, and computational models, this work shows that: (1) Layers 2/3 of RSG contain a physiologically, morphologically, and computationally unique principal neuron, the Low-Rheobase (LR) cell, whose intrinsic properties make it optimized to encode persistent spatial information, such as direction; (2) These LR neurons are preferentially targeted by spatial inputs from the anterior thalamus (ADAV) and dorsal subiculum (DS), facilitated by the precise sublaminar organization of LR dendrites and these spatial afferents localized to layers 1a and 3; (3) The unique depressing nature of ADAV head direction (HD) synaptic inputs to LR neurons enables these cells to conjunctively encode direction and compute head speed; (4) In contrast, RSG regular-spiking (RS) neurons are targeted by mostly nonspatial claustral and anterior cingulate inputs, facilitated by the overlap of dendrites and

afferents in layers 1b/c and 5; and (5) LR activity is not directly modulated by cholinergic neurotransmission, a surprising finding that suggests their spatial computations are independent of precise brain-state and do not rely on cholinergic tone. Here, we discuss the significance of these findings and propose future work to further parse this navigational circuit.

5.2 Key Findings and Future Directions for the Characterization of Low-Rheobase Neurons

5.2.1 Low-Rheobase Neurons Are Physiologically and Morphologically Distinct from other Principal Cells

Classical anatomical studies of the retrosplenial cortex (RSC) have reported the presence of small, granular-like neurons localized to layers 2/3 of RSG (Vogt and Peters, 1981; Wyss et al., 1990). Vogt and Peters (1981) noted that “although this layer appears granular, it contains small pyramidal cells.” Similarly, Wyss et al. (1990) stated that large pyramidal neurons were located in the deeper layers, but the superficial layers “consist primarily of small, pyramidal neurons that have oval or pyramidal shaped cell bodies with short basal dendrites…and a larger apical dendrite.” Indeed, these small pyramidal neurons inspired the naming of the “granular” RSC, but the physiological and computational features of these distinguishing cells remained entirely unknown.

Kurotani et al. (2012) reported that the small pyramidal cells in layer 2 of the rat RSG exhibited a late-spiking property due to a high expression of Kv1 channels, and thus they named these neurons late-spiking cells (Kurotani et al., 2012). In our studies, we performed whole-cell patch clamp recordings in over 500 RSG neurons in mice to measure their physiological and morphological properties. In accordance with previous studies, we found that the small pyramidal cells do indeed express a late-spiking phenotype, but this is not unique to these neurons, as both fast-spiking (FS) interneurons and, to a lesser degree, RS neurons in this region also exhibit pronounced late-spiking firing properties (Figure 2-1, Table 2-1). However, these small pyramidal cells do exhibit a series of unique intrinsic and firing properties, including a significantly higher input resistance and low rheobase compared to both FS and RS neurons (Figure 2-1, Table 2-1) and lack of spike frequency adaptation (Figure 2-1, Table 2-1). This unique combination of intrinsic properties results in a neuronal subtype that can easily be made to fire and is capable of consistent persistent activity without adaptation. Thus, the key, unique computational features of LR cells are their hyperexcitability (i.e., low rheobase) and lack of spike-frequency adaptation. As such, we have named these neurons Low-Rheobase (LR) cells.

The finding of a distinct principal neuron subtype in RSG is significant for several reasons. First, the RSC has been heavily implicated in a wide variety of critical functions, including learning, memory, spatial navigation, imagination, and planning (Alexander et al., 2020; Alexander and Nitz, 2017; Chang et al., 2020; Chrastil, 2018; Hinman et al., 2018; Mao et al., 2018; Miller et al., 2020, 2019). It is also a key contributor to disease profiles, becoming significantly impaired in diseases with spatial

disorientation symptoms, such as Alzheimer's disease (Chen et al., 2017; Hou et al., 2020; Minoshima et al., 1997; Nagano-Saito et al., 2004; Nestor et al., 2003; Pengas et al., 2010; Potvin-Desrochers et al., 2019; Scheff et al., 2015). The discovery and classification of this unique LR principal subtype is an essential step in identifying the cells and circuits that ultimately facilitate the RSC's role in maintaining complex behaviors.

Second, there is general consensus in retrosplenial research that the RSC serves to integrate both allocentric and egocentric information to generate complex spatial representations and therefore facilitate its navigational functions (Alexander et al., 2020; Miller et al., 2020; van Wijngaarden et al., 2020; Vann and Aggleton, 2002), but this conclusion is informed largely by anatomical, computational, and gross lesion studies (Bicanski and Burgess, 2018; Harker and Whishaw, 2004; Hindley et al., 2014; Keene and Bucci, 2009, 2008; Pothuizen et al., 2010; van Groen and Wyss, 2003, 1992, 1990; Vann et al., 2003; Vann and Aggleton, 2002). The identification of this LR neuron as a unique principal neuron in RSG in addition to the common RS neuron provides a possible framework by which converging streams of information may be integrated within this region. Indeed, the presence of two distinct principal neurons with differential contributions to spatial coding has been noted in several structures involved in navigation, including the dentate gyrus (GoodSmith et al., 2017; Leutgeb et al., 2007; Scharfman, 2019, 1992; Senzai and Buzsáki, 2017), CA1 (Danielson et al., 2016; Lee et al., 2014; Mizuseki et al., 2011; Soltesz and Losonczy, 2018), and subiculum (Simonnet and Brecht, 2019; Yamawaki et al., 2019a). It is thus both possible and likely that a similar parallel coding scheme may be implemented in RSG. Based on the narrow spike

widths and lack of spike frequency adaptation in LR neurons compared to RS neurons, we hypothesize that LR cells are more likely to encode persistent inputs, such as those involved in head direction, and contribute heavily to retaining a consistent directional bearing. In contrast, RS cells are more likely to encode transient inputs, such as those involved in cue detection, rather than persistent inputs.

5.2.2 Low-Rheobase Neurons are Optimized to Precisely Encode Persistent Direction Information

In order to test our predictions that LR neurons are capable of encoding persistent information, we utilized computational modeling of LR and RS cells and *in vivo* spike trains from postsubicular HD cells (Peyrache and Buzsaki, 2015, Figure 2-9). The postsubiculum contains a relatively high percentage of HD cells (Blair and Sharp, 1995; Taube et al., 1990), which are bursty and fire a series of rapid spikes at rates of 150-250 Hz (Peyrache et al., 2015). These same neurons also fire long-duration trains of persistent spikes which are thought to be critical for maintaining a sense of orientation when the animal is remaining still (Peyrache et al., 2015; Taube and Bassett, 2003; Yoshida and Hasselmo, 2009). We found that computationally, LR cells can indeed encode persistent postsubicular information with a high signal-to-noise ratio that improves the longer the LR cell receives these inputs (Figure 2-9). These results provide the first evidence that the LR neurons in RSG, specifically, are capable of encoding persistent spatial inputs, a key function attributed to the RSC (Ino et al., 2007; Osawa et al., 2007; Vann et al., 2009).

The finding that LR neurons can encode persistent information over long durations has significant implications for their role in supporting the path integration functions of the RSC. Path integration, or “spatial updating,” is the process of maintaining an accurate spatial representation through the integration of sensory cues in the environment, location, orientation, and self-motion (Barry and Burgess, 2014; Etienne and Jeffery, 2004; McNaughton et al., 1991). HD signals represent a stage of this process, as they are oriented to landmark cues in the environment but are also sensitive to self-motion cues (Muir et al., 2009; Stackman et al., 2002; Stackman and Taube, 1997; J. S. Taube et al., 1990; Taube et al., 1990), reflecting a convergence of environmental allocentric and self-motion egocentric information. HD information is communicated via persistent firing (Taube and Muller, 1998), but this persistent HD signal is not sufficient to maintain stable representations on its own. Specifically, HD tuning curves, which represent the preferred orientation for an individual HD cell, can drift and change when visual signals are removed or displaced, and these drifts are directly correlated with mistakes in navigation behaviors (Taube et al., 1990; Valerio and Taube, 2012). This implies that the HD signal needs to be integrated with a more stable spatial representation that is continuously updated to provide the most accurate cognitive map. Our results indicate that LR neurons may serve as the site of this integration.

First, LR cells are computationally optimized to encode persistent direction inputs, while retrosplenial RS cell encoding is inconsistent. Second, the superficial layers of RSG where LR neurons reside are the main target of inputs from regions which contain large proportions of HD cells (van Groen et al., 1993; van Groen and

Wyss, 2003, 1990; Yamawaki et al., 2019b), and the results presented in Chapter 3 verify that LR cells are indeed the main target of these inputs. Third, computational models of path integration predict that the RSC serves as the necessary site for “spatial transformation” of egocentric self-motion and allocentric environmental cues due to its anatomical connections with spatial, sensory, and motor regions (Bicanski and Burgess, 2018; Byrne et al., 2007; Page and Jeffery, 2018). To corroborate this, lesions of the RSC result in impaired directional tuning and landmark control by ADAV HD cells (Clark et al., 2010). These findings indicate that stable and accurate representations of direction by HD cells may rely on the integration of direction representations with updated environmental information in the RSG, and our findings show that LR neurons are the only pyramidal subtype in RSG capable of accurately encoding, and thus integrating, direction signals. Thus, it is likely that this unique ability of LR neurons to reliably encode persistent input underlies retrosplenial contributions to the larger path integration circuit.

5.2.4 Future Directions

Perhaps the single most important gap in the field’s knowledge regarding superficial RSG neurons is the lack of information on their *in vivo* spike patterns. To our knowledge, no *in vivo* awake, behavioral recordings to date have attempted to precisely target L2/3 of RSG, likely due to its relatively inaccessible position at the midline. While some studies have shown electrode tracks passing through superficial RSG (Alexander et al., 2020; Jacob et al., 2017; Miller et al., 2020), none have reported confirmed single

units in these layers nor attempted to distinguish between LR and RS cells. This severely limits any conclusions we can make regarding how these cells contribute to the navigation and memory functions of the RSC in the behaving animal. Our precise characterization of differences in spike width and adaptation between LR and RS neurons will likely help the field to identify these distinct neurons using precisely planned extracellular recordings.

However, the most effective way to identify these cells *in vivo* would be the identification of a unique neural marker. Future studies should aim to identify transcriptional signatures of LR neurons. Single-cell patch sequencing would enable identifying the neuron in the slice by measuring its intrinsic properties before identifying any unique transcriptional markers (Cadwell et al., 2017; Fuzik et al., 2015; Hedlund and Deng, 2018; Li et al., 2016; Mahfooz and Ellender, 2021; Muñoz-Manchado et al., 2018). Alternatively, RNAseq could be performed on a microdissection of layers 2/3 of RSG and compared to a microdissection of a well-classified cortical region, such as layer 2/3 of barrel cortex (Belgard et al., 2011). This would identify potential unique markers that may be attributed to LR neurons, as they comprise the majority of neurons in L2/3 of RSG (Figure 2-3). These candidate markers could then be more closely examined with single-cell patch seq, as previously suggested. Identifying a unique biomarker for LR neurons would be significantly beneficial for multiple reasons. First, it would allow for the creation of a transgenic line in which LR neurons exclusively express cre-recombinase that can be used to visualize LR neurons by adding a cre-dependent fluorescent tag. It could also be coupled with an optogenetic or

chemogenetic construct to allow the modulation of LR neurons in both the slice and *in vivo*, providing an avenue for directly assessing the behavioral correlates of LR activity.

Lastly, our study has extensively characterized LR neurons and their local connectivity with other superficial RSG neurons, but nothing is known about their downstream targets. Our morphological results show that LR neurons do not ramify locally, instead projecting their axons into the corpus callosum (Figure 2-7). The lack of local connectivity reported here (Figure 2-6) also support the notion that LR cells are targeting neurons outside of the superficial layers, and likely even outside of the local RSG. Retrograde injection and electroporation investigations have reliably shown that contralateral projections between retrosplenial hemispheres are predominantly derived from superficial cells (Sempere-Ferràndez et al., 2018; Sripanidkulchai and Wyss, 1987; van Groen and Wyss, 2003), with a large portion of the labeled cells being small L2/3 pyramidal cells that reflect LR neuron soma size (Sripanidkulchai and Wyss, 1987). These anatomical findings strongly suggest that LR neurons in one hemisphere may project to the contralateral RSG to facilitate an interhemispheric spatial code, but selective labeling or optogenetic control of LR neurons is needed to verify this hypothesis. This again relies on the identification of a unique biomarker for LR cells that would allow the creation of a transgenic line. Once this transgenic line is established, selectively labeling these neurons would allow for visually tracing their axons to downstream targets. Optogenetic experiments could also selectively stimulate neurons in one hemisphere while synaptic transmission could be measured via patch clamp in the contralateral hemisphere to determine the contralateral targets of these potential LR projections. Collectively, these proposed experiments have the potential to provide an

avenue for the investigation of LR neurons *in vivo* and LR output to downstream targets, both of which remain the largest challenges to the field with respect to this specific circuit.

5.3 Key Findings and Future Directions for the Parallel Spatial and Nonspatial Circuits of RSG

5.3.1 Low-Rheobase Neurons Receive Targeted Spatial Inputs

Previous anatomical work has shown that spatially relevant regions such as the anterior thalamus (ADAV), dorsal subiculum (DS), and hippocampal formation project predominantly to the superficial layers of the granular subdivision of RSC (Nitzan et al., 2020; van Groen et al., 1993; van Groen and Wyss, 2003, 1990; Wyss and van Groen, 1992; Yamawaki et al., 2019b, 2019a), and these inputs recruit both superficial and deep pyramidal cells (Nitzan et al., 2020; Yamawaki et al., 2019b, 2019a). We aimed to compare the synaptic dynamics of these inputs to LR and RS neurons to provide the first detailed look at functional responses to thalamic and subicular afferents in layers 2/3 of RSG.

We found that the precise organization of LR dendrites and incoming axons facilitated a circuit in which LR neurons are optimized to receive spatial signals from both ADAV and DS at their apical and basal dendrites in layers 1a and 3, respectively (Figure 3-6). In contrast, RS dendrites are localized most strongly to layers 1b/c and 5, which do not receive targeted inputs from either ADAV or DS (Figures 3-2 & 3-5). This

results in LR neurons exhibiting significantly stronger responses to these spatially relevant inputs compared to RS cells (Figures 3-2 & 3-5).

These results are significant for a few reasons. First, they provide the first evidence that LR neurons do indeed receive converging signals from multiple spatially relevant regions. Indeed, both ADAV and DS contain high proportions of spatially modulated neurons (Blair and Sharp, 1995; Taube et al., 1990; Taube, 1995), and the reciprocal connections of ADAV and the RSC have been attributed as essential for maintaining accurate directional coding (Clark et al., 2010; Garden et al., 2009). Thus, LR neurons are a primary site of convergence for multiple streams of spatial information, receiving putative HD signals from ADAV at their distal apical dendrites and axis and boundary cell inputs from the DS at their proximal apical and basal dendrites. This strongly establishes LR neurons as key components of the retrosplenial navigational circuit, particularly since the integration of multiple streams and types of distance and direction information is often stated as the key computational function of the RSC as a whole (Burgess et al., 2001; Byrne et al., 2007; Epstein, 2008; Ichinohe et al., 2003; Maguire, 2001; van Wijngaarden et al., 2020). Second, our supplemental examinations show that LR neurons are more strongly driven by ADAV input than layer 5 RS cells, further highlighting the defining role that LR cells are likely to serve with respect to the navigational functions of RSG. Thus, these findings ultimately establish LR cells as the predominant spatial correlate in RSG.

5.3.2 Regular-Spiking Neurons Receive Targeted Nonspatial Inputs

The work presented in this dissertation has also provided the first functional examination of claustral (CLA) and anterior cingulate (ACC) inputs to the RSC, as previous connectivity studies relied on anatomical imaging (van Groen and Wyss, 2003, 1990; Wang et al., 2017; Zingg et al., 2018) and thus could not determine the cellular targets or synaptic dynamics of these inputs. We found that RS neurons in RSG are preferentially targeted by both CLA and ACC afferents, exhibiting significantly stronger responses to these inputs than LR neurons (Figures 3-3 & 3-4). This finding is significant, as it establishes parallel circuits in RSG that differentially encode spatial and nonspatial inputs. The RS neurons may facilitate integration of other key inputs to RSG that supplement the spatial coding supported by LR cells. This is of particular importance since the RSC is heavily associated with a wide array of functions in addition to navigation, including memory and fear conditioning (Buckley and Mitchell, 2016; De Sousa et al., 2019; Kwapis et al., 2015; Sigwald et al., 2020; Todd and Bucci, 2015; Valenstein et al., 1987; Vann et al., 2009; Wang et al., 2019). As such, parallel circuits engaging distinct neuronal subtypes are likely to facilitate its diverse functions.

Notably, our results suggest RS neurons of the RSG may be key contributors to the fear conditioning functions of the RSC. Indeed, both the CLA and ACC have been heavily implicated in fear-associated behaviors (Cho et al., 2017; Frankland et al., 2004; Han et al., 2003; Ipser et al., 2013; Steenland et al., 2012; Vakolyuk et al., 1980; Vetere et al., 2017), and ablation of putative RS cells located near the boundary of layers 3/5 in RSC resulted in contextual fear amnesia (Sigwald et al., 2020). These findings suggest that the RS cells examined in our study, which were located almost exclusively along the L3/5 border, are involved in the fear-related functions of the RSC (Lukoyanov and

Lukoyanova, 2006; Yamawaki et al., 2019a). The preferential targeting of these RS neurons by CLA and ACC afferents likely supports the encoding of fear-associated signals by these RS cells, as well. However, the work presented in this dissertation did not explicitly test the behavioral relevance of these inputs, and thus future investigation to confirm the role of these inputs in fear conditioning is still needed.

From the navigational perspective, it is also likely that RS neurons of the RSG are involved in spatial coding, but dependent on inputs from LR. Our supplementary results (Supplemental Figure 3-3S) show that inputs from contralateral RSG preferentially and strongly target RS neurons, with almost no recruitment of LR neurons. We have previously discussed the possibility that LR neurons project contralaterally to the other RSG hemisphere, and our results presented in this dissertation indicate that RS neurons may be the preferential target of such contralateral projections (Supplemental Figure 3-3S). Thus, we hypothesize that spatial signals integrated and computed by LR neurons are subsequently transmitted to RS cells in the contralateral RSG, specifically, providing an interhemispheric code of direction and rotational speed information. This code may then be transmitted to the secondary motor cortex (M2), as extensive reciprocal connections between RSC RS neurons and M2 to facilitate the communication of spatial and motor signals have been reported (Yamawaki et al., 2016). Thus, RS cells may support the interhemispheric comparison of direction and speed signals with motor efference signals to sharpen retrosplenial orientation coding.

5.3.3 The Synaptic Dynamics of ADAV Inputs to Low-Rheobase Neurons Enable Conjunctive Encoding of Direction and Computation of Head Speed

Perhaps the most significant finding of this dissertation is the unique rotational head speed computations generated by LR neurons in RSG. Multiple specialized spatial neurons have been reported in RSC, including HD cells (Chen et al., 1994; Cho and Sharp, 2001; Jacob et al., 2017; Lozano et al., 2017), axis cells (Jacob et al., 2017), and egocentric boundary vector cells (Alexander et al., 2020; Laurens et al., 2019). However, little work has determined the mechanisms by which these cells integrate or generate their spatial codes, either at the cell or population level (Miller et al., 2020, 2019). Thus, our findings regarding the LR neuron's conjunctive encoding of head direction and computation of rotational head speed provide the first mechanistic identification of a unique, well-classified neuronal subtype in RSG that facilitates the spatial coding properties of this region. Specifically, we found that the depressing synapses from ADAV inputs to LR apical dendrites allow LR neurons to compute angular head speed from HD signals, facilitating a robust angular speed rate code generated by these LR cells (Figure 3-8).

Apart from identifying a neural mechanism that supports retrosplenial control of navigation, these findings also provide new predictions on LR neuron activity *in vivo*. Specifically, our results predict that LR neuron activity will be correlated with angular head speed with a small lag (Figures 3-8 & 3-9). A large proportion of LR cells will also likely show conjunctive encoding of both head direction and speed (Figure 3-10). While extensive future work is still needed to verify these predictions *in vivo*, a recent study

has produced probe recordings of neurons in RSG that encode angular velocity in the behaving animal as a result of vestibular and visual inputs (Keshavarzi et al., 2021). Aligning with our predictions, a large proportion of these angular head velocity cells are correlated with both the velocity and direction of head movements, indicating conjunctive encoding of the two (Keshavarzi et al., 2021). It is important to note that these findings included a large population of neurons that cannot all be attributed to LR cells, as both putative inhibitory and RSD neurons also exhibited angular head velocity tuning. This suggests that the speed code extracted from direction inputs by LR neurons may supplement speed signals extracted from sensory inputs to RSC in order to provide a multifaceted and robust retrosplenial speed signal, underlying the RSC's role in the integration of direction and sensory signals to generate complex spatial representations.

5.3.4 Future Directions

The optogenetic and computational work presented in this dissertation provide key novel insights into the circuitry and spatial computations employed by the RSG to support its navigational functions, but it also opens doors to new questions which should be investigated further.

First, our modeling work so far has focused on understanding the computational implications of thalamic inputs to LR cells. Future work will be needed to understand how these thalamic inputs interact precisely with dorsal subiculum inputs. Given the diversity of spatial and directional encoding seen in the dorsal subiculum (Bicanski and Burgess, 2020; Derdikman, 2009; Lever et al., 2009; Olson et al., 2017; Simonnet and

Brecht, 2019), computational models will allow for the rigorous undertanding of how each possible type of subicular input (e.g. axis versus boundary vector cells) to LR cells interacts with thalamic head direction inputs. Very recent work on understanding the tuning properties of subicular cells in a projection-specific manner will help to narrow the functional range of possible dorsal subicular inputs to LR cells (Kitanishi et al., 2021). We anticipate that one key impact of dorsal subicular inputs to LR cells will be to impose a spatial filter on the angular speed and directional predictions stated above. In particular, the precise organization of layer 1 dendrites and axons may make LR cells most responsive to the near-synchronous arrival of inputs from both thalamic head direction cells (at distal apical dendrites in L1a) and dorsal subicular boundary vector or axis cells (at more proximal apical dendrite locations in lower L1). Similar cooperative dendritic activation patterns are also a hallmark of integration of entorhinal and CA3 inputs by CA1 pyramidal cells, where they help to overcome the effects of strong dendritic inhibition and shape the firing of place cells (Ahmed and Mehta, 2009; Golding and Spruston, 1998; Kamondi et al., 1998; Takahashi et al., 2012).

Second, we have only reported the synaptic dynamics and signaling to principal neurons in RSG, leaving the role of inhibitory interneurons in these circuits completely unexplored. Another important consideration within the circuits examined here is the role of feedforward inhibition. Matrix TC inputs evoke feedforward inhibition to regulate cortical signaling through both disinhibition (Anastasiades et al., 2021; Delevich et al., 2015) and the disynaptic inhibition of pyramidal neurons (Cruikshank et al., 2012; Yamawaki et al., 2019b, 2019a). Similarly, ClaC inputs invoke feedforward inhibition in several cortical regions, particularly through recruitment of neuropeptide Y (NPY) and,

to a lesser degree, FS cells (Jackson et al., 2018). Long-range inhibitory signals from CA1 of the hippocampus also target apical dendrites in retrosplenial layer 1a, converging with excitatory anterior thalamic inputs, to precisely regulate these TC inputs and establish a hippocampo-thalamo-retrosplenial network (Yamawaki et al., 2019b). This fine-grained laminar overlap strongly suggests that these inhibitory signals may regulate responses to matrix TC input more strongly for LR than layer 5 RS cells and should be investigated further, particularly in the context of integration of spatial information processing. Thus, extensive future optogenetic circuit mapping studies should explicitly examine the synaptic dynamics of and inhibitory interneuron responses to these converging inputs in RSG. Such experiments would provide a profile for inhibitory recruitment by these inputs and provide a more comprehensive view of the circuit as a whole. Future work should also examine the effect of feedforward inhibition on the subpopulations of retrosplenial principal neurons in response to these converging inputs in order to establish a thorough understanding of the circuitry facilitating retrosplenial information processing, particularly with regards to head direction signals.

Third, extensive examination of the contralateral circuit between retrosplenial hemispheres would provide valuable insights into the interhemispheric and ultimate output of spatial coding performed by the RSC. As previously mentioned, anatomical evidence shows that layers 2/3 RSG neurons send projections to the homotypic region of the contralateral hemisphere (Sripanidkulchai and Wyss, 1987; van Groen and Wyss, 2003), suggesting that the LR neurons which dominate layers 2/3 may at least in part contribute to these projections. Based on our supplemental findings that RS neurons receive strong and selective inputs from contralateral projections (Supplemental Figure

3-3S), we have predicted that LR neurons in one hemisphere, which receive unilateral inputs from directional cells in ADAV, transmit their conjunctive head direction and rotational speed signals to RS cells in the contralateral RSG, specifically. This would provide a circuit that enables a hemispheric switch of head direction and rotation information that could be integrated with motor signals via the RS neurons. Extensive experimental work is still needed to investigate this contralateral circuit to determine whether the contralateral projections are indeed arising from LR neurons and how the RS neurons encode these signals, as has been suggested in previous sections of this chapter.

Interestingly, egocentric boundary vector cells in RSD have also been shown to exhibit unique hemispheric coding properties, such that EBCs with a leftward preferred orientation were most often located in the right hemisphere (Alexander et al., 2020; van Wijngaarden et al., 2020), and extracellular simulation studies have shown monosynaptic connections between RSD hemispheres (Sempere-ferràndez et al., 2019; Sempere-Ferràndez et al., 2018). Such contralateral flips in directional tuning have not been observed in other spatially relevant regions such as the anterior thalamus, suggesting that these contralateral circuits in the RSC, which may be facilitated by LR neurons, may play a role in its unique navigational codes. Currently, there is no transgenic line or unique marker that can label LR neurons, so we are unable to selectively drive activity in the LR population and measure responses in the contralateral hemisphere, and we have already discussed the potential experiments that could help identify such a marker in the previous section. Our supplemental experiments reported here used a nonspecific injection of channelrhodopsin (ChR2) into

one hemisphere of RSG, and this was not limited to LR neurons or even superficial layers, instead labeling cells across the layers. Future work should aim to isolate LR projections in order to carefully examine this specific contralateral circuit. Such studies would provide essential insight into the downstream targets of LR neurons, as well as the role of RS cells in this spatial circuit.

Lastly, an interesting avenue for future investigation would be to examine the reciprocal projections of layer 6 corticothalamic RSG cells to ADAV. Indeed, the RSC provides dense connections to ADAV (van Groen et al., 1993; van Groen and Wyss, 2003, 1990), and disrupting these reciprocal connections impairs directional coding by ADAV HD cells (Clark et al., 2010). This suggests that retrosplenial output is at least partly supporting ADAV directional tuning, and examining these layer 6 projections may help identify underlying mechanisms. Taken together, these suggested future directions would provide an exhaustive view of the larger navigational circuit employed by the RSG.

5.4 Key Findings and Future Directions for the Cholinergic Modulation of RSG Neurons

5.4.1 Low-Rheobase Neurons are not Directly Modulated by Cholinergic Tone

Because cholinergic signaling is tightly associated with active navigation (Hamlin et al., 2013; Solari and Hangya, 2018; Winkler et al., 1995; Yoder et al., 2017), we examined how RSG neurons are directly modulated by cholinergic tone. These

experiments are the first to explore the effects of cholinergic signaling in RSG at the cellular level. Surprisingly, we found that LR neurons are not directly modulated by cholinergic signaling, showing no slow afterdepolarization potentials (sADPs) or persistent activity (Figures 4-1 & 4-2). In contrast, RS neurons across the layers exhibited sADPs and persistent firing (Figures 4-1 & 4-2). This finding is significant because it suggests that LR neurons can robustly encode and compute spatial signals regardless of cholinergic neurotransmission. In other words, these specialized cells do not rely on cholinergic input to perform their navigational functions and can exhibit consistent activity both when the animal is standing still and when it is actively moving.

It is also important to note that LR neurons remain the only clearly defined cortical principal neuron that is not directly affected by cholinergic modulation. Superficial and deep layer neurons in other cortical regions reliably display persistent firing (Egorov et al., 2002; Jochems et al., 2013; Ratté et al., 2018; Seamans et al., 2003; Yan et al., 2009; Yoshida et al., 2008; Zhang and Seguela, 2010) or exhibit sADPs (Gulledge et al., 2009). The only exception, to our knowledge, is two studies which report that neurons in the superficial layers of ACC exhibit a lower percentage of persistently firing cells compared to other regions (Ratté et al., 2018; Zhange and Segula, 2010). However, both of these studies used lower concentrations of CCh compared to our protocol (10 µM versus 40 µM), and they did not examine sADPs. In order to explore this difference, we recorded from superficial ACC neurons following our higher CCh protocols and examined both sADP amplitudes and persistence. Under our experimental conditions, we recorded clear sADPs followed by persistent firing in 100% of ACC layer 2/3 neurons tested (Supplemental Figure 4-1S), thus establishing LR

neurons as the only clearly defined principal neuronal subtype that has been shown to exhibit no features of persistent activity in response to cholinergic input.

5.4.2 Regular-Spiking and Intrinsically-Bursting Neurons are Universally Modulated by Cholinergic Signaling

In contrast to our findings showing lack of persistent activity or sADPs in LR cells, superficial and deep layer RS cells and layer 5 intrinsically-bursting (IB) neurons showed robust persistent firing responses to cholinergic signaling (Figures 4-1 & 4-2). This persistence was independent of morphological and anatomical features (Figure 4-4), as well as sex, indicating that persistence is a ubiquitous feature of non-LR principal neurons in RSG. Additionally, persistence in RS cells was reliant on M1 acetylcholine receptor activity (Figure 4-3), which is consistent with what has been reported in other regions (Navaroli et al., 2012; Yan et al., 2009). These findings are the first to directly assess cholinergic modulation in pyramidal cells in RSG, and they indicate that with the exception of LR neurons, cholinergic induction of persistence in RSG follows the same mechanisms as other cortical regions.

These results also suggest that RS and IB cells may support the path integration functions of the RSC (Chrastil et al, 2017, 2015; Cooper and Mizumori, 1999; Sherrill et al., 2013). As discussed in Chapter 4, persistent activity is thought to support working memory and path integration (Hasselmo, 2008; McNaughton et al., 2006; Yoshida et al., 2012), and computational models of regions like the MEC suggest that the integration of direction and speed signals modulates the firing rate of persistent cells to create a rate

code of position (Hasselmo, 2008). While this dissertation has shown that RS neurons do not receive inputs from spatial regions, it also predicts that RS neurons are targeted by projections from contralateral LR neurons. If this prediction is true, RS cells would receive the integrated direction and speed code generated by LR neurons in the contralateral hemisphere, resulting in modulated RS firing rates that provide an updated rate code of position similar to what has been predicted in the MEC. Thus, RS and IB cells may underly the retrosplenial role in path integration by providing a rate code that is spatially modulated by contralateral LR inputs, but extensive future work is needed to verify this.

5.4.3 Future Directions

The cholinergic system is heavily implicated in spatial navigation (Hamlin et al., 2013; Solari and Hangya, 2018; Winkler et al., 1995; Yoder et al., 2017), and careful examination of cholinergic modulation of the RSC will aid in establishing a comprehensive mechanistic view of retrosplenial control of navigation. First, identifying the exact computational function of RS and IB cell persistence in RSG remains a critical gap in current knowledge. Our results have shown that cholinergic-induced persistent activity is a ubiquitous feature of RS and IB neurons in this region. This well conserved firing property suggests it must serve an important role in the coding functions of these neurons, but no experimental work to our knowledge has identified the computational benefits of cholinergic induced persistent activity in RSG.

Second, while our results show that LR activity is not directly modulated by cholinergic tone, cholinergic signaling in RSG may still influence LR cell coding of space through the modulation of thalamocortical and other spatial inputs to these cells. Indeed, there is a high expression of muscarinic receptors localized to both the presynaptic ADAV axons and terminals and postsynaptic RSG neurons (Vogt, 1984; Vogt and Burns, 1988), and cholinergic signaling in other cortical regions directly impacts thalamocortical signaling through the reduction of synaptic potential amplitudes via muscarinic receptor activation (Gil et al., 1997; Hsieh et al., 2000) and enhancement of postsynaptic responses via nicotinic receptor activation (Gil et al., 1997; Hasselmo, 2006). Similarly, selective suppression of corticocortical versus thalamocortical signaling via cholinergic receptor activation in neocortical regions is suggested to mediate precise spatial processing by serving as a focusing mechanism to filter unnecessary sensory information (Castro-Alamancos and Oldford, 2002). It is likely that cholinergic modulation of thalamocortical afferents also exists in RSG, as there is distinct laminar overlap between basal forebrain and ADAV projections that may result in the convergence of cholinergic and thalamocortical signaling on LR dendrites at the synapse level. This would enable modulation of ADAV inputs to LR cells that could have a profound effect on the spatial coding of LR neurons, as we have shown that the precise synaptic dynamics of these thalamic direction inputs enable the computation of angular speed. Future work should utilize a combination of optogenetic circuit mapping and pharmacological intervention to investigate if and how ADAV synaptic dynamics change in the presence of increased cholinergic signaling in order to comprehensively assess the spatial computations performed by LR neurons during navigation.

Lastly, we also must consider the effects of cholinergic signaling on inhibitory neurons in RSG, as we have shown that the superficial layers represent a network dominated by feedforward inhibition (Figure 2-6). Due to the relatively high I→E connectivity, cholinergic modulation of inhibitory signaling in superficial RSG is likely to have a profound impact on LR activity. Indeed, cholinergic signaling induces feedforward inhibition on cortical layer 2/3 pyramidal cells via the activation of nicotinic receptors on neighboring inhibitory interneurons (Arroyo et al., 2014, 2012; Kawaguchi and Kubota, 1997; Letzkus et al., 2011; Obermayer et al., 2017; Verhoog et al., 2016), suggesting similar recruitment of inhibition may occur in the RSC during states of high cholinergic tone, such as navigation. This could be investigated using similar methods employed in this dissertation but recording from inhibitory interneurons in the superficial RSG to directly assess how they respond to cholinergic signaling. Such work would provide valuable insights into the currently unexplored influence of local inhibition on the navigational functions of the RSC.

5.5 Implications for Retrosplenial Impairment in Disease

Patients with damage to their RSC display spatial disorientation reflecting a specific impairment in orientation and not necessarily location (Bottini et al., 1990; Ino et al., 2007; Osawa et al., 2007; Takahashi et al., 1997; Valenstein et al., 1987). This manifests as an awareness of the current location and target location but lack of awareness on how to navigate from one to the other (Ino et al., 2007; Osawa et al.,

2007; Valenstein et al., 1987). One case study of a patient who suffered a hemorrhage in his left RSC reports the following:

> "[the patient] suddenly lost his knowledge of his route to his house while returning home after work. He could recognize buildings and the landscape and therefore understand where he was, but the landmarks that he recognized did not provoke directional information about any other places with respect to those landmarks. Consequently, he could not determine which direction to proceed to go home" (Ino et al., 2007).

A similar account of disorientation in a separate patient is as follows:

> "Although the patient was able to comply with his daily activities, he needed someone's help to get out of his home. The patient asserted that he could visually recognize different places and streets, but he did not remember the routes to reach them or move between them" (Grossi et al., 2007).

However, this account is from a patient in the early stages of Alzheimer's disease (AD). This exact profile of spatial disorientation is seen in 93% of patients with AD, but it is not a result of memory impairment (Monacelli et al., 2003). Rather, this results from an inability to link familiar objects or locations with larger spaces in the environment (Monacelli et al., 2003), reflecting the exact same orientation impairment exhibited by patients with retrosplenial damage.

The RSC is severely understudied in AD literature, but retrosplenial dysfunction is likely a key component of early pathogenesis in AD. In presymptomatic, or "prodromal" stages of AD, the RSC is one of the first regions to show dysfunction, exhibiting hypometabolism (Minoshima et al., 1997; Nestor et al., 2003), impaired

functional connectivity (Nestor et al., 2003), atrophy (Pengas et al., 2010), and a reduction in number of synapses (Scheff et al., 2015). These degenerative changes in the RSC precede the formation of amyloid plaques or neurofibrillary tangles in the medial temporal lobe (Aggleton et al., 2016), indicating the involvement of RSC dysfunction early in AD pathogenesis. These findings of RSC impairment in AD coupled with the similarity in disorientation profiles shared between patients with RSC damage and AD strongly implicate the RSC as a key contributor to AD pathology. Indeed, the findings presented in this dissertation show that the RSG, specifically, contains a cell type and circuit optimized to encode and compute orientation information and that the RSG is directly modulated by cholinergic tone. Disruptions in cholinergic modulation and synaptic health that are present in AD (Aghourian et al., 2017; Contestabile, 2011; Nordberg, 2001; Nyakas et al., 2011) are likely to disrupt these navigational processes in RSG, likely leading to the disorientation symptoms seen in AD.

We propose that future work focused on AD pathophysiology and disease progression should aim to precisely characterize these impairments in RSC function. Experiments should examine the health of retrosplenial neurons, specifically LR cells, over the course of disease progression to determine when and how they begin to show impaired spatial coding. The entire circuit should also be closely investigated to identify changes in key spatial inputs and cholinergic modulation of this region. This work would provide a comprehensive profile of disease progression in RSC, providing a novel avenue for the identification of new therapies that target this disorientation profile or, perhaps more significant, new disease markers that can be used for earlier diagnosis and intervention.

Notably, this specific profile of disorientation is not limited to only RSC damage and AD. Patients with Parkinson's disease (PD) also exhibit the same difficulties with navigation in familiar environments, with one case study reporting:

> "I [the patient] used to walk alone in the wood, fog or no fog, but when the symptoms of Parkinson's disease appeared, I noticed I could not orient myself anymore, and in case of fog, I got lost. Now I am too disabled to get lost anymore" (Hovestadt et al., 1987).

Similar to AD, neuroimaging studies of patients with PD report changes in retrosplenial connectivity and activity (Chen et al., 2017; Hou et al., 2020; Nagano-Saito et al., 2004; Potvin-Desrochers et al., 2019), suggesting that RSC impairment may be conserved in diseases which show navigational challenges specifically regarding orientation. Indeed, retrosplenial impairment is not noted in frontotemporal dementia (FTD; Tan et al., 2013; Tu et al., 2015), where disorientation symptoms are rare (Hodges et al., 2004; Lindau et al., 2000). This suggests that retrosplenial dysfunction may be a conserved feature of degenerative and other diseases which exhibit similar profiles of disorientation, again highlighting the need for a detailed understanding of the mechanisms underlying retrosplenial control of navigation.

5.6 Concluding Remarks

The work communicated in this dissertation substantially advances the field through the identification and detailed classification of the cell types, circuits, and computations that support the RSG's role in navigation. Our comprehensive

investigations reveal a novel specialized cell type, which we name the Low-Rheobase (LR) neuron, localized in the superficial layers of RSG that receive precisely targeted spatial inputs to facilitate the conjunctive encoding of direction and computation of speed information. This work transcends the behavioral and anatomical retrosplenial literature by providing specific mechanisms underlying retrosplenial navigational control. More importantly, our work highlights the importance of precise, multifaceted characterization of retrosplenial cell types and functional connectivity to better understand retrosplenial circuits and computations in both health and disease.

BIBLIOGRAPHY

1. Abel T, Lattal KM. 2001. Molecular mechanisms of memory acquisition, consolidation and retrieval. *Curr Opin Neurobiol*. doi:10.1016/S0959-4388(00)00194-X

2. Abbott LF, Varela JA, Sen K, Nelson SB. 1997. Synaptic depression and cortical gain control. *Science (80-)* **275**:220–224. doi:10.1126/science.275.5297.221

3. Acharya L, Aghajan ZM, Vuong C, Moore JJ, Mehta MR. 2016. Causal Influence of Visual Cues on Hippocampal Directional Selectivity. *Cell* **164**:197–207. doi:10.1016/j.cell.2015.12.015

4. Aggleton JP, Christiansen K. 2015. The subiculum: The heart of the extended hippocampal systemProgress in Brain Research. Elsevier B.V. pp. 65–82. doi:10.1016/bs.pbr.2015.03.003

5. Aggleton JP, Wright NF, Vann SD, Saunders RC. 2012. Medial temporal lobe projections to the retrosplenial cortex of the macaque monkey. *Hippocampus* **22**:1883–1900. doi:10.1002/hipo.22024

6. Aggleton JP, Pralus A, Nelson AJD, Hornberger M. 2016. Thalamic pathology and memory loss in early Alzheimer's disease: Moving the focus from the medial temporal lobe to Papez circuit. *Brain*. doi:10.1093/brain/aww083

7. Aghourian M, Legault-Denis C, Soucy JP, Rosa-Neto P, Gauthier S, Kostikov A, Gravel P, Bedard MA. 2017. Quantification of brain cholinergic denervation in Alzheimer's disease using PET imaging with [18F]-FEOBV. *Mol Psychiatry* **22**:1531–1538. doi:10.1038/mp.2017.183

8. Ahmed OJ, Mehta MR. 2009. The hippocampal rate code: anatomy, physiology, and theory. *Trends Neurosci* **32**:329-338. doi:10.1016/j.tins.2009.01.009

9. Ainge JA, Van Der Meer MAA, Langston RF, Wood ER. 2007. Exploring the role of context-dependent hippocampal activity in spatial alternation behavior. *Hippocampus* **17**:988–1002. doi:10.1002/hipo.20301

10. Alan Agresti, editor. 2007. An Introduction to Categorical Data Analysis, 2nd ed. Wiley-Interscience. doi:10.1198/jasa.2008.s251

11. Albasser MM, Poirier GL, Warburton EC, Aggleton JP. 2007. Hippocampal lesions halve immediate-early gene protein counts in retrosplenial cortex: Distal dysfunctions in a spatial memory system. *Eur J Neurosci* **26**:1254–1266. doi:10.1111/j.1460-9568.2007.05753.x

12. Alexander AS, Carstensen LC, Hinman JR, Raudies F, William Chapman G, Hasselmo ME. 2020. Egocentric boundary vector tuning of the retrosplenial cortex. *Sci Adv* **6**. doi:10.1126/sciadv.aaz2322

13. Alexander AS, Rangel LM, Tingley D, Nitz DA. 2018. Neurophysiological signatures of temporal coordination between retrosplenial cortex and the hippocampal formation. *Behav Neurosci* **132**:453–468. doi:10.1037/bne0000254

14. Alexander AS, Nitz DA. 2017. Spatially periodic activation patterns of retrosplenial cortex encode route sub-spaces and distance travelled. *Curr Biol* **27**.

15. Alexander AS, Nitz DA. 2015. Retrosplenial cortex maps the conjunction of internal and external spaces. *Nat Neurosci* **18**:1143–1151.

16. Alvernhe A, Save E, Poucet B. 2011. Local remapping of place cell firing in the Tolman detour task. *Eur J Neurosci* **33**:1696–1705. doi:10.1111/j.1460-9568.2011.07653.x

17. Amaral DG, Dolorfo C, Alvarez-Royo P. 1991. Organization of CA1 projections to the subiculum: A PHA-L analysis in the rat. *Hippocampus* **1**:415–435. doi:10.1002/hipo.450010410

18. Anastasiades PG, Collins DP, Carter AG. 2021. Mediodorsal and Ventromedial Thalamus Engage Distinct L1 Circuits in the Prefrontal Cortex. *Neuron* **109**:314-330.e4. doi:10.1016/j.neuron.2020.10.031

19. Andersen P, Bland BH, Dudar JD. 1973. Organization of the hippocampal output. *Exp Brain Res* **17**:152–168. doi:10.1007/BF00235025

20. Andrade R. 1991. Cell excitation enhances muscarinic cholinergic responses in rat association cortex. *Brain Res* **548**:81–93. doi:10.1016/0006-8993(91)91109-E

21. Anzalone S, Roland J, Vogt B, Savage L. 2009. Acetylcholine efflux from retrosplenial areas and hippocampal sectors during maze exploration. *Behav Brain Res* **201**:272–278. doi:10.1016/j.bbr.2009.02.023

22. Arnold HM, Burk JA, Hodgson EM, Sarter M, Bruno JP. 2002. Differential cortical acetylcholine release in rats performing a sustained attention task versus behavioral control tasks that do not explicitly tax attention. *Neuroscience*

114:451–460. doi:10.1016/S0306-4522(02)00292-0

23. Arroyo S, Bennett C, Aziz D, Brown SP, Hestrin S. 2012. Prolonged disynaptic inhibition in the cortex mediated by slow, non-α7 nicotinic excitation of a specific subset of cortical interneurons. *J Neurosci* **32**:3859–3864. doi:10.1523/JNEUROSCI.0115-12.2012

24. Arroyo S, Bennett C, Hestrin S. 2014. Nicotinic modulation of cortical circuits. *Front Neural Circuits*. doi:10.3389/fncir.2014.00030

25. Auger SD, Mullally SL, Maguire EA. 2012. Retrosplenial cortex codes for permanent landmarks. *PLoS One* **7**:43620. doi:10.1371/journal.pone.0043620

26. Barry C, Lever C, Hayman R, Hartley T, Burton S, O'Keefe J, Jeffery K, Burgess N. 2006. The boundary vector cell model of place cell firing and spatial memory. *Rev Neurosci*. doi:10.1515/REVNEURO.2006.17.1-2.71

27. Barry C, Burgess N. 2014. Neural mechanisms of self-location. *Curr Biol*. doi:10.1016/j.cub.2014.02.049

28. Barthas F, Kwan AC. 2017. Secondary Motor Cortex: Where 'Sensory' Meets 'Motor' in the Rodent Frontal Cortex. *Trends Neurosci*. doi:10.1016/j.tins.2016.11.006

29. Beierlein M, Gibson JR, Connors BW. 2003. Two Dynamically Distinct Inhibitory Networks in Layer 4 of the Neocortex. *J Neurophysiol* **90**:2987–3000. doi:10.1152/jn.00283.2003

30. Belgard TG, Marques AC, Oliver PL, Abaan HO, Sirey TM, Hoerder-Suabedissen A, García-Moreno F, Molnár Z, Margulies EH, Ponting CP. 2011. A transcriptomic atlas of mouse neocortical layers. *Neuron* **71**:605–616. doi:10.1016/j.neuron.2011.06.039

31. Berger-Sweeney J, Heckers S, Mesulam MM, Wiley RG, Lappi DA, Sharma M. 1994. Differential effects on spatial navigation of immunotoxin-induced cholinergic lesions of the medial septal area and nucleus basalis magnocellularis. *J Neurosci* **14**:4507–4519. doi:10.1523/jneurosci.14-07-04507.1994

32. Bertil Hille. 2001. Ion channels of excitable membranes, 3rd ed. Sunderland, Massachusetts, USA: Sinauer associates Inc.

33. Bianchi R, Wong RKS. 1994. Carbachol-induced synchronized rhythmic bursts in CA3 neurons of guinea pig hippocampus in vitro. *J Neurophysiol* **72**:131–138. doi:10.1152/jn.1994.72.1.131

34. Bicanski A, Burgess N. 2020. Neuronal vector coding in spatial cognition. *Nat*

Rev Neurosci. doi:10.1038/s41583-020-0336-9

35. Bicanski A, Burgess N. 2018. A neural-level model of spatial memory and imagery. *Elife* **7**. doi:10.7554/eLife.33752

36. Bicanski A, Burgess N. 2016. Environmental Anchoring of Head Direction in a Computational Model of Retrosplenial Cortex. *J Neurosci* **36**:11601–11618. doi:10.1523/JNEUROSCI.0516-16.2016

37. Bigl V, Woolf NJ, Butcher LL. 1982. Cholinergic projections from the basal forebrain to frontal, parietal, temporal, occipital, and cingulate cortices: A combined fluorescent tracer and acetylcholinesterase analysis. *Brain Res Bull* **8**:727–749. doi:10.1016/0361-9230(82)90101-0

38. Blair HT, Lipscomb BW, Sharp PE. 1997. Anticipatory Time Intervals of Head-Direction Cells in the Anterior Thalamus of the Rat: Implications for Path Integration in the Head-Direction Circuit. *J Neurophysiol* **78**:145–159. doi:10.1152/jn.1997.78.1.145

39. Blair HT, Sharp PE. 1995. Anticipatory head direction signals in anterior thalamus: Evidence for a thalamocortical circuit that integrates angular head motion to compute head direction. *J Neurosci* **15**:6260–6270. doi:10.1523/jneurosci.15-09-06260.1995

40. Bottini G, Cappa S, Geminiani G, Sterzi R. 1990. Topographic disorientation-A case report. *Neuropsychologia* **28**:309–312. doi:10.1016/0028-3932(90)90024-I

41. Botvinick MM. 2007. Conflict monitoring and decision making: Reconciling two perspectives on anterior cingulate function. *Cogn Affect Behav Neurosci* **7**:356–366.

42. Brennan EKW, Sudhakar SK, Jedrasiak-Cape I, John TT, Ahmed OJ. 2020. Hyperexcitable Neurons Enable Precise and Persistent Information Encoding in the Superficial Retrosplenial Cortex. *CellReports* **30**:1598-1612.e8. doi:10.1016/j.celrep.2019.12.093

43. Brennan EKW, Jedrasiak-Cape I, Kailasa S, Rice SP, Kumar Sudhakar S, Ahmed OJ. 2021. Thalamus and claustrum control parallel layer 1 circuits in retrosplenial cortex. *eLife* **10:**e62207. doi:10.7554/eLife.62207

44. Brotons-Mas JR, Schaffelhofer S, Guger C, O'Mara SM, Sanchez-Vives M V. 2017. Heterogeneous spatial representation by different subpopulations of neurons in the subiculum. *Neuroscience* **343**:174–189. doi:10.1016/j.neuroscience.2016.11.042

45. Brown JW, Braver TS. 2005. Learned Predictions of Error Likelihood in the

Anterior Cingulate Cortex. *Science (80-)* **307**:1118–1121.

46. Brown SP, Mathur BN, Olsen SR, Luppi PH, Bickford ME, Citri A. 2017. New breakthroughs in understanding the role of functional interactions between the neocortex and the claustrum. *J Neurosci* **37**:10877–10881. doi:10.1523/JNEUROSCI.1837-17.2017

47. Buckley MJ, Mitchell AS. 2016. Retrosplenial Cortical Contributions to Anterograde and Retrograde Memory in the Monkey. *Cereb Cortex*. doi:10.1093/cercor/bhw054

48. Burgess N, Maguire EA, Spiers HJ, O'Keefe J. 2001. A temporoparietal and prefrontal network for retrieving the spatial context of lifelike events. *Neuroimage* **14**:439–453. doi:10.1006/nimg.2001.0806

49. Burgess N, Becker S, King JA, O'Keefe J. 2001. Memory for events and their spatial context: Models and experimentsPhilosophical Transactions of the Royal Society B: Biological Sciences. Royal Society. pp. 1493–1503. doi:10.1098/rstb.2001.0948

50. Burman KJ, Reser DH, Richardson KE, Gaulke H, Worthy KH, Rosa MGP. 2011. Subcortical projections to the frontal pole in the marmoset monkey. *Eur J Neurosci* **34**:303–319. doi:10.1111/j.1460-9568.2011.07744.x

51. Burke SN, Maurer AP, Nematollahi S, Uprety AR, Wallace JL, Barnes CA. 2011. The influence of objects on place field expression and size in distal hippocampal CA1. *Hippocampus* **21**:783–801. doi:10.1002/hipo.20929

52. Buzsáki G. 2015. Hippocampal sharp wave-ripple: A cognitive biomarker for episodic memory and planning. *Hippocampus* **25**:1073–1188. doi:10.1002/hipo.22488

53. Byrne P, Becker S, Burgess N. 2007. Remembering the past and imagining the future: A neural model of spatial memory and imagery. *Psychol Rev* **114**:340–375. doi:10.1037/0033-295X.114.2.340

54. Cadwell CR, Scala F, Li S, Livrizzi G, Shen S, Sandberg R, Jiang X, Tolias AS. 2017. Multimodal profiling of single-cell morphology, electrophysiology, and gene expression using Patch-seq. doi:10.1038/nprot.2017.120

55. Campbell MG, Ocko SA, Mallory CS, Low IIC, Ganguli S, Giocomo LM. 2018. Principles governing the integration of landmark and self-motion cues in entorhinal cortical codes for navigation. *Nat Neurosci* **21**:1096–1106. doi:10.1038/s41593-018-0189-y

56. Carnevale NT, Hines ML. 2006. The NEURON Book. Cambridge: Cambridge

University Press.

57. Carter CS, Braver TS, Barch DM, Botvinick MM, Noll D, Cohen JD. 1998. Anterior cingulate cortex, error detection, and the online monitoring of performance. *Science (80-)* **280**:747–749. doi:10.1126/science.280.5364.747

58. Castro-Alamancos MA, Oldford E. 2002. Cortical sensory suppression during arousal is due to the activity-dependent depression of thalamocortical synapses. *J Physiol* **541**:319–331. doi:10.1113/jphysiol.2002.016857

59. Chang HR, Esteves IM, Neumann AR, Sun J, Mohajerani MH, McNaughton BL. 2020. Coordinated activities of retrosplenial ensembles during resting-state encode spatial landmarks. *Philos Trans R Soc B Biol Sci* **375**. doi:10.1098/rstb.2019.0228

60. Chen B, Wang S, Sun W, Shang X, Liu H, Liu G, Gao J, Fan G. 2017. Functional and structural changes in gray matter of parkinson's disease patients with mild cognitive impairment. *Eur J Radiol* **93**:16–23. doi:10.1016/j.ejrad.2017.05.018

61. Chen LL, Lin L-H, Green Edward J, Barnes -Bruce CA, Mcnaughton L, Chert LL, Lin ' L-H, Green E J, Barnes CA, Mcnaughton BL. 1994. Head-direction cells in the rat posterior cortex I. anatomical distribution and behavioral modulation, Exp Brain Res. Springer-Verlag.

62. Cho J, Sharp PE. 2001. Head direction, place, and movement correlates for cells in the rat retrosplenial cortex. *Behav Neurosci* **115**:3–25. doi:10.1037/0735-7044.115.1.3

63. Cho J-H, Rendall SD, Gray JM. 2017. Brain-wide maps of Fos expression during fear learning and recall. *Learn Mem* **24**:169–181. doi:10.1101/lm.044446

64. Chrastil ER. 2018. Heterogeneity in human retrosplenial cortex: A review of function and connectivity. *Behav Neurosci*.

65. Chrastil ER, Sherrill KR, Aselcioglu I, Hasselmo ME, Stern CE. 2017. Individual Differences in Human Path Integration Abilities Correlate with Gray Matter Volume in Retrosplenial Cortex, Hippocampus, and Medial Prefrontal Cortex. *eneuro*. doi:10.1523/eneuro.0346-16.2017

66. Chrastil ER, Sherrill KR, Hasselmo ME, Stern CE. 2015. There and back again: Hippocampus and retrosplenial cortex track homing distance during human path integration. *J Neurosci* **35**:15442–15452. doi:10.1523/JNEUROSCI.1209-15.2015

67. Clark BJ, Bassett JP, Wang SS, Taube JS. 2010. Impaired Head Direction Cell Representation in the Anterodorsal Thalamus after Lesions of the Retrosplenial

Cortex. *J Neurosci* **30**:5289.

68. Clascá F, Rubio-Garrido P, Jabaudon D. 2012. Unveiling the diversity of thalamocortical neuron subtypes. *Eur J Neurosci* **35**:1524–1532. doi:10.1111/j.1460-9568.2012.08033.x

69. Collins DP, Anastasiades PG, Marlin JJ, Correspondence AGC. 2018. Reciprocal Circuits Linking the Prefrontal Cortex with Dorsal and Ventral Thalamic Nuclei. *Neuron* **98**:366-379.e4. doi:10.1016/j.neuron.2018.03.024

70. Connors BW, Gutnick MJ. 1990. Intrinsic firing patterns of diverse neocortical neurons. *Trends Neurosci* **13**:99–104.

71. Contestabile A. 2011. The history of the cholinergic hypothesis. *Behav Brain Res*. doi:10.1016/j.bbr.2009.12.044

72. Cooper BG, Manka TF, Mizumori SJY. 2001. Finding your way in the dark: The retrosplenial cortex contributes to spatial memory and navigation without visual cues. *Behav Neurosci* **115**:1012–1028. doi:10.1037/0735-7044.115.5.1012

73. Cooper BG, Mizumori SJY. 2001. Temporary inactivation of the retrosplenial cortex causes a transient reorganization of spatial coding in the hippocampus. *J Neurosci* **21**:3986–4001. doi:10.1523/jneurosci.21-11-03986.2001

74. Cooper BG, Mizumori SJY. 1999. Retrosplenial cortex inactivation selectively impairs navigation in darkness. *Neuroreport* **10**:625–630.

75. Crick FC, Koch C. 2005. What is the function of the claustrum? *Philos Trans R Soc B Biol Sci* **360**:1271–1279. doi:10.1098/rstb.2005.1661

76. Cruikshank SJ, Ahmed OJ, Stevens TR, Patrick SL, Gonzalez AN, Elmaleh M, Connors BW. 2012. Thalamic control of layer 1 circuits in prefrontal cortex. *J Neurosci* **32**:17813–17823.

77. Cullen KE, Taube JS. 2017. Our sense of direction: progress, controversies and challenges. *Nat Neurosci* **20**:1465–1473. doi:10.1038/nn.4658

78. Czajkowski R, Jayaprakash B, Wiltgen B, Rogerson T, Guzman-Karlsson MC, Barth AL, Trachtenberg JT, Silva AJ. 2014. Encoding and storage of spatial information in the retrosplenial cortex. *Proc Natl Acad Sci U S A* **111**:8661–8666. doi:10.1073/pnas.1313222111

79. Da Costa NM, Fürsinger D, Martin KAC. 2010. The synaptic organization of the claustral projection to the cat's visual cortex. *J Neurosci* **30**:13166–13170. doi:10.1523/JNEUROSCI.3122-10.2010

80. Danielson NB, Zaremba JD, Kaifosh P, Bowler J, Ladow M, Losonczy A. 2016. Sublayer-Specific Coding Dynamics during Spatial Navigation and Learning in Hippocampal Area CA1. *Neuron* **91**:652–665. doi:10.1016/j.neuron.2016.06.020

81. de la Rocha J, Parga N. 2008. Thalamocortical transformations of periodic stimuli: The effect of stimulus velocity and synaptic short-term depression in the vibrissa-barrel system. *J Comput Neurosci* **25**:122–140. doi:10.1007/s10827-007-0068-0

82. de Sousa AF, Cowansage KK, Zutshi I, Cardozo LM, Yoo EJ, Leutgeb S, Mayford M. 2019. Optogenetic reactivation of memory ensembles in the retrosplenial cortex induces systems consolidation. *Proc Natl Acad Sci U S A* **116**:8576–8581. doi:10.1073/pnas.1818432116

83. Dégenètais E, Thierry A-M, Glowinski J, Gioanni Y. 2002. Electrophysiological properties of pyramidal neurons in the rat prefrontal cortex: an in vivo intracellular recording study. *Cereb Cortex* **12**:1–16. doi:10.1093/cercor/12.1.1

84. Delevich K, Tucciarone J, Huang ZJ, Li B. 2015. The mediodorsal thalamus drives feedforward inhibition in the anterior cingulate cortex via parvalbumin interneurons. *J Neurosci* **35**:5743–5753. doi:10.1523/JNEUROSCI.4565-14.2015

85. Dembrow NC, Chitwood RA, Johnston D. 2010. Projection-specific neuromodulation of medial prefrontal cortex neurons. *J Neurosci* **30**:16922–16937. doi:10.1523/JNEUROSCI.3644-10.2010

86. Derdikman D. 2009. Are the boundary-related cells in the subiculum boundary-vector cells? *J Neurosci*. doi:10.1523/JNEUROSCI.4176-09.2009

87. Devinsky O, Morrell MJ, Vogt BA. 1995. Contributions of anterior cingulate cortex to behaviour. *Brain* **118**:279–306. doi:10.1093/brain/118.1.279

88. Donoghue JP, Carroll KL. 1987. Cholinergic modulation of sensory responses in rat primary somatic sensory cortex. *Brain Res* **408**:367–371. doi:10.1016/0006-8993(87)90407-0

89. Dragoi G, Buzsáki G. 2006. Temporal Encoding of Place Sequences by Hippocampal Cell Assemblies. *Neuron* **50**:145–157. doi:10.1016/j.neuron.2006.02.023

90. Duguid I, Branco T, London M, Chadderton P, Häusser M. 2012. Tonic inhibition enhances fidelity of sensory information transmission in the cerebellar cortex. *J Neurosci* **32**:11132–43. doi:10.1523/JNEUROSCI.0460-12.2012

91. Dupire A, Kant P, Mons N, Marchand AR, Coutureau E, Dalrymple-Alford J, Wolff M. 2013. A role for anterior thalamic nuclei in affective cognition: Interaction with

environmental conditions. *Hippocampus* **23**:392–404. doi:10.1002/hipo.22098

92. Eckenstein FP, Baughman RW, Quinn J. 1988. An anatomical study of cholinergic innervation in rat cerebral cortex. *Neuroscience* **25**:457–474. doi:10.1016/0306-4522(88)90251-5

93. Egorov A V., Hamam BN, Fransén E, Hasselmo ME, Alonso AA. 2002. Graded persistent activity in entorhinal cortex neurons. *Nature* **420**:173–178. doi:10.1038/nature01171

94. Elduayen C, Save E. 2014. The retrosplenial cortex is necessary for path integration in the dark. *Behav Brain Res* **272**:303–307. doi:http://dx.doi.org/10.1016/j.bbr.2014.07.009

95. Epstein RA. 2008. Parahippocampal and retrosplenial contributions to human spatial navigation. *Trends Cogn Sci* **12**:388–396.

96. Erisir A, Lau D, Rudy B, Leonard CS. 1999. Function of specific K(+) channels in sustained high-frequency firing of fast-spiking neocortical interneurons. *J Neurophysiol* **82**:2476–89. doi:10.1152/jn.1999.82.5.2476

97. Erlich JC, Bialek M, Brody CD. 2011. A cortical substrate for memory-guided orienting in the rat. *Neuron* **72**:330–343. doi:10.1016/j.neuron.2011.07.010

98. Etienne AS, Jeffery KJ. 2004. Path integration in mammals. *Hippocampus*. doi:10.1002/hipo.10173

99. Evans T, Bicanski A, Bush D, Burgess N. 2016. How environment and self-motion combine in neural representations of space. *J Physiol* **594**:6535–6546. doi:10.1113/JP270666

100. Feng L, Zhao T, Kim J. 2015. Neutube 1.0: A new design for efficient neuron reconstruction software based on the swc format. *eNeuro* **2**. doi:10.1523/ENEURO.0049-14.2014

101. Ferguson KA, Cardin JA. 2020. Mechanisms underlying gain modulation in the cortex. *Nat Rev Neurosci*. doi:10.1038/s41583-019-0253-y

102. Frank LM, Brown EN, Wilson M. 2000. Trajectory encoding in the hippocampus and entorhinal cortex. *Neuron* **27**:169–178. doi:10.1016/S0896-6273(00)00018-0

103. Frankland PW, Bontempi B, Talton LE, Kaczmarek L, Silva AJ. 2004. The Involvement of the Anterior Cingulate Cortex in Remote Contextual Fear Memory. *Science (80-)* **304**:881–883. doi:10.1126/science.1094804

104. Fu X, Ye H, Jia H, Wang X, Chomiak T, Luo F. 2019. Muscarinic acetylcholine

receptor-dependent persistent activity of layer 5 intrinsic-bursting and regular-spiking neurons in primary auditory cortex. *J Neurophysiol* **122**:2344–2353. doi:10.1152/jn.00184.2019

105. Fuhrmann G, Markram H, Tsodyks M. 2017. Spike Frequency Adaptation and Neocortical Rhythms. *J Neurophysiol* **88**:761–770. doi:10.1152/jn.2002.88.2.761

106. Fuhs MC, Touretzky DS. 2006. A spin glass model of path integration in rat medial entorhinal cortex. *J Neurosci* **26**:4266–4276. doi:10.1523/JNEUROSCI.4353-05.2006

107. Funahashi M, Stewart M. 1997. Presubicular and parasubicular cortical neurons of the rat: Functional separation of deep and superficial neurons in vitro. *J Physiol* **501**:387–403. doi:10.1111/j.1469-7793.1997.387bn.x

108. Fuzik J, Zeisel A, Máté Z, Calvigioni D, Yanagawa Y, Szabó G, Linnarsson S, Harkany T. 2015. Integration of electrophysiological recordings with single-cell RNA-seq data identifies neuronal subtypes. *Nat Biotechnol* **34**. doi:10.1038/nbt.3443

109. Fyhn M, Hafting T, Treves A, Moser MB, Moser EI. 2007. Hippocampal remapping and grid realignment in entorhinal cortex. *Nature* **446**:190–194. doi:10.1038/nature05601

110. Garden DLF, Massey P V., Caruana DA, Johnson B, Warburton EC, Aggleton JP, Bashir ZI. 2009. Anterior thalamic lesions stop synaptic plasticity in retrosplenial cortex slices: expanding the pathology of diencephalic amnesia. *Brain* **132**:1847–1857. doi:10.1093/brain/awp090

111. Gil M, Ancau M, Schlesiger MI, Neitz A, Allen K, De Marco RJ, Monyer H. 2018. Impaired path integration in mice with disrupted grid cell firing. *Nat Neurosci*. doi:10.1038/s41593-017-0039-3

112. Gil Z, Connors BW, Amitai Y. 1997. Differential regulation of neocortical synapses by neuromodulators and activity. *Neuron* **19**:679–686. doi:10.1016/S0896-6273(00)80380-3

113. Giovannini MG, Rakovska A, Benton RS, Pazzagli M, Bianchi L, Pepeu G. 2001. Effects of novelty and habituation on acetylcholine, GABA, and glutamate release from the frontal cortex and hippocampus of freely moving rats. *Neuroscience* **106**:43–53. doi:10.1016/S0306-4522(01)00266-4

114. Goldberg EM, Clark BD, Zagha E, Nahmani M, Erisir A, Rudy B. 2008. K+ Channels at the Axon Initial Segment Dampen Near-Threshold Excitability of Neocortical Fast-Spiking GABAergic Interneurons. *Neuron* **58**:387–400. doi:10.1016/J.NEURON.2008.03.003

115. Golding, NL, Spruston, N. 1998. Dendritic sodium spikes are variable triggers of axonal action potentials in hippocampal CA1 pyramidal neurons. *Neuron* **21**:1189-1200. doi:10.1016/s0896-6273(00)80635-2

116. Goll Y, Atlan G, Citri A. 2015. Attention: The claustrum. *Trends Neurosci*. doi:10.1016/j.tins.2015.05.006

117. Golomb D, Donner K, Shacham L, Shlosberg D, Amitai Y, Hansel D. 2007. Mechanisms of firing patterns in fast-spiking cortical interneurons. *PLoS Comput Biol* **3**:e156. doi:10.1371/journal.pcbi.0030156

118. Goodridge JP, Dudchenko PA, Worboys KA, Golob EJ, Taube JS. 1998. Cue control and head direction cells. *Behav Neurosci* **112**:749–761. doi:10.1037//0735-7044.112.4.749

119. Goodridge JP, Taube JS. 1997. Interaction between the postsubiculum and anterior thalamus in the generation of head direction cell activity. *J Neurosci* **17**:9315–9330. doi:10.1523/jneurosci.17-23-09315.1997

120. GoodSmith D, Chen X, Wang C, Kim SH, Song H, Burgalossi A, Christian KM, Knierim JJ. 2017. Spatial Representations of Granule Cells and Mossy Cells of the Dentate Gyrus. *Neuron* **93**:677-690.e5. doi:10.1016/j.neuron.2016.12.026

121. Greicius MD, Supekar K, Menon V, Dougherty RF. 2009. Resting-State Functional Connectivity Reflects Structural Connectivity in the Default Mode Network. *Cereb Cortex* **19**:72–78. doi:10.1093/cercor/bhn059

122. Grossi D, Fasanaro AM, Cecere R, Salzano S, Trojano L. 2007. Progressive topographical disorientation: A case of focal Alzheimer's disease. *Neurol Sci* **28**:107–110. doi:10.1007/s10072-007-0797-x

123. Gu Y, Lewallen S, Kinkhabwala AA, Domnisoru C, Yoon K, Gauthier JL, Fiete IR, Tank DW. 2018. A Map-like Micro-Organization of Grid Cells in the Medial Entorhinal Cortex. *Cell* **175**:736-750.e30. doi:10.1016/j.cell.2018.08.066

124. Guan D, Tkatch T, Surmeier DJ, Armstrong WE, Foehring RC. 2007. Kv2 subunits underlie slowly inactivating potassium current in rat neocortical pyramidal neurons. *J Physiol* **581**:941–960. doi:10.1113/jphysiol.2007.128454

125. Guariglia CC, Nitrini R. 2009. Topographical disorientation in alzheimer's disease. *Arq Neuropsiquiatr* **67**:967–972. doi:10.1590/S0004-282X2009000600001

126. Gulledge AT, Bucci DJ, Zhang SS, Matsui M, Yeh HH. 2009. M1 receptors mediate cholinergic modulation of excitability in neocortical pyramidal neurons. *J*

Neurosci **29**:9888–9902. doi:10.1523/JNEUROSCI.1366-09.2009

127. Guo K, Yamawaki N, Svoboda K, Shepherd GMG. 2018. Anterolateral motor cortex connects with a medial subdivision of ventromedial thalamus through cell type-specific circuits, forming an excitatory thalamo-cortico-thalamic loop via layer 1 apical tuft dendrites of layer 5B pyramidal tract type neurons. *J Neurosci* **38**:8787–8797. doi:10.1523/JNEUROSCI.1333-18.2018

128. Guo Z V., Li N, Huber D, Ophir E, Gutnisky D, Ting JT, Feng G, Svoboda K. 2014. Flow of cortical activity underlying a tactile decision in mice. *Neuron* **81**:179–194. doi:10.1016/j.neuron.2013.10.020

129. Guterstam A, Björnsdotter M, Gentile G, Ehrsson HH. 2015. Posterior cingulate cortex integrates the senses of self-location and body ownership. *Curr Biol* **25**:1416–1425. doi:10.1016/j.cub.2015.03.059

130. Gyengesi, E, Andrews, Z, Paxinos, G, Zaborszky, L. 2013. Distribution of secretagogin-containing neurons in the basal forebrain of mice, with special reference to the cholinergic corticopetal system. *Brain Res Bulletin* **94**:1-8. doi:10.1016/j.brainresbull.2013.01.009

131. Hafting T, Fyhn M, Molden S, Moser MB, Moser EI. 2005. Microstructure of a spatial map in the entorhinal cortex. *Nature* **436**:801–806. doi:10.1038/nature03721

132. Haj-Dahmane S, Andrade R. 1998. Ionic mechanism of the slow afterdepolarization induced by muscarinic receptor activation in rat prefrontal cortex. *J Neurophysiol* **80**:1197–1210. doi:10.1152/jn.1998.80.3.1197

133. Hamlin AS, Windels F, Boskovic Z, Sah P, Coulson EJ. 2013. Lesions of the Basal Forebrain Cholinergic System in Mice Disrupt Idiothetic Navigation. *PLoS One* **8**:53472. doi:10.1371/journal.pone.0053472

134. Han CJ, O'Tuathaigh CM, Van Trigt L, Quinn JJ, Fanselow MS, Mongeau R, Koch C, Anderson DJ. 2003. Trace but not delay fear conditioning requires attention and the anterior cingulate cortex. *Proc Natl Acad Sci U S A* **100**:13087–13092. doi:10.1073/pnas.2132313100

135. Hanbery J, Jasper H. 1953. Independence of diffuse thalamo-cortical projection system shown by specific nuclear destructions. *J Neurophysiol* **16**:252–271.

136. Hanks TD, Kopec CD, Brunton BW, Duan CA, Erlich JC, Brody CD. 2015. Distinct relationships of parietal and prefrontal cortices to evidence accumulation. *Nature* **520**:220–223. doi:10.1038/nature14066

137. Hargreaves EL, Yoganarasimha D, Knierim JJ. 2007. Cohesiveness of spatial

and directional representations recorded from neural ensembles in the anterior thalamus, parasubiculum, medial entorhinal cortex, and hippocampus. *Hippocampus* **17**:826–841. doi:10.1002/hipo.20316

138. Harker KT, Whishaw IQ. 2004. A reaffirmation of the retrosplenial contribution to rodent navigation: reviewing the influences of lesion, strain, and task. *Neurosci Biobehav Rev* **28**:485–496. doi:http://dx.doi.org/10.1016/j.neubiorev.2004.06.005

139. Hasselmo ME. 2008. Grid cell mechanisms and function: Contributions of entorhinal persistent spiking and phase resetting. *Hippocampus* **18**:1213–1229. doi:10.1002/hipo.20512

140. Hasselmo ME. 2006. The role of acetylcholine in learning and memory. *Curr Opin Neurobiol*. doi:10.1016/j.conb.2006.09.002

141. Hattori R, Danskin B, Babic Z, Mlynaryk N, Komiyama T. 2019. Area-Specificity and Plasticity of History-Dependent Value Coding During Learning. *Cell* **177**:1858–1872. doi:10.1016/j.cell.2019.04.027

142. Hattox AM, Nelson SB. 2007. Layer V neurons in mouse cortex projecting to different targets have distinct physiological properties. *J Neurophysiol* **98**:3330–3340. doi:10.1152/jn.00397.2007

143. Häusser M. 2001. Synaptic function: Dendritic democracy. *Curr Biol*. doi:10.1016/S0960-9822(00)00034-8

144. Hedlund E, Deng Q. 2018. Single-cell RNA sequencing: Technical advancements and biological applications. *Mol Aspects Med*. doi:10.1016/j.mam.2017.07.003

145. Heilman KM, Sypert GW. 1977. Korsakoff's syndrome resulting from bilateral fornix lesions. *Neurology* **27**:490.

146. Henderson VW, Mack W, Williams BW. 1989. Spatial Disorientation in Alzheimer's disease. *Arch Neurol* **46**:391–394. doi:10.1001/archneur.1989.00520400045018

147. Henseler J, Ringle CM, Sinkovics RR. 2009. The use of partial least squares path modeling in international marketing. *Adv Int Mark* **20**:277–319. doi:10.1108/S1474-7979(2009)0000020014

148. Herkenham M. 1986. New Perspectives on the Organization and Evolution of Nonspecific Thalamocortical Projections. Springer, Boston, MA. pp. 403–445. doi:10.1007/978-1-4613-2149-1_11

149. Herkenham M. 1980. Laminar Organization of Thalamic Projections to Rat

Neocortex. *Science (80-)* **179**:283–285. doi:10.1126/science.179.4070.283

150. Hestrin S, Armstrong WE. 1996. Morphology and physiology of cortical neurons in layer I. *J Neurosci* **16**:5290–5300. doi:10.1523/jneurosci.16-17-05290.1996

151. Hindley EL, Nelson AJD, Aggleton JP, Vann SD. 2014. Dysgranular retrosplenial cortex lesions in rats disrupt cross-modal object recognition. *Learn Mem* **21**:171–179. doi:10.1101/lm.032516.113

152. Hindley EL, Nelson AJD, Aggleton JP, Vann SD. 2014. The rat retrosplenial cortex is required when visual cues are used flexibly to determine location. *Behav Brain Res* **263**:98–107. doi:10.1016/j.bbr.2014.01.028

153. Hines, Carnevale. 2001. Neuron: A Tool for Neuroscientists. *Neurosci* **7**:123–135. doi:10.1177/107385840100700207

154. Hinman JR, Dannenberg H, Alexander AS, Hasselmo ME. 2018. Neural mechanisms of navigation involving interactions of cortical and subcortical structures. *J Neurophysiol*. doi:10.1152/jn.00498.2017

155. Hodges JR, Davies RR, Xuereb JH, Casey B, Broe M, Bak TH, Kril JJ, Halliday GM. 2004. Clinicopathological correlates in frontotemporal dementia. *Ann Neurol* **56**:399–406. doi:10.1002/ana.20203

156. Hodgkin AL, Huxley AF. 1952. A quantitative description of membrane current and its application to conduction and excitation in nerve. *J Physiol* **117**:500–544.

157. Holmgren C, Harkany T, Svennenfors B, Zilberter Y. 2003. Pyramidal cell communication within local networks in layer 2/3 of rat neocortex. *J Physiol* **551**:139–153. doi:10.1111/j.1469-7793.2003.00139.x

158. Honda Y, Ishizuka N. 2015. Topographic distribution of cortical projection cells in the rat subiculum. *Neurosci Res* **92**:1–20. doi:10.1016/j.neures.2014.11.011

159. Hooks BM, Mao T, Gutnisky DA, Yamawaki N, Svoboda K, Shepherd GMG. 2013. Organization of cortical and thalamic input to pyramidal neurons in mouse motor cortex. *J Neurosci* **33**:748–760. doi:10.1523/JNEUROSCI.4338-12.2013

160. Hou Y, Yuan X, Wei Q, Ou R, Yang J, Gong Q, Shang H. 2020. Primary disruption of the default mode network subsystems in drug-naïve Parkinson's disease with mild cognitive impairments. *Neuroradiology* **62**:685–692. doi:10.1007/s00234-020-02378-z

161. Hovestadt A, de Jong GJ, Meerwaldt JD. 1987. Spatial disorientation as an early symptom of Parkinson's disease. *Neurology* **37**:485–487. doi:10.1212/wnl.37.3.485

162. Hsieh CY, Cruikshank SJ, Metherate R. 2000. Differential modulation of auditory thalamocortical and intracortical synaptic transmission by cholinergic agonist. *Brain Res* **880**:51–64. doi:10.1016/S0006-8993(00)02766-9

163. Hunsaker MR, Rosenberg JS, Kesner RP. 2008. The role of the dentate gyrus, CA3a,b, and CA3c for detecting spatial and environmental novelty. *Hippocampus* **18**:1064–1073. doi:10.1002/hipo.20464

164. Ichinohe N, Rockland KS. 2002. Parvalbumin positive dendrites co-localize with apical dendritic bundles in rat retrosplenial cortex. *Neuroreport* **13**:757–761.

165. Ichinohe N, Knight A, Ogawa M, Ohshima T, Mikoshiba K, Yoshihara Y, Terashima T, Rockland KS. 2008. Unusual patch-matrix organization in the retrosplenial cortex of the reeler mouse and shaking rat kawasaki. *Cereb Cortex* **18**:1125–1138. doi:10.1093/cercor/bhm148

166. Ichinohe N, Yoshihara Y, Hashikawa T, Rockland KS. 2003. Developmental study of dendritic bundles in layer 1 of the rat granular retrosplenial cortex with special reference to a cell adhesion molecule, OCAM. *Eur J Neurosci* **18**:1764–1774. doi:10.1046/j.1460-9568.2003.02900.x

167. Inagaki HK, Inagaki M, Romani S, Svoboda K. 2018. Low-dimensional and monotonic preparatory activity in mouse anterior lateral motor cortex. *J Neurosci* **38**:4163–4185. doi:10.1523/JNEUROSCI.3152-17.2018

168. Ino T, Doi T, Hirose S, Kimura T, Ito J, Fukuyama H. 2007. Directional Disorientation Following Left Retrosplenial Hemorrhage: A Case Report with fMRI Studies. *Cortex* **43**:248–254.

169. Insausti R, Herrero MT, Witter MP. 1998. Entorhinal cortex of the rat: Cytoarchitectonic subdivisions and the origin and distribution of cortical efferents. *Hippocampus*.

170. Ipser JC, Singh L, Stein DJ. 2013. Meta-analysis of functional brain imaging in specific phobia. *Psychiatry Clin Neurosci* **67**:311–322. doi:10.1111/pcn.12055

171. Ironside R, Guttmacher M. 1929. The corpus callosum and its tumours. *Brain* **52**:442–483.

172. Iwase M, Kitanishi T, Mizuseki K. 2020. Cell type, sub-region, and layer-specific speed representation in the hippocampal–entorhinal circuit. *Sci Rep* **10**:1–23. doi:10.1038/s41598-020-58194-1

173. Jackson J, Karnani MM, Zemelman B V, Burdakov D, Lee AK. 2018. Inhibitory Control of Prefrontal Cortex by the Claustrum. *Neuron* **99**:1029-1039.e4.

doi:10.1016/j.neuron.2018.07.031

174. Jacob P-Y, Casali G, Spieser L, Page H, Overington D, Jeffery K. 2017. An independent, landmark-dominated head-direction signal in dysgranular retrosplenial cortex. *Nat Neurosci*. doi:10.1038/nn.4465

175. Jankowski MM, O'Mara SM. 2015. Dynamics of place, boundary and object encoding in rat anterior claustrum. *Front Behav Neurosci* **9**:250. doi:10.3389/fnbeh.2015.00250

176. Jiang X, Shen S, Cadwell CR, Berens P, Sinz F, Ecker AS, Patel S, Tolias AS. 2015. Principles of connectivity among morphologically defined cell types in adult neocortex. *Science (80-)* **350**. doi:10.1126/science.aac9462

177. Jin J, Cheng J, Lee KW, Amreen B, McCabe KA, Pitcher C, Liebmann T, Greengard P, Flajolet M. 2019. Cholinergic neurons of the medial septum are crucial for sensorimotor gating. *J Neurosci* **39**:5234–5242. doi:10.1523/JNEUROSCI.0950-18.2019

178. Jinde S, Zsiros V, Jiang Z, Nakao K, Pickel J, Kohno K, Belforte JE, Nakazawa K. 2012. Hilar Mossy Cell Degeneration Causes Transient Dentate Granule Cell Hyperexcitability and Impaired Pattern Separation. *Neuron* **76**:1189–1200. doi:10.1016/j.neuron.2012.10.036

179. Jochems A, Reboreda A, Hasselmo ME, Yoshida M. 2013. Cholinergic receptor activation supports persistent firing in layer III neurons in the medial entorhinal cortex. *Behav Brain Res* **254**:108–115. doi:10.1016/j.bbr.2013.06.027

180. Jochems A, Yoshida M. 2013. Persistent firing supported by an intrinsic cellular mechanism in hippocampal CA3 pyramidal cells. *Eur J Neurosci* **38**:2250–2259. doi:10.1111/ejn.12236

181. Johnson A, Redish AD. 2007. Neural ensembles in CA3 transiently encode paths forward of the animal at a decision point. *J Neurosci* **27**:12176–12189. doi:10.1523/JNEUROSCI.3761-07.2007

182. Jones EG. 2001. The thalamic matrix and thalamocortical synchrony. *Trends Neurosci*. doi:10.1016/S0166-2236(00)01922-6

183. Jones EG. 1998. Viewpoint: The core and matrix of thalamic organization. *Neuroscience*. doi:10.1016/S0306-4522(97)00581-2

184. Kaboodvand N, Bäckman L, Nyberg L, Salami A. 2018. The retrosplenial cortex: A memory gateway between the cortical default mode network and the medial temporal lobe. *Hum Brain Mapp* **39**:2020–2034. doi:10.1002/hbm.23983

185. Kamondi A, Laszlo A., Buzsaki G. 1998. Dendritic spikes are enhanced by cooperative network activity in the intact hippocampus. *J Neurosci* **18**: 3919-3928. doi:10.1523/JNEUROSCI.18-10-03919.1998

186. Katche C, Dorman G, Slipczuk L, Cammarota M, Medina JH. 2013. Functional integrity of the retrosplenial cortex is essential for rapid consolidation and recall of fear memory. *Learn Mem* **20**:170–3. doi:10.1101/lm.030080.112

187. Kawaguchi Y, Kubota Y. 1997. GABAergic cell subtypes and their synaptic connections in rat frontal cortex. *Cereb Cortex* **7**:476–486.

188. Kawaguchi Y. 1997. Selective cholinergic modulation of cortical GABAergic cell subtypes. *J Neurophysiol* **78**:1743–1747. doi:10.1152/jn.1997.78.3.1743

189. Kawasaki H, Palmieri C, Avoli M. 1999. Muscarinic receptor activation induces depolarizing plateau potentials in bursting neurons of the rat subiculum. *J Neurophysiol* **82**:2590–2601. doi:10.1152/jn.1999.82.5.2590

190. Keene CS, Bucci DJ. 2009. Damage to the retrosplenial cortex produces specific impairments in spatial working memory. *Neurobiol Learn Mem* **91**:408–414. doi:10.1016/j.nlm.2008.10.009

191. Keene CS, Bucci DJ. 2008a. Contributions of the Retrosplenial and Posterior Parietal Cortices to Cue-Specific and Contextual Fear Conditioning. *Behav Neurosci* **122**:89–97. doi:10.1037/0735-7044.122.1.89

192. Keene CS, Bucci DJ. 2008b. Neurotoxic Lesions of Retrosplenial Cortex Disrupt Signaled and Unsignaled Contextual Fear Conditioning. *Behav Neurosci* **122**:1070–1077. doi:10.1037/a0012895

193. Keshavarzi S, Bracey EF, Faville RA, Campagner D, Tyson AL, Lenzi SC, Branco T, Margrie TW. 2021. The retrosplenial cortex combines internal and external cues to encode head velocity during navigation. *bioRxiv*. doi:10.1101/2021.01.22.427789

194. Kilgard MP, Merzenich MM. 1998. Cortical map reorganization enabled by nucleus basalis activity. *Science (80-)* **279**:1714–1718. doi:10.1126/science.279.5357.1714

195. Kim W Bin, Cho JH. 2020. Encoding of contextual fear memory in hippocampal–amygdala circuit. *Nat Commun* **11**:1–22. doi:10.1038/s41467-020-15121-2

196. Kim SM, Ganguli S, Frank LM. 2012. Spatial information outflow from the hippocampal circuit: distributed spatial coding and phase precession in the subiculum. *J Neurosci* **32**:11539–58. doi:10.1523/JNEUROSCI.5942-11.2012

197. Kim J, Matney CJ, Roth RH, Brown SP. 2016. Synaptic organization of the neuronal circuits of the claustrum. *J Neurosci* **36**:773–784. doi:10.1523/JNEUROSCI.3643-15.2016

198. Kimura F. 1999. Acetylcholine suppresses the spread of excitation in the visual cortex revealed by optical recording: Possible differential effect depending on the source of input. *Eur J Neurosci* **11**:3597–3609. doi:10.1046/j.1460-9568.1999.00779.x

199. Kinnavane L, Vann SD, Nelson AJD, O'Mara SM, Aggleton JP. 2018. Collateral projections innervate the mammillary bodies and retrosplenial cotex: A new category of hippocampal cells. *eneuro* **5**.

200. Kitanishi T, Matsuo N. 2017. Organization of the claustrum-to-entorhinal cortical connection in mice. *J Neurosci* **37**:269–280. doi:10.1523/JNEUROSCI.1360-16.2016

201. Kitanishi T, Umaba R, Mizuseki K. 2021. Robust information routing by dorsal subiculum neurons. *Sci Adv* **7**:eabf1913. doi:10.1126/sciadv.abf1913

202. Kloosterman F, Witter MP, Van Haeften T. 2003. Topographical and laminar organization of subicular projections to the parahippocampal region of the rat. *J Comp Neurol* **455**:156–171. doi:10.1002/cne.10472

203. Knauer B, Jochems A, Valero-Aracama MJ, Yoshida M. 2013. Long-lasting intrinsic persistent firing in rat CA1 pyramidal cells: A possible mechanism for active maintenance of memory. *Hippocampus* **23**:820–831. doi:10.1002/hipo.22136

204. Knierim JJ. 2003. Hippocampal remapping: Implications for spatial learning and navigation In: Jeffrey KJ, editor. The Neurobiology of Spatial Behaviour. Oxford University Press.

205. Koga K, Li X, Chen T, Steenland HW, Descalzi G, Zhuo M. 2010. In vivo whole-cell patch-clamp recording of sensory synaptic responses of cingulate pyramidal neurons to noxious mechanical stimuli in adult mice. *Mol Pain* **6**:62. doi:10.1186/1744-8069-6-62

206. Koike BDV, Farias KS, Billwiller F, Almeida-Filho D, Libourel P-A, Tiran-Cappello A, Parmentier R, Blanco W, Ribeiro S, Luppi P-H, Queiroz CM. 2017. Electrophysiological evidence that the retrosplenial cortex displays a strong and specific activation phased with hippocampal theta during paradoxical (REM) sleep. *J Neurosci*.

207. Kropff E, Carmichael JE, Moser MB, Moser EI. 2015. Speed cells in the medial entorhinal cortex. *Nature* **523**:419–424. doi:10.1038/nature14622

208. Kurotani T, Miyashita T, Wintzer M, Konishi T, Sakai K, Ichinohe N, Rockland KS. 2013. Pyramidal neurons in the superficial layers of rat retrosplenial cortex exhibit a late-spiking firing property. *Brain Struct Funct* **218**:239–254. doi:10.1007/s00429-012-0398-1

209. Kwapis JL, Jarome TJ, Lee JL, Gilmartin MR, Helmstetter FJ. 2014. Extinguishing trace fear engages the retrosplenial cortex rather than the amygdala. *Neurobiol Learn Mem* **113**:41–54. doi:10.1016/j.nlm.2013.09.007

210. Kwapis JL, Jarome TJ, Lee JL, Helmstetter FJ. 2015. The retrosplenial cortex is involved in the formation of memory for context and trace fear conditioning. *Neurobiol Learn Mem* **123**:110–116. doi:10.1016/j.nlm.2015.06.007

211. Laurens J, Abrego A, Cham H, Popeney B, Yu Y, Rotem N, Aarse J, Asprodini E, Dickman JD, Angelaki D. 2019. Multiplexed code of navigation variables in anterior limbic areas. *bioRxiv* 684464. doi:10.1101/684464

212. Lee JLC. 2013. Mechanisms and Functions of Hippocampal Memory ReconsolidationMemory Reconsolidation. Elsevier Inc. pp. 43–68. doi:10.1016/B978-0-12-386892-3.00003-2

213. Lee S-H, Marchionni I, Bezaire M, Varga C, Danielson N, Lovett-Barron M, Losonczy A, Soltesz I. 2014. Parvalbumin-positive basket cells differentiate among hippocampal pyramidal cells. *Neuron* **82**:1129–44. doi:10.1016/j.neuron.2014.03.034

214. Letzkus JJ, Wolff SBE, Meyer EMM, Tovote P, Courtin J, Herry C, Lüthi A. 2011. A disinhibitory microcircuit for associative fear learning in the auditory cortex. *Nature* **480**:331–335. doi:10.1038/nature10674

215. Leutgeb JK, Leutgeb S, Moser M-B, Moser EI. 2007. Pattern Separation in the Dentate Gyrus and CA3 of the Hippocampus. *Science (80-)* **315**:961–966. doi:10.1126/science.1135801

216. Lever C, Burton S, Jeewajee A, O'Keefe J, Burgess N. 2009. Boundary vector cells in the subiculum of the hippocampal formation. *J Neurosci* **29**:9771–9777. doi:10.1523/JNEUROSCI.1319-09.2009

217. Levey AI. 1993. Immunological localization of m1-m5 muscarinic acetylcholine receptors in peripheral tissues and brain. *Life Sci* **52**:441–448. doi:10.1016/0024-3205(93)90300-R

218. Li CL, Li KC, Wu D, Chen Y, Luo H, Zhao JR, Wang SS, Sun MM, Lu YJ, Zhong YQ, Hu XY, Hou R, Zhou BB, Bao L, Xiao HS, Zhang X. 2016. Somatosensory neuron types identified by high-coverage single-cell RNA-sequencing and

functional heterogeneity. *Cell Res* **26**:83–102. doi:10.1038/cr.2015.149

219. Li N, Daie K, Svoboda K, Druckmann S. 2016. Robust neuronal dynamics in premotor cortex during motor planning. *Nature* **532**:459–464. doi:10.1038/nature17643

220. Lindau M, Almkvist O, Kushi J, Boone K, Johansson SE, Wahlund LO, Cummings JL, Miller BL. 2000. First symptoms - Frontotemporal dementia versus Alzheimer's disease. *Dement Geriatr Cogn Disord* **11**:286–293. doi:10.1159/000017251

221. Liu C, Yen CCC, Szczupak D, Ye FQ, Leopold DA, Silva AC. 2019. Anatomical and functional investigation of the marmoset default mode network. *Nat Commun* **10**:1–8. doi:10.1038/s41467-019-09813-7

222. Liu PW, Bean BP. 2014. Kv2 channel regulation of action potential repolarization and firing patterns in superior cervical ganglion neurons and hippocampal CA1 pyramidal neurons. *J Neurosci* **34**:4991–5002. doi:10.1523/JNEUROSCI.1925-13.2014

223. Liu YH, Wang XJ. 2001. Spike-frequency adaptation of a generalized leaky integrate-and-fire model neuron. *J Comput Neurosci* **10**:25–45. doi:10.1023/A:1008916026143

224. Locke RE, Nerbonne JM. 1997. Role of voltage-gated K+ currents in mediating the regular-spiking phenotype of callosal-projecting rat visual cortical neurons. *J Neurophysiol* **78**:2321–35. doi:10.1152/jn.1997.78.5.2321

225. Lozano YR, Page H, Jacob P-Y, Lomi E, Street J, Jeffery K. 2017. Retrosplenial and postsubicular head direction cells compared during visual landmark discrimination. *Brain Neurosci Adv* **1**:239821281772185. doi:10.1177/2398212817721859

226. Luchicchi A, Bloem B, Viaña JNM, Mansvelder HD, Role LW. 2014. Illuminating the role of cholinergic signaling in circuits of attention and emotionally salient behaviors. *Front Synaptic Neurosci*. doi:10.3389/fnsyn.2014.00024

227. Lukoyanov N V., Lukoyanova EA. 2006. Retrosplenial cortex lesions impair acquisition of active avoidance while sparing fear-based emotional memory. *Behav Brain Res* **173**:229–236. doi:10.1016/j.bbr.2006.06.026

228. Luntz-Leybman V, Bickford PC, Freedman R. 1992. Cholinergic gating of response to auditory stimuli in rat hippocampus. *Brain Res* **587**:130–136. doi:10.1016/0006-8993(92)91437-J

229. Magistretti J, Ma L, Shalinsky MH, Lin W, Klink R, Alonso A. 2004. Spike

Patterning by Ca2+-Dependent Regulation of a Muscarinic Cation Current in Entorhinal Cortex Layer II Neurons. *J Neurophysiol* **92**:1644–1657. doi:10.1152/jn.00036.2004

230. Maguire E. 2001. The retrosplenial contribution to human navigation: a review of lesion and neuroimaging findings. *Scand J Psychol* **42**:225–238.

231. Mahfooz K, Ellender TJ. 2021. Combining Whole-Cell Patch-Clamp Recordings with Single-Cell RNA SequencingMethods in Molecular Biology. Humana Press Inc. pp. 179–189. doi:10.1007/978-1-0716-0818-0_9

232. Mao D, Kandler S, McNaughton BL, Bonin V. 2017. Sparse orthogonal population representation of spatial context in the retrosplenial cortex. *Nat Commun* **8**:243. doi:10.1038/s41467-017-00180-9

233. Mao D, Molina LA, Bonin V, McNaughton BL. 2020. Vision and Locomotion Combine to Drive Path Integration Sequences in Mouse Retrosplenial Cortex. *Curr Biol* **30**:1680-1688.e4. doi:10.1016/j.cub.2020.02.070

234. Mao D, Neumann AR, Sun J, Bonin V, Mohajerani MH, McNaughton BL. 2018. Hippocampus-dependent emergence of spatial sequence coding in retrosplenial cortex. *Proc Natl Acad Sci U S A* **115**:8015–8018. doi:10.1073/pnas.1803224115

235. Marchette SA, Vass LK, Jack R, Epstein RA. 2014. Anchoring the neural compass: coding of local spatial reference frames in human medial parietal lobe **17**. doi:10.1038/nn.3834

236. Martina M, Jonas P. 1997. Functional differences in Na+ channel gating between fast-spiking interneurons and principal neurones of rat hippocampus. *J Physiol* **505**:593–603.

237. Marx M, Günter RH, Hucko W, Radnikow G, Feldmeyer D. 2012. Improved biocytin labeling and neuronal 3D reconstruction. *Nat Protoc* **7**:394–407. doi:10.1038/nprot.2011.449

238. Maunsell JHR, Van Essen DC. 1983. Functional properties of neurons in middle temporal visual area of the macaque monkey. I. Selectivity for stimulus direction, speed, and orientation. *J Neurophysiol* **49**:1127–1147. doi:10.1152/jn.1983.49.5.1127

239. McKinney M, Coyle JT, Hedreen JC. 1983. Topographic analysis of the innervation of the rat neocortex and hippocampus by the basal forebrain cholinergic system. *J Comp Neurol* **217**:103–121. doi:10.1002/cne.902170109

240. McNaughton BL, Barnes CA, O'Keefe J. 1983. The contributions of position, direction, and velocity to single unit activity in the hippocampus of freely-moving

rats. *Exp Brain Res* **52**:41–49. doi:10.1007/BF00237147

241. McNaughton BL, Battaglia FP, Jensen O, Moser EI, Moser MB. 2006. Path integration and the neural basis of the “cognitive map.” *Nat Rev Neurosci*. doi:10.1038/nrn1932

242. McNaughton BL, Chen LL, Markus EJ. 1991. “‘Dead reckoning,’” landmark learning, and the sense of direction: A neurophysiological and computational hypothesis. *J Cogn Neurosci*. doi:10.1162/jocn.1991.3.2.190

243. Mendez-Lopez M, Arias JL, Bontempi B, Wolff M. 2013. Reduced cytochrome oxidase activity in the retrosplenial cortex after lesions to the anterior thalamic nuclei. *Behav Brain Res* **250**:264–273. doi:10.1016/j.bbr.2013.04.052

244. Mesulam MM, Mufson EJ, Wainer BH, Levey AI. 1983. Central cholinergic pathways in the rat: An overview based on an alternative nomenclature (Ch1-Ch6). *Neuroscience* **10**:1185–1201. doi:10.1016/0306-4522(83)90108-2

245. Milczarek MM, Vann SD. 2020. The retrosplenial cortex and long-term spatial memory: from the cell to the network. *Curr Opin Behav Sci*. doi:10.1016/j.cobeha.2020.01.014

246. Milczarek MM, Vann SD, Sengpiel F. 2018. Spatial Memory Engram in the Mouse Retrosplenial Cortex. *Curr Biol* **28**:1975-1980.e6. doi:10.1016/j.cub.2018.05.002

247. Miller AMP, Mau W, Smith DM. 2019. Retrosplenial Cortical Representations of Space and Future Goal Locations Develop with Learning. *Curr Biol* **29**:2083-2090.e4. doi:10.1016/j.cub.2019.05.034

248. Miller AMP, Serrichio AC, Smith DM. 2020. Dual-Factor Representation of the Environmental Context in the Retrosplenial Cortex. *Cereb Cortex*. doi:10.1093/cercor/bhaa386

249. Minces V, Pinto L, Dan Y, Chiba AA. 2017. Cholinergic shaping of neural correlations. *Proc Natl Acad Sci U S A* **114**:5725–5730. doi:10.1073/pnas.1621493114

250. Minoshima S, Giordani B, Berent S, Frey KA, Foster NL, Kuhl DE. 1997. Metabolic reduction in the posterior cingulate cortex in very early Alzheimer’s disease. *Ann Neurol* **42**:85–94. doi:10.1002/ana.410420114

251. Miyashita T, Rockland KS. 2007. GABAergic projections from the hippocampus to the retrosplenial cortex in the rat. *Eur J Neurosci* **26**:1193–1204.

252. Mizuseki K, Diba K, Pastalkova E, Buzsáki G. 2011. Hippocampal CA1 pyramidal

cells form functionally distinct sublayers. *Nat Neurosci* **14**:1174–1181. doi:10.1038/nn.2894

253. Mohanty A, Engels AS, Herrington JD, Heller W, Ringo Ho M-H, Banich MT, Webb AG, Warren SL, Miller GA. 2007. Differential engagement of anterior cingulate cortex subdivisions for cognitive and emotional function. *Psychophysiology* **44**:343–351. doi:10.1111/j.1469-8986.2007.00515.x

254. Monacelli AM, Cushman LA, Kavcic V, Duffy CJ. 2003. Spatial disorientation in Alzheimer's disease: The remembrance of things passed. *Neurology* **61**:1491–1497. doi:10.1212/WNL.61.11.1491

255. Morison RS, Dempsey EW. 1941. A STUDY OF THALAMO-CORTICAL RELATIONS. *Am J Physiol Content* **135**:281–292. doi:10.1152/ajplegacy.1941.135.2.281

256. Muir GM, Brown JE, Carey JP, Hirvonen TP, Della Santina CC, Minor LB, Taube JS. 2009. Disruption of the head direction cell signal after occlusion of the semicircular canals in the freely moving chinchilla. *J Neurosci* **29**:14521–14533. doi:10.1523/JNEUROSCI.3450-09.2009

257. Muñoz-Manchado AB, Bengtsson Gonzales C, Zeisel A, Munguba H, Bekkouche B, Skene NG, Lönnerberg P, Ryge J, Harris KD, Linnarsson S, Hjerling-Leffler J. 2018. Diversity of Interneurons in the Dorsal Striatum Revealed by Single-Cell RNA Sequencing and PatchSeq. *Cell Rep* **24**:2179-2190.e7. doi:10.1016/j.celrep.2018.07.053

258. Murakami M, Vicente MI, Costa GM, Mainen ZF. 2014. Neural antecedents of self-initiated actions in secondary motor cortex. *Nat Neurosci* **17**:1574–1582. doi:10.1038/nn.3826

259. Murakoshi H, Trimmer JS. 1999. Identification of the Kv2.1 K+ channel as a major component of the delayed rectifier K+ current in rat hippocampal neurons. *J Neurosci* **19**:1728–35.

260. Nagano-Saito A, Kato T, Arahata Y, Washimi Y, Nakamura A, Abe Y, Yamada T, Iwai K, Hatano K, Kawasumi Y, Kachi T, Dagher A, Ito K. 2004. Cognitive- and motor-related regions in Parkinson's disease: FDOPA and FDG PET studies. *Neuroimage* **22**:553–561. doi:10.1016/j.neuroimage.2004.01.030

261. Nakamura S, Baratta M V, Pomrenze MB, Dolzani SD, Cooper DC. 2012. High fidelity optogenetic control of individual prefrontal cortical pyramidal neurons in vivo. *F1000Research* **1**:1–7. doi:10.12688/f1000research.1-7.v1

262. Narikiyo K, Mizuguchi R, Ajima A, Shiozaki M, Hamanaka H, Johansen JP, Mori K, Yoshihara Y. 2020. The claustrum coordinates cortical slow-wave activity. *Nat*

Neurosci **23**:741–753. doi:10.1038/s41593-020-0625-7

263. Navaroli VL, Zhao Y, Boguszewski P, Brown TH. 2012. Muscarinic receptor activation enables persistent firing in pyramidal neurons from superficial layers of dorsal perirhinal cortex. *Hippocampus* **22**:1392–1404. doi:10.1002/hipo.20975

264. Nestor PJ, Fryer TD, Ikeda M, Hodges JR. 2003. Retrosplenial cortex (BA 29/30) hypometabolism in mild cognitive impairment (prodromal Alzheimer's disease). *Eur J Neurosci* **18**:2663–2667. doi:10.1046/j.1460-9568.2003.02999.x

265. Neymotin SA, Lazarewicz MT, Sherif M, Contreras D, Finkel FH, Lytton WW. 2011. Ketamine Disrupts Theta Modulation of Gamma in a Computer Model of Hippocampus. *J Neurosci* **31**:11733–11743.

266. Nitz DA. 2006. Tracking route progression in the posterior parietal cortex. *Neuron* **49**:747–756. doi:10.1016/j.neuron.2006.01.037

267. Nitzan N, McKenzie S, Beed P, English DF, Oldani S, Tukker JJ, Buzsáki G, Schmitz D. 2020. Propagation of hippocampal ripples to the neocortex by way of a subiculum-retrosplenial pathway. *Nat Commun* **11**:1–17. doi:10.1038/s41467-020-15787-8

268. Nordberg A. 2001. Nicotinic receptor abnormalities of Alzheimer's disease: therapeutic implications. *Biol Psychiatry* **49**:200–10. doi:10.1016/s0006-3223(00)01125-2

269. Nyakas C, Granic I, Halmy LG, Banerjee P, Luiten PGM. 2011. The basal forebrain cholinergic system in aging and dementia. Rescuing cholinergic neurons from neurotoxic amyloid-β42 with memantine. *Behav Brain Res* **221**:594–603. doi:10.1016/j.bbr.2010.05.033

270. O'Keefe J, Dostrovsky J. 1971. The hippocampus as a spatial map. Preliminary evidence from unit activity in the freely-moving rat. *Brain Res* **34**:171–175. doi:10.1016/0006-8993(71)90358-1

271. O'Keefe J, Recce ML. 1993. Phase relationship between hippocampal place units and the EEG theta rhythm. *Hippocampus* **3**:317–330. doi:10.1002/hipo.450030307

272. O'Mara S. 2006. Controlling hippocampal output: The central role of subiculum in hippocampal information processing. *Behav Brain Res* **174**:304–312. doi:10.1016/j.bbr.2006.08.018

273. Obermayer J, Verhoog MB, Luchicchi A, Mansvelder HD. 2017. Cholinergic modulation of cortical microcircuits is layer-specific: Evidence from rodent, monkey and human brain. *Front Neural Circuits*. doi:10.3389/fncir.2017.00100

274. Odagiri S, Meguro R, Asano Y, Tani T, Ichinohe N. 2011. Single Axon Branching Analysis in Rat Thalamocortical Projection from the Anteroventral Thalamus to the Granular Retrosplenial Cortex. *Front Neuroanat* **5**:63. doi:10.3389/fnana.2011.00063

275. Oh SW, Harris JA, Ng L, Winslow B, Cain N, Mihalas S, Wang Q, Lau C, Kuan L, Henry AM, Mortrud MT, Ouellette B, Nguyen TN, Sorensen SA, Slaughterbeck CR, Wakeman W, Li Y, Feng D, Ho A, Nicholas E, Hirokawa KE, Bohn P, Joines KM, Peng H, Hawrylycz MJ, Phillips JW, Hohmann JG, Wohnoutka P, Gerfen CR, Koch C, Bernard A, Dang C, Jones AR, Zeng H. 2014. A mesoscale connectome of the mouse brain. *Nature* **508**:207–214. doi:10.1038/nature13186

276. Olson JM, Li JK, Montgomery SE, Nitz DA. 2020. Secondary Motor Cortex Transforms Spatial Information into Planned Action during Navigation. *Curr Biol* **30**:1845-1854.e4. doi:10.1016/j.cub.2020.03.016

277. Olson JM, Tongprasearth K, Nitz DA. 2017. Subiculum neurons map the current axis of travel. *Nat Neurosci* **20**:170–172. doi:10.1038/nn.4464

278. Opalka AN, Huang W qiang, Liu J, Liang H, Wang D V. 2020. Hippocampal Ripple Coordinates Retrosplenial Inhibitory Neurons during Slow-Wave Sleep. *Cell Rep* **30**:432-441.e3. doi:10.1016/j.celrep.2019.12.038

279. Opalka AN, Wang D V. 2020. Hippocampal efferents to retrosplenial cortex and lateral septum are required for memory acquisition. *Learn Mem* **27**:310–318. doi:10.1101/LM.051797.120

280. Osawa A, Maeshima S, Kunishio K. 2007. Topographic disorientation and amnesia due to cerebral hemorrhage in the left retrosplenial region. *Eur Neurol*. doi:10.1159/000109572

281. Overstreet-Wadiche L, McBain CJ. 2015. Neurogliaform cells in cortical circuits. *Nat Rev Neurosci*. doi:10.1038/nrn3969

282. Packer AM, Yuste R. 2011. Cellular/Molecular Dense, Unspecific Connectivity of Neocortical Parvalbumin-Positive Interneurons: A Canonical Microcircuit for Inhibition? *J Neurosci* **31**. doi:10.1523/JNEUROSCI.3131-11.2011

283. Page HJI, Jeffery KJ. 2018. Landmark-based updating of the head direction system by retrosplenial cortex: A computational model. *Front Cell Neurosci* **12**:191. doi:10.3389/fncel.2018.00191

284. Parikh V, Kozak R, Martinez V, Sarter M. 2007. Prefrontal Acetylcholine Release Controls Cue Detection on Multiple Timescales. *Neuron* **56**:141–154. doi:10.1016/j.neuron.2007.08.025

285. Pengas G, Hodges JR, Watson P, Nestor PJ. 2010. Focal posterior cingulate atrophy in incipient Alzheimer's disease. *Neurobiol Aging* **31**:25–33. doi:10.1016/j.neurobiolaging.2008.03.014

286. Pérez-Escobar JA, Kornienko O, Latuske P, Kohler L, Allen K. 2016. Visual landmarks sharpen grid cell metric and confer context specificity to neurons of the medial entorhinal cortex. *Elife* **5**. doi:10.7554/eLife.16937

287. Peters A. 1979. Thalamic input to the cerebral cortex. *Trends Neurosci* **2**:183–185. doi:10.1016/0166-2236(79)90074-2

288. Peters A, Feldman ML. 1976. The projection of the lateral geniculate nucleus to area 17 of the rat cerebral cortex. I. General description. *J Neurocytol* **5**:63–84. doi:10.1007/BF01176183

289. Peyrache A, Buzsaki G. 2015. Extracellular recordings from multi-site silicon probes in the anterior thalamus and subicular formation of freely moving mice. CRCNS.org. doi:http://dx.doi.org/10.6080/K0G15XS1

290. Peyrache A, Lacroix MM, Petersen PC, Buzsáki G. 2015. Internally organized mechanisms of the head direction sense. *Nat Neurosci* **18**:569–575. doi:10.1038/nn.3968

291. Picciotto MR, Higley MJ, Mineur YS. 2012. Acetylcholine as a Neuromodulator: Cholinergic Signaling Shapes Nervous System Function and Behavior. *Neuron*. doi:10.1016/j.neuron.2012.08.036

292. Pinto L, Goard MJ, Estandian D, Xu M, Kwan AC, Lee SH, Harrison TC, Feng G, Dan Y. 2013. Fast modulation of visual perception by basal forebrain cholinergic neurons. *Nat Neurosci* **16**:1857–1863. doi:10.1038/nn.3552

293. Poirier GL, Aggleton JP. 2009. Post-surgical interval and lesion location within the limbic thalamus determine extent of retrosplenial cortex immediate-early gene hypoactivity. *Neuroscience* **160**:452–469. doi:10.1016/j.neuroscience.2009.02.021

294. Polack PO, Friedman J, Golshani P. 2013. Cellular mechanisms of brain state-dependent gain modulation in visual cortex. *Nat Neurosci* **16**:1331–1339. doi:10.1038/nn.3464

295. Pothuizen HHJ, Davies M, Aggleton JP, Vann SD. 2010. Effects of selective granular retrosplenial cortex lesions on spatial working memory in rats. *Behav Brain Res* **208**:566–575. doi:10.1016/j.bbr.2010.01.001

296. Pothuizen HHJ, Davies M, Albasser MM, Aggleton JP, Vann SD. 2009. Granular

and dysgranular retrosplenial cortices provide qualitatively different contributions to spatial working memory: evidence from immediate-early gene imaging in rats. *Eur J Neurosci* **30**:877–888. doi:10.1111/j.1460-9568.2009.06881.x

297. Potvin-Desrochers A, Mitchell T, Gisiger T, Paquette C. 2019. Changes in Resting-State Functional Connectivity Related to Freezing of Gait in Parkinson's Disease. *Neuroscience* **418**:311–317. doi:10.1016/j.neuroscience.2019.08.042

298. Poulter S, Lee SA, Dachtler J, Wills TJ, Lever C. 2021. Vector trace cells in the subiculum of the hippocampal formation. *Nat Neurosci* **24**:266–275. doi:10.1038/s41593-020-00761-w

299. Powell A, Connelly WM, Vasalauskaite A, Nelson AJD, Vann SD, Aggleton JP, Sengpiel F, Ranson A. 2020. Stable Encoding of Visual Cues in the Mouse Retrosplenial Cortex. *Cereb Cortex* **30**:4424–4437. doi:10.1093/cercor/bhaa030

300. Puccini GD, Sanchez-Vives M V, Compte A. 2007. Integrated Mechanisms of Anticipation and Rate-of-Change Computations in Cortical Circuits. *PLoS Comput Biol* **3**:e82. doi:10.1371/journal.pcbi.0030082

301. Rahman J, Berger T. 2011. Persistent activity in layer 5 pyramidal neurons following cholinergic activation of mouse primary cortices. *Eur J Neurosci* **34**:22–30. doi:10.1111/j.1460-9568.2011.07736.x

302. Rasmusson DD. 2000. The role of acetylcholine in cortical synaptic plasticity. *Behav Brain Res* **115**:205–218. doi:10.1016/S0166-4328(00)00259-X

303. Ratté S, Karnup S, Prescott SA. 2018. Nonlinear relationship between spike-dependent calcium influx and TRPC channel activation enables robust persistent spiking in neurons of the anterior cingulate cortex. *J Neurosci* **38**:1788–1801. doi:10.1523/JNEUROSCI.0538-17.2018

304. Redish AD, Elga AN, Touretzky DS. 1996. A coupled attractor model of the rodent Head Direction system. *Netw Comput Neural Syst* **7**:671–685. doi:10.1088/0954-898X_7_4_004

305. Renouard L, Billwiller F, Ogawa K, Clément O, Camargo N, Abdelkarim M, Gay N, Scoté-Blachon C, Touré R, Libourel PA, Ravassard P, Salvert D, Peyron C, Claustrat B, Léger L, Salin P, Malleret G, Fort P, Luppi PH. 2015. The supramammillary nucleus and the claustrum activate the cortex during REM sleep. *Sci Adv* **1**:e1400177. doi:10.1126/sciadv.1400177

306. Riekkinen P, Kuitunen J, Riekkinen M. 1995. Effects of scopolamine infusions into the anterior and posterior cingulate on passive avoidance and water maze navigation. *Brain Res* **685**:46–54. doi:10.1016/0006-8993(95)00422-M

307. Robertson CE, Hermann KL, Mynick A, Kravitz DJ, Kanwisher N. 2016. Neural Representations Integrate the Current Field of View with the Remembered 360° Panorama in Scene-Selective Cortex. *Curr Biol* **26**:2463–2468. doi:10.1016/j.cub.2016.07.002

308. Robertson RT, Kaitz SS. 1981. Thalamic connections with limbic cortex. I. Thalamocortical projections. *J Comp Neurol* **195**:501–525. doi:10.1002/cne.901950308

309. Rodriguez-Moreno J, Porrero C, Rollenhagen A, Rubio-Teves M, Casas-Torremocha D, Alonso-Nanclares L, Yakoubi R, Santuy A, Merchan-Pérez A, DeFelipe J, Lübke JHR, Clasca F. 2020. Area-specific synapse structure in branched posterior nucleus axons reveals a new level of complexity in thalamocortical networks. *J Neurosci* **40**:2663–2679. doi:10.1523/JNEUROSCI.2886-19.2020

310. Roth ED, Yu X, Rao G, Knierim JJ. 2012. Functional differences in the backward shifts of ca1 and ca3 place fields in novel and familiar environments. *PLoS One* **7**:36035. doi:10.1371/journal.pone.0036035

311. Rose M. 1927. Gyrus limbicus anterior and Regio regrosplenialis (Cortex holoprototychos quinquestratificatus): Vergleichende Architektonik bei Tier und Mensch. *J Psychol Neurol* **35**:65–173.

312. Rubio-Garrido P, Pe´rezpe´rez-De-Manzo F, Porrero CC, Galazo MJ, Clasca FC. 2009. Thalamic Input to Distal Apical Dendrites in Neocortical Layer 1 Is Massive and Highly Convergent. *Cereb Cortex Oct* **19**:2380–2395. doi:10.1093/cercor/bhn259

313. Salerno MT, Cortimiglia R, Crescimanno G, Amato G, Infantellina F. 1984. Effects of claustrum stimulation on spontaneous bioelectrical activity of motor cortex neurons in the cat. *Exp Neurol* **86**:227–239. doi:10.1016/0014-4886(84)90183-3

314. Saper, CB. 1984. Organization of cerebral cortical afferent systems in the rat. II. Magnocellular basal nucleus. *J Comp Neurology.* doi.org/10.1002/cne.902220302

315. Sargolini F, Fyhn M, Hafting T, McNaughton BL, Witter MP, Moser MB, Moser EI. 2006. Conjunctive representation of position, direction, and velocity in entorhinal cortex. *Science (80-)* **312**:758–762. doi:10.1126/science.1125572

316. Sarter M, Hasselmo ME, Bruno JP, Givens B. 2005. Unraveling the attentional functions of cortical cholinergic inputs: Interactions between signal-driven and cognitive modulation of signal detection. *Brain Res Rev*. doi:10.1016/j.brainresrev.2004.08.006

317. Sarter M, Lustig C. 2020. Forebrain cholinergic signaling: Wired and phasic, not tonic, and causing behavior. *J Neurosci*. doi:10.1523/JNEUROSCI.1305-19.2019

318. Sarter M, Lustig C, Howe WM, Gritton H, Berry AS. 2014. Deterministic functions of cortical acetylcholine. *Eur J Neurosci* **39**:1912–1920. doi:10.1111/ejn.12515

319. Savelli F, Yoganarasimha D, Knierim JJ. 2008. Influence of boundary removal on the spatial representations of the medial entorhinal cortex. *Hippocampus* **18**:1270–1282. doi:10.1002/hipo.20511

320. Scharfman HE. 2019. The Dentate Gyrus and Temporal Lobe Epilepsy: An "Exciting" Era. *Epilepsy Curr* 153575971985595. doi:10.1177/1535759719855952

321. Scharfman HE. 1992. Differentiation of rat dentate neurons by morphology and electrophysiology in hippocampal slices: granule cells, spiny hilar cells and aspiny "fast-spiking" cells. *Epilepsy Res Suppl* **7**:93–109.

322. Scheff SW, Price DA, Ansari MA, Roberts KN, Schmitt FA, Ikonomovic MD, Mufson EJ. 2015. Synaptic change in the posterior cingulate gyrus in the progression of Alzheimer's disease. *J Alzheimer's Dis* **43**:1073–1090. doi:10.3233/JAD-141518

323. Seamans JK, Nogueira L, Lavin A. 2003. Synaptic Basis of Persistent Activity in Prefrontal Cortex In Vivo and in Organotypic Cultures. *Cereb Cortex* **13**:1242–1250. doi:10.1093/cercor/bhg094

324. Sempere-Ferràndez A, Andrés-Bayón B, Geijo-Barrientos E. 2018. Callosal responses in a retrosplenial column. *Brain Struct Funct* **223**:1051–1069. doi:10.1007/s00429-017-1529-5

325. Sempere-ferràndez A, Martínez S, Geijo-barrientos E. 2019. Synaptic mechanisms underlying the intense firing of neocortical layer 5B pyramidal neurons in response to cortico-cortical inputs. *Brain Struct Funct* 1–14. doi:10.1007/s00429-019-01842-8

326. Senzai Y, Buzsáki G. 2017. Physiological Properties and Behavioral Correlates of Hippocampal Granule Cells and Mossy Cells. *Neuron* **93**:691-704.e5. doi:10.1016/j.neuron.2016.12.011

327. Sharp PE. 2006. Subicular place cells generate the same "map" for different environments: Comparison with hippocampal cells. *Behav Brain Res*. doi:10.1016/j.bbr.2006.05.034

328. Sharp PE. 1999. Subicular place cells expand or contract their spatial firing

pattern to fit the size of the environment in an open field but not in the presence of barriers: comparison with hippocampal place cells. *Behav Neurosci* **113**:643–62. doi:10.1037//0735-7044.113.4.643

329. Sharp PE, Green C. 1994. Spatial correlates of firing patterns of single cells in the subiculum of the freely moving rat. *J Neurosci* **14**:2339–2356. doi:10.1523/jneurosci.14-04-02339.1994

330. Sherrill KR, Erdem UM, Ross RS, Brown TI, Hasselmo ME, Stern CE. 2013. Hippocampus and retrosplenial cortex combine path integration signals for successful navigation. *J Neurosci* **33**:19304–19313. doi:10.1523/JNEUROSCI.1825-13.2013

331. Shibata H. 1993. Efferent projections from the anterior thalamic nuclei to the cingulate cortex in the rat. *J Comp Neurol* **330**:533–542. doi:10.1002/cne.903300409

332. Shibata H, Kondo S, Naito J. 2004. Organization of retrosplenial cortical projections to the anterior cingulate, motor, and prefrontal cortices in the rat. *Neurosci Res* **49**:1–11. doi:10.1016/j.neures.2004.01.005

333. Shibata H, Naito J. 2007. Organization of anterior cingulate and frontal cortical projections to the retrosplenial cortex in the rat. *J Comp Neurol* **506**:30–45.

334. Shine JP, Valdés-Herrera JP, Hegarty M, Wolbers T. 2016. The Human Retrosplenial Cortex and Thalamus Code Head Direction in a Global Reference Frame. *J Neurosci* **36**:6371.

335. Shine JP, Valdés-Herrera JP, Tempelmann C, Wolbers T. 2019. Evidence for allocentric boundary and goal direction information in the human entorhinal cortex and subiculum. *Nat Commun* **10**:1–10. doi:10.1038/s41467-019-11802-9

336. Sigwald EL, de Olmos S, Lorenzo A. 2020. Retrograde and anterograde contextual fear amnesia induced by selective elimination of layer IV-Va neurons in the granular retrosplenial cortex (A29). *Neurobiol Learn Mem* **171**:107229. doi:10.1016/j.nlm.2020.107229

337. Sigwald EL, Genoud ME, Giachero M, de Olmos S, Molina VA, Lorenzo A. 2016. Selective neuronal degeneration in the retrosplenial cortex impairs the recall of contextual fear memory. *Brain Struct Funct* **221**:1861–1875. doi:10.1007/s00429-015-1008-9

338. Simonnet J, Brecht M. 2019. Burst firing and spatial coding in subicular principal cells. *J Neurosci* **39**:3651–3662. doi:10.1523/JNEUROSCI.1656-18.2019

339. Smith JB, Radhakrishnan H, Alloway KD. 2012. Rat claustrum coordinates but

does not integrate somatosensory and motor cortical information. *J Neurosci* **32**:8583–8588. doi:10.1523/JNEUROSCI.1524-12.2012

340. Smythies J, Edelstein L, Ramachandran V. 2012. Hypotheses relating to the function of the claustrum. *Front Integr Neurosci* **6**. doi:10.3389/fnint.2012.00053

341. Solari N, Hangya B. 2018. Cholinergic modulation of spatial learning, memory and navigation. *Eur J Neurosci*. doi:10.1111/ejn.14089

342. Soma S, Shimegi S, Osaki H, Sato H. 2012. Cholinergic modulation of response gain in the primary visual cortex of the macaque. *J Neurophysiol* **107**:283–291. doi:10.1152/jn.00330.2011

343. Soma S, Shimegi S, Suematsu N, Sato H. 2013. Cholinergic modulation of response gain in the rat primary visual cortex. *Sci Rep* **3**:1–7. doi:10.1038/srep01138

344. Soltesz I, Losonczy A. 2018. CA1 pyramidal cell diversity enabling parallel information processing in the hippocampus. *Nat Neurosci* **21**:484–493. doi:10.1038/s41593-018-0118-0

345. Sripanidkulchai K, Wyss JM. 1987. The laminar organization of efferent neuronal cell bodies in the retrosplenial granular cortex. *Brain Res* **406**:255–269. doi:10.1016/0006-8993(87)90790-6

346. Stackman RW, Clark AS, Taube JS. 2002. Hippocampal spatial representations require vestibular input. *Hippocampus*. doi:10.1002/hipo.1112

347. Stackman RW, Taube JS. 1997. Firing properties of head direction cells in the rat anterior thalamic nucleus: Dependence on vestibular input. *J Neurosci* **17**:4349–4358. doi:10.1523/jneurosci.17-11-04349.1997

348. Stancampiano R, Cocco S, Cugusi C, Sarais L, Fadda F. 1999. Serotonin and acetylcholine release response in the rat hippocampus during a spatial memory task. *Neuroscience* **89**:1135–1143. doi:10.1016/S0306-4522(98)00397-2

349. Steenland HW, Li X-Y, Zhuo M. 2012. Predicting Aversive Events and Terminating Fear in the Mouse Anterior Cingulate Cortex during Trace Fear Conditioning. doi:10.1523/JNEUROSCI.5566-11.2012

350. Sterratt D, Graham B, Gillies A, Willshaw D. 2011. Principles of computational modeling in neuroscience, 1st ed. Cambridge, UK: Cambridge University press.

351. Stevens FL, Hurley RA, Taber KH. 2011. Anterior cingulate cortex: Unique role in cognition and emotion. *J Neuropsychiatry Clin Neurosci* **23**:121–125. doi:10.1176/jnp.23.2.jnp121

352. Stewart S, Jeewajee A, Wills TJ, Burgess N, Lever C. 2014. Boundary coding in the rat subiculum. *Philos Trans R Soc B Biol Sci* **369**. doi:10.1098/rstb.2012.0514

353. Storm JF. 1988. Temporal integration by a slowly inactivating K+ current in hippocampal neurons. *Nature* **336**:379–381.

354. Sudhakar SK, Hong S, Raikov I, Publio R, Lang C, Close T, Guo D, Negrello M, De Schutter E. 2017. Spatiotemporal network coding of physiological mossy fiber inputs by the cerebellar granular layer. *PLOS Comput Biol* **13**:e1005754. doi:10.1371/journal.pcbi.1005754

355. Sudhakar SK, Torben-Nielsen B, De Schutter E. 2015. Cerebellar nuclear neurons use time and rate coding to transmit purkinje neuron pauses. *PLoS Comput Biol* **11**:1–23. doi:10.1371/journal.pcbi.1004641

356. Sugar J, Witter M, van Strien N, Cappaert N. 2011. The retrosplenial cortex: Intrinsic connectivity and connections with the (para)hippocampal region in the rat. An interactive connectome. *Front Neuroinform* **5**. doi:10.3389/fninf.2011.00007

357. Sul JH, Jo S, Lee D, Jung MW. 2012. Role of rodent secondary motor cortex in value-based action selection. *Nat Neurosci* **14**. doi:10.1038/nn.2881

358. Sutherland RJ, Wishaw IQ, Kolb B. 1988. Contributions of cingulate cortex to two forms of spatial learning and memory. *J Neurosci* **8**:1863–1872. doi:10.1523/jneurosci.08-06-01863.1988

359. Swanson LW, Cowan WM. 1977. An autoradiographic study of the organization of the efferet connections of the hippocampal formation in the rat. *J Comp Neurol* **172**:49–84. doi:10.1002/cne.901720104

360. Szymusiak R, Alam N, McGinty D. 2000. Discharge patterns of neurons in cholinergic regions of the basal forebrain during waking and sleep. *Behav Brain Res* **115**:171–182. doi:10.1016/S0166-4328(00)00257-6

361. Tahvildari B, Fransén E, Alonso AA, Hasselmo ME. 2007. Switching between “on” and “off” states of persistent activity in lateral entorhinal layer III neurons. *Hippocampus* **17**:257–263. doi:10.1002/hipo.20270

362. Takahashi N, Kawamura M, Shiota J, Kasahata N, Hirayama K. 1997. Pure topographic disorientation due to right retrosplenial lesion. *Neurology* **49**:464–469.

363. Takahashi N, Kitamura K, Matsuo N, Mayford M, Kano M, Matsuki N, Ikegaya Y. 2012. Locally synchronized synaptic inputs. *Science* **20**:353-356.

doi:10.1126/science.1210362

364. Tan RH, Wong S, Hodges JR, Halliday GM, Hornberger M. 2013. Retrosplenial cortex (BA 29) volumes in behavioral variant frontotemporal dementia and alzheimer's disease. *Dement Geriatr Cogn Disord* **35**:177–182. doi:10.1159/000346392

365. Taube JS. 2010. Interspike Interval Analyses Reveal Irregular Firing Patterns at Short, But Not Long, Intervals in Rat Head Direction Cells. *J Neurophysiol* **104**:1635–1648. doi:10.1152/jn.00649.2009

366. Taube JS. 1998. Head direction cells and the neurophysiological basis for a sense of direction. *Prog Neurobiol* **55**:225–256. doi:10.1016/S0301-0082(98)00004-5

367. Taube JS. 1995. Head direction cells recorded in the anterior thalamic nuclei of freely moving rats. *J Neurosci* **15**:70–86. doi:10.1523/jneurosci.15-01-00070.1995

368. Taube JS, Bassett JP. 2003. Persistent Neural Activity in Head Direction Cells. *Cereb Cortex* **13**:1162–1172. doi:10.1093/cercor/bhg102

369. Taube JS, Muller RU, Ranck JB. 1990. Head-direction cells recorded from the postsubiculum in freely moving rats. I. Description and quantitative analysis. *J Neurosci* **10**:420–435.

370. Taube J S, Muller RU, Ranck JB. 1990. Head-direction cells recorded from the postsubiculum in freely moving rats. I. Description and quantitative analysis. *J Neurosci* **10**:420–35.

371. Taxidis J, Anastassiou CA, Diba K, Koch C. 2015. Local Field Potentials Encode Place Cell Ensemble Activation during Hippocampal Sharp Wave Ripples. *Neuron* **87**:590–604. doi:10.1016/j.neuron.2015.07.014

372. Tengelsen LA, Robertson RT, Yu J. 1992. Basal forebrain and anterior thalamic contributions to acetylcholinesterase activity in granular retrosplenial cortex of rats. *Brain Res* **594**:10–18. doi:10.1016/0006-8993(92)91024-9

373. Thuault SJ, Malleret G, Constantinople CM, Nicholls R, Chen I, Zhu J, Panteleyev A, Vronskaya S, Nolan MF, Bruno R, Siegelbaum SA, Kandel ER. 2013. Prefrontal cortex HCN1 channels enable intrinsic persistent neural firing and executive memory function. *J Neurosci* **33**:13583–13599. doi:10.1523/JNEUROSCI.2427-12.2013

374. Todd Travis P., DeAngeli NE, Jiang MY, Bucci DJ. 2017. Retrograde amnesia of contextual fear conditioning: Evidence for retrosplenial cortex involvement in

configural processing. *Behav Neurosci* **131**:46–54. doi:10.1037/bne0000183

375. Todd Travis P, Jiang MY, DeAngeli NE, Bucci DJ. 2017. Intact renewal after extinction of conditioned suppression with lesions of either the retrosplenial cortex or dorsal hippocampus. *Behav Brain Res*. doi:http://dx.doi.org/10.1016/j.bbr.2016.11.033

376. Todd TP, Bucci DJ. 2015. Retrosplenial Cortex and Long-Term Memory: Molecules to Behavior. *Neural Plast* **2015**:9. doi:10.1155/2015/414173

377. Todd TP, Meyer HC, Bucci DJ. 2015. Contribution of the retrosplenial cortex to temporal discrimination learning. *Hippocampus* **25**:137–141. doi:10.1002/hipo.22385

378. Treves A. 1993. Mean field analysis of neuronal spike dynamics. *Network* **4**:259–284. doi:10.1088/0954-898X

379. Tsiola A, Hamzei-Sichani F, Peterlin Z, Yuste R. 2003. Quantitative morphologic classification of layer 5 neurons from mouse primary visual cortex. *J Comp Neurol* **461**:415–428. doi:10.1002/cne.10628

380. Tsodyks M, Pawelzik K, Markram H. 1998. Neural Networks with Dynamic Synapses. *Neural Comput* **10**:821–835. doi:10.1162/089976698300017502

381. Tu S, Wong S, Hodges JR, Irish M, Piguet O, Hornberger M. 2015. Lost in spatial translation - A novel tool to objectively assess spatial disorientation in Alzheimer's disease and frontotemporal dementia. *Cortex* **67**:83–94. doi:10.1016/j.cortex.2015.03.016

382. Vakolyuk NI, Kosterina A V, Shlumukova AR. 1980. Spontaneous Electrical Activity of the Claustrum. *Neurophysiology* **12**:113–120.

383. Vale R, Campagner D, Iordanidou P, Arocas OP, Tan YL, Stempel AV, Keshavarzi S, Petersen R, Margrie T, Branco T. 2020. A cortico-collicular circuit for accurate orientation to shelter during escape. *bioRxiv* 2020.05.26.117598. doi:10.1101/2020.05.26.117598

384. Valenstein E, Bowers D, Verfaellie M, Heilman KM, Day A, Watson RT. 1987. Retrosplenial amnesia. *Brain* **110**:1631–1646.

385. Valerio S, Taube JS. 2012. Path integration: How the head direction signal maintains and corrects spatial orientation. *Nat Neurosci* **15**:1445–1453. doi:10.1038/nn.3215

386. van der Meer MAA, Redish AD. 2009. Covert expectation-of-reward in rat ventral striatum at decision points. *Front Integr Neurosci* **3**:1.

doi:10.3389/neuro.07.001.2009

387. Van Der Werf YD, Witter MP, Groenewegen HJ. 2002. The intralaminar and midline nuclei of the thalamus. Anatomical and functional evidence for participation in processes of arousal and awareness, Brain Research Reviews.

388. van Groen T, Kadish I, Wyss JM. 2004. Retrosplenial cortex lesions of area Rgb (but not of area Rga) impair spatial learning and memory in the rat. *Behav Brain Res* **154**:483–491.

389. van Groen T, Vogt BA, Wyss JM. 1993. Interconnections Between the Thalamus and Retrosplenial Cortex in the Rodent BrainNeurobiology of Cingulate Cortex and Limbic Thalamus. Birkhäuser Boston. pp. 123–150. doi:10.1007/978-1-4899-6704-6_4

390. van Groen T, Wyss JM. 2003. Connections of the retrosplenial granular b cortex in the rat. *J Comp Neurol* **463**:249–263. doi:10.1002/cne.10757

391. van Groen T, Wyss JM. 1992. Connections of the retrosplenial dysgranular cortex in the rat. *J Comp Neurol* **315**:200–216.

392. van Groen T, Wyss JM. 1990. Connections of the retrosplenial granular a cortex in the rat. *J Comp Neurol* **300**:593–606. doi:10.1002/cne.903000412

393. van Groen T, Wyss JM. 1995. Projections from the anterodorsal and anteroveniral nucleus of the thalamus to the limbic cortex in the rat. *J Comp Neurol* **358**:584–604. doi:10.1002/cne.903580411

394. van Wijngaarden JBG, Babl SS, Ito HT. 2020. Entorhinal-retrosplenial circuits for allocentric-egocentric transformation of boundary coding. *Elife* **9**:1–25. doi:10.7554/eLife.59816

395. Vann SD, Aggleton JP, Maguire EA. 2009. What does the retrosplenial cortex do? *Nat Rev Neurosci* **10**:792–802. doi:10.1038/nrn2733

396. Vann SD, Aggleton JP. 2005. Selective dysgranular retrosplenial cortex lesions in rats disrupt allocentric performance of the radial-arm maze task. *Behav Neurosci* **119**:1682–1686. doi:10.1037/0735-7044.119.6.1682

397. Vann SD, Aggleton JP. 2002. Extensive cytotoxic lesions of the rat retrosplenial cortex reveal consistent deficits on tasks that tax allocentric spatial memory. *Behav Neurosci* **116**:85–94. doi:10.1037/0735-7044.116.1.85

398. Vann SD, Kristina Wilton LA, Muir JL, Aggleton JP. 2003. Testing the importance of the caudal retrosplenial cortex for spatial memory in rats. *Behav Brain Res* **140**:107–118. doi:http://dx.doi.org/10.1016/S0166-4328(02)00274-7

399. Vedder LC, Miller AMP, Harrison MB, Smith DM. 2016. Retrosplenial cortical neurons encode navigational cues, trajectories and reward locations during goal directed navigation. *Cereb Cortex*. doi:10.1093/cercor/bhw192

400. Verhoog MB, Obermayer J, Kortleven CA, Wilbers R, Wester J, Baayen JC, De Kock CPJ, Meredith RM, Mansvelder HD. 2016. Layer-specific cholinergic control of human and mouse cortical synaptic plasticity. *Nat Commun* **7**:1–13. doi:10.1038/ncomms12826

401. Vetere G, Kenney JW, Tran LM, Xia F, Steadman PE, Parkinson J, Josselyn SA, Frankland PW. 2017. Chemogenetic Interrogation of a Brain-wide Fear Memory Network in Mice. *Neuron* **94**:363-374.e4. doi:10.1016/j.neuron.2017.03.037

402. Vierling-Claassen D, Cardin JA, Moore CI, Jones SR. 2010. Computational modeling of distinct neocortical oscillations driven by cell-type selective optogenetic drive: separable resonant circuits controlled by low-threshold spiking and fast-spiking interneurons. *Front Hum Neurosci* **4**:198. doi:10.3389/fnhum.2010.00198

403. Vesuna S, Kauvar I V., Richman E, Gore F, Oskotsky T, Sava-Segal C, Luo L, Malenka RC, Henderson JM, Nuyujukian P, Parvizi J, Deisseroth K. 2020. Deep posteromedial cortical rhythm in dissociation. *Nature* **586**:87–94. doi:10.1038/s41586-020-2731-9

404. Viejo G, Peyrache A. 2020. Precise coupling of the thalamic head-direction system to hippocampal ripples. *Nat Commun* **11**:1–14. doi:10.1038/s41467-020-15842-4

405. Vogt BA. 1984. Afferent specific localization of muscarinic acetylcholine receptors in cingulate cortex. *J Neurosci* **4**:2191–2199. doi:10.1523/jneurosci.04-09-02191.1984

406. Vogt BA, Burns DL. 1988. Experimental localization of muscarinic receptor subtypes to cingulate cortical afferents and neurons. *J Neurosci* **8**:643–652. doi:10.1523/jneurosci.08-02-00643.1988

407. Vogt BA, Miller MW. 1983. Cortical connections between rat cingulate cortex and visual, motor, and postsubicular cortices. *J Comp Neurol* **216**:192–210. doi:10.1002/cne.902160207

408. Vogt BA, Peters A. 1981. Form and distribution of neurons in rat cingulate cortex: Areas 32, 24, and 29. *J Comp Neurol* **195**:603–625. doi:10.1002/cne.901950406

409. Wang C, Chen X, Knierim JJ. 2020. Egocentric and allocentric representations of space in the rodent brain. *Curr Opin Neurobiol*. doi:10.1016/j.conb.2019.11.005

410. Wang G, Xie H, Wang L, Luo W, Wang Y, Jiang J, Xiao C, Xing F, Guan JS. 2019. Switching from Fear to No Fear by Different Neural Ensembles in Mouse Retrosplenial Cortex. *Cereb Cortex* **29**:5085–5097. doi:10.1093/cercor/bhz050

411. Wang Q, Ng L, Harris JA, Feng D, Li Y, Royall JJ, Oh SW, Bernard A, Sunkin SM, Koch C, Zeng H. 2017. Organization of the connections between claustrum and cortex in the mouse. *J Comp Neurol* **525**:1317–1346. doi:10.1002/cne.24047

412. Whishaw IQ. 1985. Cholinergic receptor blockade in the rat impairs locale but not taxon strategies for place navigation in a swimming pool. *Behav Neurosci* **99**:979–1005. doi:10.1037/0735-7044.99.5.979

413. Whishaw IQ, Maaswinkel H, Gonzalez CLR, Kolb B. 2001. Deficits in allothetic and idiothetic spatial behavior in rats with posterior cingulate cortex lesions. *Behav Brain Res* **118**:67–76. doi:10.1016/S0166-4328(00)00312-0

414. White MG, Mathur BN. 2018. Frontal cortical control of posterior sensory and association cortices through the claustrum. *Brain Struct Funct* **223**:2999–3006. doi:10.1007/s00429-018-1661-x

415. Whitesell JD, Liska A, Coletta L, Hirokawa KE, Bohn P, Williford A, Groblewski PA, Graddis N, Kuan L, Knox JE, Ho A, Wakeman W, Nicovich PR, Nguyen TN, van Velthoven CTJ, Garren E, Fong O, Naeemi M, Henry AM, Dee N, Smith KA, Levi B, Feng D, Ng L, Tasic B, Zeng H, Mihalas S, Gozzi A, Harris JA. 2021. Regional, Layer, and Cell-Type-Specific Connectivity of the Mouse Default Mode Network. *Neuron* **109**:545-559.e8. doi:10.1016/j.neuron.2020.11.011

416. Wilber AA, Clark BJ, Forster TC, Tatsuno M, McNaughton BL. 2014. Interaction of egocentric and world-centered reference frames in the rat posterior parietal cortex. *J Neurosci* **34**:5431–5446. doi:10.1523/JNEUROSCI.0511-14.2014

417. Wilson MA, McNaughton BL. 1994. Reactivation of hippocampal ensemble memories during sleep. *Science (80-)* **265**:676–679. doi:10.1126/science.8036517

418. Winkler J, Suhr ST, Gage FH, Thal LJ, Fisher LJ. 1995. Essential role of neocortical acetylcholine in spatial memory. *Nature* **375**:484–487. doi:10.1038/375484a0

419. Witter MP. 2006. Connections of the subiculum of the rat: Topography in relation to columnar and laminar organization. *Behav Brain Res* **174**:251–264. doi:10.1016/j.bbr.2006.06.022

420. Wood ER, Dudchenko PA, Robitsek RJ, Eichenbaum H. 2000. Hippocampal neurons encode information about different types of memory episodes occurring

in the same location. *Neuron* **27**:623–633. doi:10.1016/S0896-6273(00)00071-4

421. Wu R-L, Barish ME. 1992. Two pharmacologically and kinetically distinct transient potassium currents in cultured embryonic mouse hippocampal neurons. *J Neurosci* **12**:2235–2246.

422. Wyss JM, van Groen T. 1992. Connections between the retrosplenial cortex and the hippocampal formation in the rat: A review. *Hippocampus* **2**:1–11. doi:10.1002/hipo.450020102

423. Wyss JM, van Groen T, Sripanidkulchai K. 1990. Dendritic bundling in layer I of granular retrosplenial cortex: Intracellular labeling and selectivity of innervation. *J Comp Neurol* **295**:33–42. doi:10.1002/cne.902950104

424. Xue M, Atallah B V, Scanziani M. 2014. Equalizing excitation-inhibition ratios across visual cortical neurons. *Nature* **511**:596–600. doi:10.1038/nature13321

425. Yamada-Hanff J, Bean BP. 2013. Persistent sodium current drives conditional pacemaking in CA1 pyramidal neurons under muscarinic stimulation. *J Neurosci* **33**:15011–15021. doi:10.1523/JNEUROSCI.0577-13.2013

426. Yamawaki N, Borges K, Suter BA, Harris KD, Shepherd GMG. 2014. A genuine layer 4 in motor cortex with prototypical synaptic circuit connectivity. *Elife* **3**:e05422. doi:10.7554/eLife.05422

427. Yamawaki N, Corcoran KA, Guedea AL, Shepherd GMG, Radulovic J. 2019a. Differential Contributions of Glutamatergic Hippocampal→Retrosplenial Cortical Projections to the Formation and Persistence of Context Memories. *Cereb Cortex* **29**:2728–2736. doi:10.1093/cercor/bhy142

428. Yamawaki N, Li X, Lambot L, Ren LY, Radulovic J, Shepherd GM. 2019b. Long-range inhibitory intersection of a retrosplenial thalamocortical circuit by apical tuft-targeting CA1 neurons. *Nat Neurosci* **22**:618–626. doi:10.1101/427179

429. Yamawaki N, Radulovic J, Shepherd GMG. 2016. A corticocortical circuit directly links retrosplenial cortex to M2 in the mouse. *J Neurosci* **36**:9365–9374.

430. Yamawaki N, Suter BA, Wickersham IR, Shepherd GMG. 2016b. Combining optogenetics and electrophysiology to analyze projection neuron circuits. *Cold Spring Harb Protoc* **2016**:840–847. doi:10.1101/pdb.prot090084

431. Yan HD, Villalobos C, Andrade R. 2009. TRPC channels mediate a muscarinic receptor-induced afterdepolarization in cerebral cortex. *J Neurosci* **29**:10038–10046. doi:10.1523/JNEUROSCI.1042-09.2009

432. Yoder RM, Chan JHM, Taube JS. 2017. Acetylcholine contributes to the

integration of self-movement cues in head direction cells. *Behav Neurosci* **131**:312–324. doi:10.1037/bne0000205

433. Yoshida M, Fransén E, Hasselmo ME. 2008. mGluR-dependent persistent firing in entorhinal cortex layer III neurons. *Eur J Neurosci* **28**:1116–1126. doi:10.1111/j.1460-9568.2008.06409.x

434. Yoshida M, Hasselmo ME. 2009. Persistent firing supported by an intrinsic cellular mechanism in a component of the head direction system. *J Neurosci* **29**:4945–4952. doi:10.1523/JNEUROSCI.5154-08.2009

435. Yoshida M, Knauer B, Jochems A. 2012. Cholinergic modulation of the CAN current may adjust neural dynamics for active memory maintenance, spatial navigation and time-compressed replay. *Front Neural Circuits* **6**:10. doi:10.3389/fncir.2012.00010

436. Yoshimura Y, Callaway EM. 2005. Fine-scale specificity of cortical networks depends on inhibitory cell type and connectivity. *Nat Neurosci* **8**. doi:10.1038/nn1565

437. Yousuf H, Nye AN, Moyer, Jr. JR. 2020. Heterogeneity of Neuronal Firing Type and Morphology in Retrosplenial Cortex of Male F344 Rats. *J Neurophysiol* **123**. doi:10.1152/jn.00577.2019

438. Zannone S, Brzosko Z, Paulsen O, Clopath C. 2018. Acetylcholine-modulated plasticity in reward-driven navigation: a computational study. *Sci Rep* **8**:1–20. doi:10.1038/s41598-018-27393-2

439. Zhang Z, Seguela P. 2010. Metabotropic Induction of Persistent Activity in Layers II/III of Anterior Cingulate Cortex. *Cereb Cortex* **20**:2948–2957. doi:10.1093/cercor/bhq043

440. Zingg B, Dong HW, Tao HW, Zhang LI. 2018. Input–output organization of the mouse claustrum. *J Comp Neurol* **526**:2428–2443. doi:10.1002/cne.24502